Polarimetric Radiometers and their Applications

Søbjærg, Sten Schmidl; Skou, Niels

Publication date:
2003

Document Version
Early version, also known as pre-print

Polarimetric Radiometers and their Applications

Sten Schmidl Søbjærg

Technical University of Denmark, Ørsted-DTU, Electromagnetic Systems

29th November 2002

Summary

A new space borne L-band radiometer, known as SMOS, is currently under phase-B studies at the European Space Agency. With high resolution the instrument is intended for measurements of soil moisture and ocean salinity. The influence from other effect must be known, however, and studies of Earth signatures at L-band are carried out prior to the mission, thus involving assembly of new L-band radiometers as well as field campaigns.

This thesis describes the design and integration of a new airborne radiometer, measuring the full Stokes vector. Initial considerations include evaluation of the influence from the aircraft motion on the measured parameters. It is shown how knowledge of the aircraft attitude to a 0.05° level is necessary, and how corrections can be applied to the measured data. The instrument design involves concept studies, and traditional implementations of polarimetric radiometers are studied. A new radiometer type may be attractive, however, enabled by the availability of new analog to digital converters: the digital subharmonic sampling radiometer. The radiometer has a very simple analog front-end, only with an RF-filter and amplifiers, while all further data processing is moved to the digital domain. The RF is sampled at a lower frequency without down conversion, and it is shown, how a proper selection of the sampling frequency can lead to a combined digitizing and conversion to base band using the well known frequency band aliasing.

The radiometer study is a technology development, opening future perspectives for signal processing, increasing the total radiometer performance, and a digital radiometer has a unique flexibility for reconfiguration. Adaptive filtering of the input signal will provide an opportunity to filter out unidentified RF-interference in the analog pass band, and a band extension beyond the protected 27 MHz bandwidth is thus possible, as well as an active protection within the band. The other perspective is the opportunity to achieve smaller and less power consuming instruments with the digital technique, along with the potential reduction of the front-end drifts, typically the limiting factor for receiver stability.

Based on the study, a radiometer of the digital subharmonic sampling type is constructed, and evaluation of the complete system shows the expected performance in instrument sensitivity. In stability the design goal of 100 mK drift within 15 minutes of operation is reached, and the instrument is thus useable for field campaigns aiming at determination of potential Earth signatures of importance for the SMOS mission.

Field experiments over a land site at Institut National de la Recherche Agronomique in Avignon, France as well as an airborne experiment over Danish ocean target sites are carried out. The Avignon experiment demonstrates the calibration of the EMIRAD radiometer over a period of four month, and it is demonstrated that a calibration within 1 K is achievable. The experiment also proves the presence of polarimetric signatures under special soil conditions, when the instrument is scanned over a range of azimuth look angles. Bare soil, plowed and sowed in a wave pattern of 8 cm height, is shown to give 10 K of peak-to-peak variation in the measured signals, and more than 15 K variation with the look angle is identified in a cornfield with 80 cm crop. The experiments identify both a 1st and a 2nd harmonic component, and thus it is shown, that some polarimetric signatures, known from

measurements of wind driven patterns on the sea surface at higher frequencies, are also present at land sites. The experiment concludes, that a potential risk exist, that results from SMOS may be influenced by these effects, when large homogenous areas are observed.

The other field campaign aimed at identification of eventual wind driven sea surface signatures at L-band. At higher frequencies it is well known, that some Kelvin of variation may result from a 360° azimuth scan, and the effect is important for the SMOS mission in order to evaluate the necessity for a wind direction dependent data correction. As part of the experiment four flights have been carried out; one technical test flight and three scientific flights at wind speeds of 3.6 m/sec., 5.1 m/sec. and 11.0 m/sec, respectively. Methods for correction of the measured signals in order to remove the influence from the aircraft attitude are tested, and it is demonstrated, how a large-scale platform movement, e.g. a ±45° roll variation, may provide a good model for the correction.

For all flights it was noticed, that large noise was still present in the signals after the corrections, and peak-to-peak variations of several Kelvin were noticed. From the first two scientific flights, no azimuth signatures were identified, and the data analysis indicated, that derived azimuth directions resulted from a random distribution. A conclusion based on these data is not possible, however, as the statistical background is too small compared to the amount of noise. For the high-wind case a larger number of circles were measured, and the flight altitude was varied in order to investigate, if a larger antenna footprint, i.e. a larger spatial integration, would decrease the noise. The data shows, however, that no decrease can be proven, and instead the circles are treated as equal samples of the same sea pattern. Averaging shows, that the 2nd, 3rd and 4th Stokes parameters have a random behavior, and from the statistical analysis it is seen, that less then 30 mK of harmonic magnitude can be identified in the parameters. Due to the limited number of signatures, however, the statistical uncertainty of this value is large, and additional experiments are needed to improve the precision.

The 1st Stokes parameter has a clear 490 mK 2nd harmonic component. It is shown, however, that the signature has a significant correlation with the downwelling galactic background radiation as a function of the azimuth look angle, and a calculation of the background level for one of the circles shows, that a significant fraction of the signature can be removed. The effect must be subject for further investigation, however, and individual corrections for all measured data must be modeled in order to correct the SMOS data.

Resumé

Et nyt rumbaseret L-bånds radiometer, kendt som SMOS, er under igangværende fase-B studier hos det Europæiske Rumagentur, ESA. Instrumentet er tiltænkt målinger af jordfugtighed samt saltholdighed i havet med høj opløsning. Indflydelse fra eventuelle andre effekter skal dog kendes, og studier af signaturer fra jorden ved L-bånd udføres forud for missionen, hvilket således involverer opbygning af nye L-bånds radiometre såvel som feltkampagner.

Denne afhandling beskriver designet og integrationen af et nyt luftbårent radiometer, der måler den fulde Stokes vektor. Forundersøgelser involverer bestemmelse af betydningen af flyets bevægelser for de målte værdier. Det er vist, hvorledes kendskab til flyets orientering ned til et 0,05° niveau er nødvendig, og hvordan korrektioner kan udføres på måledata. Instrumentdesignet omfatter konceptstudier, og traditionelle opbygninger af polarimetriske radiometre undersøges. En ny radiometertype kan dog være interessant, muliggjort af tilgængeligheden af nye analog-til-digital-konvertere: Det digitale radiometer med subharmonisk sampling. Radiometeret har en meget simpel analog frontsektion, kun med et RF-filter og forstærkere, mens al videre databehandling er flyttet til det digitale domæne. RF samples med en lav frekvens uden nedkonvertering, og det illustreres, hvorledes et hensigtsmæssigt valg af samplingsfrekvens kan føre til en kombineret digitalisering og konvertering til basisbånd ved benyttelse af velkendt frekvensbåndsaliasering.

Radiometerstudiet er en teknologiudvikling, der åbner fremtidige perspektiver for signalbehandling, der forøger radiometres samlede ydeevne, og et digitalt radiometer har en unik fleksibilitet for rekonfigurering. Adaptiv filtrering af inputsignalet vil give en mulighed for at frafiltrere uidentificeret RF-interferens i det analoge pasbånd, og såvel en udvidelse hinsides de beskyttede 27 MHz båndbredde som en aktiv beskyttelse indenfor dette bånd er således mulig. Det andet perspektiv er muligheden for at opnå fysisk mindre og mindre strømforbrugende instrumenter med den digitale teknik, sammen med den potentielle reduktion af drift i frontsektionen, som typisk er den begrænsende faktor for modtagerens stabilitet.

Med baggrund i undersøgelserne opbygges et radiometer at den subharmoniske sampling type, og en evaluering af det samlede system viser den forventede instrumentfølsomhed. For stabiliteten er designmålet på maksimum 100 mK drift indenfor 15 minutters operation nået, og instrumentet er således brugbart til feltkampagner, der stiler efter bestemmelse af potentielle jordsignaturer med betydning for SMOS missionen.

Felteksperimenter over et landområde på Institut National de la Recherche Agronomique i Avignon i Frankrig såvel som et luftbårent eksperiment over danske havområder er udført. Avignon-eksperimentet demonstrerer kalibreringen af EMIRAD radiometeret over en periode på fire måneder, og det vises, at en absolut kalibrering indenfor 1 K er opnåelig. Eksperimentet efterviser også tilstedeværelsen af polarimetriske signaturer under specielle jordforhold, når instrumentet skannes over et interval af azimuth-observationsretninger. Bar jord, pløjet og sået i et bølgemønster med en højde på 8 cm, vises at resultere i et målt signal med 10 K variation fra yderpunkt til yderpunkt, og mere end 15 K variation som funktion af

observationsretningen kan identificeres, når majsafgrøden har nået en højde på 80 cm. Eksperimenterne identificerer såvel en 1. som en 2. harmonisk komponent, og således vises det, at polarimetriske signaturer, kendt fra målinger af vindmønstre over havet ved højere frekvenser, også er til stede på landområder. Fra eksperimentet kan det konkluderes, at der er en potentiel risiko for, at SMOS' resultater påvirkes af disse effekter, når store, homogene landområder observeres.

Den anden feltkampagne sigtede på identifikation af eventuelle vinddrevne havoverflade-signaturer ved L-bånd. Ved højere frekvenser er det velkendt, at nogle Kelvin variation vil forekomme ved et 360° azimuthskan, og effekten er vigtig for SMOS missionen for at vurdere nødvendigheden af en vindretningsafhængig dataopretning. Som en del af eksperimentet blev udført fire flyvninger; en teknisk testflyvning og tre videnskabelige flyvninger ved vindhastigheder på henholdsvis 3,6 m/s, 5,1 m/s og 11,0 m/s. Metoder til opretning af de målte signaler med hensyn til indflydelsen fra flyets bevægelser er undersøgt, og det er vist, hvorledes flybevægelser i stor skala, f.eks. en ±45° roll variation, kan give en god model for korrektionen.

For alle flyvninger blev det bemærket, at et stort støjsignal stadig var til stede efter opretningerne, og yderpunktsvariationer på indtil flere Kelvin blev set. Fra de første to videnskabelige flyvninger blev der ikke identificeret nogen polarimetrisk signatur, og dataanalysen tydede på, at de fundne retninger for azimuthsignaturer var tilfældige. En egentlig konklusion baseret på disse data er dog ikke mulig, da det statistiske materiale er for ringe sammenlignet med støjen. På flyvningen med den høje vindhastighed blev flere cirkler målt, og flyvehøjden blev varieret for at undersøge, om et større måleområde, dvs. en større rumlig integration, ville reducere støjen. Data viser dog, at ingen reduktion kan eftervises, og i stedet behandles cirklerne som ækvivalente udfald fra den samme havoverflade. Midling viser, at 2., 3. og 4. Stokes parameter opfører sig som et tilfældigt signal, og det vises, at sandsynligvis mindre end 30 mK stammer fra deterministiske, harmoniske signaler. På grund af det ringe antal signaturer er der dog stor statistisk usikkerhed på dette resultat, og yderligere eksperimenter behøves for at forbedre præcisionen.

Den 1. Stokes parameter har en tydelig 490 mK 2. harmonisk komponent. Det vises dog, at signaturen har en betydelig korrelation med den nedfaldende kosmiske baggrundsstråling som funktion af observationsvinklen, og beregning af baggrundsniveauer for én af cirklerne viser, at en betydelig del af signaturen kan fjernes. Effekten må dog underkastes yderligere undersøgelser, og individuelle korrektioner til alle målte data skal modelleres med henblik på at oprette data fra SMOS.

Preface

The present Ph.D. study was carried out from February 1st, 1999 to November 29th, 2002 at the Danish Center for Remote Sensing. The center is a part of the Electromagnetic Systems section at the Ørsted-DTU department at the Technical University of Denmark, Copenhagen. The effective study period has been 36 month, as a total of 10 month of leave is included in the period mentioned above. These periods of leave have been spent at the Danish Center for Remote Sensing, assisting the digital system design group developing a high-speed digital front end with 2 GHz sampling for their future synthetic aperture radar system.

Five month of the Ph.D. study has been spent at Institut National de la Recherche Agronomique, Avignon, France. One month in March 1999 concerned the field measurement with the MIRAS radiometer, an L-band synthetic aperture radiometer, developed by the European Space Agency. One month was spent on experiment planing and preparation at the INRA test site in November 2000, and additional three month, from April 2001 to June 2001, were spent on field measurements at the test site, using the EMIRAD radiometer, developed as a part of the Ph.D. study.

The present study is closely related to ongoing studies at the European Space Agency concerning the L-band radiometer mission SMOS, currently under phase-B studies.

To this thesis five selected papers are appended. The papers are written or contributed to as a part of the Ph.D. study, and they are closely linked to the studies, described in the thesis. Two papers describe the special problems with synchronization of analog to digital converters, and two papers describe the complete EMIRAD polarimetric radiometer system, including instrument evaluations. The last paper describes some preliminary results of the EMIRAD airborne campaign. Three conference and workshop presentations without paper submission were given during the study, all concerning different stages of the data analysis from the airborne campaign.

Professor Niels Skou acted as project supervisor.

Thesis Overview

The thesis is naturally divided in four parts. Chapter 1 and 2 give a short introduction to the project, and some basic parameters of the EMIRAD L-band radiometer are defined. Likewise general considerations are made with respect to the installation of a new polarimetric radiometer on a moving platform. Chapter 3 and 4 present the implementation of polarimetric radiometers, and different classical radiometers are compared to the new concept: the digital radiometer with subharmonic sampling. Chapter 3 gives an end-to-end analysis of the theory behind this new radiometer, and a list of advantages and drawbacks is presented, resulting in the choice for this implementation. Chapter 4 describes the technical details in the implementation and the considerations about each building block of the complete system. The chapter also includes a thorough system test, evaluating the instrument with respect to field applications.

The third part of the thesis includes chapter 5 and 6, and they give a description of the two field campaigns, involving the EMIRAD radiometer. Chapter 5 concerns the installation over the Avignon land site, and it leads to a precise evaluation of the long-term stability of the instrument as well as an analysis of polarimetric signatures from the land surface. Chapter 6 presents the airborne circle flight campaign, aiming at identification of wind driven polarimetric signatures from the ocean surface at L-band. Chapter 7 and 8 form the last thesis part, chapter 7 giving a general discussion of the instrument implementation and the field experiments, and chapter 8 concluding the work.

Acknowledgements

First of all I want to thank Professor Niels Skou and the Danish Center for Remote Sensing for hosting the Ph.D. study. I want to thank all the DCRS group for their assistance during the work, and a special thanks goes to Jesper Rotbøll, who contributed to many details of the EMIRAD radiometer assembly, from analog component characterization to the full mechanical design of the instrument. Likewise I want to thank Dr. Brian Laursen for his assistance to get the project work started.

My warm thoughts go to Dr. David M. LeVine, Goddard Space Flight Center, Greenbelt, and Dr. Chris Ruf, University of Michigan, for always interesting and inspiring dialogs during their stay at the Danish Center for Remote Sensing. And special thanks to Dr. David M. LeVine for his valuable help with the data analysis of the wind driven signatures, and for his calculation of downwelling galactic background radiation.

For an interesting and valuable stay in Avignon I want to thank Dr. Jean-Pierre Wigneron, who arranged the campaign at Institut National de la Recherche Agronomique and contributed financially to the experiment. I want to thank the entire INRA team for their daily assistance during the campaign, and special thanks to Dr. André Chanzy for opening his department to me. Thanks also to Alla Petrovna Søbjærg for her help with the in-situ data collection during the campaign.

DHI Water and Environment and Vagner Jacobsen as well as Mærsk Oil and Gas Inc. are acknowledged for providing meteorological data from the oilrigs in the North Sea. The information is important in-situ data for the interpretation and understanding of the results from the airborne campaign. Finally I want to acknowledge the Technical University of Denmark for their financial support to the Ph.D. study. Thanks to the European Space Agency for supporting the airborne campaign financially, and thanks to the Royal Danish Air Force for providing the necessary aircraft support for the campaign.

Technical University of Denmark
Lyngby, November 29th, 2002

Sten Schmidl Søbjærg

List of papers

The following papers, appended to this thesis, have been written or contributed to as a part of the Ph.D. study. The total work load for the two papers (A) and (D) has been approximately 50%, and for both papers, the main contribution as well as the conference presentation has been done by the first author. For the papers (B) and (C) the contents is fully based on the work and design done within the Ph.D. project. The first author has implemented the design. The first and second author have contributed equally to the paper writing, and both have been present at the conference presentation. The paper (E) is based on the first results of the airborne campaign, and all contents is based on the work of the Ph.D. study.

A. Sten Schmidl Søbjærg & Erik Lintz Christensen
”2 GHz Self-aligning Tandem A/D Converter for SAR”
Proceedings of IGARSS’01, vol. V, pp. 2028-2030, July 2001.

B. Jesper Rotbøll, Sten Schmidl Søbjærg & Niels Skou
”L-Band Polarimetric Correlation Radiometer with Subharmonic Sampling”
Proceedings of IGARSS’01, vol. IV, pp 1571-1574, July 2001.

C. Jesper Rotbøll, Sten Schmidl Søbjærg & Niels Skou
”A novel L-band polarimetric radiometer featuring subharmonic sampling”
Special issue of Radio Science, accepted, in press.

D. Jørgen Dall, Sten Schmidl Søbjærg & Erik Lintz Christensen
“Synchronization of tandem A/D converter for SAR”
Proceedings of EuSAR 2002, pp 323-326.

E. Sten Schmidl Søbjærg, Jesper Rotbøll & Niels Skou
“L-band polarimetric radiometer measurement of wind signatures on the sea surface”
Proceedings of IGARSS’02, pp. 1364-1366, July 2002.

List of papers

The following conference and workshop presentations without paper submission have been given as a part of the Ph.D. study:

A. Sten Schmidl Søbjærg, Jesper Rotbøll and Niels Skou
"L-band polarimetric radiometer measurement of wind signatures on the sea surface"
Specialist meeting on microwave remote sensing,
5-9 November 2001, Millennium Hotel, Boulder, Colorado

B. Sten Schmidl Søbjærg & Niels Skou
"Airborne Polarimetric L-band Radiometer Calibration and Motion Compensation"
Second International Microwave Radiometer Calibration Workshop, uCal 2002,
9-11 October 2002, Universitat Politècnica de Catalunya, Barcelona, Spain

C. Sten Schmidl Søbjærg & Niels Skou
"L-band Ocean Salinity Airborne Campaign, LOSAC"
Campaign Workshop, First results of WISE/EuroSTARRS/LOSAC
4-6 November 2002, CESBIO, Toulouse, France

Contents

1. Introduction

Polarimetric radiometers have been used over the past decade to identify and characterize geophysical properties. At the Technical University of Denmark, DTU, polarimetric radiometers, operating at 16 GHz and 34 GHz have been successfully implemented and operated during airborne campaigns. Previous projects over the world [1-6] aimed at measuring the wind driven signal from the ocean surface and demonstrate the possible extraction of the wind direction from the polarimetric signature, combining frequencies, and using a model function for the brightness temperature as a function of the azimuth look angle relative to the wind direction.

Radiometers at lower frequencies may be used to recognize properties like soil moisture over land areas and sea surface salinity, SSS [7]. A project for these purposes, known as the MIRAS, Microwave Imaging Radiometer with Aperture Synthesis, demonstrator project, has previously been carried out at the European Space Agency, ESA, demonstrating potentials for a future space borne radiometer, and some initial results have been produced [8].

Figure 1.1. The MIRAS demonstrator, operated by the European Space Agency in order to demonstrate the potential for a future space borne L-band radiometer.

The space borne mission, known as SMOS, Soil Moisture and Ocean Salinity [9-12], is currently under phase-B studies at ESA, and it is planed for launch by the end of 2006. A picture simulation of the complete instrument is shown in figure 1.2 [13]. The instrument is planed to operate within the protected L-band, ranging from 1400 MHz to 1427 MHz, and like MIRAS it will be a two-dimensional synthetic aperture radiometer, SARad [14, 15], using a large number of small antennas in a Y-shape to synthesize a larger antenna. With three arms having a length of 4.3 meters each and an array of correlators, the SMOS instrument will be an imaging radiometer, producing a number of snapshots of the scene, it passes over.

To extract the desired geophysical parameters from the images produced by SMOS, model functions must exist for the different types of scenes, and eventual other parameters, influencing in the received signals, must be known. For both ocean and land scenes some

model functions exist [16-20], but some important contributors to the total signals are not well modeled, and it is unknown, if they may cause problems for the parameter retrieval from the SMOS images.

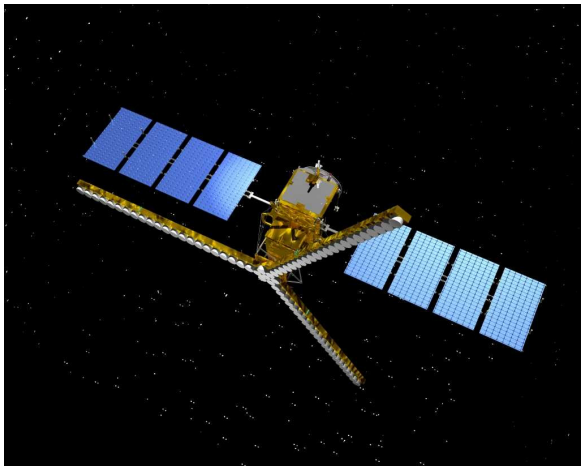

Figure 1.2. Simulation of the soil moisture and ocean salinity, SMOS, instrument, scheduled for launch by the European Space Agency in 2006.[13]

For the ocean measurements, one of these contributors is expected to be the wind driven surface pattern, and with the experience from the work at higher frequencies, it is likely, that signals may vary with the azimuth look direction, relative to the wind. It is unknown, however, if the magnitude will be large enough to influence the measurement results, and no field measurements can presently provide information about it. Wave patterns in general are typical contributors to radiometric signals, and for the measurements over land - and especially over agricultural land - the possibility exist, that wave patterns, e.g. from plowing and crops in row structures, will add a significant contribution to the total result.

To investigate some of these unknown parameters, the need for new polarimetric L-band radiometers rises, and this project will participate in filling some of the voids. The project is launched as a combined study of technology and geoscience, and the results are thus a combination of collected background information, technology development, field work and scientific data analysis, which is found in the following chapters.

Chapter two will give a short introduction to classic and polarimetric radiometry, introducing the Stokes vector in its two forms. Radiometer calibration will be introduced, and special focus will be on the determination of polarimetric channels, third and fourth Stokes parameters. The measurement situation for the present measurement campaigns is analyzed, and demands for the new radiometer are identified. Some special problems appear, when polarimetric radiometers are mounted on a moving platform like an aircraft, as the attitude will change continuously during the flight track. These problems are analyzed with respect to the present radiometer setup, and methods for motion compensation are introduced.

The practical implementation of polarimetric radiometers is discussed in chapter three, and different well-known configurations as well as the new subharmonic sampling radiometer are introduced. A deeper analysis of the properties of the new radiometer type is carried out with special focus on linearity, sensitivity, and stability. It is shown, how relatively simple digital processing can be used for implementation of a full polarimetric radiometer, using only two

analog channels and taking benefit from a digital inphase/quadrature demodulation. Finally subjects like offset adjustment and phase coherence are discussed, and solutions are provided for the radiometer implementation. The chapter is concluded with a summary of advantages and drawbacks of the digital radiometer, selecting this radiometer type for the implementation of the EMIRAD L-band radiometer.

Chapter four describes the actual implementation of the radiometer, and some technical details are investigated regarding the electronics and mechanical engineering. The chapter shows the different parts of the radiometer system, and a complete system construction and description is made from end to end, including calibration system, analog electronics, digital front-end, data transfer and control software. Initial tests of essential components are shown, and the chapter is concluded with a full linearity control measurement as well as a system calibration and stability test, proving if the instrument is suited for the scientific campaigns.

The scientific fieldwork is centered in the chapters five and six. Chapter five describes the five-month measurement campaign, which was carried out in corporation with Institut National de la Recherche Agronomique, INRA, in Avignon, France. The purpose of the experiment is double. A group at INRA works on modeling the brightness temperature from land surfaces as a function of the soil moisture [18-20], taking into account the effect from several other contributors, such as vegetation bio mass, field crop type, surface condition etc. These analyses are beyond the scope of this project, and the primarily focus of the chapter is on eventual polarimetric signatures, which may add a contribution to the brightness temperature, measured by SMOS. From a technical point of view, the Avignon campaign is also a test site for long term calibration of the instrument, and some considerations are made, concerning these issues.

The primary scientific campaign of the EMIRAD radiometer is, however, the measurement of eventual polarimetric signatures from the sea surface, and a description of the flights and the results is given in chapter six. The analysis involves calibration, stability checks during the flights, as well as motion compensation as mentioned in chapter two. For the different steps of processing, a software package is developed, and the final results from three flights are processed and presented. A discussion of the results follow, and details about the recorded signatures are discussed.

The technical and scientific work is discussed as a whole in chapter seven and suggestions for future work is presented with background in the achieved results. Comments on the implemented radiometer type and the scientific campaigns are made in the end of this section. General conclusions regarding the total project follow in chapter eight.

2. Polarimetric radiometry

This chapter introduces the traditional and the polarimetric radiometry. After a short general introduction to brightness temperature measurements and apparent brightness temperatures, the polarimetric radiometry is presented. Stokes vector, often used to characterize a polarimetric signal, is introduced, and the two forms of the vector are shown. Calibration of radiometers is discussed, and needs for the new EMIRAD radiometer are identified on the background of SMOS. Finally, some special problems of radiometer installation on a moving platform are identified, e.g. during an airborne field campaign, and the influence of the motion on the measured parameters is analyzed.

2.1. Basic radiometry

Radiometry is basically the measurement of natural, thermal radiation from objects. The radiation density, the brightness, of an object depends on the nature of the object, and for a black body, the radiation will be given by Planck's radiation law [21]. In the microwave frequency range Planck's law may be approximated with Rayleigh-Jeans law, shown in equation 2.1, where k is Boltzmann's constant ($k = 1.38*10^{-23}$ J/K), λ the wavelength of observation, and T the physical temperature of the object.

$$B_{bb} = \frac{2kT}{\lambda^2} \tag{2.1}$$

Non-black objects reflect a part of the incident radiation, and as they absorb less energy, the emission is likewise reduced, in order to maintain thermal stability. The emission from such objects in the direction (θ,φ) is characterized by the emissivity, $e(\theta,\varphi)$, as shown in equation 2.2, expressing the emission relative to the emission from a black body with the same physical temperature.

$$e(\theta,\varphi) = \frac{B(\theta,\varphi)}{B_{bb}} = \frac{T_B(\theta,\varphi)}{T} \tag{2.2}$$

It is seen that the brightness may be replaced by the brightness temperature, $T_B(\theta,\varphi)$, using 2.1, and usually this parameter is used to characterize objects under observation. For an antenna covering a fraction of the total angular space, the received power will be given by the integral of the brightness over the antenna pattern in a limited bandwidth, B, and for an antenna with a single polarization, only half of the total power will be received.

The apparent brightness temperature at the antenna is the composed brightness temperature from all objects, contributing to the total power. Figure 2.1 illustrates a typical situation, when an antenna observes a plain surface. The apparent brightness temperature will be given by equation 2.3, where T_d is the downwelling radiation from the atmosphere and from space, T_b is the brightness temperature of the surface, and T_l is the temperature of the atmosphere, being a possible loss on the radiation path to the antenna. The loss is given by η, and the reflection coefficient at the surface is ρ.

$$T_{AP} = (1-\eta)T_l + \eta(T_b + \rho T_d) \tag{2.3}$$

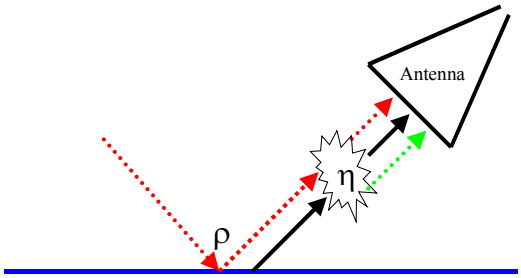

Figure 2.1. A typical measurement situation. The received power is a composite of contributions from different objects, reflected and attenuated.

A radiometer is a receiver, calibrated to measure the incident power at the antenna, and a simple setup is shown in figure 2.2. The square law detector is used in order to calculate the signal power directly from the electric field, collected by the antenna.

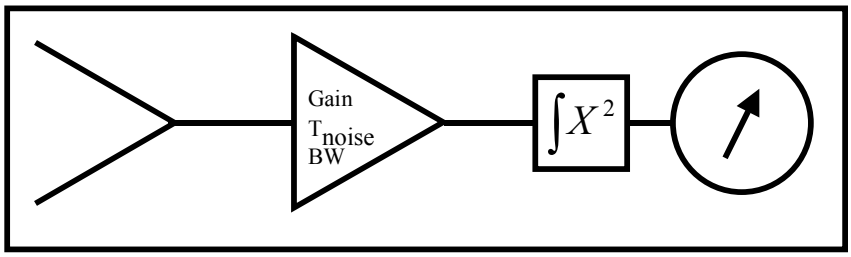

Figure 2.2. A simple radiometer, measuring the power, received by the antenna in the bandwidth, BW, multiplied by the gain, G, and added to the noise temperature, T_{noise}.

The instrument output is determined by the Gain, G, the receiver noise, T_{noise}, and the bandwidth of the receiver, and the output is given by equation 2.4, following from 2.1 after the spatial integration and polarization of the antenna and the bandwidth of the receiver.

$$P = k \cdot B \cdot G \cdot \left(T_{AP} + T_{noise}\right) \tag{2.4}$$

2.2. Polarimetric radiometry

As mentioned above, the signal received by the radiometer antenna depends on the antenna polarization. Two different, independent measurements will thus result from measurements with a horizontally polarized antenna and a vertically polarized antenna. The two brightness temperatures are referred to as T_H and T_V, respectively, and added together, they will represent the full incident power to the antenna. The difference T_V - T_H indicates, if the signal is unpolarized, i.e. random polarized, or if one of the polarizations is dominant, e.g. due to the reflection geometry of the object under observation.

The geometry is not necessarily oriented in a horizontal/vertical structure, and independent information will origin from $T_{45} - T_{-45}$, describing the difference brightness temperature from an antenna system tilted 45° relative to horizontal and vertical. Likewise independent information will originate from $T_r - T_l$, where T_r and T_l represent the right handed and left

handed polarizations, respectively. All in all this leads to Stokes vector [22], defined in equation 2.5.

$$\overline{T_B} = \begin{pmatrix} I \\ Q \\ U \\ V \end{pmatrix} = \begin{pmatrix} T_V + T_H \\ T_V - T_H \\ T_{45^o} - T_{-45^o} \\ T_l - T_r \end{pmatrix} \tag{2.5}$$

From equation 2.1 follows 2.6, describing the vertical and the horizontal brightness temperatures, when the wave propagates in a medium with the impedance z.

$$\begin{aligned} T_V &= \frac{\lambda^2}{kz}\left\langle E_V^2 \right\rangle \\ T_H &= \frac{\lambda^2}{kz}\left\langle E_H^2 \right\rangle \end{aligned} \tag{2.6}$$

The two components of the 3rd Stokes parameter may be derived from the horizontal and vertical polarization as described in 2.7 and 2.8.

$$\begin{aligned} T_{45} &= \frac{\lambda^2}{2kz}\left\langle (E_V + E_H)(E_V + E_H)^* \right\rangle \\ &= \frac{\lambda^2}{2kz}\left\langle \left(E_V E_V^* + E_V E_H^* + E_H E_V^* + E_H E_V^*\right) \right\rangle \\ &= \frac{\lambda^2}{2kz}\left\langle \left(E_V E_V^* + 2\,\mathrm{Re}\left(E_V E_H^*\right) + E_H E_V^*\right) \right\rangle \\ &= \frac{1}{2}T_V + \frac{1}{2}T_H + \frac{\lambda^2}{2kz}\left\langle \left(2\,\mathrm{Re}\left(E_V E_H^*\right)\right) \right\rangle \end{aligned} \tag{2.7}$$

$$\begin{aligned} T_{-45} &= \frac{\lambda^2}{2kz}\left\langle (-E_V + E_H)(-E_V + E_H)^* \right\rangle \\ &= \frac{\lambda^2}{2kz}\left\langle \left(E_V E_V^* - E_V E_H^* - E_H E_V^* + E_H E_V^*\right) \right\rangle \\ &= \frac{\lambda^2}{2kz}\left\langle \left(E_V E_V^* - 2\,\mathrm{Re}\left(E_V E_H^*\right) + E_H E_V^*\right) \right\rangle \\ &= \frac{1}{2}T_V + \frac{1}{2}T_H - \frac{\lambda^2}{2kz}\left\langle \left(2\,\mathrm{Re}\left(E_V E_H^*\right)\right) \right\rangle \end{aligned} \tag{2.8}$$

It follows, that the 3rd Stokes parameter, U, can be expressed as 2.9, and likewise by multiplying E_V with $e^{-\pi/2}$, the 4th Stokes parameter, V, can be expressed as 2.10.

$$U = \frac{\lambda^2}{kz}\left\langle 2\,\mathrm{Re}\left(E_V E_H^*\right) \right\rangle \tag{2.9}$$

$$V = \frac{\lambda^2}{kz}\left\langle 2\,\mathrm{Im}\left(E_V E_H^*\right) \right\rangle \tag{2.10}$$

From 2.6, 2.9, and 2.10 follows the definition of the full stokes vector, expressed by electrical field vectors in equation 2.11.

$$\overline{T_B} = \begin{pmatrix} I \\ Q \\ U \\ V \end{pmatrix} = \begin{pmatrix} T_V + T_H \\ T_V - T_H \\ T_{45^o} - T_{-45^o} \\ T_l - T_r \end{pmatrix} = \frac{\lambda^2}{k \cdot z} \begin{pmatrix} \langle E_V^2 \rangle + \langle E_H^2 \rangle \\ \langle E_V^2 \rangle - \langle E_H^2 \rangle \\ 2\,\mathrm{Re}\langle E_V E_H^* \rangle \\ 2\,\mathrm{Im}\langle E_V E_H^* \rangle \end{pmatrix} \tag{2.11}$$

The sensitivity, ΔT, for a simple radiometer as shown in figure 2.2 is given by 2.12 [23], where τ is the observation time, B the signal bandwidth, T_A the apparent temperature, and T_N the receiver noise temperature.

$$\Delta T = \frac{T_A + T_N}{\sqrt{B\tau}} \tag{2.12}$$

For the Stokes parameters, all defined as a sum or a difference between two brightness temperatures, the sensitivity will be given as 2.13, where the square root of 2 origins from the stochastic nature of the signals.

$$\Delta I = \Delta Q = \Delta U = \Delta V = \sqrt{2}\,\frac{T_A + T_N}{\sqrt{B\tau}} \tag{2.13}$$

2.3. Radiometer calibration

Calibration of the radiometer receiver is necessary for the interpretation of the output data. The basic parameters, such as the radiometer bandwidth, the receiver gain, and the receiver noise must be determined in order to evaluate the apparent brightness temperature, T_A. Like any other instrument, the radiometer may be calibrated by application of a known input brightness temperature to the antenna followed by measurement of the output. When sufficient points are measured, the transfer function of the instrument is known, and the radiometer is ready for operation.

Practically the calibration of radiometers is more complicated, and some problems must be considered. The radiometer bandwidth, B, is determined by the sum of filters in the receiver, and for normal operating temperature changes, the bandwidth may be assumed constant. The gain and the noise temperature, however, typically change with the physical temperature of the receiver components, thus changing the output. A full model of the behavior of every component as a function of its operating conditions might be made up, but for practical applications, this approach is not useable. Uncertainties might add up, giving a very poor calibration.

The other approach, used in all practical radiometers, is temperature stabilization of the full receiver, keeping the changes of the receiver characteristics at a low level. Assuming receiver linearity, a single two-point calibration of the output voltage as a function of the input brightness temperature will then be sufficient, and the radiometer will be ready for operation. For a full end-to-end calibration, large-scale references will be needed, however, as the full antenna aperture should observe a homogenous, known target. This is typically done with an absorbing material, behaving like a black body at the radiometer operating frequency. Stabilizing the absorber at the desired physical temperature thus provides a known brightness temperature to the radiometer. Problems may occur to keep the temperature stabilized, and

generally the full calibration is only suitable in the laboratory, but not when the radiometer is operated in the field.

Despite of the temperature regulation of the receiver, long-term drifts may change the transfer function, and in the field the receiver block may be calibrated using some switches between the amplifiers and the antenna, thus applying known brightness temperatures to the temperature sensitive section. Correction for components in front of the switches are then applied later by reversal of equation 2.14, where η is the front-end component loss, T_L their physical temperature, and T_A the apparent antenna temperature [21].

$$T_M = \eta \cdot T_L + (1-\eta)T_A \qquad (2.14)$$

The frequency of observation of the calibration references is determined by the purpose of the radiometer and the demands for precision. Frequent calibration will provide better knowledge of the precise receiver parameters, but it will reduce the antenna observation time, thus reducing the radiometer sensitivity according to equation 2.12 and 2.13. For some airborne or space borne measurement situations calibration is not possible during mapping, as the calibration sequence will lead to missing information in the image. For these radiometers it is essential, that a useful calibration can be carried out right before and right after the map, and that the receiver is stabilized during the target observation.

A typical setup is illustrated in figure 2.3, where a temperature stabilized receiver is calibrated using a black body reference target along with a noise diode to add a known portion of noise to the input signal. The situation will provide two calibration points, which is enough to calibrate the receiver within its linear range.

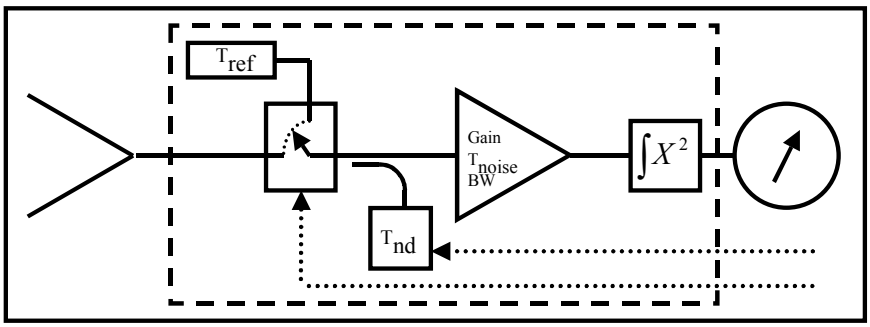

Figure 2.3. A simple radiometer calibration setup, providing two calibration points; the black body reference and the reference plus a well defined power from the noise diode. The receiver is temperature stabilized within the dotted frame.

2.4. Definition the new EMIRAD L-band radiometer

The new EMIRAD L-band radiometer will be part of the preparation for the "Soil Moisture and Ocean Salinity", SMOS, mission, currently under phase-B studies at the European Space Agency, ESA. Prior to the mission information about a range of geophysical parameters have to be studied in order to understand their contribution to the finally measured brightness temperatures. Primary parameters are - as indicated in the mission name - soil moisture and ocean salinity. But as other effects may influence on the brightness temperature, it is essential

to understand these effects in order to correct for their contributions, at least to the level of desired accuracy of the primary parameters.

For measurements of the ocean, the brightness temperature towards the radiometer depends on the salinity, the water temperature and on the frequency band of the radiometer, as well as on the incidence angle and the surface roughness. The Klein-Swift model [16] describes the dependence on frequency, sea surface salinity (SSS), water temperature, and incidence angle. Figure 2.4 shows a plot of the brightness temperature as function of the sea surface salinity for typical values of the parameters, frequency = 1.4135 GHz, Temperature = 20.0° C, and incidence angle = 35°.

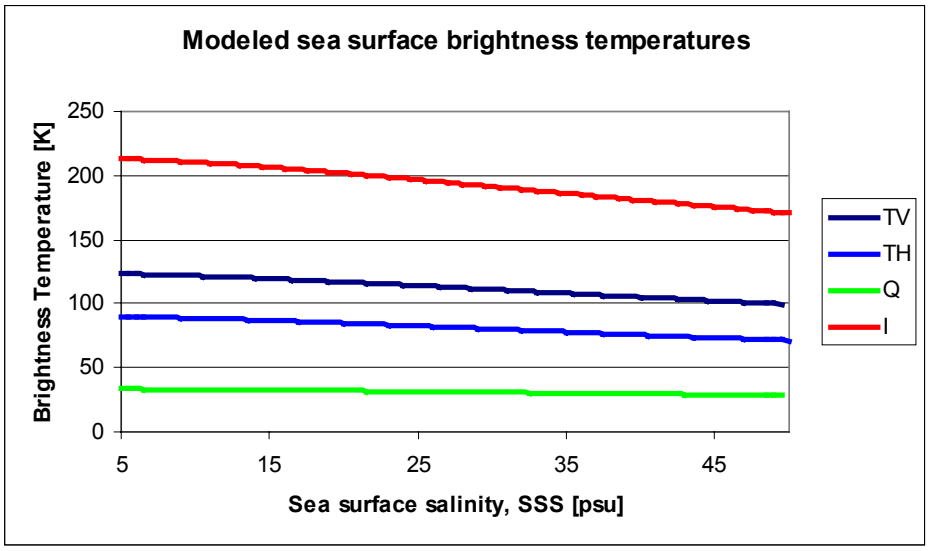

Figure 2.4. Klein-Swift model of sea surface brightness temperature as a function of the sea surface salinity, when frequency = 1.4135 GHz, temperature = 20.0 °C, and incidence angle = 35 °. The curves show the vertical and horizontal brightness temperatures and the two first Stokes parameters, I and Q.

The ocean measurements from SMOS are expected to provide oceanographic research with information on layer processes and ocean currents, and the scientific goal for the salinity accuracy is 0.1 psu [7, 9, 10]. From figure 2.4 it is seen, that the brightness temperature sensitivity to the salinity is of the order of 1.0 K/psu in best cases, demanding a necessary precision for all remaining parameters to this level.

As the frequency band may be assumed constant, and as the sea surface temperature is well monitored by existing space borne sensors, these effects may be corrected to the desired accuracy. The wind driven surface roughness, however, is not well understood at L-band, and no model describing the azimuth signatures at these frequencies exist. Models used at higher frequencies [17] can be extrapolated to 1.4 GHz, but results are not consistent, and no field measurements exist for verification.

A potential problem for SMOS measurements is thus, that the wind driven signal may be larger then the desired 0.1 K, and that no sufficient information on the wind direction dependence is available for correction. To investigate these problems, ESA supports a

number of campaigns, targeting ocean measurements at different wind conditions. The WISE, wind and salinity experiment [24], targets measurements of the sea surface brightness temperature at different incidence angles and different wind speeds from the Casablanca oilrig in the western Mediterranean Sea, approximately 50 km off the coast of Spain. The LOSAC, L-band Ocean Salinity Airborne Campaign [25], targets the determination of an eventual azimuth signature, and for this measurement, the new EMIRAD L-band radiometer will be used.

The ideal situation for the azimuth signature characterization is one snapshot of a single spot on the sea surface, measured from all azimuth angles and a range of incidence angles simultaneously. As this desire is unrealistic in real measurement situations, a number of compromises have to be made, and some compromises relate directly to the instrument under development.

Mounting the radiometer fixed in a side-looking position in the aircraft, a full 360° signature can be obtained by flying a circle pattern, letting the radiometer observe the same spot on the sea surface from all sides. During this measurement any change in the radiometer calibration, i.e. drift, as well as changes of the sea surface will directly influence the output result. Assuming a constant sea surface, the design target for the EMIRAD radiometer is a maximum drift of 0.1 K during the acquisition of a full circle.

The flight time for a circle pattern depends on the aircraft type as well on the acceptable aircraft roll angle during the data take. A C-130 aircraft from the Royal Danish Air Force, RDAF, is available for the measurements, and it will be able to carry the weight of the radiometer. For this aircraft a circle with constant roll angle equal to 5° will take approximately 15 minutes, which will be the overall design target for the radiometer stability.

2.5. Platform attitude and motion compensation

An important issue in polarimetric measurements is the orientation of the antenna relative to the object being measured. The first Stokes parameter, I, is the total power, and for the measurement of this value two antennas with orthogonal polarizations are needed. The other parameters also demand two orthogonal polarizations, but requirements are also related to the orientation of the antennas. The linear polarizations, Q and U, use similar antennas, and only a rotation of the antenna system defines the difference between the two parameters. The circular polarization, V, is independent from rotation, and only the polarization purity of the antenna limits the isolation from the other parameters [26, 27].

The rotation, and thus the possible mixing of Q and U, is described in several papers [28]. For a clockwise rotation, illustrated in figure 2.5, the measured Stokes vector, $\underline{T_B}$', is given by equation 2.15, where I, Q, U, and V is the true Stokes vector, and θ is the rotation angle.

$$\underline{T_B'} = \begin{pmatrix} I' \\ Q' \\ U' \\ V' \end{pmatrix} = \begin{pmatrix} 1 & 0 & 0 & 0 \\ 0 & \cos(2\theta) & \sin(2\theta) & 0 \\ 0 & -\sin(2\theta) & \cos(2\theta) & 0 \\ 0 & 0 & 0 & 1 \end{pmatrix} \begin{pmatrix} I \\ Q \\ U \\ V \end{pmatrix} = \begin{pmatrix} I \\ Q*\cos(2\theta)+U\sin(2\theta) \\ -Q*\sin(2\theta)+U\cos(2\theta) \\ V \end{pmatrix} \qquad (2.15)$$

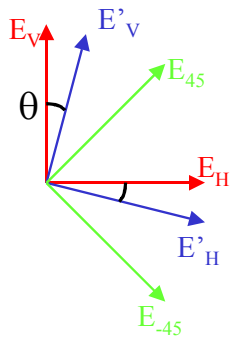

Figure 2.5. Relation between true and measured Stokes parameters, when the antenna plane is rotated clockwise by the angle θ.

For the present radiometer, installed for measurements over the ocean, the influence from an eventual rotation can be estimated with a simple example. Assume typical values for the Stokes parameters, Q = 50 K, and U = 1 K, and assume a rotation angle from –2° to 2°. The resulting errors, i.e. $\Delta Q = Q' - Q$, and $\Delta U = U' - U$, are shown in figure 2.6, and for θ = -0.5°, the errors are ΔQ = 25 mK, and ΔU = 872 mK.

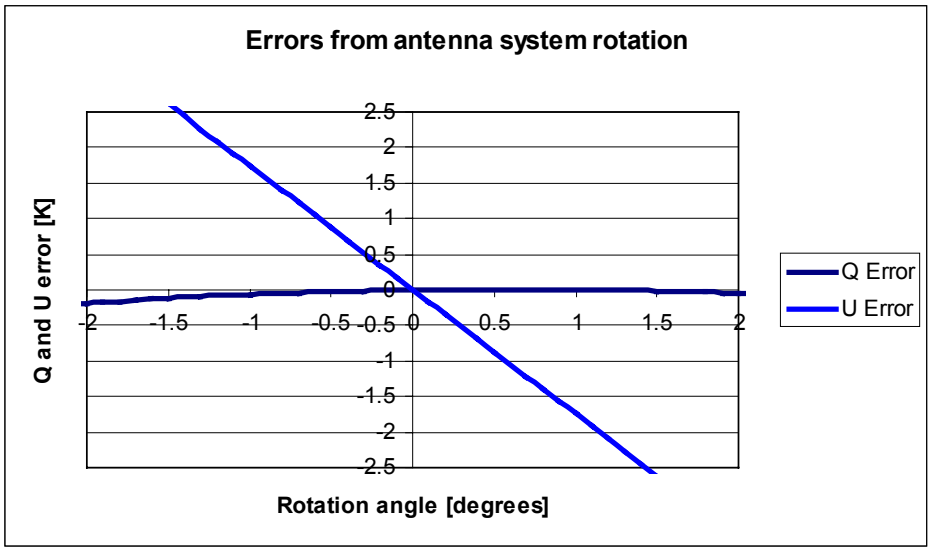

Figure 2.6. Errors in the 2nd (Q) and 3rd (U) Stokes parameters at typical values, Q = 50 K, U = 1 K, and rotation (θ) ranging from –2 ° to 2 °.

Targeting a sensitivity of 0.1 K, the rotation must be monitored continuously during radiometer operation, and it must be determined with a precision of down to 0.05° in order to enable corrections to the desired level. In an airborne campaign, the monitoring can be carried out using an inertial navigation unit, INU, which can give a precision of 0.05°, and corrections may be applied to the measured parameters by inversion of equation 2.15.

The antenna installation determines the connection between the aircraft attitude and the eventual rotation. Generally the aircraft attitude will be measured as heading, pitch and roll in the specified order [29], and a vector in the fixed Earth coordinate system will thus be described in the aircraft coordinate system by a series of rotations around the different axis.

Likewise the transformation from the aircraft coordinate system to the fixed coordinate system is done by the reverse series of inversions, removing roll, pitch and heading in the specified order.

The aircraft coordinate system is defined as a standard rectangular right-handed coordinate system, with the x-axis pointing from tail to nose, the y-axis from the left to the right wing, and the z-axis hence pointing down. With this definition, and with the Honeywell definition of the aircraft attitude, roll will be a positive rotation around the x-axis, while pitch will describe a positive rotation around the y-axis. The transformation of a vector in the aircraft coordinate system, $\underline{v_a} = (x',y',z')$, to its coordinates in the fixed coordinate system, $\underline{v_f} = (x,y,z)$, is given by the transformation matrix $\underline{A}$ in the relation $\underline{v_f} = \underline{A}\,\underline{v_a}$, where ϕ is the pitch angle and φ is roll. The matrix is shown in equation 2.16.

$$\underline{A} = \begin{pmatrix} \cos(\phi) & 0 & \sin(\phi) \\ 0 & 1 & 0 \\ -\sin(\phi) & 0 & \cos(\phi) \end{pmatrix} \begin{pmatrix} 1 & 0 & 0 \\ 0 & \cos(\varphi) & -\sin(\varphi) \\ 0 & \sin(\varphi) & \cos(\varphi) \end{pmatrix} = \begin{pmatrix} \cos(\varphi) & \sin(\phi)\sin(\varphi) & \sin(\phi)\cos(\varphi) \\ 0 & \cos(\varphi) & -\sin(\varphi) \\ -\sin(\phi) & \cos(\phi)\sin(\varphi) & \cos(\phi)\cos(\varphi) \end{pmatrix} \quad (2.16)$$

In the present situation, the antenna will be mounted side-looking with a fixed depression, and the rotation angle may be found by evaluating the angle, β, between the horizontal polarization unity vector, $\underline{x_{ha}} = (x',y',z') = (-1,0,0)$, of the antenna and the fixed vertical unity vector, $\underline{z_{vf}} = (x,y,z) = (0,0,-1)$. Subtracting 90°, the nominal difference between the horizontal and vertical polarizations, will give the rotation angle, θ. Equation 2.17 gives the results, using 2.16 to transform the coordinates.

$$\underline{x_{hf}} = \underline{A}\,\underline{x_{ha}} = \begin{pmatrix} -\cos(\varphi) \\ 0 \\ \sin(\varphi) \end{pmatrix}$$

$$\cos(\beta) = \frac{\underline{x_{hf}} \cdot \underline{z_{vf}}}{\left|\underline{x_{hf}}\right| \cdot \left|\underline{z_{vf}}\right|} = -\sin(\phi) \quad (2.17)$$

$$\theta = \beta - 90° = \phi$$

The true incidence angle at the sea surface may be found using the same procedure. The direction of the antenna beam (into the antenna) will be described by the unity vector $\underline{x_{aa}} = (0, -\cos(d), -\sin(d))$, where d is the depression angle. In the fixed coordinate system, the pointing vector will be given by equation 2.18

$$\underline{x_{af}} = \underline{A}\,\underline{x_{aa}} = \begin{pmatrix} -\cos(d)\sin(\phi)\sin(\varphi) - \sin(d)\sin(\phi)\cos(\varphi) \\ -\cos(d)\cos(\varphi) + \sin(d)\sin(\varphi) \\ -\cos(d)\cos(\phi)\sin(\varphi) - \sin(d)\cos(\phi)\cos(\varphi) \end{pmatrix} \quad (2.18)$$

The incidence angle, α, is the angle between the antenna beam and the vertical unity vector at the sea surface, given by $\underline{z_{vf}} = (x,y,z) = (0,0,-1)$. It is found by equation 2.19.

$$\cos(\alpha) = \frac{\underline{x_{af}} \cdot \underline{z_{vf}}}{\left|\underline{x_{af}}\right| \cdot \left|\underline{z_{vf}}\right|} = (\cos(d)\cos(\phi)\sin(\varphi) + \sin(d)\cos(\phi)\cos(\varphi))$$
$$\cos(\alpha) = \cos(\phi)(\cos(d)\sin(\varphi) + \sin(d)\cos(\varphi)) \qquad (2.19)$$
$$\cos(\alpha) = \cos(\phi)\sin(\varphi + d) = \cos(\phi)\cos(\varphi + d - 90°)$$

For small pitch angles, a good approximation to the equation is 2.20, which may be used to determine the desired roll angles during the airborne campaign.

$$\alpha = 90° - d - \varphi \qquad (2.20)$$

The last parameter of interest for the airborne measurements is the look direction relative to the aircraft heading. As the heading is given by the unity vector $\underline{x}_{nf}$=(1,0,0) in the fixed coordinate system, and the antenna pointing will be the projection, $\underline{x}_{apf}$, of $\underline{x}_{af}$ to the fixed (x,y)-plane, the angle between these two vectors will define the desired angle. The length of the projection is described by equation 2.21, and the look direction, ξ, follows in equation 2.22

$$\left|\underline{x_{apf}}\right| = \sqrt{1 - (\cos(d)\cos(\phi)\sin(\varphi) + \sin(d)\cos(\phi)\cos(\varphi))^2}$$
$$\left|\underline{x_{apf}}\right| = \sqrt{1 - \cos^2(\phi)(\cos(d)\sin(\varphi) + \sin(d)\cos(\varphi))^2} \qquad (2.21)$$
$$\left|\underline{x_{apf}}\right| = \sqrt{1 - \cos^2(\phi)\sin^2(d + \varphi)}$$

$$\cos(\xi) = \frac{\underline{x_{apf}} \cdot \underline{x_{nf}}}{\left|\underline{x_{apf}}\right| \cdot \left|\underline{x_{nf}}\right|} = \frac{\cos(d)\sin(\phi)\sin(\varphi) + \sin(d)\sin(\phi)\cos(\varphi)}{\sqrt{1 - \cos^2(\phi)\sin^2(d + \varphi)}}$$
$$\cos(\xi) = \frac{\sin(\phi)\sin(d + \varphi)}{\sqrt{1 - \cos^2(\phi)\sin^2(d + \varphi)}} \qquad (2.22)$$

Knowing the look direction relative to the aircraft heading, hdg, the antenna look direction relative to Earth north will be given by equation 2.23.

$$\psi = hdg + \xi \qquad (2.23)$$

As the results show, the three primary parameters, antenna rotation, antenna look direction, and incidence angle, may vary as a result of the aircraft motion. The look direction may be added to the attitude parameters for plotting and analysis of results, and antenna rotation may be corrected using the reverse equation 2.15. Incidence angle variations, however, will cause the incident brightness temperature to vary as described by the Klein-Swift model. For a typical situation, frequency = 1.4135 GHz, sea surface temperature = 10.0° C, and sea surface salinity = 35 psu, the modeled sea surface brightness temperature as well as the 2nd Stokes parameter, Q, can be seen in figure 2.7 as a function of the incidence angle.

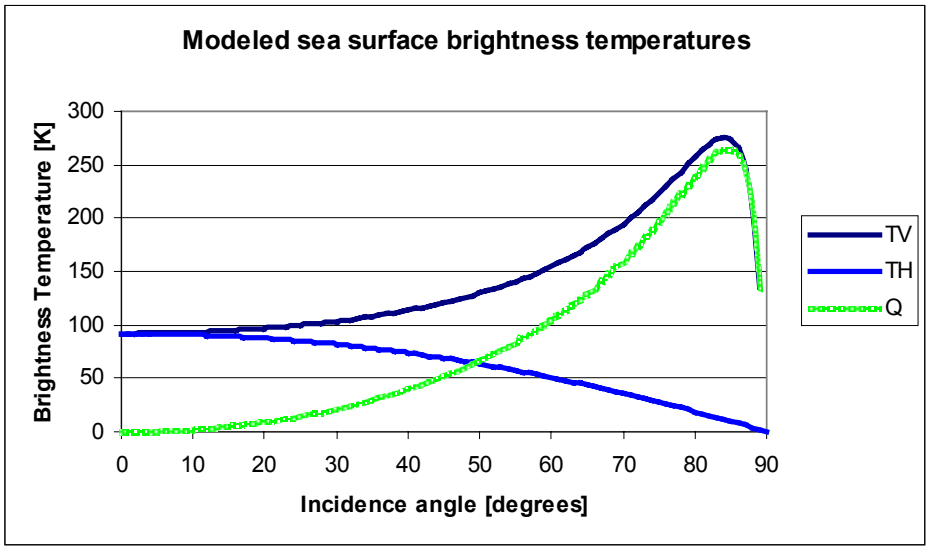

Figure 2.7. Klein-Swift model of sea surface brightness temperature and second Stokes parameter as a function of the incidence angle, when frequency = 1.4135 GHz, sea surface temperature = 10.0 °C, and sea surface salinity = 35 psu.

In the range of interest, between 20° and 65° incidence angle, the typical variations for T_V are about 1.5 K/° and about -1 K/° for T_H. $Q = T_V - T_H$, will thus vary about 2.5 K/°, rising need for knowledge about the incidence angle in the order of 0.05°, when a sensitivity of 0.1 K is targeted.

When looking for an azimuth signature, the nominal roll angle must be absolutely constant, and eventual variations must be corrected for. The Klein-Swift model can be used for this purpose, as an integration of the model within the antenna pattern will provide the theoretical input to the radiometer for a given incidence angle. The error, i.e. the modeled brightness temperature at the actual incidence angle, T(inc.), minus the modeled brightness temperature at the nominal incidence angle, T(nom.), may be calculated using equation 2.24, and the contribution can be subtracted from the measured values.

$$\delta T = T(inc.) - T(nom.) \tag{2.24}$$

An alternative approach to the theoretical corrections, described in this chapter, is a simple statistical correction, where it may be assumed, that each of the four Stokes parameters can be described as a linear function of the two attitude parameters, roll and pitch, when variations are small. For a single parameter, e.g. the first Stokes parameter, I, the dependence on the incidence angle, α, is determined by equation 2.25 [30].

$$a_{I\alpha} = \frac{\langle I\alpha \rangle - \langle I \rangle \langle \alpha \rangle}{\langle \alpha^2 \rangle - \langle \alpha \rangle^2} \tag{2.25}$$

Corrections can follow, as the error signal will be given by equation 2.26, which can be subtracted from the measured brightness temperatures.

$$\Delta I = a_{I\alpha} \cdot \left(\alpha_{inc.} - \alpha_{nom.}\right) \tag{2.26}$$

Likewise the dependence on pitch may be determined, and the same determination is used for the other Stokes parameters.

A third approach for the corrections may be the acquisition of large-scale variations at constant flight heading, followed by the creation of a look-up table, LUT, with averaged brightness temperatures for each attitude parameter value. Interpolation based on the table will create a model function based on actual values for the specific instrument, and 2.24 can be used to find the errors, which must be subtracted from the measured values.

3. Polarimetric radiometers

This chapter describes the implementation of polarimetric radiometers. A short introduction to the advantages and drawbacks of traditional radiometers, known as polarization combining and correlation radiometers, is given, and the new implementation, using high-speed digital components, is introduced. The subharmonic sampling process is described, and possible problems are identified. Some solutions to the mentioned problems are presented, and the radiometer output is characterized with relation to linearity and sensitivity.

3.1. Basic polarimetric radiometers

From the definition of Stokes vector in chapter 2 it is seen, that the 3rd and 4th Stokes parameters may be regarded as the complex correlation between the horizontal and vertical channels. But each of them may also be regarded as the difference between two orthogonal polarizations, linear polarizations turned 45° relative to normal horizontal/vertical and right/left hand circular polarizations, respectively. These two definitions lead to the two basic polarimetric radiometer types, known as the polarization combining radiometer and the correlation radiometer.

The simplest polarization combining radiometer consists of six parallel antennas and receivers, each measuring one of the six polarizations included in Stokes vector, T_v, T_h, T_{45}, T_{-45}, T_r, and T_l, symbolizing the vertical and horizontal polarizations, the linear polarizations tilted 45°, and the two circular polarizations. Instead of six independent antennas, a standard antenna configuration with a dual polarized antenna, observing horizontal, H-pol, and vertical, V-pol, polarizations, along with an orthomode transducer, OMT, can be used. The four remaining signals can be derived from the two measured signals by addition, subtraction and 90 degrees phase shift of the electrical field signals as indicated in 3.1a-d.

$$E_{45} = \frac{1}{\sqrt{2}}\left(E_V + E_H\right)$$

$$E_{-45} = \frac{1}{\sqrt{2}}\left(E_V - E_H\right)$$

$$E_r = \frac{1}{\sqrt{2}}\left(E_V + E_{H,-90\,\mathrm{deg}}\right) \qquad \text{(3.1a-d)}$$

$$E_l = \frac{1}{\sqrt{2}}\left(E_V - E_{H,-90\,\mathrm{deg}}\right)$$

This gives the block diagram shown in figure 3.1 for the parallel polarization combining radiometer. The important advantage of this radiometer type is the continuous measurement of all channels, ensuring the full integration time and sensitivity. The obvious drawback is the implementation of six parallel receivers and the complicated front-end hardware. These structures are not only heavy and potentially power-consuming, but stability problems may occur, as it may be difficult to track all receivers in temperature, causing risk of double gain errors, as each parameter is calculated as a combination of two outputs [31].

A variation of the parallel polarization combining radiometer is the switching polarization combining radiometer, which is based on a single receiver, time-multiplexed to observe each of the six desired polarizations. The block diagram can be seen in figure 3.2. It also measures each Stokes parameter as a combination of two outputs, but it has the obvious advantage, that it needs only one receiver. The second, third, and fourth Stokes parameters are thus calculated as a difference between two different input signals to the same receiver, and it gives the advantage, that variations in noise temperature will cancel as it is known from a traditional Dicke radiometer. Likewise gain variations will be downscaled to influence only the difference signal instead of the full input brightness temperatures. Drawbacks of the multiplexing radiometer is the loss of sensitivity due to the reduced observation time for each polarization (only 1/6 of the total observation time), as well as the substantial losses in the complex polarization combining networks in front of the receiver. Finally, there is a risk that the observed target is fluctuating during the measurement period, giving rise to uncertainties or errors in the calculated Stokes parameters.

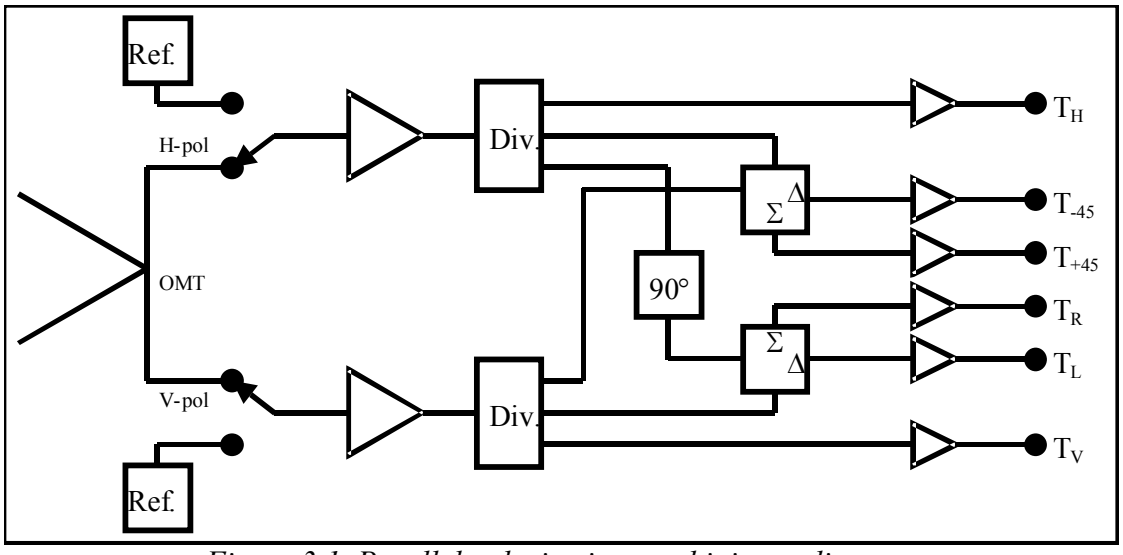

Figure 3.1. Parallel polarization combining radiometer.

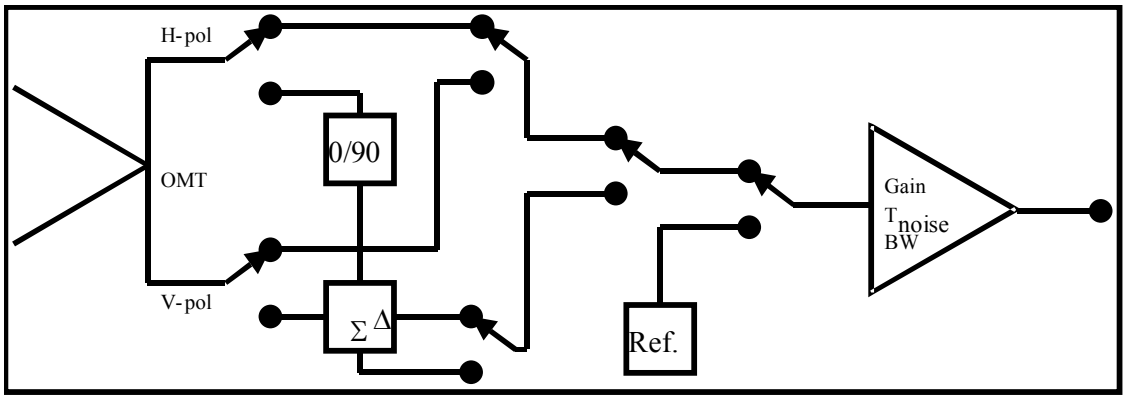

Figure 3.2. Multiplex polarization combining radiometer.

The Stokes vector definition with complex correlation shows a different polarimetric radiometer implementation, the coherent correlation radiometer shown in figure 3.3. The radiometer consists of two parallel receiver channels, measuring the two basic polarizations

needed for determination of the first and second Stokes parameters, and it thus gives rise for the same potential stability problems with receiver drifts as mentioned for the parallel polarization combining radiometer. Parallel measurement of all polarizations, however, ensures maximum sensitivity.

The third and fourth Stokes parameters are calculated as the complex correlation, ρ, between the input channels multiplied by the system temperature, T_{sys}, i.e. the total brightness temperature including the system noise, as shown in equation 3.2a-b.

$$U + iV = 2\langle V_V(t) \cdot V_H(t) \rangle = 2T_{SYS} \cdot \rho$$
$$T_{SYS} = \sqrt{(T_V + T_N) \cdot (T_H + T_N)} \qquad (3.2a\text{-}b)$$

The correlation is independent from the input level, and it is normalized to the interval [-1; 1] as expressed in equation 3.3.

$$\rho = \frac{\langle x(t) y(t) \rangle}{\sqrt{\langle x^2(t) \rangle \langle y^2(t) \rangle}} \qquad (3.3)$$

The sensitivity to uncertainties in the system is determined as a combination of the sensitivity to the system temperature and the sensitivity to the correlation as expressed by equation 3.4

$$\Delta U = \Delta\rho \cdot T_{SYS} + \rho \cdot \Delta T_{SYS} \qquad (3.4)$$

As ρ is usually small – a few percent – even several Kelvin of ΔT_{sys} will be reduced to a level below the radiometric sensitivity. Variations in the correlation, however, will be scaled up by the system temperature, but as modern digital correlators are almost perfect, very good stability may be reached.

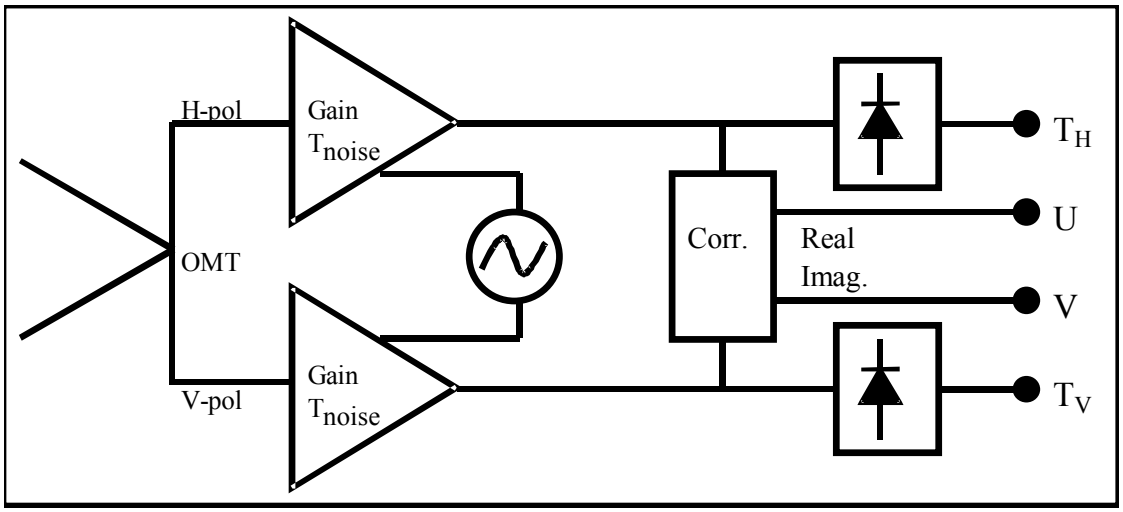

Figure 3.3. Coherent correlation radiometer.

A serious drawback of the correlation radiometer is the local oscillator, which is generally a power-consuming device. The oscillator is necessary for the correlator, as it is typically not able to operate directly on the RF-signals. Another serious drawback in the correlation radiometer is the coherent design, which makes the phase characteristics of the two receivers very important for the measured third and fourth Stokes parameters. For a narrow band signal

and small phase variations, a rotation of the complex plane will result, while larger variation or larger bandwidths will reduce the correlation between the signals.

3.2. Polarimetric radiometer with subharmonic sampling

As it is seen in the previous section, the traditional polarimetric radiometers all have a number of advantages and drawbacks. Common to them is that they have a large amount of analog electronics, which is connected to some drawbacks. One of the most important drawbacks is the sensitivity of the analog components, concerning temperature and power supply. Changes in these parameters will directly influence the calibration of the radiometer, changing the phase, the gain, and the noise temperature constants, and even a small noise contribution to the power supply voltage may add noise to the measured results. Problems of this kind can be dealt with, however, and the sensitive components may be temperature stabilized and powered through a well-regulated linear power supply.

The obvious drawback in this design is that a large and heavy temperature stabilized box is needed for the enclosure of the full receiver chains. Likewise a large and heavy power supply unit will be needed, as linear power supplies need a large transformer, running at the typical 50 Hz / 60 Hz / 400 Hz main AC power supply, and as such devices have typical efficiencies less than 50 %. Along with the fact that different analog components, needed for a radiometer front-end, typically will run at different power voltages, the power supply unit may easily take up a major part of the full radiometer size and weight.

With view of the increasing performance and use of digital electronics, it is obvious to consider eventual new implementations of radiometers, taking advantage of some new components. In many electronic devices, the boundary between the analog and the digital domains has been pushed further towards the front-end, thus reducing the total amount of analog components. In a radiometer, the gain from a reduction of the analog section is obvious, and ideally one could imagine a radiometer digitizing the signals right after the antenna and orthomode transducer elements, doing all gain and filtering in the digital domain.

Practically, however, there are some problems in this kind of implementation, and basically one of the limitations is the low signal level of the natural radiation. Sampling a full spectrum, limited only by the frequency characteristic of the antenna will cause an extremely large dynamic range from radar and communication signals to the natural background radiation, giving need for an almost unlimited number of bits in the digitized signal. Moreover, the noise figure of any analog to digital converter will add thousands of Kelvin to the signal, making this kind of implementation fully unrealistic.

The described problems can be solved, if a low noise amplifier, LNA, and a reasonable filter is added to the front-end before the analog to digital converter. This will give the simplified block diagram, shown in figure 3.4. Another limitation to the basic implementation of the digital radiometer is the signal bandwidth at the analog to digital converter. The analog filter, however, will limit this demand, and assuming a rectangular filter, the bandwidth at the converter will be only the desired radiometer bandwidth.

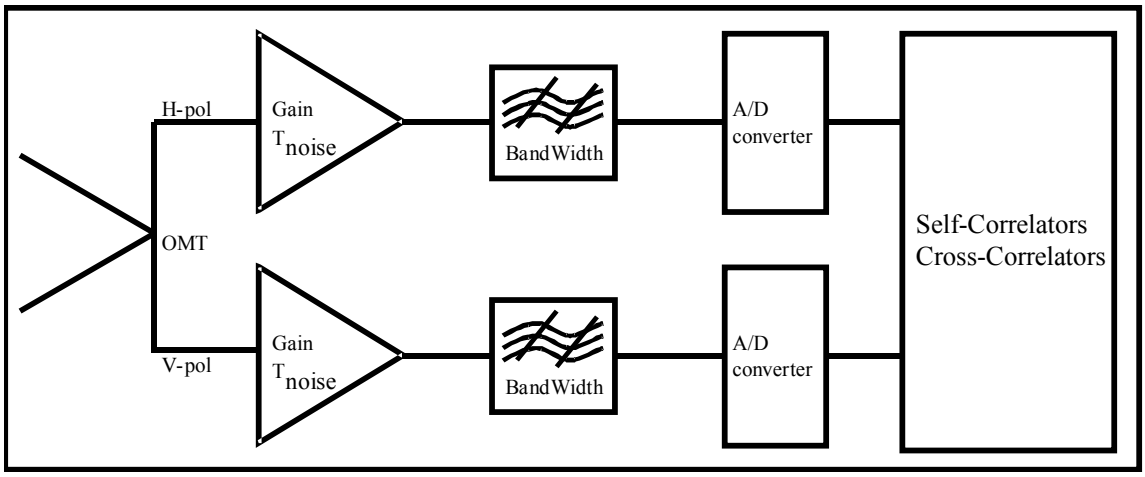

Figure 3.4. Digital radiometer with a low noise amplifier and an analog filter.

The sampling process can be described as a multiplication of the input signal with a series of pulses, known as delta functions, spaced by the sampling time, $T=1/f_s$, where f_s is the sampling frequency [32]. This multiplication in the time domain will be described as a convolution between the two signals in the frequency domain. The Fourier transform of the sampling signal is a series of delta functions, spaced by the sampling frequency, f_s, and the convolution will describe a series of copies of the original input signal spectrum.

For a base-band signal, the consequence of the convolution is, that two copies of the signal will overlap in the frequency domain, if $f_s < 2*f_{max}$, where f_{max} is the maximum frequency present in the signal. This condition is known as the Nyquist condition. For a band-pass signal, limited by the frequencies f_{min} and f_{max}, however, overlap will not necessarily occur, if the Nyquist condition is not fulfilled, as overlapping of the frequency range from DC to f_{min} will be harmless and create no conflict.

Copies of the input frequency f_i will follow the harmonics of the sampling frequency, and f_i will appear in the output frequency spectrum at all frequencies equal to $f_o = f_i + n*f_s$, where n is an integer. If the sampling frequency is chosen properly, no output frequency, f_o, can be reached by more than one input frequency. The principle is illustrated in figure 3.5a, where the green spectrum is the original input spectrum, and the black line is the applied sampling frequency. The yellow lines show the 2nd harmonics of the sampling frequency, and the blue and red specters are the results of the convolution. In the example, no overlapping occurs, but it is seen, that a small increase in the sampling frequency will cause the two, negative and positive, specters to overlap as illustrated in figure 3.5b.

For further increase of the sampling frequency, as illustrated in figure 3.5c, overlapping stops, as the harmonic of the sampling frequency, $n*f_s$, falls outside the signal spectrum again. The conditions may be expressed as $n*f_s < f_{min}$ and $n*f_s > f_{max.}$ Continuing the sampling frequency increase, it is seen, that the next overlapping will occur, when the dark blue specters will meet the light blue at $f_s/2$. The condition may be expressed as $(n+½)*f_s < f_{min}$ and $(n+½)*f_s > f_{max}$.

Combined, the two sets of conditions for sampling may be expressed in equation 3.5, where m represents an integer.

$$f_s \le \frac{f_{\min}}{m}$$
$$f_s \ge \frac{f_{\max}}{(m+0.5)} \qquad (3.5)$$
$$m = n/2$$

For each value of m, an interval may be defined, and the sum of these intervals represents the total set of frequencies, which can sample the input band pass signal alias free.

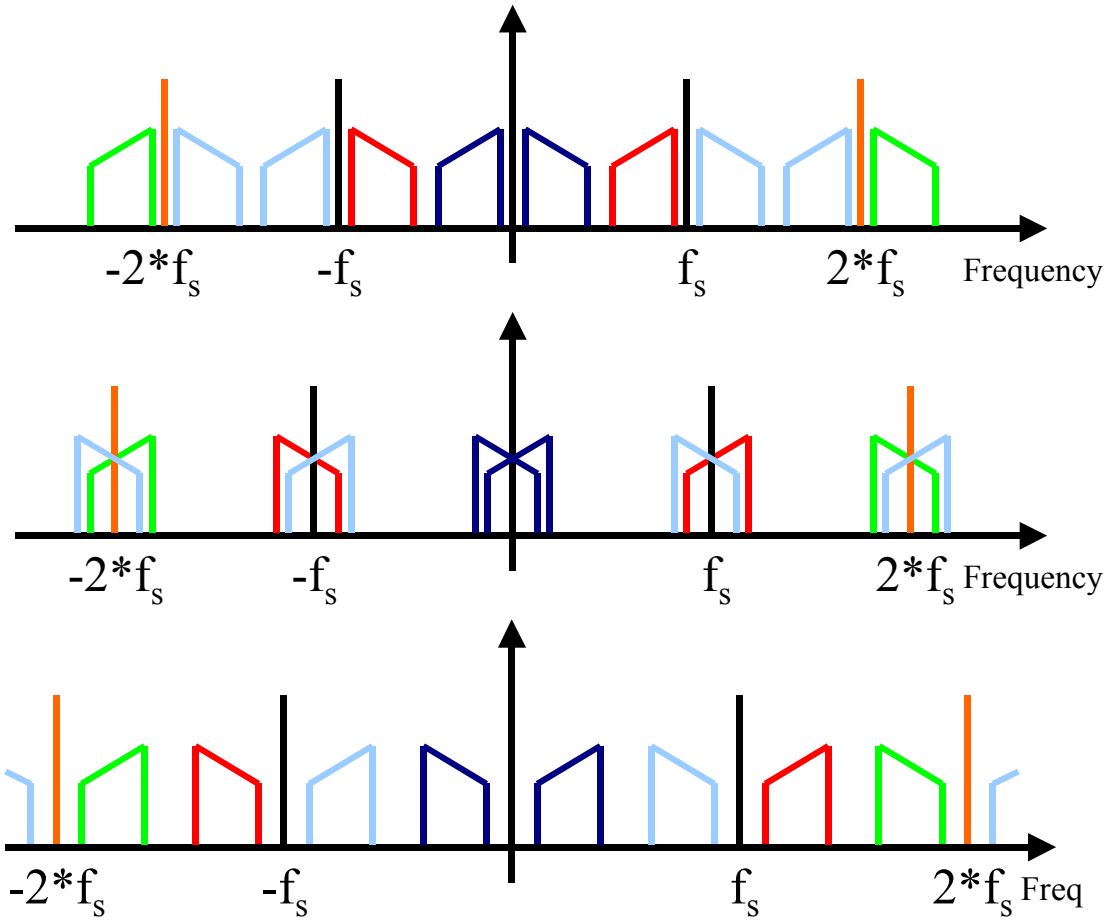

Figure 3.5. Frequency spectrum for a band pass signal sampled with the frequency f_s. The green spectrum is the input signal spectrum, while the other specters are the aliases, created by the sampling process. The sampling frequency is shown with the black lines, and its harmonics are shown in yellow

a) No aliasing in the frequency domain, nf_s below the signal spectrum.*
b) Aliasing in the frequency domain, as nf_s falls within the signal spectrum.*
c) Alias-free sampling, nf_s above the signal spectrum.*

The signal processing is done in the digital domain, and a determination of the input power level will be a simple self-multiplication with integration, according to the Stokes vector definition. The process, also known as self-correlation, is described by equation 3.6.

$$\rho_{self} = \left\langle v_1(t)^2 \right\rangle \tag{3.6}$$

Determination of the 3rd Stokes parameter follows from cross-correlation as described by equation 3.7.

$$\rho_{cross} = \left\langle v_1(t) v_2(t) \right\rangle \tag{3.7}$$

The fourth Stokes parameter is also determined by a cross correlation, but a 90° phase shift of one of the input channels is needed prior to the correlation determination in order to get the imaginary part of the correlation. In a traditional correlation radiometer a 90° hybrid is added to each radiometer channel, and the 0°/0° correlation will give the 3rd Stokes parameter, while the 0°/90° correlation will give the complex part and thus the 4th Stokes parameter. The 90°/0° and the 90°/90° will also provide the two Stokes parameters, but as the information will be redundant, no additional information or signal to noise ratio may be gained.

The phase shift can be placed before or after the digitization. If it is analog, a third analog to digital converter is needed for the phase-shifted channel, increasing the cost and the power-consumption of the digital front-end by 50 %. Synchronization between the inphase and the quadrature channels will be essential, but the digital correlator unit will be simple.

Alternatively, the phase shift may be done in the digital domain. A finite impulse response, FIR, filter must be included in each channel, and it can be placed in a field programmable gate array, FPGA, or in a dedicated signal processor. Drawback of this method is that it requires a higher real-time digital calculation performance, and some over-sampling of the signal spectrum will be necessary for the filter to perform properly. Advantage is, however, that no sampling skew occurs between the two phases, and additional reduction of the analog circuitry is possible.

A third alternative is a full digital I/Q demodulation, as described in [33]. The analog signals are over-sampled by a factor of two, and subsequently each signal is modulated by $\cos(f_s/4) = [1,0,-1,0]$ and $\sin(f_s/4) = [0,1,0,-1]$, where f_s is the sampling frequency. Simple low-pass filters with a minimum number of 1's in the coefficients as described in [34] may in this case replace the 90° phase shifter filter, and the total digital complexity may be reduced. The only disadvantage is the over sampling, but the reduced complexity, replacing binary multipliers with binary shifters and adders, will typically reduce the total need for FPGA resources. With a small modification, the digital demodulation method allows for complete symmetry between the inphase and the quadrature channels. Instead of modulation with $\cos(f_s/4)$ and $\sin(f_s/4)$, $\cos(f_s/4 + 45°) = [1,-1,-1,1]$ and $\cos(f_s/4 - 45°) = [1,1,-1,-1]$ may be used, allowing for application of the same filter coefficients in each channel.

3.3. Characterization of the digital radiometer output

Based on the initial description of the digital radiometer, the detailed implementation can be discussed. Equations for characterization of the radiometer output must be described, and the expected output from a digital radiometer must be calculated with respect to linearity and sensitivity. As typical fast analog to digital converters are limited to 8, 10 or 12 bits, the

output analysis curves will be based on an ideal 8-bit converter. Assuming a white noise input signal, covering a limited bandwidth, B, samples from the analog to digital converters will follow a Gaussian distribution with standard deviation α, described by formula 3.8 [35].

$$f(x) = \frac{1}{\alpha\sqrt{2\pi}} e^{\left(\frac{-x^2}{2\alpha^2}\right)} \tag{3.8}$$

The probability that a sample will fall within a certain range, described by the limits v_1 and v_2, is given by equation 3.9.

$$P(v_1 \le x \le v_2) = \int_{v1}^{v2} f(x)dx \tag{3.9}$$

If the analog to digital converter has a total of N bits, the total voltage range from V_{min} to V_{max} is divided in 2^N sub-ranges, 2^N-2 equally sized intervals and two over-ranges. The mean self-correlator output is found as the sum over the full output range of the squared bit value multiplied by the probability of sampling the value, determined by the limits, V_{i1} and V_{i2}. This leads to formula 3.10, describing the output from the detection.

$$\begin{aligned} I &= \sum_{i=0}^{i=255} i^2 \cdot P(X = i) \\ I &= \sum_{i=0}^{i=255} i^2 \cdot \int_{vi1}^{vi2} f(x)dx \end{aligned} \tag{3.10}$$

The interval limits, vi_1 and vi_2 are defined by the analog to digital converter, and for a converter with N bits, covering a voltage range V_{min} to V_{max}, the distance between intervals will be given by 3.11

$$d = \frac{V\max - V\min}{2^N - 2} \tag{3.11}$$

The (i+1)'th interval will start at V_{min}+d*(i-1), and it will end at V_{min}+d*i. The first and last interval will represent the over-ranges, from -∞ to V_{min} and from V_{max} to +∞, respectively.

The output will depend on the parameter α, representing the effective voltage (rms voltage) of the input noise, determined by the input power level, P_{in}, and the input impedance, R, as described by 3.12

$$P_{in} = \frac{\alpha^2}{R} \tag{3.12}$$

The input power level depends on the input brightness temperature and the RF-gain. In the example below the effective noise voltage from a 500 K (including 100 K receiver noise) input is set to be 16 dB below the maximum input range of the converter, and the integrator output is shown in figure 3.6 for an 8-bit quantization. Normalization of the output values with respect to the input brightness temperature will provide the radiometer gain, and for the present example the results are seen in figure 3.7.

The demand for gain linearity depends on the application of the radiometer under construction, and for some applications a selection of the input signal range to cover only the lower part of the curve may be enough. If an error of 1 % can be accepted, the range from 100 K to 600 K in the figure, forming an almost flat plateau, will be useable, and the RF-gain may be adjusted to cover the actual input range. Due to the receiver noise, the lowest input values, below 100 K in this example, will never be used. For radiometers with higher

dynamic range or very strict demands for linearity and absolute level determination, a reversal of the transfer function may be necessary, eventually using a series of polynomials or a look-up table. It must be noticed, that a reduction of the number of bits from the analog to digital converter, i.e. a reduction of the number of quantization levels, will cause a more expressed unlinearity, and the need for corrections will be increased.

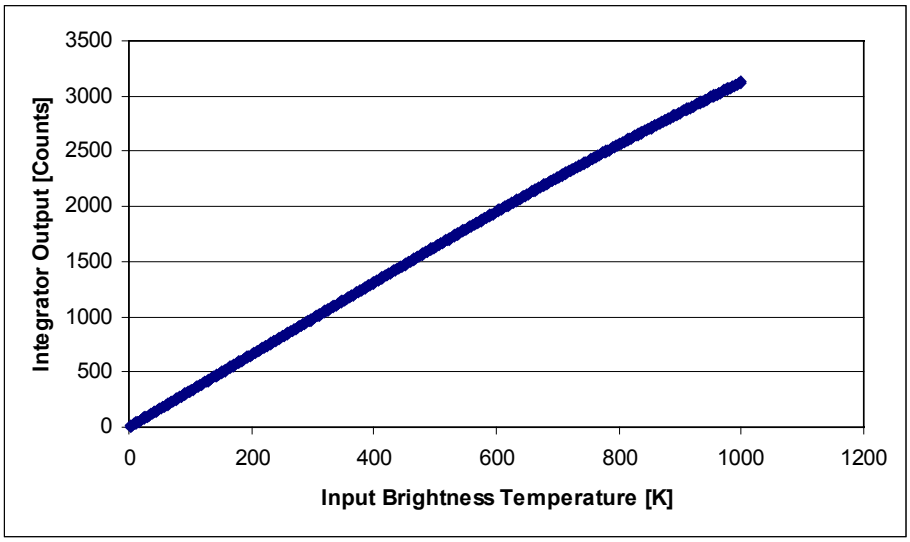

Figure 3.6. Output from square law integrator following an eight-bit analog to digital converter, fed with a Gaussian distributed signal, having a standard deviation 16 dB below the maximum input range at 500 K.

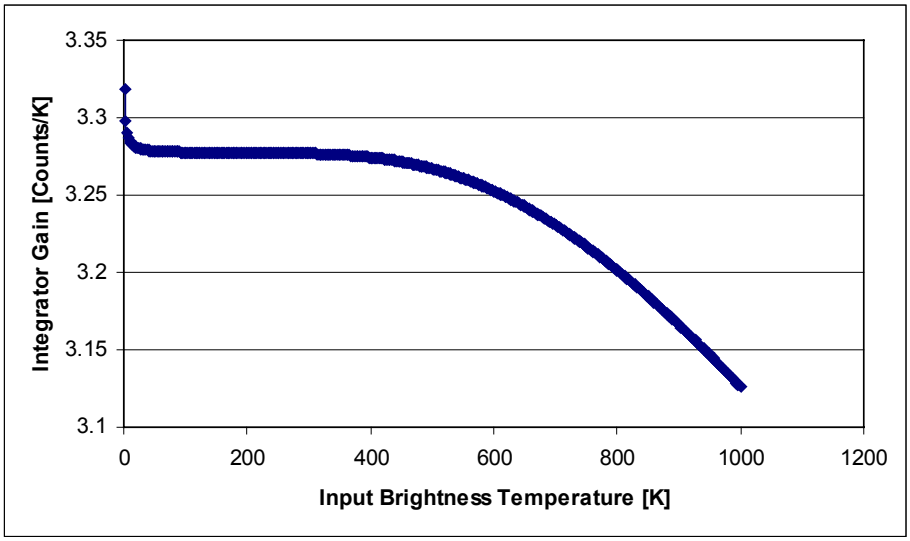

Figure 3.7. Gain of a square law integrator following an eight-bit analog to digital converter, fed with a Gaussian distributed signal, having a standard deviation 16 dB below the maximum input range at 500 K.

The sensitivity of the radiometer compared to a traditional radiometer can be derived from the statistical assumption and the output model, calculating the standard deviation, α_{Rad}, of the output signal. The standard deviation is given by equation 3.13 [36], where x(n) represents the squared samples from the analog to digital converter. The second term is the radiometer output, calculated above, while the first term is given by equation 3.14,

representing the fourth order moment of the analog to digital converter output. The sensitivity is equal to the standard deviation of the detector output, α_{Rad}, divided by the square root of the number of independent samples in a measurement series, $f_s*\tau$, where f_s is the Nyquist sampling frequency and τ the integration period length.

$$\alpha_{Rad} = \left\langle x^2(n) \right\rangle - \left\langle x(n) \right\rangle^2 \tag{3.13}$$

$$\left\langle x^2(n) \right\rangle = \sum_{i=0}^{i=255} i^4 \cdot P(x=i)$$

$$\left\langle x^2(n) \right\rangle = \sum_{i=0}^{i=255} i^4 \cdot \int_{vi1}^{vi2} f(x)dx \tag{3.14}$$

The digital radiometer sensitivity is plotted in figure 3.8 relative to the sensitivity of a traditional radiometer. The RF-gain is selected as in the above example, letting the effective noise voltage from a 500 K input be 16 dB below the maximum range of the analog to digital converter.

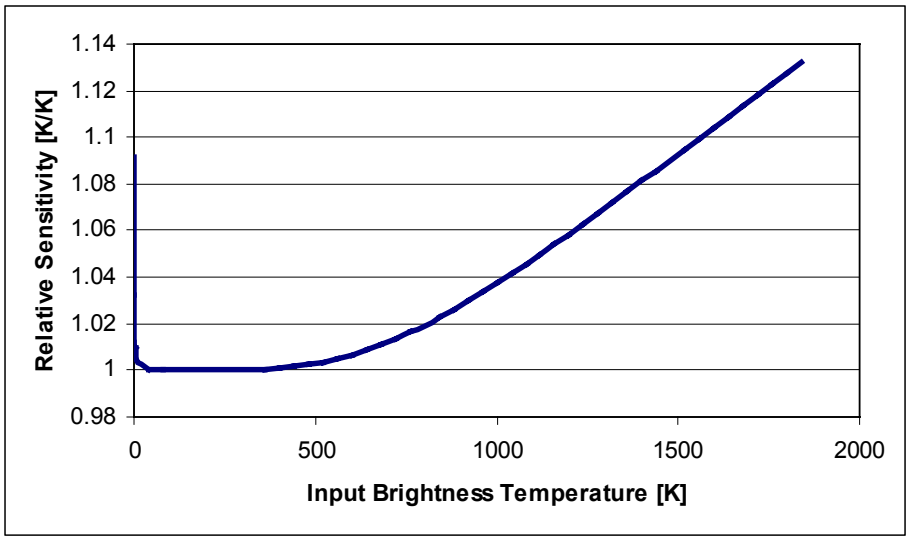

Figure 3.8. Sensitivity of a digital radiometer with 8-bit quantization relative to a traditional radiometer. The RF-gain lets the noise voltage from a 500 K input be 16 dB below the maximum input level of the analog to digital converter.

From the figure it is seen, that a normal radiometer input range up to 500 K will provide a sensitivity, almost equal to a traditional radiometer. The worse sensitivity for very small signals origins from the quantization noise of the converter, but for practical applications it is not a problem, as the contribution from the receiver noise will be approximately 100 K. The high-end increase is due to the saturation of the converter, limiting the gain of the radiometer. Again it should be noticed, that a reduction of the number of quantization levels is possible, but the relative sensitivity will increase. For only three quantization levels, the optimum sensitivity is thus a factor of 1.238 larger than for an ideal radiometer [36].

The correlation channel outputs may be analyzed similarly, and it is assumed that the two inputs to the correlator can be described by a two-dimensional Gaussian distribution, characterized by the correlation, ρ [36]. The probability density function is given by equation 3.15.

$$f(x,y) = \frac{1}{\alpha^2 2\pi\sqrt{1-\rho^2}} e^{\left(\frac{-(x^2+y^2-2\rho xy)}{2\alpha^2(1-\rho^2)}\right)} \tag{3.15}$$

The channel output will be given by equation 3.16, where the interval limits vi_1 and vi_2 as well as vk_1 and vk_2 will be identical to the limits used in equation 3.10 for the detection channels. They characterize the quantization of the voltage range V_{min} to V_{max} to N bits, done by the analog to digital converter.

$$I = \sum_{i=0}^{i=255}\sum_{k=0}^{k=255} i \cdot k \cdot P(X=i; Y=k)$$
$$I = \sum_{i=0}^{i=255}\sum_{k=0}^{k=255} i \cdot k \cdot \int_{vi1}^{vi2}\int_{vk1}^{vk2} f(x,y)dxdy \tag{3.16}$$

Calculations of the output are similar to the calculation for the detection channels for the highest correlation, ρ=1. In the example above it is shown, that an effective noise voltage for 500 K at a level 16 dB below the maximum range for the converter will cause an unlinearity less than 1 %. For lower correlations the calculations show, that the unlinearity error will stay below 1 % of the resulting signal, which is negligible in the present radiometer. Similarly the sensitivity will stay unaffected as indicated in the example above for the detection channel.

The correlator output will be very sensitive, however, to a possible DC offset in the sampled signals, typically due to the DC-coupling of the input track/hold amplifier of the analog to digital converter. Offsets, $V_{offset1}$ and $V_{offset2}$, will contribute directly to the result with an error equal to $(V_{offset1} * V_{offset2})/R$, where R is input impedance as in equation 3.12.

Assuming a stable DC-level, the determination and removal of the unwanted contribution is easy. For AC-signals, the mean of the collected samples must be zero, and determination of the sample average will thus provide the necessary information, which eventually can be combined with a feedback to the DC offset adjustment of the converter circuit, solving the problem. If the converter does not have an offset adjustment opportunity, the DC value can be subtracted from each sample before processing, giving the same result.

The DC measurement will be a statistical determination, based on the sampled values. For a period of length τ, the number of independent samples, N, used for the determination, will be given as $N = f_s * \tau$, where f_s is the sampling frequency at the Nyquist sampling rate. A Gausssian distributed input signal with an rms level, α, will thus give a DC level determination with a standard deviation described by equation 3.17

$$\Delta V_{DC} = \frac{\alpha}{\sqrt{N}} = \frac{\alpha}{\sqrt{f_S \cdot \tau}} \tag{3.17}$$

Another potential problem in the implementation of the digital radiometer is the phase coherence between the two input channels. Phase mismatch or time delays will lead to de-correlation between the two channels, following the auto-correlation for the input signals. For a base-band signal within a rectangular bandwidth, B, the de-correlation will be described by equation 3.18, where τ is the time delay.

$$\rho(\tau) = \rho(0) \cdot \frac{\sin(\pi B \tau)}{\pi B \tau} \tag{3.18}$$

For a narrow-band signal with the bandwidth, B, located at the frequency n*B, where n is an integer, the real and the imaginary part of the auto-correlation will follow equation 3.19 and 3.20, respectively [36].

$$\rho(\tau) = \rho(0) \cdot \frac{\sin(\pi B \tau)}{\pi B \tau} \cos\left(2\pi\left(n + \frac{1}{2}\right) B \tau\right) \tag{3.19}$$

$$\rho(\tau) = \rho(0) \cdot \frac{\sin(\pi B \tau)}{\pi B \tau} \sin\left(2\pi\left(n + \frac{1}{2}\right) B \tau\right) \tag{3.20}$$

The result is known as a fringe-wash pattern, letting the magnitude of the real and imaginary part of the auto-correlation function follow the de-correlation for the base-band signal, but causing a rotation in the imaginary plane. For a signal with 25 MHz bandwidth and n = 5, the auto-correlation functions may be seen in figure 3.9.

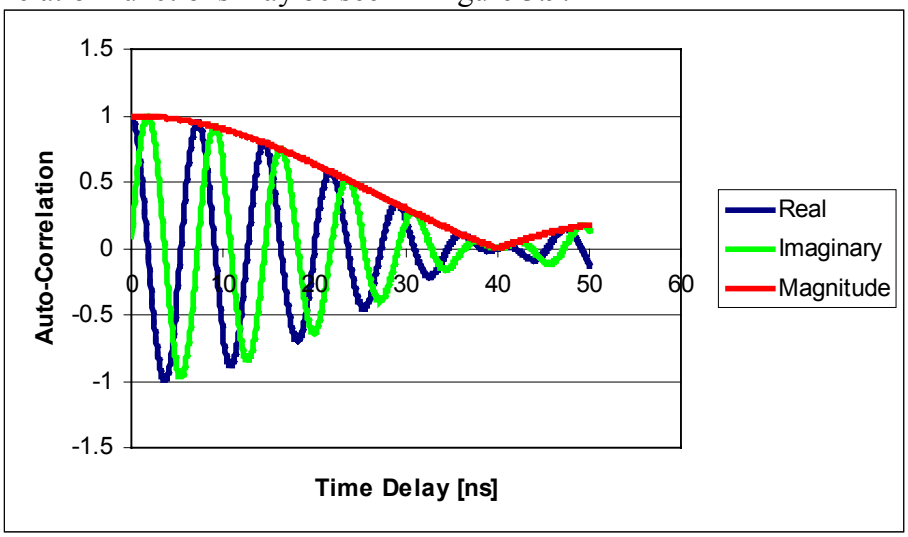

Figure 3.9. Auto-correlation for a 25 MHz signal centered at 125 MHz. The magnitude of the complex correlation follows the auto-correlation for a 25 MHz band pass signal, while the oscillations depend in the RF-signal frequency.

For the present radiometer the factor n is equal to 56, and a delay of 10 psec. will cause an error of 0.005 in the real part and 0.09 in the imaginary part. For typical 3rd and 4th Stokes parameters, U = 1 K and V = 0.0 K, the consequence is a loss of 5 mK in the third Stokes parameter, while the fourth Stokes parameter will be increased by 100 mK.

In a traditional correlation radiometer, the RF circuits will be phase matched prior to the system assembly, and due to the down conversion to base-band (or IF), the oscillations in the auto-correlation pattern will be removed. Phase mismatch problems in the section behind the mixer will thus be almost negligible. In the digital radiometer, however, signals are sampled directly at RF, including the analog to digital converters as phase critical components, and a technique for estimation of time delays must hence be included in the radiometer system.

As described in paragraph 3.2, the complex correlation may be calculated in different ways, depending on the inphase/quadrature demodulation of the input signals. For a radiometer with digital demodulation or digital 90° phase shift of one of the inputs, only two analog to

digital converters are used, and only one delay is unknown, τ_0, between the two input channels. If the 90° phase shift is made in the analog domain, three converters are used, and two delays, τ_0 between the 0°/0° channels, and τ_{90} between the 0°/90° channels must be estimated.

Techniques of delay estimation based on correlation measurements are described in [37, 38], and it is outlined, how a feed-back loop, feeding a digital delay circuit, can control and adjust the sampling delays. The papers describe the situation of synchronizing analog to digital converters, sampling the same signal in phase and in quadrature. The same correlation technique may be used in the radiometer, applying a known correlation to the two radiometer channels and adjusting the sampling delays to reach the expected output.

A known correlation may be created by a noise diode, adding correlated noise, T_C, to the two channels. If the inputs are switched to calibration references, the input brightness, $T_N + T_L$, will be known and partly correlated, and the level of correlation will be described by 3.21, where T_N is the receiver noise contribution.

$$\rho = \frac{T_C}{T_L + T_C + T_N} \tag{3.21}$$

For noise injected in phase in the two channels, the imaginary part of the correlation must be zero, and the adjustment, τ_{90}, can be determined and applied. Likewise the sampling delay for the real part, τ_0, can be adjusted, if the noise is injected in quadrature, i.e. shifted 90° before injection in one of the receiver channels. With the adjustments done, the ratio between the output correlation and the expected correlation can be calculated, giving a calibration constant, compensating for eventual de-correlation in the RF-section of the radiometer.

If the digital 90° phase shift is implemented, the phase shift of the noise will not be necessary, as the digital phase shift will remain constant and be independent from the sampling delays. If the analog implementation is selected, however, the two phases for the noise will provide each of the two delays, τ_0 and τ_{90}. Alternatively, the inphase noise should be used for both estimations, and τ_0 should be estimated as the delay, giving the maximum real part of the correlation. As the slope of the real correlation part is zero for optimum delay, however, the precision of the estimation will be reduced compared to the zero crossing for the imaginary part.

3.4. Selection of EMIRAD L-band radiometer implementation

Following the description of the digital radiometer, advantages and drawbacks of the digital implementation can be collected, and the list below shows a brief summary, showing advantages as "+", drawbacks as "-", and neutral comments as "•".

+ The reduced number of analog components reduces the total size and weight of the radiometer. The smaller size will ease the temperature stabilization of the instrument and hence improves the accuracy.

+ The reduced number of analog components may reduce the total power-consumption of the radiometer, as the local oscillator is left out. The analog to digital converter, however, is a critical component, but future technologies are expected to be less power-consuming.
+ Detection channels and correlation channels are measured with the same circuit, referring all four Stokes parameters to the same calibration. The third and fourth Stokes parameters are thus determined directly as $<E_V E_H^*>$independent from changes in the receiver noise.
+ The digital radiometer enables for advanced digital signal processing before the final signal detection. A frequency analysis, based on the fast Fourier transform, FFT, will provide information about eventual RF-interference in a fraction of the frequency band, enabling for adaptive filtering. Alternatively, the frequency band may be subdivided digitally, enabling for parallel evaluation and integration of each sub band individually. The methods may be used both for a potential larger system bandwidth, filtering out only peaks identified in the spectrum, or it may be used for removal of unidentified RF-interference within the protected L-band.
• All system gain is at RF-level. Possible risk of gain-loops must be observed in the implementation.
• Fewer analog components will generally reduce the total number of temperature dependent components, but to some extent the advantage will be reduced, as the use of RF-amplifiers instead of IF-amplifiers will demand use of FET (field effect transistor) technologies, having a higher temperature coefficient compared to traditional bipolar technologies.
• The concept is never demonstrated, and unknown problems may rise during instrument assembly.
• Cross coupling is a general problem in correlation radiometers, and the isolation between the input channels is critical. A coupling signal will be correlated with the full signal in the correlator unit, reducing the effect of the isolation by the square root. 20 dB of isolation will let 300 K input couple as 3 K, causing a correlation signal of 30 K, equal to an effective isolation of only 10 dB!
- Present choice of analog to digital converters for the desired frequency band is limited, as the input must be able to handle the RF frequencies. Those available are rather power-consuming, and a thermal stabilization of the converters, including their sample/hold amplifier is thus hard to achieve. Future technologies are expected to decrease the problem, however.
- The sampling delay adjustment is rather critical, and even small errors may influence the correlation channels, de-correlating the input signals and/or mixing the third and fourth Stokes parameters. Adjustment methods have been proposed, but they have not been demonstrated yet.
- All analog filtering must be done at RF-level. The filter must thus feature a very narrow relative pass-band and high isolation in the side bands. The isolation must be higher than the isolation in a traditional correlation radiometer, as all side-band noise will be aliased to the resulting base-band. Additional filtering may to some extent be added in the digital domain, but the sampling frequency must be selected properly to avoid aliasing between interfering side bands and the desired band, as this noise will not be removable in the resulting signal.

- The presence of high-speed digital electronics in a radiometer is a potential risk, and good isolation must be maintained between the analog and the digital parts. Moreover the use of digital frequencies with harmonics within the desired radiometer pass band should be avoided, and edges of digital signals should be slowed down as much as possible in order to avoid high order harmonics.

With the specified needs for the EMIRAD L-band radiometer and the list of advantages and drawbacks, the radiometer type for the final implementation can be selected. Basically, all four types of radiometers are possible: the switching polarization combining radiometer, the parallel polarization combining radiometer, the superheterodyne correlation radiometer, and the subharmonic sampling correlation radiometer.

Traditionally, the polarimetric radiometers of the Technical University of Denmark have been of the correlation type, and some technical experience already exist, in the design of receivers with high isolation and of digital correlators. The radiometers have been made for measurements at higher frequencies, however, and the digital radiometer was thus not an option, due to the limitations of existing analog to digital converters.

The overall design driver for the new L-band polarimetric radiometer is the high level of stability, keeping the effects of drifts below a level of 0.1 K during acquisition of an azimuth signature from the sea surface. Likewise the sensitivity must be kept below this level. The sensitivity level may be reached with adjustment of the integration time, but increase of the data acquisition time may increase the problems of maintaining stable conditions and thus radiometer stability. Moreover the instrument is intended for use in an airborne campaign, and constraints exist, regarding the minimum speed of the aircraft and radius of a circle with fixed incidence angle. Moreover long data acquisition times should be avoided, as the sea surface state must remain stable during data acquisition. All in all this leads to the exclusion of the switching polarization combining radiometer.

The parallel polarization combining radiometer will be a very large and heavy instrument for the present purpose, as thermal stabilization will demand rather large boxes for the receivers. Adding the fact, that three Stokes parameters are determined as a difference between two different outputs, causing increased risk for drift problems, the parallel polarization combining radiometer is not selected for implementation.

Correlation radiometers can be made rather compact, and with the demand for good thermal isolation and stability, especially the digital radiometer may be a good choice. Technologically it might be more risky than a traditional correlation radiometer, but taking advantage of modern technology of analog to digital converters, and taking special care about the potential risks, the new radiometer should be able to fulfil the demands for the radiometer. Taking the right precautions, none of the drawbacks are directly endangering the final design.

Finally, it should be added, that a radiometer of the direct subharmonic sampling type would provide a concept demonstration for future systems, and some valuable experiences may result.

4. The EMIRAD L-band radiometer

In this chapter the actual implementation of the EMIRAD L-band radiometer is presented. Following the basic presentation of the radiometer block diagram, some initial tests are made in order to evaluate the digital implementation. A power budget for the total system is set up, calibration strategies are considered, and the analog front-end is designed along with a printed circuit board containing the digital correlators. The chapter is concluded with a characterization of the total system, some calibrations are done, and the radiometer stability is evaluated using simple laboratory setups.

4.1. Radiometer block diagram

With the choice of the direct digital radiometer with subharmonic sampling for the implementation of the new EMIRAD radiometer, a basic block diagram of the complete design can be made. Figure 4.1 shows this diagram in a simplified form, and main components are seen to be the antenna, the orthomode transducer, OMT, the analog gain and filter stage, analog to digital converters, and a correlator unit.

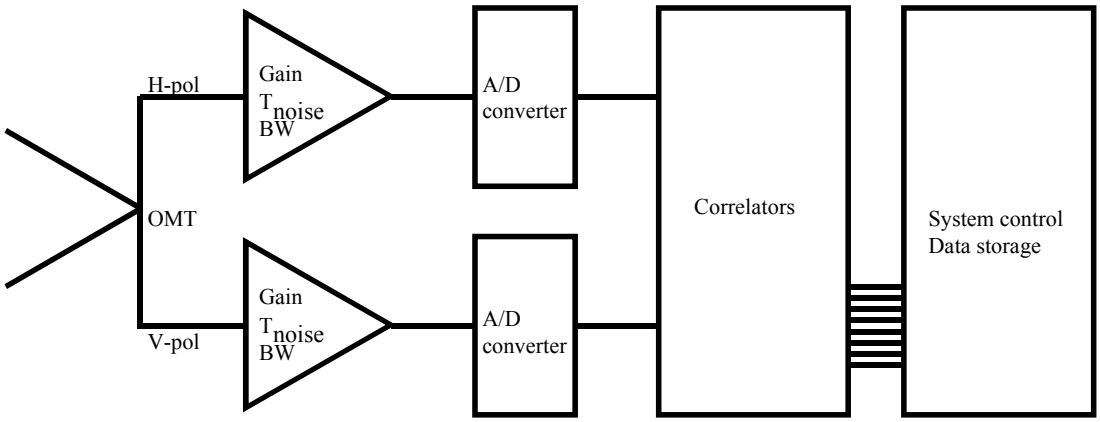

Figure 4.1. Simple block diagram of new L-band EMIRAD polarimetric radiometer. The RF-stage is characterized by gain, noise temperature, and frequency band.

As stated in the presentation of the digital radiometer in chapter three, the RF front-end block contains the full system gain and the full analog filtering, while detection, integration, down conversion etc. is done in the digital domain. The block diagram shows the end-to-end system, including the correlator block and the digital back-end. The correlators are both self-correlators for the signal power detection and cross-correlators used for determination of the 3rd and 4th Stokes parameters.

4.2. Calibration strategy for the radiometer

The demands for calibration and for long-term/short-term stability depend on the application. As the EMIRAD radiometer is planed for use in airborne campaigns measuring wind driven azimuth signatures over the ocean down to a magnitude of 0.1 K, and also intended for use

over a land test site during several month, a set of demands for the calibration system appears.

During the flights, the short-term stability is the overall design driver, while the need for absolute calibration is more relaxed. The absolute level should stay within a few Kelvin in order to keep the motion compensation for roll variations within scale, but the magnitude of the azimuth signature will be almost independent from an eventual bias. At least one reference target is needed for evaluation and monitoring of the drift and the reference target may also be used as a calibration point for the absolute level. For the correlation channels injection of correlated noise in the two receiver channels will enable bias adjustment and eventual phase correction.

For the polarimetric and soil moisture experiment at the Avignon test site the absolute calibration is essential, however, and an eventual drift will directly influence the results. The experiment runs during five month, and the measurement conditions must be considered changing from day to day, and even within a series of measurements, which can take several hours to carry out. Direct sun radiation on the instrument may influence the temperature stabilization, and it should be assumed that instrument gain and noise temperature could vary due to heating of the electronics. It must thus be assumed that each point of measurement must contain observations of at least two reference targets in order to make an individual calibration. The demand for absolute calibration precision is defined by the soil moisture signals under observation, and to provide new information to the models, a calibration within 1 K to 2 K is necessary for the vertical and horizontal brightness temperatures. For the polarimetric azimuth signatures, the absolute calibration demand is relaxed like in the ocean circle flights, while a minimal drift within the acquisition of a full signature is essential.

To fulfil all demands, the instrument needs at least two reference targets for absolute level calibration as well as a correlated and uncorrelated noise source for calibration of the third and fourth Stokes parameters. Finally, a reference target is needed for evaluation of stability during data acquisition of azimuth signatures, giving a total of five different calibration sources. For implementation this is unpractical, however, and some of the demands may easily be combined. Two targets per radiometer channel for absolute calibration are needed, and they may at the same time serve as stability evaluation references. If one of the targets is individual for each channel, it gives the uncorrelated noise source, and selecting the other target common, e.g. a shared noise diode, the correlated source is also available.

The individual target is easy to implement, as it demands only a simple switch and a temperature stabilized and temperature monitored matched load, providing a black body with known physical temperature. As no connection between the two exist, the noise from the two sources must be absolutely uncorrelated.

The common target can be a noise diode with a power splitter and attenuators to adjust the power level. A major concern, however, is the physical connection between the two channels, provided by the feed network from the noise diode to each of the two channels. It may enable a cross coupling of the input signal, and according to the comments in chapter 3 it should be observed, that the isolation between the channels is better than 70 dB in order to avoid cross coupling, influencing the correlation channels.

The noise diode will be a quite stable target, and monitoring its temperature will allow calculation of a first order model for the output power. The input signal in each of the two channels will not be 100 % correlated, as the uncorrelated receiver noise will be added to the signal in each channel. The level of correlation will be known, however, as the observation of the uncorrelated noise will provide information about the receiver noise, and together the two points will give information for calibration of the third and fourth Stokes parameters.

4.3. The analog to digital converter

A central component in the digital radiometer with subharmonic sampling is the analog to digital converter, ADC, which performs the sampling and the down conversion of the analog RF-signal. The situation is special compared to many traditional uses of analog to digital converters, where normally the analog signal is band limited around DC, and the sampling frequency, f_s, is greater than two times the maximum signal frequency, f_{max}, to avoid aliasing in the frequency domain.

In the EMIRAD case, the sampling frequency is intended to be in the range between 55 MHz and 120 MHz, while the signal frequencies cover the band from 1400 MHz to 1427 MHz. For the analog to digital converter this special situation means, that precautions should be taken, when the component is selected. The sampling frequency is usually the limiting parameter, and converters will typically be specified relative to their maximum sampling frequency, regarding clock jitter, sampling window, effective number of bits, ENOB, and input signal bandwidth.

In EMIRAD the input signal frequency determines the necessary performance of the ADC, and using the RF-frequency directly, the component choice is limited. Some of the first discrete converters, specified to run at these input frequencies, appeared on the market in 1998 under the name MAX104, provided by Maxim semiconductors. The device is specified with a 2.2 GHz analog 3 dB bandwidth, a maximum sampling frequency of 1.0 GHz, and a test/demo board including the necessary support electronics is available.

Some initial tests were carried out with the purpose to evaluate the effective number of bits from the converter, when it was operated at 100 MHz clock frequency and input frequencies ranging from 1 MHz to 1401 MHz. The data output was collected using a Tektronix TLA704 logic analyzer with a total memory depth of 64 Kbytes, which with a sampling speed of 100 MHz gives a total duration of one data set of 0.65 ms.

Each data set is Fourier transformed, an eventual DC is removed by high pass filtering the output with a 50 kHz cut-off, and the power in the selected input frequency, P_{signal}, is calculated, using a 50 kHz window around the frequency. The integrated side lobe power, P_{isl}, is calculated by summing all remaining contributions in the frequency spectrum, including eventual harmonics etc. The result is defined as the signal-to-integrated-noise, SIN, given by equation 4.1.

$$SIN_{dB} = 10 \cdot \log_{10}\left(\frac{P_{signal}}{P_{isl}}\right) \tag{4.1}$$

The effective number of bits is defined from the assumption that an ideal converter will give a signal output at maximum signal level, only adding the quantization noise. Assuming a converter with a range from –1 to +1, the signal power will be equal to 0.5. The error from the quantization may be regarded as a random noise [39], rectangular distributed from -d/2 to d/2, where d is the distance between two quantization levels, given by $2/(2^n-1)$, where n is the number of bits. The noise power is given by equation 4.2, and the signal-to-noise-ratio is defined by equation 4.3

$$P_N = \frac{1}{d}\int_{-d/2}^{d/2} e^2 de = \frac{d^2}{12} = \frac{4\cdot\left(2^n-1\right)^{-2}}{12} \tag{4.2}$$

$$SNR_{dB} = 10\cdot\log_{10}\left(\frac{3}{2}\left(2^n-1\right)^2\right) \approx 1.76 + n\cdot 6.02 \tag{4.3}$$

For an noiseless converter SNR will be equal to SIN, but for a real converter, SIN will be degraded by the converter noise, thus degrading the effective number of bits, defined as the number of bits needed to give the measured signal-to-noise ratio.

For the 8-bit MAX104 mounted on the test/demo board, a maximum value of 7.59 bit vas measured. A 10 MHz input signal was sampled at 100 MHz, using a Miteq crystal with a noise level at -80 dBc as clock generator and a HP8640B analog signal generator with noise below -65 dBc as input source. The number of bits is almost equal to the specified number, 7.60 bits, in the MAX104 data sheet, and as expected the number of bit decreases, when the input frequency is increased, showing 6.98 at 501 MHz input. For the 1401 MHz input frequency, the test equipment limits the measurement, as a HP8648D with performance of only -48 dBc replaced the HP8640B, which has a maximum frequency of 550 MHz. At 10 MHz the HP4648D shows 5.96 effective bits, and this number is only reduced to 5.92 at 1401 MHz. Due to the poor test equipment, it can only be concluded, that the performance is between 5.92 bits and 6.98 bits, but for the radiometer this result is satisfactory, and the MAX104 can be used for the implementation.

A serious drawback of the MAX104, however, is its relatively large power-consumption, which is approximately 10 W/channel in the basic configuration. This value does not only increase the demands for the power supply, but it also creates a heat flux from the chip. It may influence the possibilities of isolating the converter from changes in the surrounding temperature, and it may raise a demand for forced air cooling of the instrument.

A number of power supply pins enables the use of different voltage levels for the input amplifier, the track and hold circuit and the digital output stage, and by applying the minimum voltage for each stage, the power consumption may be reduced by 25 %. It will, on the other hand, increase the number of power supplies necessary, and thus the total system size and weight.

Generally, the characteristics of the MAX104 makes it useable for the present technology demonstration, and as it is easily available on the market during the project period, it is a reasonable choice for the EMIRAD L-band radiometer. It is, however, unsuitable for eventual future radiometers, which consists of a larger number of receivers, e.g. a synthetic aperture radiometer, SARad, but several newer and more attractive devices are scheduled for

production and sale in near future, pushing the present power supply and heat problems in the background.

4.4. The analog front-end

The analog front-end should contain the full system gain, the analog filters, calibration targets, switches, and the external components like antenna and orthomode transducer, OMT.

The antenna design is not a direct part of the radiometer design project, but specifications should be set up in order to select a suitable design for the airborne campaign. Size and weight is limited by the C-130 aircraft, available for the missions, and as the antenna beam width will determine the range of incidence angles covered in a single target point, the design should aim for the narrowest beam in order to reach the best resolution. Aiming for a side looking installation, the maximum length of the total antenna system is limited to 3 meters, and the aperture of the antenna is limited by the 90 cm wide C-130 parachute door, giving an approximate minimum beam width of 15°. The antenna should be dual polarized, and the cross coupling between the two channels should be minimized.

External components in the front-end, including the antenna, orthomode transducer and RF-cables, are placed outside the calibration system of the radiometer, and corrections for their losses will have to be applied in the signal processing. Corrections are based on measurements of the physical temperature of the components, T_L, and the loss of the component, η, according to equation 4.4, where T_M is the measured brightness temperature, and T_A the antenna brightness temperature.

$$T_M = \eta \cdot T_L + (1-\eta)T_A \tag{4.4}$$

Assuming a loss of 0.1 dB and an antenna brightness temperature of 100 K, the measured brightness temperature will be equal to 104.39 K for a 293 K physical temperature. An uncertainty of 1° C on the physical temperature, e.g. due to the size of the antenna and the airflow around it, will change the estimate for the antenna brightness temperature by 0.03 K, which is beneath the 0.1 K sensitivity, required for the radiometer. For a 0.5 dB loss, the 1° C uncertainty, however, will result in a 0.13 K error on the estimate of T_A, enough to exceed the maximum error limit. It is hence essential, that external components, which are not temperature controlled and thus hard to determine the precise physical temperature of, have as low losses as possible.

With these results, two approaches for the external circuitry can be made. Either make all components as small as possible and include the whole system in a temperature stabilized environment or select implementations with minimum loss. The physical small solution might include a patch antenna, feed network, and radiometer built together in a single temperature stabilized box. The low-loss solution would aim for a horn antenna, a wave-guide based orthomode transducer and low-loss RF-cables, connecting the antenna system to a temperature stabilized radiometer input.

For the patch antenna design, it may be realistic to determine the physical temperature with a precision of 0.2° C, allowing for total losses of 1.76 dB, which is realistic to reach in typical patch antenna layouts, including feeds. For the low loss system, 1° C is a realistic temperature determination, and total losses must in this case be kept beneath 0.41 dB. Both antenna systems are realistic to manufacture and install in the aircraft, but due to the simplicity of the low-loss system and the simple manufacturing, it was chosen for the EMIRAD L-band radiometer.

The analog gain and filtering is included in a temperature stabilized box, common for both the H-channel and the V-channel, but divided by a base plate, carrying the components and ensuring thermal tracking of the two channels. The RF filter must contain all the analog system gain of the instrument. Additional filtering may be applied in the digital domain, but as the digitizing process will cause aliasing in the frequency spectrum, the bands, overlapping the desired band, can not be removed later and must be suppressed sufficiently in the RF section.

A traditional L-band radiometer will use only the protected L-band, ranging from 1400 MHz to 1427 MHz, and it should secure sufficient side-band suppression, typical at least -60 dB, at the band limits. In the digital radiometer, an extension of the band with subsequent selective digital filtering is possible. The full analog pass band must be digitized alias free, however, and the dynamic range of the analog to digital converter must be able to handle the radiometric signal along with an eventual RF-interference from other users of the band. In worst cases, the dynamic range should be of the order of the side-band suppression in a traditional RF-filter, 60 dB, equal to 10 bits. As the EMIRAD L-band radiometer will use a converter with only 8 bits, and as it is intended as a digital radiometer demonstration, planed for applications in field campaigns, no band extensions are included, and the analog filter will aim for –60 dB suppression of the side band. Practically, it is decided to specify a filter with -3 dB limits at 1403 MHz and 1424 MHz, -20 dB limits at the protected band limits, and –60 dB suppression at all other frequencies from DC to the cut-off frequency of the analog to digital converter.

The total RF gain must be matched to the analog to digital converter specifications, and it must take into account the eventual unlinearity of the digital detection due to saturation of the converter. Figure 3.7 shows the effect of saturation for a Gaussian distributed input signal with an effective noise voltage for 500 K, which is 16 dB below the maximum input signal range, ±250 mV. The EMIRAD L-band radiometer will have an antenna brightness temperature ranging from 0 K to 300 K, 100 K noise added from the calibration noise diode, and additional about 100 K from the receiver noise. A total input range up to 500 K is thus to be assumed, and accepting a maximum error from the unlinearity of 0.5 % below the low input signal plateau, the input level shown in the figure is acceptable.

The other gain range limitation is the noise induced by the finite number of bits and the noise added by the converter. With an 8-bit converter, providing 6 effective bits at the L-band input frequency, equation 4.3 will give a signal to noise ratio of 37.75 dB for a full input signal, ranging from –250 mV to +250 mV. As the maximum input is reduced by 16 dB, the signal to noise ratio for a 500 K input signal is 21.75 dB, equal to a worst-case additional noise temperature from the analog to digital converter of 3.34 K, which is acceptable.

The 16 dB gap to the maximum converter signal is equal to an input level of –15 dBm in a 50 Ω transmission line. The radiometer front-end input is determined by formula 4.5, where T is the brightness temperature, B the bandwidth, and k Boltzmann's constant.

$$P_{in} = k \cdot T \cdot B \tag{4.5}$$

For 500 K input brightness temperature and 25 MHz bandwidth, the input signal thus equals –97.6 dBm, demanding a total radiometer gain of 82.6 dB. Practically the gain will be divided between a low-noise-amplifier in front of the filter and the remaining system gain behind it to avoid saturation due to RF interference.

The noise temperature of the receiver is determined by low noise amplifier and the external losses, as indicated in formula 4.6.

$$T_N = (F - 1 + \eta) \cdot T_0 \tag{4.6}$$

T_N is the noise temperature, F is the noise figure of the receiver (dominated by the low noise amplifier), η is the loss in front of the receiver, and T_0 is the standard temperature, 290 K.

Last component to consider in the RF section is the 90° phase shifter, mentioned in chapter 3. It is needed to measure the 4th Stokes parameter, and it may be placed in the analog section as well as in the digital. To ensure a simple digital design for the initial demonstration, the phase shifter is included in the analog section, enabling for both solutions in the final operative setup. Along with the calibration targets, the total analog system for the EMIRAD L-band radiometer is shown in figure 4.2, where the dashed line shows the separation between the temperature regulated box and the external components

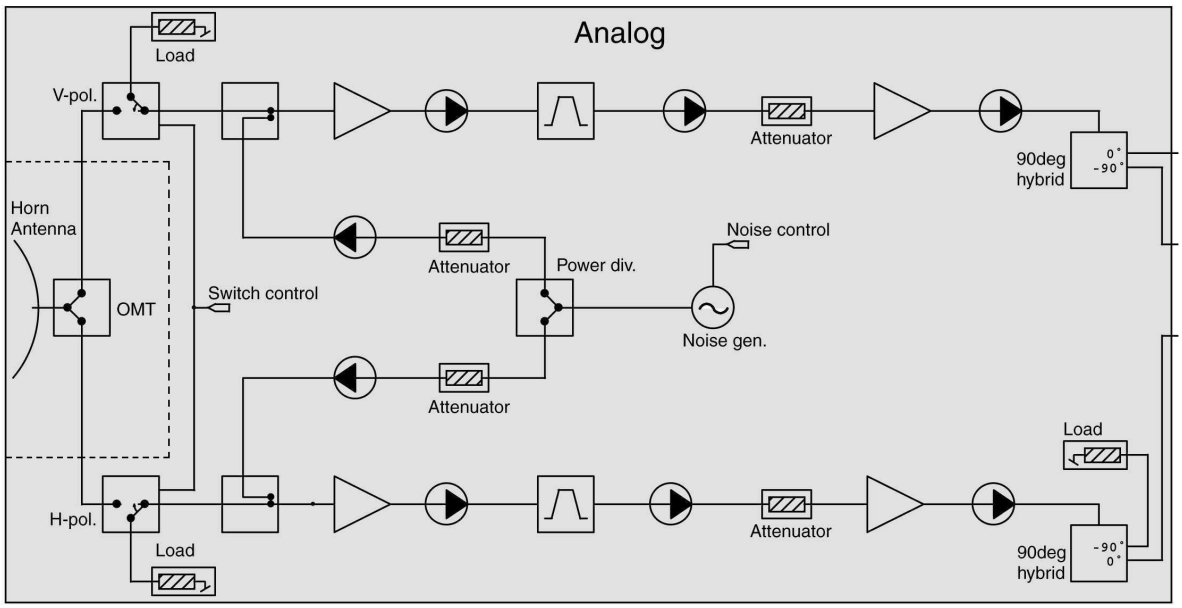

Figure 4.2. Detailed block diagram of the RF section of the EMIRAD L-band polarimetric radiometer. The dashed line shows the separation between the temperature regulated box and the external circuitry.

The chains of analog circuits in each of the receiver channels have been phase matched to better than 5 degrees, equal to a delay of 10 psec., before assembly. Special care is taken in order to match the components in the noise generator feed network, and network analyzer results show a match better than 2 degrees. A photograph of a full radiometer channel is shown in figure 4.3.

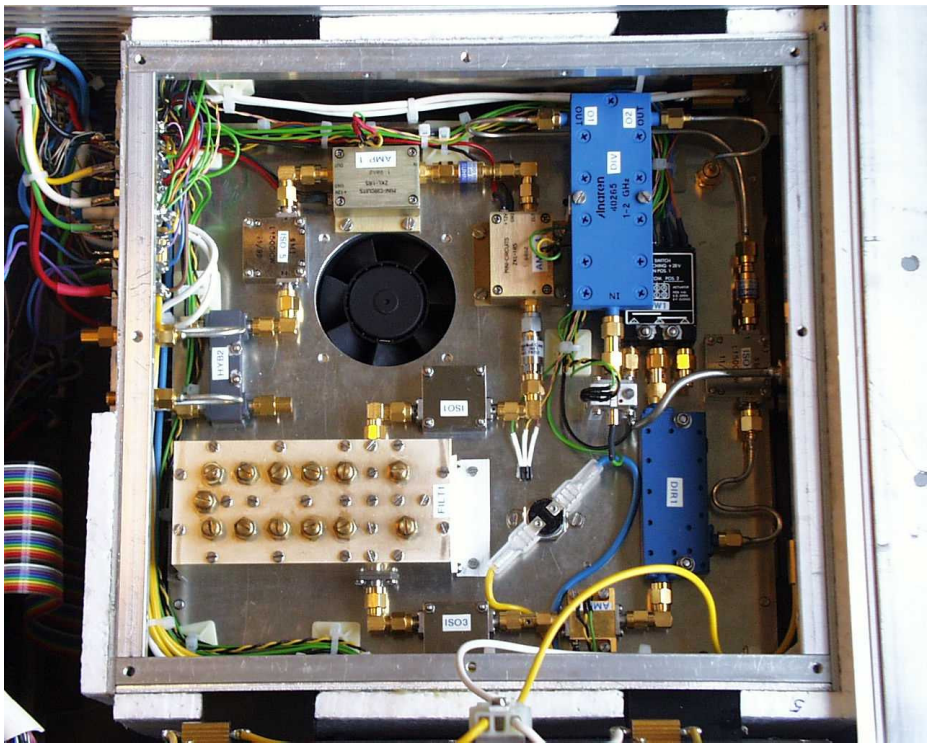

Figure 4.3. Photograph of the horizontal channel of the RF section of the L-band EMIRAD polarimetric radiometer.

4.5. The digital front-end

The circuitry containing the analog to digital converters, the correlator array, and the integrators is referred to as the digital front-end. In this design it is all collected on a single printed circuit board, PCB, with three input channels. The channels represent the three outputs from the RF section, the inphase output from each polarization and the quadrature output from the vertical channel for determination of the fourth Stokes parameter without digital filtering in the first version.

With the experience from the analog to digital converter characterization, the MAX104, supporting input frequencies up to 2.2 GHz, is selected for the radiometer. Three units are needed, and the output from each unit is guided to a field programmable gate array, FPGA, which will contain firmware for performance of the signal power detection, the correlation measurements, and the integration. The subharmonic sampling principle, presented in chapter 3, is used, and any sampling frequency, f, complying with formula 4.7, where n is an integer, can be selected.

$$f \le \frac{f_{\min}}{m}$$
$$f \ge \frac{f_{\max}}{(m+0.5)} \qquad (4.7)$$
$$m = n/2$$

For the EMIRAD radiometer with a –20 dB passband from 1400 MHz to 1427 MHz, the lowest sampling frequency intervals are shown in figure 4.4. The lowest possible sampling frequency interval is [54.885 MHz; 54.902 MHz], but as it leaves only 8.5 kHz for eventual frequency drift, a higher choice is preferred. The limit is set by the maximum input to the FPGA, and avoiding the newest (and most expensive) families like Altera APEX and Xilinx Virtex, typical frequencies from 80 MHz to 100 MHz are specified.

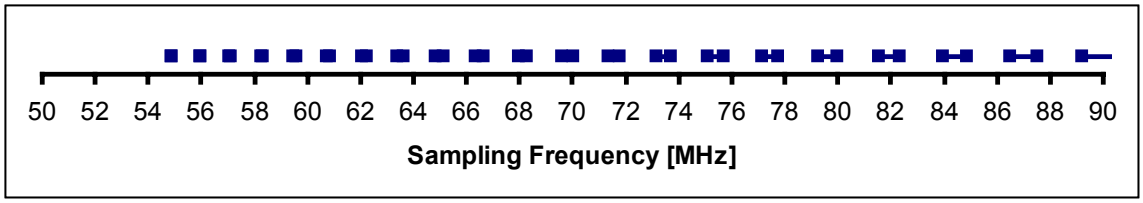

Figure 4.4. Possible sampling frequencies for the digital front-end of the EMIRAD radiometer, when the covered frequency band is from 1400 MHz to 1427 MHz.

An Altera 10K100E-3 is selected for this implementation due to its relatively large number of gates and its internal memory. It provides approximately 90 MHz input frequency, depending on the exact firmware, and leaving a margin for eventual add-ons to the firmware, a sampling frequency of 63.5 MHz can be selected.

Apart from the signal detection, correlation, and integration, the digital front-end must provide all interfacing to the analog to digital converters. Important are setup signals, input signal decoding, DC offset adjustment, and sampling delay control. The signal decoding is rather simple, as the output data from the analog to digital converter is offset binary, covering the input range [-250 mV; +250 mV] with the 256 binary values, representing the lowest input voltage with 0, and the highest with 255. A 0 mV-input voltage will result in an output value of 127.5, practically represented by values 127 and 128 toggling on the output port. Internally, the format may be converted to traditional 2's complement by toggling the value of the most significant bit and adding a 9th dummy bit, which is always one, representing the value ½.

With a 2's complement data format the determination of the DC level is done with a simple integration of the analog to digital converter output data, and the offset input to the converter can be adjusted with a small digital to analog converter, DAC. The sampling delay determination is described in chapter 3, and digital clock delay components are integrated in the digital front-end. The delay coefficients are supplied from the FPGA, and as well as the DC offsets, they are locked during data acquisition and only adjusted during a setup sequence, initiated by the system control computer.

Cross-correlation calculation is performed on the three pairs of inputs, and self-correlation determines the signal level for each of the three input channels. These results along with a

measurement of the actual DC levels, and a reference counter, giving the number of samples integrated, is provided as output from the digital front-end at the end of each integration period. The time of integration is variable, as an external synchronization signal determines the end of each period, and only the number of available bits in the internal counters limits the period, which may be up to 4 seconds.

Internally, the integration periods may be subdivided, as a long integration period will exclude the possibility of sorting out short intervals, polluted by RF-interference. Typical origins of such interference are L-band radars, transmitting pulses of a few microseconds at rates around 1 kHz. A typical subperiod could be 100 μsec., and results exceeding a predefined threshold should be rejected, before the remaining results from the subperiods are integrated together and packed. The threshold can be fixed or it can be relative to the signal level in the previous full integration period, but in both cases it should be noticed, that the subperiod length is limited by the signal standard deviation. For a 300 K input and 100 μsec. subintegration the standard deviation will be 6 K, and as the margin to the threshold should be at least 10 dB in order to avoid unlinearities, the example needs a threshold 60 K above the signal level, i.e. 360 K.

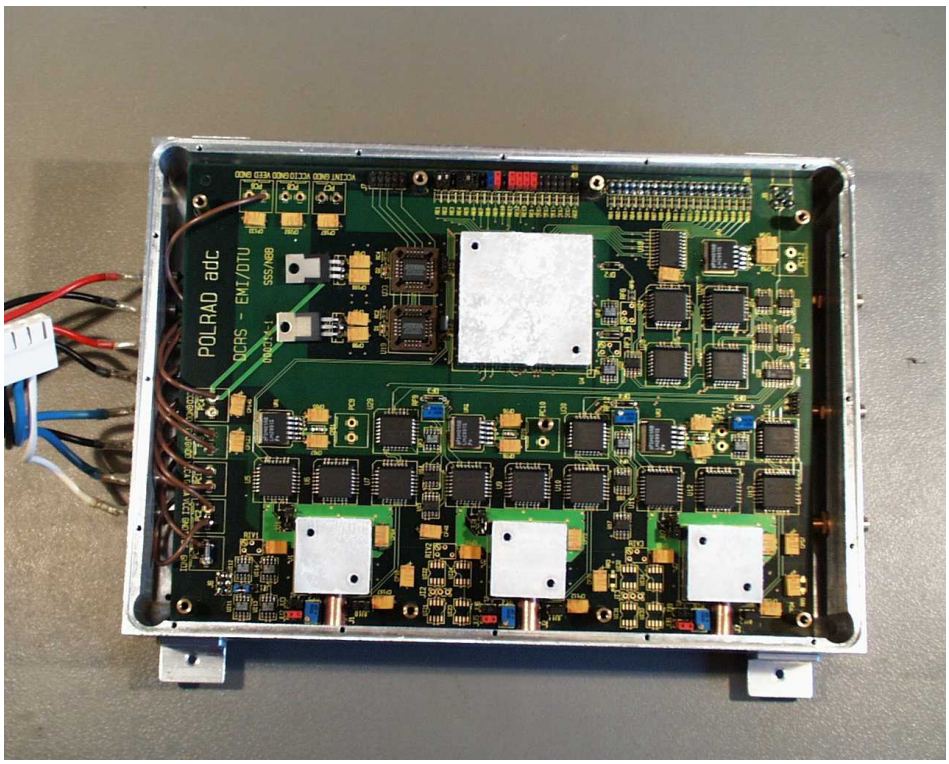

Figure 4.5. Photograph of the digital front-end of the L-band EMIRAD polarimetric radiometer. The whole system is placed in a shielded box to avoid eventual RF loop-back from the printed circuit board lines to the antenna.

This limitation makes the time-domain filter able to filter out large-scale RF-interference, while small-scale interference will proceed through the system. Methods for small-scale interference filtering, based on the different statistical behavior of natural signals (Gaussian distributed) and man made signals (typically sinusoidal), have been considered but not

implemented in the first version. Initial tests on the laboratory roof indicate few RF-interference problems, and the instrument will primarily be applied in ocean flights, approximately 200 km from coastlines, where the risk of RF-interference has been considered rather low.

A photograph of the digital front-end is shown in figure 4.5, where it seen, that the whole board is enclosed in a shielded box. This is necessary due to the danger of RF loop-back in a subharmonic sampling system, where all system gain is at RF level. With more than 80 dB gain in the RF section, even a small leak, e.g. from the input lines of the analog to digital converters, may cause a gain-loop saturating the receivers and in worst cases destroying the system.

4.6. The system back-end

The digital back-end of the EMIRAD radiometer is responsible for the instrument control and the data transfer from the digital front-end to the final data storage. It is also responsible for all real time tasks, such as calibration, collection of housekeeping data etc., and finally it must take care of data formatting and time stamping in order to synchronize data originating from different units.

A part of the control system must reside locally in the radiometer system, while the operator interface must be located in an independent unit, located away from the radiometer. This is necessary for most practical applications, e.g. in an aircraft, where the radiometer should stay near the open door, where the antenna is installed, while the operator should stay some meters behind.

The unit in the radiometer must contain an interface to the digital front-end, some low frequency analog to digital converters for temperature and voltage level monitoring, and a number of line drivers, able to drive the connection to the operator unit. A small printed circuit board, PCB, is assembled for this purpose, and a small field programmable gate array, FPGA, is included for instrument control, data collection, and data formatting. The PCB is built into the radiometer box, and a 10-meter cable is used for the communication.

The other cable end is connected to a second printed circuit board, which receives the digital signal and adds a header, containing a time stamp with an accuracy of 64 μsec. The unit may collect data from up to six different units and data from peripheral sources, such as the internal aircraft control bus or a GPS receiver may be added. Data from the board is finally transmitted to the system control computer, where it is stored. A second connection from the control computer connects to a Honeywell H-764 EGI, embedded GPS/INS; a combined GPS receiver and inertial navigation unit, providing aircraft navigation data. The unit uses the same time stamp as the radiometer, and it provides aircraft attitude data with an accuracy of 0.05°. The GPS is optional, but an antenna is available for the flights, enabling the operator to monitor the actual flight tracks.

The control computer runs a real time control program, storing data from the different units, and executing commands for the radiometer. Some commands depend on the interaction with

the operator during data acquisition, and some are predefined for each flight. Predefined commands may contain information about instruments present, radiometer integration time, the desired calibration sequence, and about the frequency for acquisition of navigation data. The data is acquired from the radiometer during the flights in a compressed, binary format, containing header information, instrument condition (housekeeping) information, and raw radiometer data. The header data package includes information about the actual integration period length, switch positions, noise diode mode, and some identification bits to recognize the hardware modules. The housekeeping section contains data for the physical temperatures at 16 different points inside and outside the instrument. Some of these temperatures are used to monitor the operational state of the instrument and send alarm messages to the user in case of overheating, while some others are used for instrument calibration.

The data section includes the uncalibrated four Stokes parameters for the integration period, stored in a block floating point structure. Each data is stored as a 16 or 24-bit mantissa, while the floating-point exponent is common to all data in a polarimetric signature. This gives sufficient dynamic range for the polarimetric signatures, but as data is packed uncalibrated, the range of the values may depend on the integration time. To compensate for this dependence, a floating point exponent is packed along with the data, ensuring for sufficient dynamic range for all brightness temperature values from –500 K to 500 K for integration times from 4 msec. to 4 sec.

The packed data format is unpacked with the preprocessing program, PrPre, Polarimetric radiometer Preprocessing, which stores the measured data in a readable ASCII format. The program creates a number of files, depending on the target of observation, and calibration data is thus divided from antenna measurement data. Housekeeping data, i.e. temperatures of analog front-end components, as well as data from the inertial navigation unit are provided in separate files with synchronized time stamps.

The next processing step is carried out in the software package “DigInt”, (Digital processing and Integration), and it regards the calculation of the 3rd and the 4th Stokes parameters from the measured complex correlation, $\rho = \rho_r + i*\rho_i$. Ideally the two parameters are given by equation 4.8 and 4.9, where T_V and T_H is the vertical and horizontal brightness temperature, respectively.

$$\begin{aligned} U &= 2 \cdot \rho_r \cdot T_{SYS} \\ V &= 2 \cdot \rho_i \cdot T_{SYS} \end{aligned} \tag{4.8}$$

$$T_{SYS} = \sqrt{\left(T_V + T_{Noise,V}\right) \cdot \left(T_H + T_{Noise,H}\right)} \tag{4.9}$$

Phase adjustment, i.e. the setting of sampling delay coefficients, is done in the digital front ipment limits the measurement, as a HP8648D with performance digital converters are adjusted to sample in phase, giving the ideal phases $\varphi_1 = 0°$ and $\varphi_2 = 90°$ between the signals for determination of the real and imaginary part of the correlation, respectively.

The coefficients are left unchanged during data acquisition, however, and small drifts can occur during measurement of a track. The two parameters will change according to the

equations 3.19 and 3.20, but as typical residual drifts will be rather small, less than 20 psec., equal to 10° at the L-band frequency, the magnitude-decrease due to the decorrelation illustrated in figure 3.9 can be neglected. Additionally it should be noticedd, that the three analog to digital converters are mounted on a common heat sink, making them track in physical temperature, and hence in sampling delay. Absolute changes of 10° will thus be seen as differential errors between two inputs in the order of a few degrees maximum.

Corrections can be applied to the measured parameters, U_M and V_M, using the noise diode observations to provide the actual phase values. Equation 4.10a and 4.10b give the correction formulas, where U and V represent the true Stokes parameters, and φ_1 and φ_2 the estimated phases for the two parameters, ideally $\varphi_1 = 0°$ and $\varphi_2 = 90°$.

$$U = \frac{U_M \cdot \sin(\varphi_2) - V_M \cdot \sin(\varphi_1)}{\cos(\varphi_1)\cdot\sin(\varphi_2) - \cos(\varphi_2)\cdot\sin(\varphi_1)} = \frac{U_M \cdot \sin(\varphi_2) - V_M \cdot \sin(\varphi_1)}{\sin(\varphi_{1+}\varphi_2)}$$

$$V = \frac{V_M \cdot \cos(\varphi_1) - U_M \cdot \cos(\varphi_2)}{\cos(\varphi_1)\cdot\sin(\varphi_2) - \cos(\varphi_2)\cdot\sin(\varphi_1)} = \frac{V_M \cdot \cos(\varphi_1) - U_M \cdot \cos(\varphi_2)}{\sin(\varphi_{1+}\varphi_2)} \qquad (4.10a\text{-}b)$$

4.7. System test

Based on the elements described in the previous sections, the new EMIRAD radiometer is assembled and tested. Tests will primarily focus on the instrument linearity, calibration, and stability.

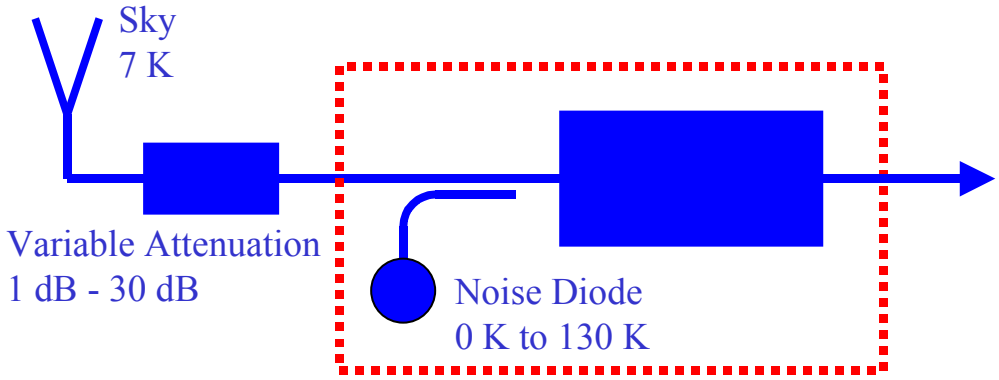

Figure 4.6. Instrument setup used for linearity evaluation. Changing the attenuation in front of the instrument and switching on and off the noise diode will provide the gain for different input brightness temperatures and thus illustrate the linearity.

For evaluation of the instrument linearity, a special experiment was set up as illustrated in figure 4.6, where the instrument antenna is pointed to the sky, providing a cold input target. The built-in calibration noise diode is used to add 130 K to the input signal, and the difference between the two measurement outputs divided by 130 K will provide the receiver gain, expressed in equation 4.11, where C(x) represents the raw digital radiometer output.

$$G = \frac{C(T_{Noise+Input}) - C(T_{Input})}{T_{Noise}} \tag{4.11}$$

Adding an attenuator to the input cable, i.e. increasing the input brightness temperature, and using 4.11 again will provide the gain at a higher input brightness temperature. For a series of attenuation settings, a curve of the gain as a function of the input brightness is thus acquired, and the results are shown in figure 4.7. As the data acquisition takes about an hour, there is a potential risk that receiver drifts will influence the result. To estimate that influence, the input calibration switch is switched to the built-in calibration load for every data point, and the gain is evaluated using the same method. These results are shown as the red and green curved in figure 4.7 for comparison.

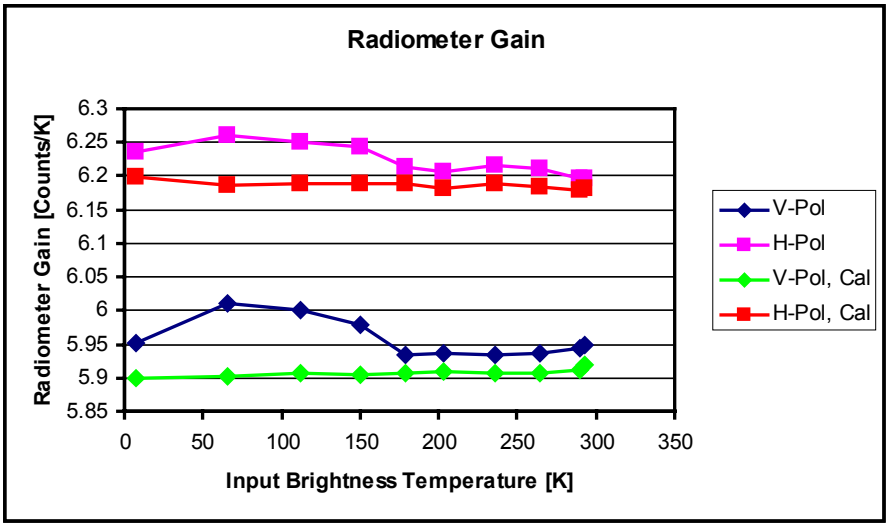

Figure 4.7. EMIRAD L-band radiometer linearity. The blue and purple curves show the gain for the vertical and horizontal radiometer channels for a range in input brightness temperatures. The green and red curves are control measurements with the built-in calibration load for each data point, showing an eventual receiver drift.

Knowing the gain curves for the two channels, the transfer function for the radiometer can be derived as an integration of the gain after low pass filtering. These curves are shown in figure 4.8, which is the calibration basis for the radiometer during field measurements. The linearity measurement shows worst-case gain variations of the order of (6.01 – 5.94)/5.94 = 1.18 %, which is slightly over the design target, but still within the acceptable range – even without correction based on the experiment. The output level in figure 4.8 is seen to be 1800 counts for 300 K input brightness temperature. Adding 100 K receiver noise gives approximately 2400 counts output, which is higher than the level calculated in figure 3.6, and used for the determination of the RF-gain. The higher unlinearity may thus be explained by a small error in the adjustment of the RF-gain, setting a higher input level than expected and thus causing a higher suppression of the high-end brightness temperatures.

Without linearity corrections, 300 K input might result in a worst-case absolute error of 2.5 K, which is unacceptable for some applications. For the azimuth signature measurements, however, an absolute error is not important, and the effect of the unlinearity is completely negligible for the small azimuth signature variations. With the linearity correction, shown in

figure 3.7, the absolute error from the unlinearity can be reduced, and the correction can be applied to the data from the campaigns in the preprocessing software.

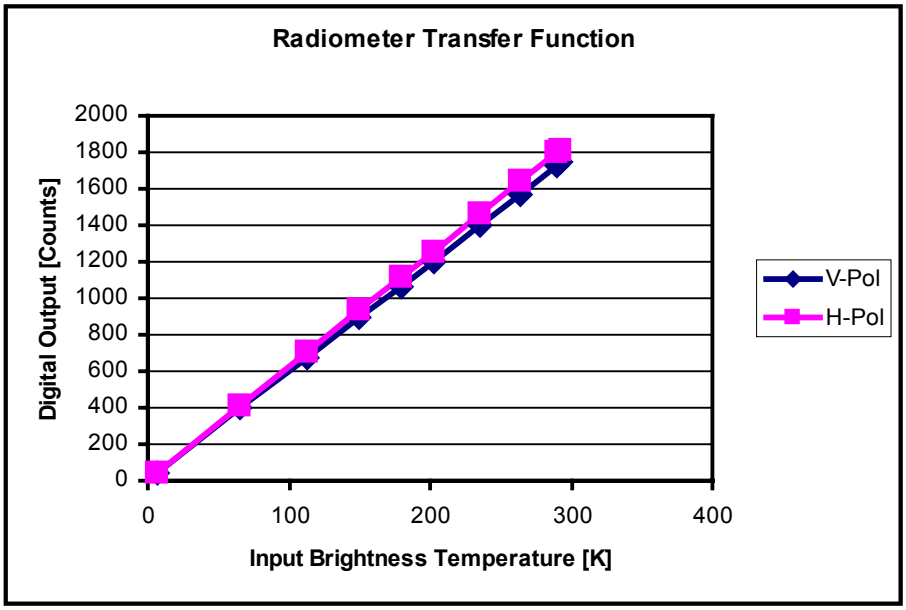

Figure 4.8. Integrated gain curves for EMIRAD L-band radiometer. The curves illustrate the total end-to end receiver transfer function for the vertical and horizontal channels.

The next radiometer parameter to investigate is the short-time and long-time stability, which is essential for the ocean flights and for the determination of eventual azimuth signatures. An experiment was set up, letting the radiometer observe the built-in calibration targets (load and load + noise diode) during 90 minutes. The half of the measurement was made, when a constant ambient temperature (9° ± 0.5° Celsius) was maintained in the laboratory. After 45 minutes an outside door was opened, and the temperature dropped to approximately 4° Celsius. The brightness temperature from each of the detection channels along with the 3rd and 4th Stokes parameters were measured every 8 msec., but integrated in the data collection software to 10 sec. to reduce the amount of data and to reduce the standard deviation (ΔT = 30 mK). T_V and T_H for the calibration load observations are shown in figure 4.9.

Figure 4.9 shows that T_H typically varies ±0.15 K during the first 45 minutes, if the single point at t = 59070 sec. is left out, and the total is thus satisfactory for a measurement of this length. When the ambient temperature is changed 5°, a drift of 0.2 K is observed, equal to a 14 dB suppression of ambient temperature changes. The time constant is approximately 20 minutes, and it is observed that the radiometer gain is unstable during this period. After the change to the new working condition, the typical variation level of ±0.15 K is restored, and all in all it can be concluded, that the horizontal channel stays within the specified limits, when the channel is not observed right after steps in the ambient conditions.

The vertical channel, T_V, has the same basic behavior, but it is noticed that it has two major dropouts of about 0.2 K during the first 45 minutes. No explanations have been found for these dropouts, but as they have a length of several minutes, ∂Gain/∂t will be rather small, and an interpolation between calibration points in the scientific measurements will be able to

correct for this error. With this modification, it may also be concluded, that the vertical channel stays within the acceptable range for the scientific applications.

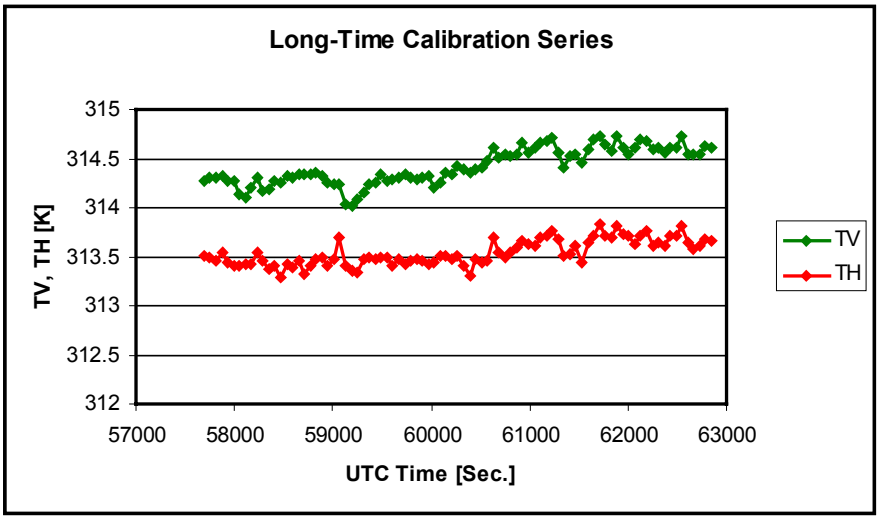

Figure 4.9. Results from the two detection channels for the long time observation of the built-in calibration load. The temperature of the load changes less than 0.1 ° Celsius during the measurement. The ambient temperature is stable 9 ° Celsius during the first 45 minutes, and decreases to 4 ° Celsius during the last 45 minutes.

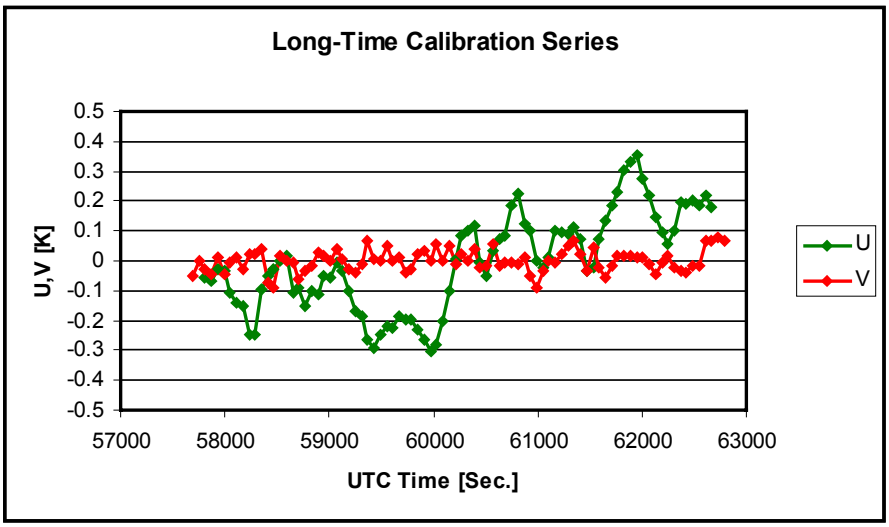

Figure 4.10. Results from the two correlation channels for the long time observation of the built-in calibration load + noise diode. The 3rd Stokes parameter is offset to zero-mean to ease the plot. The brightness of the load and the noise diode output change less than 0.1 K during the measurement. The ambient temperature is stable 9 ° Celsius during the first 45 minutes, and decreases to 4 ° Celsius during the last 45 minutes.

The correlation channels are evaluated with the noise diode switched on, and the results are seen in figure 4.10, where the 3rd Stokes parameter is offset to zero-mean to ease the plot. The curves show a behavior similar to the detection channels, and the step as result of the ambient temperature change is again easily observed. During the stabilized periods before

and after the step, a ±0.15 K variation (from the 268 K level) is observed for the 3rd Stokes parameter, while the 4th Stokes parameter stays below ±80 mK variation. It is noticed that a very high isolation is established between the two correlation parameters, indicating that the sampling delay adjustments are very precise and stable. In real observations, the 3rd Stokes parameter is expected to be in the order of maximum 10 K, and a downscaling of the error is to expect. All in all it may thus be concluded, that the correlation channels stay fully within the demands for the scientific measurements.

During the stability measurements, the standard deviation of the radiometer signals were observed. For the observations of the load in the basic integration period, 8 msec., the standard deviation was 1.17 for the horizontal channel and 1.20 for the vertical channel. Theoretically the standard deviation, ΔT, should be given by equation 4.12, where T_N is the noise temperature, T_B the input brightness temperature, B the system bandwidth, and τ the integration period.

$$\Delta T = \frac{T_B + T_N}{\sqrt{\tau B}} \tag{4.12}$$

In the EMIRAD radiometer the noise figure of the system front-end, i.e. receiver and front-end components, is approximately 1.4 dB, giving a noise temperature of $T_N = 120$ K. For the 313 K input it should be expected to see $\Delta T = 1.09$ K, which is slightly less than the observed values.

The noise temperature is calculated experimentally in the linearity experiment, using the built-in load and the noise diode as calibration targets. Results are here found to be $T_{N,V} = 125$ K and $T_{N,H} = 138$ K, which should result in a standard deviation of $\Delta T = 1.13$ K. This result still shows, that the observed ΔT is slightly (about 6 %) above the expected level, but as the value decreases by the square root of N, when N samples are integrated, no further investigations are carried out in order to find an explanation for the difference.

5. The EMIRAD field campaign, Avignon

During a period of five month, the EMIRAD radiometer was stationed at the Institut National de la Recherche Agronomique, INRA, in Avignon, France in order to take part in measurements concerning radiometric signatures from a land surface test site. The radiometer was mounted on a crane near the fields under observation, and full polarimetric signatures were measured during the growth season, along with soil and crop parameters. The campaign was part of a joint project between the Technical University of Denmark and INRA, and a full analysis of these data is beyond the scope of this project. Special interest is related to the radiometer calibration, stability, and possible polarimetric signatures from the field under observation.

5.1. The experiments

The full Avignon experiment consists of a range of measurements over the test site at the Institut National de la Recherche Agronomique, INRA. Available for the experiment was an area of approximately 150 meters by 100 meters, divided in two sub-areas by a rail track. On the rail a crane is mounted in a permanent setup, and it may be moved along all 120 meters of track length. In the height of 20 meters the crane has a carriage mounted under a 20 m boom, which may be turned around 360°. The carriage may be moved along the boom, and it can be lowered to ground level during installation and service. The carriage is preinstalled with a main power cable and an Ethernet connection.

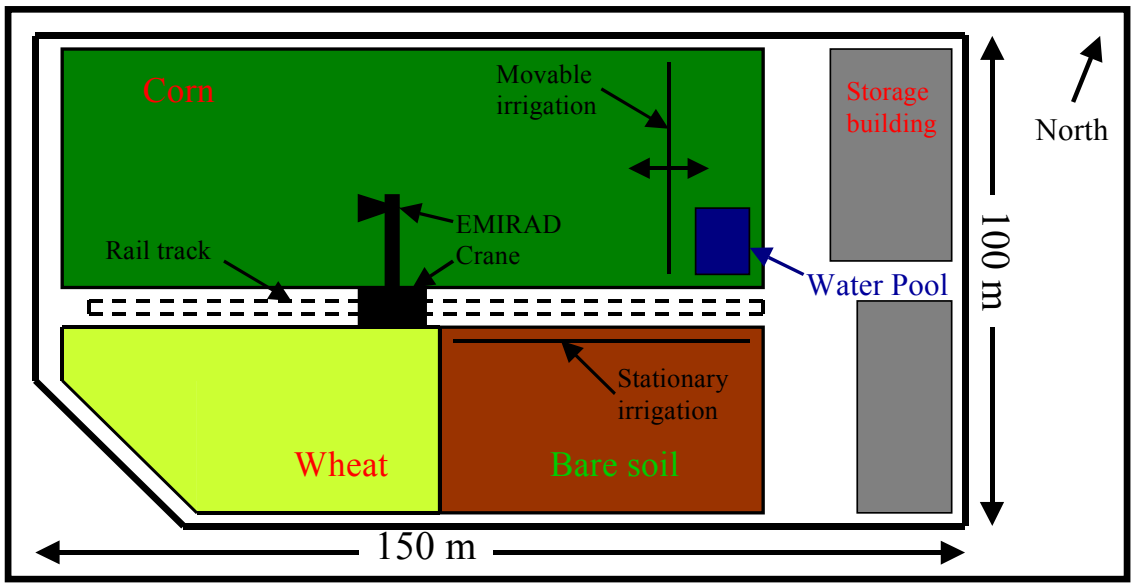

Figure. 5.1. The test site at Institut National de la Recherche Agronomique, Avignon, France. The EMIRAD L-band radiometer is mounted on the crane, 20 m above the ground. It may observe incidence angles from 0 to 60°, and 2x90° azimuth angle.

For the mounting of the radiometer on the crane a special mechanical interface was developed at INRA, and it extended the maneuvering opportunities by a 0° to 60° incidence angle variation and a -90° to 90° rotation around the vertical axis through the carriage. For attitude control two angle measurement units were mounted on the radiometer antenna, each giving an angular measurement with a precision of 0.1°. One unit measures the incidence angle relative to nadir, and the other provides the antenna rotation around the antenna axis in order to correct for eventual polarization mixing. The complete radiometer installation is shown in figure 5.2.

Figure. 5.2. The radiometer installation at Institut National de la Recherche Agronomique, Avignon, France. The EMIRAD L-band radiometer is mounted on the crane, 20 m above the cornfield. Incidence angles vary from 0 to 60°, and azimuth angles from –90° to 90°.

Experiments were carried out in the period from April 24th 2001 to July 26th 2001. Measurements were made Monday to Friday (security staff was not available during weekends and holidays) in the period, only limited by technical service periods and the weather conditions. The radiometer could not operate during rainfall and at wind speeds above 20 m/sec, limiting the total number of data acquisition days to 38.

As indicated on figure 5.1, three target areas were available. The wheat field, however, which was planned by another INRA group, was not large enough for radiometer measurements due to the antenna pattern size, and the campaign focused on the two other targets, using the corn field as primary target. Two kinds of measurement series were carried out, change of incidence angle with constant look-direction (parallel to the rail or perpendicular to the rail) and change of azimuth look-direction with constant incidence angle. The first series was primarily intended for use with INRA modeling of the influence from soil moisture on the measured brightness temperature, while the latter is used for identification of eventual azimuth signatures from the field.

Ground-truth values for the soil moisture were collected every measurement day by the INRA team. Samples were collected from the soil in a range of depths, and the soil moisture was evaluated by comparing the mass of the sample before and after drying. Equation 5.1 shows the soil moisture as a mass-ratio, α, where m_0 is the mass of the sample container, m_1

is the mass of the fresh sample, while m_2 is the mass of the dry sample.

$$\alpha = \frac{(m_1 - m_0) - (m_2 - m_0)}{m_2 - m_0} = \frac{m_1 - m_2}{m_2 - m_0} \qquad (5.1)$$

Typically, samples were collected at ten different places within the cornfield, allowing for eventual deviations to be filtered out. The sample collection was primarily of interest for the soil moisture determination experiments, done by INRA, while the information was used only for background knowledge in the azimuth signature analysis. Figure 5.3 shows a series of soil moisture samples from different depths (in cm.), collected during the season.

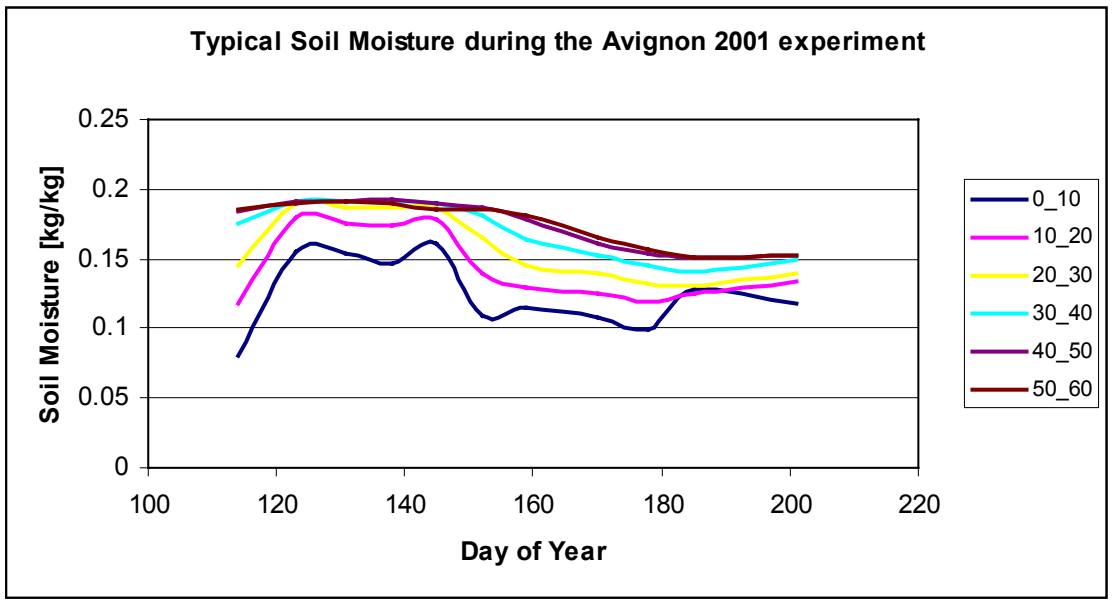

Figure. 5.3. Soil moisture measurement during the Avignon 2001 experiment. The curves show the soil moisture for one of the measurement points [kg/kg] for different depths, determined by 10 cm intervals.

5.2. Data calibration

Data from the radiometer is collected during the experiment in the floating point format, described in chapter 4. The output is sampled in a basic period of 8 msec., and each data point is observed for 30 sec., running a calibration sequence as shown in figure 5.4. Each calibration target is observed 1 sec. in every calibration block, giving a sensitivity of $\Delta T < 0.1$ K, and the remaining time is used for observation of the target. The long observation time allows for eventual time-domain filtering of the recorded data, if RF-interference is discovered. With the selected calibration, it is expected, that a sensitivity better than 0.1 K is realistic, and for the present experiment, this result is satisfactory.

For each data point, data is unpacked with the preprocessing software, “PrPre” (Polarimetric radiometer Preprocessing) and “DigInt” (Digital processing and Integration), mentioned in chapter 4. The software packages convert the data to ASCII files, corrects eventual sampling delay drifts regarding the correlation channels, and divides the data in measurement data and calibration data. Housekeeping data, i.e. data from the radiometer temperature sensors, is

synchronized to the radiometer data, enabling for corrections of the output data according to physical temperatures of active components and front-end losses.

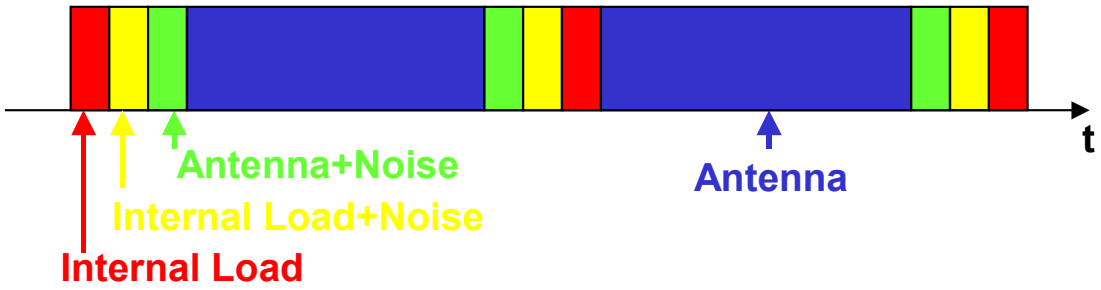

Figure 5.4. Calibration sequence for the EMIRAD L-band radiometer at the INRA test site.

With the short 8 msec. integration period the preprocessing software can calculate a preliminary calibrated data value and the standard deviation within the data file. The operator is thus able to monitor the instrument during data acquisition, and data points with RF-interference or unstable measurement conditions may be rejected immediately. A typical problem of instability is sudden wind bursts, moving the instrument, and causing the look angle or the incidence angle to vary.

When a data point is accepted, it is stored along with the antenna rotation, the azimuth look angle and the incidence angle, provided by sensors mounted directly on the radiometer antenna. Further integration is done, and a data point thus results in a single sample of the Stokes vector for each of the four targets. The complete calibration is done offline, using data from the calibration load and from the observation of load + noise, and taking into account the unlinearity, derived in chapter 4. Finally, corrections are applied according to the physical temperatures and the losses of the external components, such as antenna, orthomode transducer and RF-cables, using equation 5.2, where T_M is the measured brightness temperature, T_L the physical temperature of the component, η the loss, and T_A the incident antenna brightness temperature.

$$T_M = \eta \cdot T_L + (1-\eta) T_A \qquad (5.2)$$

To get the correct Stokes parameters, an eventual mixing of the 2nd and the 3rd Stokes parameters must be removed according to equation 2.15. The antenna rotation is provided directly in the data set, and a simple inversion of the equation provides the desired parameters.

5.3. Long-term stability

In the Avignon experiment, the long-term radiometer stability is essential, as data from different days must be combined into a single data set. The drift analysis carried out in the general instrument characterization must thus be combined with a large-scale evaluation, running parallel to the scientific experiment. For this purpose, the water pool, marked in figure 5.1 was constructed, and observation of the water surface provides a well-known calibration target. The pool was observed every three weeks, and a range of incidence angles

was covered in order to provide different input brightness temperatures for the radiometer. Figure 5.5 shows the measurement situation, and to get an impression of the possible range of observation, some simple calculations are made. With a –20 dB antenna beam width of about β = 45° and an antenna altitude of h = 1 m, the distances d1 and d2, and hence the minimum pool length, can be found, using equation 5.3.

$$d_1 = \frac{h}{\tan(90 - \alpha - \beta/2)}$$
$$d_2 = \frac{h}{\tan(90 - \alpha + \beta/2)} \qquad (5.3)$$
$$l_{\min} = d_2 - d_1$$

In the cross direction equation 5.3 is used with α = 0, and the minimum pool width is found.

The red arrows in figure 5.5 show the reflections of the incident field, and to avoid catching the mirror image of the antenna, $2*d_1$ must be greater than the projection of the half the antenna aperture, a/2, on the horizontal plane, indicated by equation 5.4.

$$\frac{2h}{\tan(90 - \alpha + \beta/2)} > \frac{a}{2}\cos(\alpha) \qquad (5.4)$$

With the given numbers, the minimum incidence angle is found to be 33°, and selecting a maximum angle of 55°, the pool dimensions must not be less than 4 meters by 1 meter. It should be noted that the geometric calculations are only approximations, as far field behavior is not directly transferable to the near field. It is thus decided to construct a pool of 6 m by 6 as shown in figure 5.6, and the results from the observations will be evaluated in order to limit the angular range if necessary.

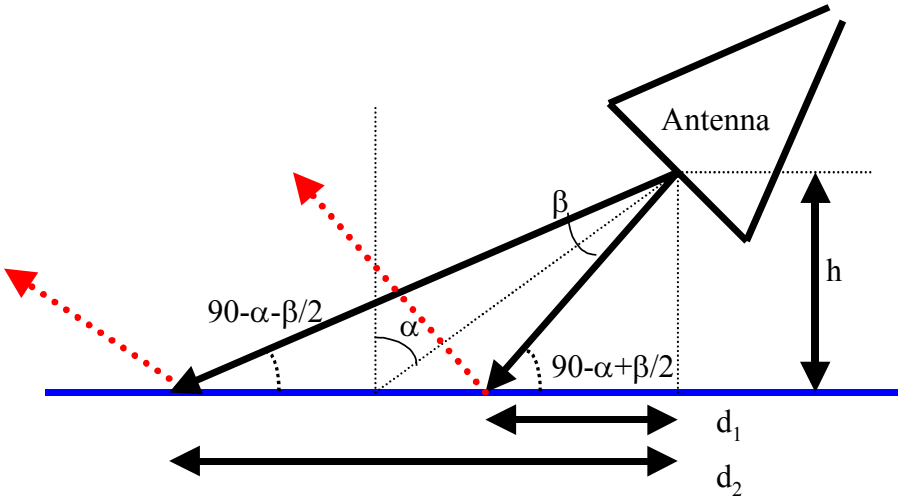

Figure 5.5. The measurement situation with the radiometer antenna over the water pool. With the incidence angle α and the antenna beam width β, the pool size can be determined.

The results from the pool observations depend on the water temperature, and to evaluate the radiometer calibration from the different days of observation, the expected brightness temperatures for the pool surface are calculated for each day of measurement. The values for

May 16th 2001 are shown in figure 5.7, where the green and orange curves show the expected values and the red and blue curves the actual radiometer output brightness temperature.

Figure 5.6. The 6 m by 6 m calibration pool used for evaluation of the long term radiometer stability during the 2001 Avignon experiment.

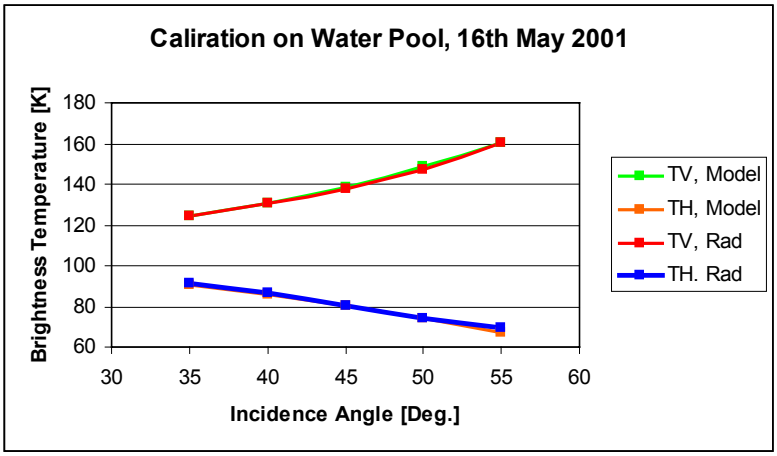

Figure 5.7. The expected (green and orange) data from the water pool at different incidence angles and the measured (red and blue) values from the 16th May calibration.

The full results from the water pool measurements are seen in table 5.1, where the expected values for all pool observations are listed along with the measured values. The last two columns show $\Delta T = T_{rad} - T_{exp}$ for each of the two polarizations. The general impression from the deviation data is, that a few point are far from the expected values, while most points show a quite fair ΔT. For the H-channel, the average deviation is 0.20 K, and the standard deviation is found to be 0.76 K. The V-channel has a 0.29 K average and a 1.63 K standard deviation. A fair evaluation should leave out the points, which are obviously far off the expected values, and it is noticed, that three from the five measurements with 35° incidence angle show a deviation larger than 2 K. Common to all the larger deviations are, that the deviation is positive, and a possible cause may be an antenna side-lobe outside the

pool or a fraction of the antenna aperture falling within the reflected beam as indicated in figure 5.5. Leaving out the five largest deviations, the standard deviation drops to 0.87 K, which is comparable to the result from the horizontal channel.

DOY	α [°]	T_V, expected [K]	T_H, expected [K]	T_V, rad. [K]	T_H, rad. [K]	ΔT_V (rad - exp)	ΔT_H (rad - exp)
136	35	124.33	90.83	123.99	91.04	-0.342	0.212
	40	130.70	85.93	130.48	86.78	-0.224	0.848
T_w = 21°C	45	138.57	80.34	137.76	80.42	-0.809	0.081
	50	148.28	74.07	146.90	74.51	-1.387	0.442
	55	160.32	67.11	160.36	69.30	0.044	2.195
143	35	125.64	91.82	125.99	92.56	0.349	0.736
	40	132.07	86.87	132.40	86.42	0.334	-0.449
T_w = 23°C	45	140.00	81.23	142.04	81.43	2.033	0.200
	50	149.80	74.89	149.11	75.20	-0.694	0.307
	55	161.94	67.86	161.59	68.93	-0.344	1.074
171	35	123.68	90.34	125.86	90.08	2.189	-0.253
	40	130.02	85.46	132.21	84.66	2.189	-0.799
T_w = 20°C	45	137.85	79.90	136.05	79.05	-1.796	-0.846
	50	147.52	73.66	147.39	73.79	-0.131	0.132
	55	159.51	66.73	159.21	65.88	-0.302	-0.854
198	40	132.07	86.87	137.36	87.58	5.292	0.716
	45	140.00	81.23	141.92	81.05	1.920	-0.172
T_w = 23°C	50	149.80	74.89	148.48	75.43	-1.323	0.543
	55	161.94	67.86	160.79	69.32	-1.146	1.465
206	35	126.94	92.81	129.18	93.19	2.242	0.378
	40	133.42	87.80	132.66	87.42	-0.764	-0.380
T_w = 25°C	45	141.43	82.11	142.29	81.23	0.860	-0.880
	50	151.31	75.70	151.08	75.39	-0.231	-0.316
	55	163.54	68.60	162.44	69.11	-1.101	0.508

Table 5.1. Expected and measured brightness temperatures from the water pool. The two right columns show the difference ΔT = Trad – Texp for each channel.

With the results, found above, it is demonstrated, that the stable pool target gives quite stable results, typically within ±1 K, during the measurement season. This result is absolutely satisfactory for the full experiment; the INRA soil moisture experiments as well as the search for eventual polarimetric signatures.

It is noticed, that the stability of ±1 K is reached, although the ambient conditions changes significantly during the experiment. In the first weeks, the air temperature was about 20° Celsius, and no direct sun radiation was on the radiometer, which enabled the internal temperature regulation to maintain the desired temperature of the analog components. In the later weeks, the air temperature raised beyond 34° Celsius, and periodically direct sun was on the instrument. This caused the operating temperature to increase by approximately 3° C, and the gain of the RF section dropped by more than 5 %. Nevertheless the instrument is able to provide output data within a standard deviation of ±1 K, and it is concluded, that the calibration strategy performs satisfactory for the defined purpose.

5.4. Polarimetric soil surface signatures

The purpose of the Avignon experiment was partly to generate well calibrated data for the INRA work on the soil moisture influence on the brightness temperature at different incidence angles and in different moisture conditions during the growth season. The other part of the experiment was the identification of eventual polarimetric azimuth signatures, using the full Stokes vector information.

During the experiment, azimuth scans were performed, and signatures were collected approximately once per week, depending on the weather conditions, at 20° incidence angle and at 40° incidence angle. The 40° measurements generally suffer from the limited size of the test area, and some look directions are corrupted, as some antenna side-lobes fall outside the desired area. The 20° scans, however, are generally quite good, and apart from a few cases of RF-interference, data is useful, and plots can be generated.

All azimuth look directions are measured relative to a line perpendicular to the rail track. For some days, a full 180° scan was possible, but as the movable irrigation, shown in figure 5.1, was unfortunately stuck in a position inside the cornfield from day 136, the scans from this day cover only 100° of the area. The first measurement was carried out on April 25th 2001, observing the cornfield, when it was still bare and without any crop. It was plowed and sowed a few days earlier, and the surface formed a wave pattern, with structures of 8 cm height, running parallel to the rail track, i.e. perpendicular to the 0° look direction.

The polarimetric result from the first measurement day, April 25th 2001, is shown in figure 5.8, where the 1st Stokes parameter is plotted with a zero mean to fit in the diagram. As expected in a sea surface wave pattern at higher frequencies [17] the signature seems to have some 1st and 2nd harmonic content in all the Stokes parameters, and a harmonic fit with a 1st and 2nd harmonic is shown in table 5.2. A plot of the harmonic fit, i.e. a filtered signature, showing only the 1st and 2nd harmonics, is shown in figure 5.9, and the length of the scan is extrapolated to cover a full circle signature.

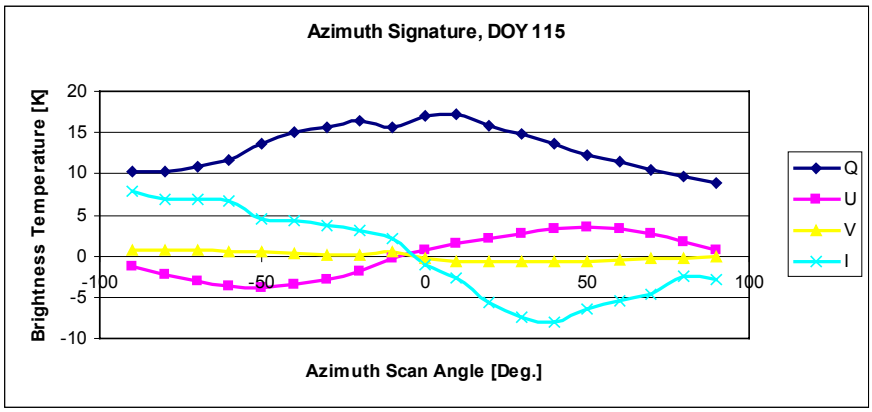

Figure 5.8. Azimuth signature from the April 25th 2001 measurement. The 1st Stokes parameter is offset to zero mean, and all azimuth angles are measured relative to a line, perpendicular to the rail track.

Harmonic	I, Mag.	I, Phase	Q, Mag.	Q, Phase	U, Mag.	U, Phase	V, Mag.	V, Phase
1	7.31	-143.47	1.64	-15.37	1.51	132.80	0.74	-150.44
2	3.18	-75.29	2.89	-1.12	2.84	73.17	0.31	-80.59

Table 5.2. 1st and 2nd harmonic fit for the full polarimetric azimuth signature from the April 25th 2001 measurement. No crop was visible on the field, and the soil had an obvious plowing/sowing signature, parallel to the rail track, i.e. perpendicular to the 0° direction.

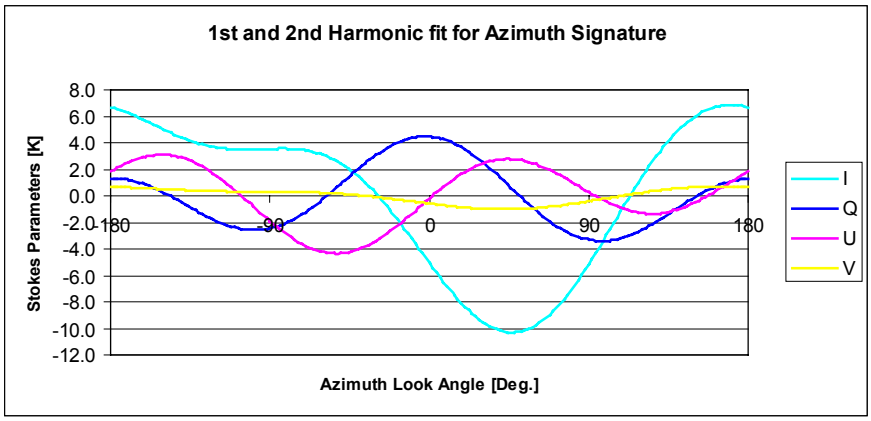

Figure 5.9. Azimuth signature from the April 25th 2001 measurement, based on the fit of the 1st and 2nd harmonic for each Stokes parameter. The signature is extrapolated to cover a full 360° scan.

Comparing figure 5.9 to a wave signature from the sea surface at higher frequencies, e.g. 34 GHz, shows some similarities. The presence of the 1st and 2nd harmonics is expected, and the cosine nature of the 2nd harmonic as well as the sine nature of the 3rd harmonic is similar. The 3rd and 4th Stokes parameters are observed to be 180° degrees out of phase, which also confirms the similarity to well known azimuth signatures from the sea surface. In the present case, the 0° look direction is comparable to the upwind look direction for a sea surface signature, which corresponds to the wave pattern, running perpendicular to the 0° look direction. The magnitude of the patterns show approximately 8 K from peak-to-peak in the 2nd and 3rd Stokes parameters, while the 4th Stoke parameter is smaller than 2 K peak-to-peak, and the relation between the magnitudes of the 3rd and the 4th harmonic is likewise comparable to the sea surface situation.

With the experience from the bare field on the 25th of April, the cornfield was observed during the growth season. The Sowing pattern decreased due to weather and irrigation, and already after two days, the height was reduced by 50 %. Additional decrease followed during a period of two weeks until a height of about 1 cm was reached. Meanwhile the crop appeared, adding approximately 1 cm per day of growth in the period of measurements.

Some polarimetric signatures from the experiment have been chosen from different phases of the growth, and they are seen in the figures 5.10 to 5.14. First of all it is noticed, that all figures show the same behavior, and the analysis based on a fit to a 1st and 2nd harmonic is continued. Comparing figure 5.10 to figure 5.8, it is seen that signature in the 2nd, 3rd, and 4th Stokes parameters have been decreased to about 50 % size, corresponding to the reduced wave height after the irrigation, applied April the 25th in the evening.

The decreasing trend for the soil wave height continued during the following two weeks, and on May 9th, 2 cm wave height was remaining. Signatures for this day are shown in figure 5.11, and the harmonic fit is presented in table 5.3. It is noted that the polarimetric signals are oriented in the same phase as in figure 5.8, except the 2nd Stokes parameter. The magnitudes, however, are reduced by approximately a factor of four since the first measurement, again corresponding to the relative reduction of the surface wave pattern.

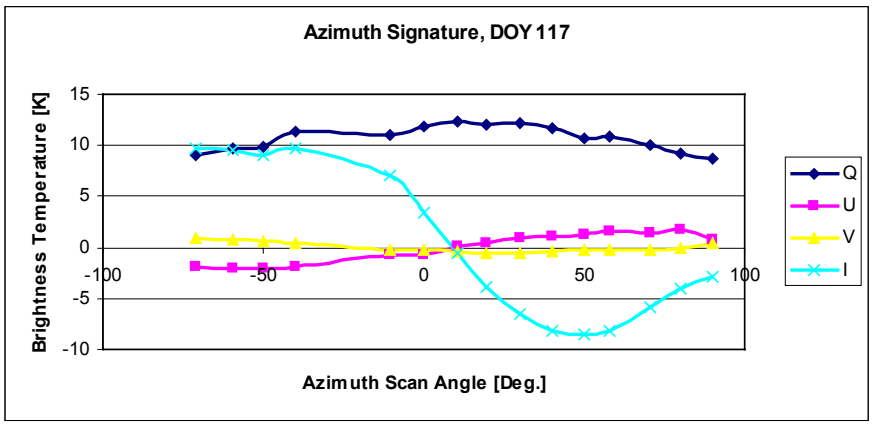

Figure 5.10. Azimuth signature from the April 27th 2001 measurement. The 1st Stokes parameter is offset to zero mean.

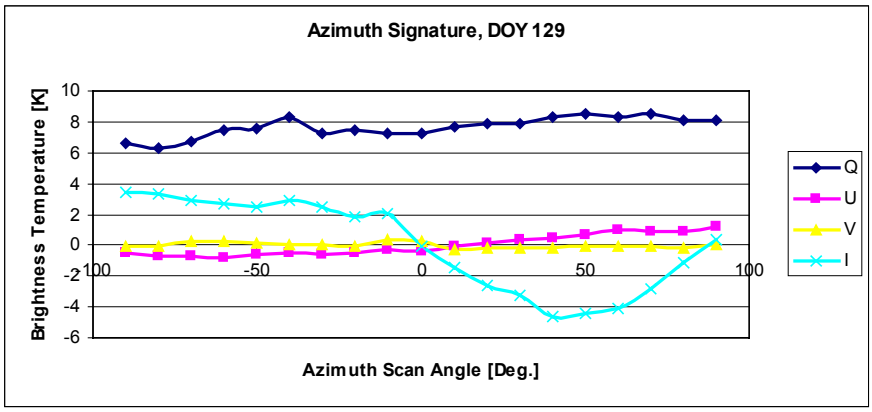

Figure 5.11. Azimuth signature from the May 9th 2001 measurement. The 1st Stokes parameter is offset to zero mean.

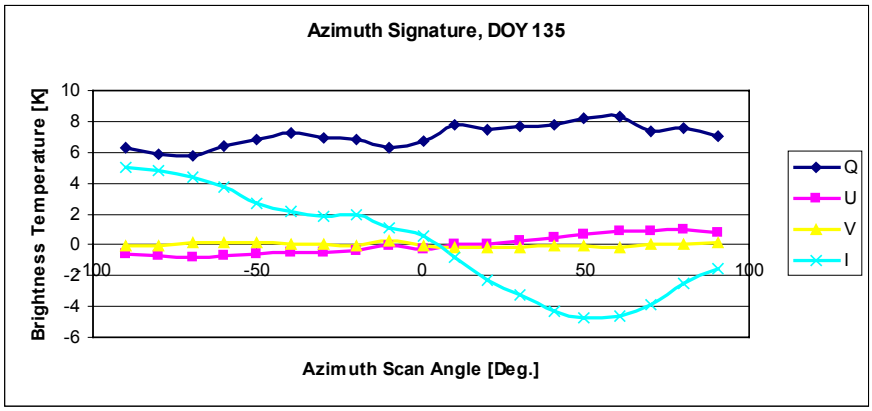

Figure 5.12. Azimuth signature from the May 15th 2001 measurement. The 1st Stokes parameter is offset to zero mean.

Figure 5.12 is obtained a week later, and a small further decrease of the wave pattern down to 1.5 cm was noticed since the acquisition of figure 5.11. The crop appeared, however, and 5 cm crop height was measured on May 15th. The harmonic fit is shown in table 5.4, and the general shape of the polarimetric signatures is again almost unchanged.

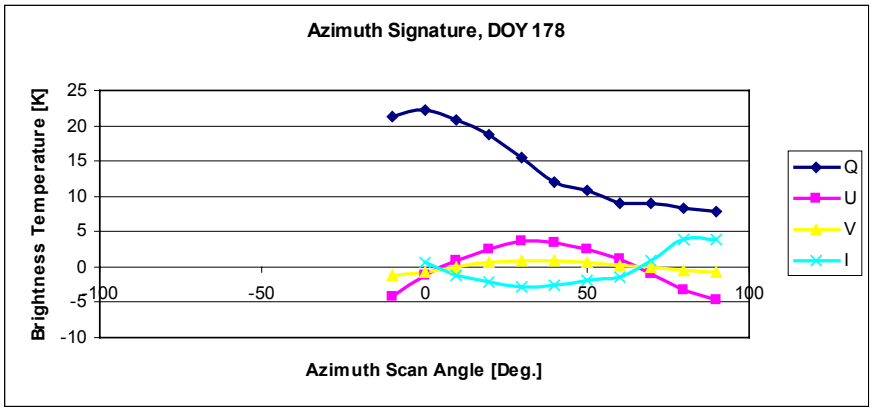

Figure 5.13. Azimuth signature from the June 27th 2001 measurement. The 1st Stokes parameter is offset to zero mean.

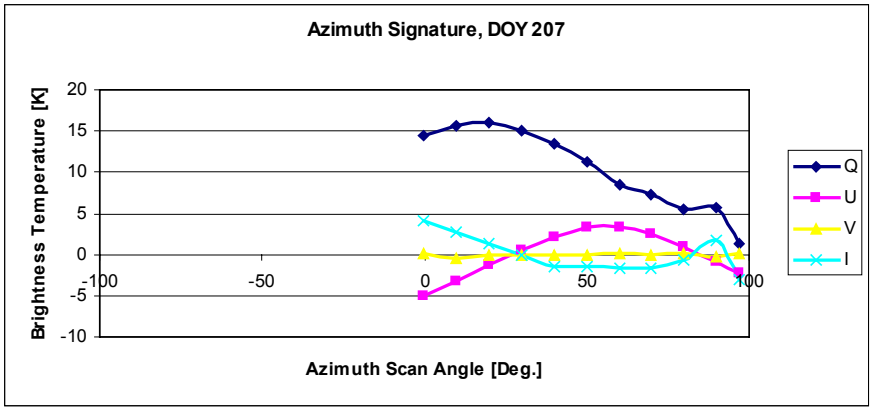

Figure 5.14. Azimuth signature from the July 26th 2001 measurement. The 1st Stokes parameter is offset to zero mean.

Harmonic	I, Mag.	I, Phase	Q, Mag.	Q, Phase	U, Mag.	U, Phase	V, Mag.	V, Phase
1	4.96	-164.14	3.10	16.84	0.94	120.22	0.06	31.29
2	3.02	-61.40	1.30	-168.72	0.06	95.81	0.18	-102.31

Table 5.3. 1st and 2nd harmonic fit for the full polarimetric azimuth signature from the May 9th 2001 measurement. Almost no crop (less than 1 cm) was visible on the field, and only a small remaining sowing signature of 2 cm was left on the soil.

Harmonic	I, Mag.	I, Phase	Q, Mag.	Q, Phase	U, Mag.	U, Phase	V, Mag.	V, Phase
1	5.85	-144.47	2.55	13.51	0.82	91.36	0.12	149.20
2	1.88	-39.77	0.96	165.98	0.13	176.59	0.15	-88.67

Table 5.4. 1st and 2nd harmonic fit for the full polarimetric azimuth signature from the May 15th 2001 measurement. The crop was 5 cm high, and only a small remaining sowing signature of 1.5 cm was left on the soil.

June 27th, the sowing pattern was completely disappeared, the crop had reached a height of 55 cm, and the polarimetric signature, shown in figure 5.13, shows a significantly increased polarimetric signature. A peak to peak variation of 15 K is observed in the 2nd Stokes parameter in the reduced angular range, and the 3rd Stokes parameter is estimated to have a similar peak-to-peak variation over the full 360° range. The variation of the 4th Stokes parameter is again ¼ of the variation of Q and U, but due to the small magnitude and the reduced angular space, the uncertainty on the parameter estimation is large.

The signature from July 26th, the last day of the campaign, is almost similar to the June 27th pattern, and all phases are identical within a few degrees. Magnitudes of the signatures are also similar, although a shift in the level of the 2nd Stokes parameter is observed. It may be explained by the increased leaf structures of the crop as well as by the small increase in the soil moisture as illustrated in figure 5.3.

5.5. Discussion

The polarimetric signatures from the Avignon 2001 experiment show a very similar pattern through all the campaign with respect to shape and phases of the four Stokes parameters. From the bare soil measurement the full 360° signature is estimated using a harmonic fit, and it is obvious, that the signal is very similar to the modeled signal from the sea surface. The phase of the signature shows, that observation perpendicular to the sowing waves of the field is similar to the sea surface observation in the upwind direction. This corresponds to the fact that upwind observations on the sea also will be perpendicular to the wave pattern. The difference in upwind/downwind is normally a sea surface specific phenomena, however, and it would be of great interest for the field observation to carry out a full 360° scan in order to exclude the risk, that small uncertainties cause the harmonic fit to show an upwind effect. The effect is present, however, in all harmonic fits done on the data, and a possible explanation for the signal is the asymmetric pattern, created by the plow and the sowing machine, when all soil is turned in the same direction.

The magnitude of the polarimetric signal is seen to depend on the sowing wave height, and for 8 cm waves, variations of 8 K peak-to-peak were observed in the 2nd and 3rd Stokes parameters. The 1st Stokes parameter shows approximately the double signal size, while the 4th Stokes parameter has 2 K peak-to-peak. For the three signatures, measured on the bare soil, the signals were shown to decrease linearly with the wave height, keeping the phase information. Basically this is expectable, and a simple model may be based on table 5.2, 5.3, and 5.4, multiplied by the wave height normalized to the 8 cm waves, causing the pattern in table 5.2.

When the sowing pattern decreased and the crop appeared the polarimetric pattern reappeared, reaching a maximum of 15 K peak-to-peak variation for the first three Stokes parameters and 2 K for the 4th. Due to instrument service, the azimuth signature is not well monitored in the period between the appearance of the crop and the maximum signal level. It is noticed, however, that the maximum signal is reached already when the crop is 0.5 m high, and although it grew to 0.8 m during the following month, adding a large extent of leaf structure, no further signal size was registered. Phases of the signals are seen to be stable

during all the series from the first signature from April 25th to the 0.8 m crop on July 26th. The background for this may be the row structure organization of the crop, following the sowing pattern of the field, hence restoring the decreasing sowing structure when the crop begins to form. A simple model for the polarimetric signal from the crop may thus be based on the same basic signature as the bare field, changing only the magnitude to a crop height dependant signal, saturated around the maximum observed signals. The dependence is subject for further investigation, however, as the measurement interruption due to the instrument service took place in June, when the saturation effect occurred.

Concluding the experiment regarding the polarimetric signatures from the cornfield it is noticed that signal magnitude changes up to 15 K are possible from the same field, when observed from different directions. Assuming a large homogenous corn area, it is thus a potential problem for a space borne mission to estimate ground parameters based on the L-band brightness temperatures, if the field has a row structure. For small fields the effect may be averaged out to some extend, as the footprint of the space borne instrument is typically much larger than the size of a single field. For large field areas, e.g. in the central USA, combined with small resolution cells as planed for SMOS, the row structure may be significant, and a potential risk of a systematic error may rise.

6. The EMIRAD field campaign, Ocean

This chapter describes the scientific measurements of wind driven ocean surface azimuth signatures using the EMIRAD L-band radiometer. A short description of the experiment setup is given, and the flight plans for the four flights are presented. The data processing and data correction is described in details for one of the flights, and finally results from all flights are presented. A discussion of the results from the flights follows, and possible theories for the nature of the observed signals are presented and verified.

Wind driven polarimetric signatures from the ocean surface have been studied by several scientific groups, using airborne radiometers. However, these studies have been concentrated at higher frequencies, typically Ku- and Ka-band. At these frequencies, the Stokes parameters show some Kelvin dependence on the azimuth look angle, when the wind speed exceeds a few meters per second. References [1-6,17] show studies of this kind, and it is shown that the polarimetric wind driven signature may be used to estimate the wind direction. At L-band, there is only very little knowledge about eventual signatures, and this chapter will describe the LOSAC, L-band Ocean Salinity Airborne Campaign, aiming at filling the void using the EMIRAD L-band radiometer. The campaign is sponsored by ESA, preparing for the SMOS mission, and the overall interest is to understand the nature of the wind driven signatures in order to evaluate, if corrections are necessary prior to salinity estimations based on the radiometer signals.

6.1 The experiments

The system, used for the LOSAC campaign, consists of the L-band radiometer itself, along with the 90x90x200 cm horn antenna. The antenna is designed to fit into the parachute door of a C-130 transport aircraft, and using two legs on the antenna structure, it can be stored during take-off, transit and landing. During measurements it can be locked at a fixed depression angle of 23°, with an option for 40°. Figure 6.1 shows the setup.

The antenna is mounted on the cargo rail of the aircraft, aligning the antenna to a side-looking position. At a straight flight, the antenna will describe a profile of the ocean surface at a constant incidence angle, given by $\alpha_i = 90° - d$, where α_i is the actual incidence angle and d the depression angle, respectively. If the aircraft rolls and the antenna looks to the right side, relative to the flight direction, the nominal incidence angle change with the roll angle, φ, is given by

$$\alpha_i = 90° - d - \varphi \tag{6.1}$$

For the present experiment, it is of great interest to measure the azimuth signatures at different incidence angles, as the SMOS field of view covers incidence angles from about 20° to 65° [10, 11]. Using 6.1, the range of desired bank angles is found to be the range from 2° to 47°, which is almost realistic in the C-130.

The operator console is located on a freight pallet, positioned in the middle of the aircraft. It holds the system control computer, including the data formatting unit, Local, the storage media and the display features. It also holds the EGI, Embedded GPS (Global Positioning System) / INU (Inertial Navigation Unit), unit, providing the control computer with actual information about aircraft heading, attitude and position. The unit is a Honeywell H-764, which provides heading and attitude better than 0.05°. The EGI is mounted directly on the pallet surface, and the pallet is locked to the aircraft cargo tracks near the antenna when mounted in the aircraft. This mounting is selected to minimize the eventual effects of stiffness problems between the INU co-ordinate system and the antenna.

Figure 6.1. The EMIRAD L-band radiometer mounted side looking in the C-130 aircraft. A) Position during take-off and landing. B) The antenna in measurement position at 23 ° depression angle.

The flight pattern is a full circle, defined by the desire to measure the full azimuth variation of the Stokes vector within the shortest possible time. The ideal situation for the measurements would be instant observation of the same point on the sea surface, from all view directions, but with the circle flight pattern, the realistic observation time is from about 30 seconds to 15 minutes. A major advantage of the circle flight is the opportunity to vary the incidence angle by changing the aircraft roll angle. Due to the aircraft dynamics, the circle radius will change according to the selected roll angle, thus moving the central point of the antenna beam in a circle shape on the surface.

The aircraft navigation and control system can be operated in different modes, depending on the flight purpose. For the circle flights, the navigator can set up the system to maintain a constant roll and pitch angle rather than a perfect circle pattern. This is advantageous in the present campaign, as the aircraft roll will change with the wind direction, when trying to perform perfect circles. By keeping the roll angle constant the corrections for incidence angle changes are significantly smaller, and the influence from uncertainties in the correction algorithm will be smaller.

To cover the SMOS range of incidence angles, circles are measured in the full possible range of the C-130, i.e. from 5° to 45°. For the 23° depression angle, formula 6.1 gives an angular range from 22° to 62°, almost covering the desired range. Figure 6.2 shows a typical flight

pattern, where it is seen, that the central point of observation is a circle shape, defined by the antenna depression, the flight circle radius, the flight altitude, and the roll angle.

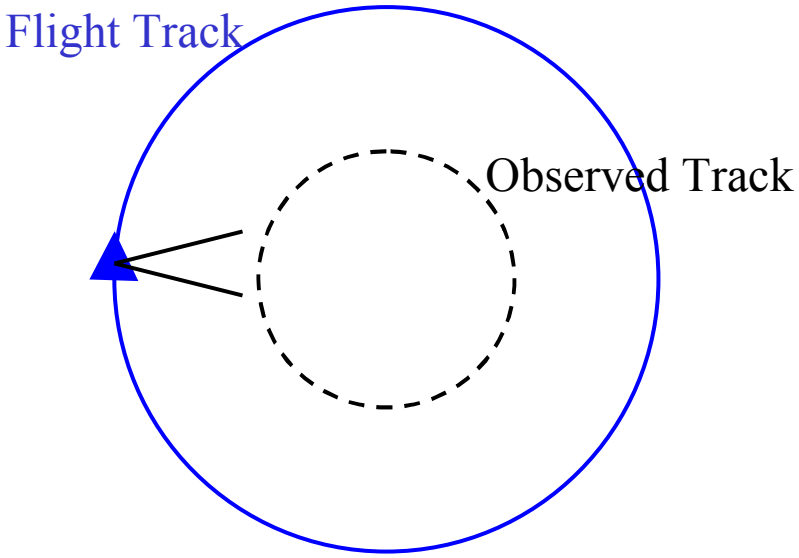

Figure 6.2. Typical circle flight pattern for the EMIRAD L-band radiometer, using the side-looking antenna installation. The observed track changes with flight altitude and roll angle.

The ideal observation situation would be a 360° measurement of a single point, but this will require adjustment of the flight altitude for each selected roll angle, as the observed circle radius changes with roll angle and flight circle radius. This will influence on the footprint size, however, and as this is not wanted, it is decided to keep the altitude constant, while the point of observation moves over the sea surface as indicated in figure 6.2. It is assumed that the surface is homogenous over the observed area, and it is likewise assumed, that the surface remains constant during the total acquisition time for a circle.

A series of test sites have been considered for the experiment, each having a number of advantages and drawbacks. One test site, which has been used in earlier campaigns at higher frequencies, is located on the North Sea, Denmark, (55.68°N, 4.70°E), between the Tyra and Gorm oilrigs, which are equipped with meteorological instruments. Advantages of this site are the possible access to ground measurements of wind and sea temperature, and the relatively large sea surface area, giving good conditions for the forming of a homogenous wind and wave field. Drawbacks are the transit flight (approximately one hour each way) from Airbase Værløse, and the relatively poor water depth at the site, 25 m to 50 m.

As an alternative site can be mentioned Kattegat, Denmark, (57.04°N, 11.07°E), between the islands Læsø and Anholt. The transit time is about 15 minutes, but as the site is located near to land at all sides, the wind field may be less homogenous. Like the North Sea site, also Kattegat has poor water depth, 7 - 8 m. Ground truth data is available from two meteorological stations on land. Other test sites have been considered, e.g. the northern Atlantic Ocean, west of Norway, due to the large water depth, easily more than 1000 m, and

open ocean conditions, which is more realistic for SMOS. Data acquisition at this site, however, will require a minimum transit flight of some three hours each way.

With background in the advantages and drawbacks, the North Sea site was selected as the primary target, and three flights took place over this site, carried out January 16th 2001, March 15th 2001, and October 25th 2001. Icing conditions caused one of the flights to be relocated for the Kattegat site, which was chosen as secondary target. This flight took place March 23rd 2001. The map in figure 6.3 shows the location of the flights, as well as the points of meteorological stations, and table 6.1 shows the details of every flight.

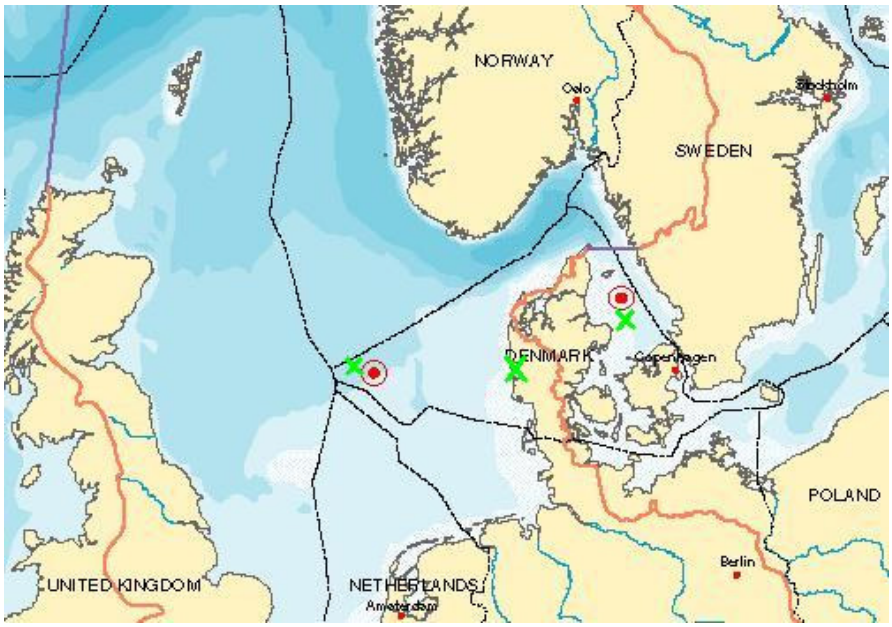

Figure 6.3. Map showing the locations of the airborne EMIRAD L-band radiometer measurements. The red circles show the two sites of data acquisition, and the green crosses show the positions of meteorological stations, providing ground truth data for wind speed, wind direction, sea surface temperature, and sea surface salinity.

6.2. Data preprocessing

The data is acquired from the radiometer during the flights in the compressed data format, containing header information, housekeeping information, and raw radiometer data. Preprocessing is done using the developed preprocessing software, "PrPre" (Polarimetric radiometer Preprocessing), mentioned in chapter 4. The software unpacks the compressed format and organizes the data in a set of files in ASCII format, depending on the target of observation. With one calibration switch and one noise diode in the instrument, there are four combinations, uncorrelated noise, correlated noise, correlated noise plus antenna, and pure antenna. Each target has its own file, and additional files contain the housekeeping data and the navigation data from the EGI unit.

The further processing is done by the software package "DigInt" (Digital processing and Integration), which is partly mentioned in Chapter 4. The first step in the processing is

Position: Time: Flight Pattern: INU:	North Sea (55.68°N, 4.70°E) 16.01.2001 / 12:15 UTC - 12:45 UTC Circle flights, Technical Test OK	No meteorological data
Position: Time: Aircraft: Flight Altitude: Flight Pattern: INU: GPS:	North Sea (55.68°N, 4.70°E) 15.03.2001 / 19:20 UTC - 20:20 UTC C-130, id: B-678 Updated recently with new auto-pilot. Can maintain stable attitude within ±0.5° for roll < 32.0° 1000 m Circle flights 52° incidence angle (3 circles) 42° incidence angle (3 circles) 35° incidence angle (3 circles) 22° incidence angle (3 circles) OK No	Meteorological station at oilrigs out of order => Ground truth data from Hvide Sande at the Danish west coast. Wind Speed: 3.6 m/sec. Wind Direction: 300 – changing! Weather: Partly clouded
Position: Time: Aircraft: Flight Altitude: Flight Pattern: INU: GPS:	Kattegat (57.04°N, 11.07°E) 23.03.2001 / 19:00 UTC - 20:10 UTC C-130, id: B-680 No updated auto pilot and navigation instruments. Manual control during data acquisition. 1000 m Circle flights 62° incidence angle (3 circles) 57° incidence angle (3 circles) 47° incidence angle (3 circles) 37° incidence angle (3 circles) 25° incidence angle (2 circles) OK No	Icing conditions over the North Sea site => flight impossible in the area Meteorological stations only available on land at the Danish east coast and on the island Anholt. Wind Speed: 5.1 m/sec. Wind Direction: 140° Weather: Clouded
Position: Time: Aircraft: Flight Pattern: Flight Pattern: Flight Pattern: INU: GPS:	North Sea (55.68°N, 4.70°E) 25.10.2001 / 17:10 UTC - 18:45 UTC C-130, id: B-679 New auto pilot. Attitude within ±0.5° for roll < 32.0° Circle flights (2000 m altitude) 55° incidence angle (3 circles) 45° incidence angle (3 circles) 35° incidence angle (3 circles) 27° incidence angle (3 circles) Circle flights (45° incidence angle) 1000 m flight altitude (3 circles) 2000 m flight altitude (3 circles) 3000 m flight altitude (3 circles) ±45° Wing Wags, ±5° Nose Wags OK Yes - Some problems with receiver	Meteorological station at oil rigs. Wind Speed: 11.0 m/sec. Wind Direction: 190° Sea Temperature: 13.4° C Wave Height: 1.2 m Weather: Almost clear sky

Table 6.1. Details for each of the four LOSAC flights, carried out with the EMIRAD L-band polarimetric radiometer.

alignment of the radiometer data, the housekeeping data, and the navigation data, followed by digital integration of the data from the acquired 8 msec. to a suitable period length. Integration can be time controlled, creating a data file with constant period length, and hence equal sensitivity. The integration can also be navigation controlled, giving data files with equal angular spacing. This will cause small variations in the sensitivity, but it may be easier to compare circles with different incidence angles, when the angular sample interval is constant. Generally the final integration periods are longer than 1 sec., keeping the sensitivity below 100 mK.

6.3. Data calibration

The calibration step of the processing involves a series of operations, intended for correction of instrument specific effects. One of these effects is the inphase/quadrature adjustment of the sampling circuit. As mentioned in chapter 4, the major adjustment is done by the digital circuitry itself on startup. Drifts in the sampling delays, however, are not adjusted during the data acquisition, and residual delays are calculated and adjusted in the software using the data from the noise diode measurements. Equation 3.19 and 3.20 are applied to find the actual phase error for each of the two correlation channels, and the software corrects the errors according to formula 4.10a-b.

Calibration of gain and noise temperature is the next correction, and it is done in two parts. The first part is the internal calibration, using the built-in load and the noise diode, determining the calibration constants at the radiometer input terminals. The step requires presence of data from the load as well as from the load with addition of noise from the noise diode. Alternatively, data from the load and data from the antenna with addition of noise from the diode may be used, as the measurement of antenna and noise along with the pure antenna data enable the gain calibration, while the load data gives the noise temperature. The latter method, however, will suffer from eventual variations in the antenna data during the calibration sequence, and the absolute calibration may deviate by several Kelvin.

An option in the calibration software is to interpolate between calibration points, and thus correct for eventual slow drifts. This method can help to remove small drift errors, but it should be used with caution, as variations may origin from quicker variations, undersampled by the calibration sequence. Moreover the method is useless without the full calibration sequence, as the uncertainty in the absolute calibration level, mentioned above, may introduce a drift over the circle track. In this situation a constant, averaged calibration may be calculated for the whole circle, or a constant calibration set can be applied in a separate file before the processing. This enables averaging of different circles, as they are referenced to the same calibration, but it will not correct a possible drift.

The second step in the data calibration includes correction for the external components, antenna, orthomode transducer, and cables. Physical temperatures of front-end components are continuously measured by the radiometer, and they are included in the data structures. The losses have been estimated in the laboratory experiments, and they are corrected for by reversal of equation 6.2, where T_M is the measured brightness temperature, T_L the physical temperature of the component causing the loss, T_A the antenna brightness temperature, and η the attenuation.

$$T_M = \eta \cdot T_L + (1-\eta)T_A \qquad (6.2)$$

All flight data have been calibrated using the same steps. Data from the January 16th 2001 technical test flight turned out to be invalid due to a feedback problem in the radiometer front-end, and due to a software problem in the control computer, data from the March 15th 2001 and the March 23rd 2001 do not include the full calibration data. Observation of the reference load with addition of noise from the noise diode is missing, and thus the absolute calibration level of these data is limited as mentioned above. Data from October 25th include all desired data, and the full calibration sequence, illustrated in figure 6.4 was carried out.

Figure 6.4. Calibration sequence for the EMIRAD L-band radiometer circle flights.

For all circles a limited drift is essential, and as described in chapter 4, tests were carried out in the laboratory prior to the flight campaigns. To validate the field data, however, data from the reference load before and after each data take was analyzed. The data was calibrated using a constant gain and noise temperature setting, and differences, $\Delta = T_{cal,start} - T_{cal,end}$, were calculated. As the circles have different radius, the time interval between calibrations varies, and table 6.2 illustrates the results for the 25th October flight.

Track length [sec]	H-pol. channel |Δ| [K]	V-pol. channel |Δ| [K]	3rd St. parameter |Δ| [K]	4th St. parameter |Δ| [K]
84	0.12	0.01	0.1	0.05
96	0.08	0.11	0.15	0.06
135	0.17	0.11	0.21	0.15
258	0.09	0.03	0.25	0.31
Mean of all	0.12	0.07	0.18	0.14
Radiometric ΔT	0.10	0.10	0.14	0.14

Table 6.2. Radiometer drift in the radiometer channels during data takes. The table shows the difference in radiometer output from the first to the last calibration sequence at different track lengths, the mean difference value, and the radiometric ΔT .

Some variations are observed in the table, but no systematic deviation may be identified. The mean deviation is found for each channel, and for comparison the radiometric sensitivity, ΔT, for the channels has been calculated for the observation time of the reference load. The typical deviations are of the order of 100 mK, and comparing to the ΔT values, no indication for larger drifts during field operation is identified.

6.4. Motion compensation

The measured radiometer data will vary with the aircraft motion as described in chapter 2. To extract the wind driven azimuth signature, corrections for the aircraft motion have to be applied. Generally two approaches can be made. One method is the application of equation 2.15 and 2.24, giving the theoretical errors to be subtracted from the measured data. The other methods are based on calculation of the corrections by using the measured data. For small corrections, the errors may be assumed to depend linearly on the measured parameters, and regression coefficients may be estimated according to equation 2.25, connecting the Stokes parameters in each track with the aircraft attitude data.

It may be expected that the methods would lead to approximately the same result, but due to the influence from noise and uncertainties in the calibration, some differences may be noticed. The theoretical approach should lead directly to the desired result, but it is limited by the performance of the model and the knowledge of sea surface parameters. In this case the Klein-Swift [16] model is used to correct for incidence angle deviations, while the geometric vector rotation is used for polarization mixing. As the real antenna pattern has a certain beam width and some side-lobes, the Klein-Swift model may not provide a precise result for each incidence angle, and there is a small potential risk, that corrections may not be exact. The vector rotation is a simple geometrical problem, and the model is just a mathematical reversal of the rotation. In both cases the calibration of the Stokes parameters is essential, as calibration errors will cause a scaling problem between the parameters and the corrections, eventually over- or underestimating the correction.

The regression analysis is based on real observations, and thus it gives the true, observed correction. Noise may be a problem here, however, as the regression line will be determined with a standard deviation depending on the number of observations. The linear approach may also be too simple for larger errors, causing risk for an over- or underestimation of the correction. The regression method also includes a potential danger. Assuming that the aircraft roll and pitch will change with the aircraft heading, an eventual real signal in the measured data, depending on the azimuth look angle and hence on the aircraft heading, will also be rejected, as it will be regarded as roll or pitch dependent. Roll and pitch variations as functions of the aircraft heading is a realistic situation, as the wind may change the aircraft attitude. The problem is minimized, however, when the aircraft navigation system is set up for constant attitude, rather than for a perfect circle. The result is that the aircraft will drift with the wind in its own coordinate system, where the wind influence is negligible.

A method between the two above mentioned could be the determination of a model function, based on measured values. Large-scale variations must be available, e.g. a ±45° roll leg, and a curve can be obtained and stored. The curve may be stored as a look-up table, and to reduce the influence from noise, it may be low pass filtered, or eventually modeled as a high order polynomial. This correction will be less noise sensitive than the regression method, and it may take into account an eventual deviation from the theoretical model function, e.g. due to unknown sea surface parameters or antenna side-lobes.

A combination of the three correction methods could be an alternative solution. Modeled deviation calculation can be the basic correction, while the regression method can be used to remove eventual residuals. The best method is not easily found from an analysis of

advantages and drawback of the different motion compensation methods, as the importance of each potential problem depends on the actual measurement situation. The developed processing software is thus able to perform all three corrections independently, and from a number of test cases, the final correction type can be chosen.

For determination of the influence from large-scale variations and for test of the correction algorithms, two special tracks were recorded on the October 25th flight, a ±45°roll, repeated two times, and a ±5° pitch, also repeated two times. The two tracks, referred to as wing wags and nose wags, respectively, were preprocessed and calibrated using the standard preprocessing and calibration steps, giving the raw results, illustrated in figure 6.5 and figure 6.6. As shown in the figures, the two tracks are not ideal, as they both contain some roll and pitch variation. It is obvious, however, that the 1st and 2nd Stokes parameters depend strongly on the roll angle, while changes in the aircraft pitch influence on the 3rd Stokes parameter. It must be noticed, that the wing wags are ±45° roll variations, causing the antenna to look slightly above the horizon for the negative roll situation. The results are thus used and corrected only for the UTC time ranges from t = 66391 sec. to t = 66403 sec. and from t = 66419 sec. to t = 66433 sec, equal to incidence angles below 70°.

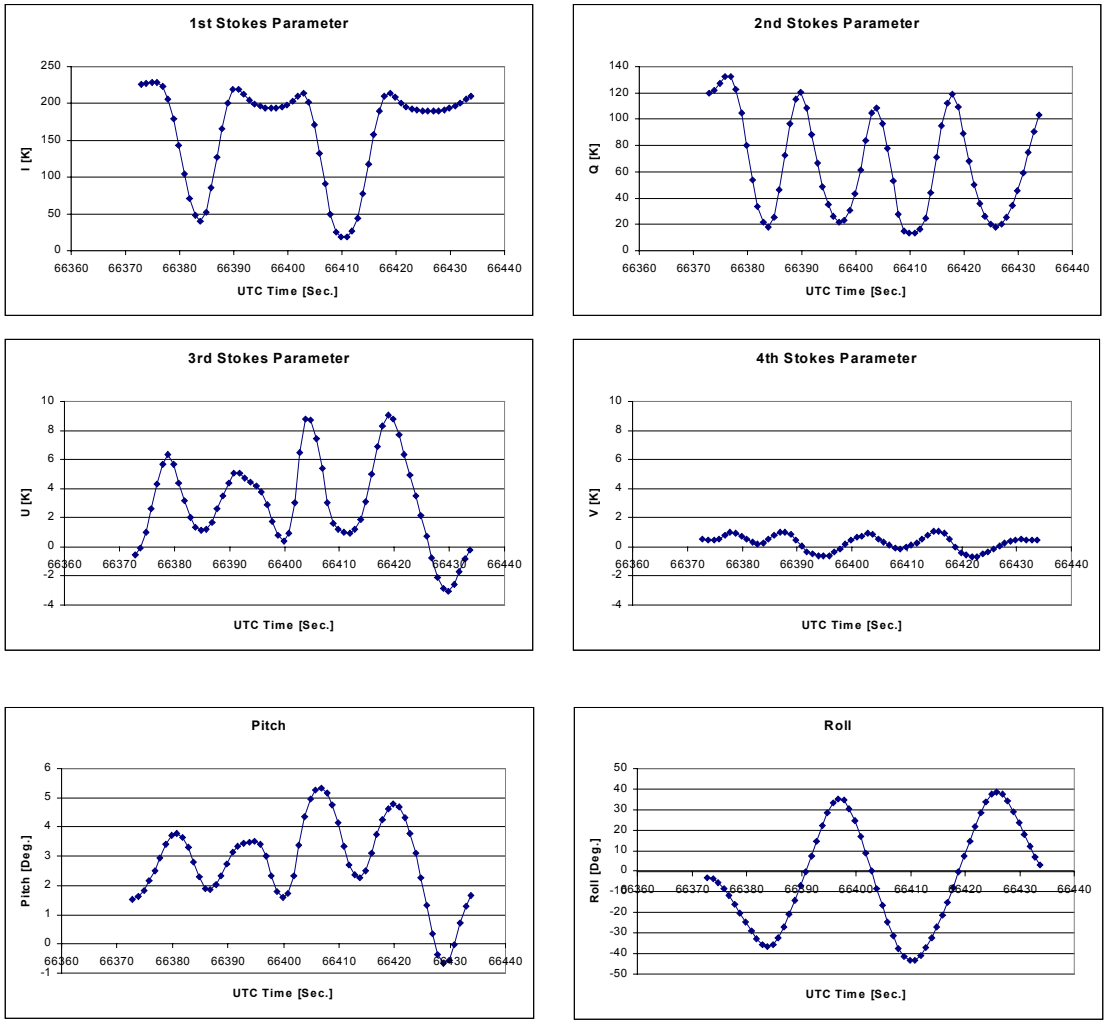

Figure 6.5. Raw data from ±45° wing wags, including the four Stokes parameters (Kelvin) as well as pitch and roll data (°).

The 1st and 2nd Stokes parameter variations are illustrated in figure 6.7a, where the horizontal and the vertical brightness temperatures are plotted against the incidence angle (red curve). The Klein-Swift model is shown in blue color, and the green curve illustrates the mean of the measured brightness temperatures in the interval from 22° to 62° incidence angle after low pass filtering, i.e. the model function useable for later corrections. Generally it is noticed, that it follows the theoretical model quite well, but for higher incidence angles, above 55°, some deviation is found, and it might be a potential problem for the Klein-Swift model based correction method.

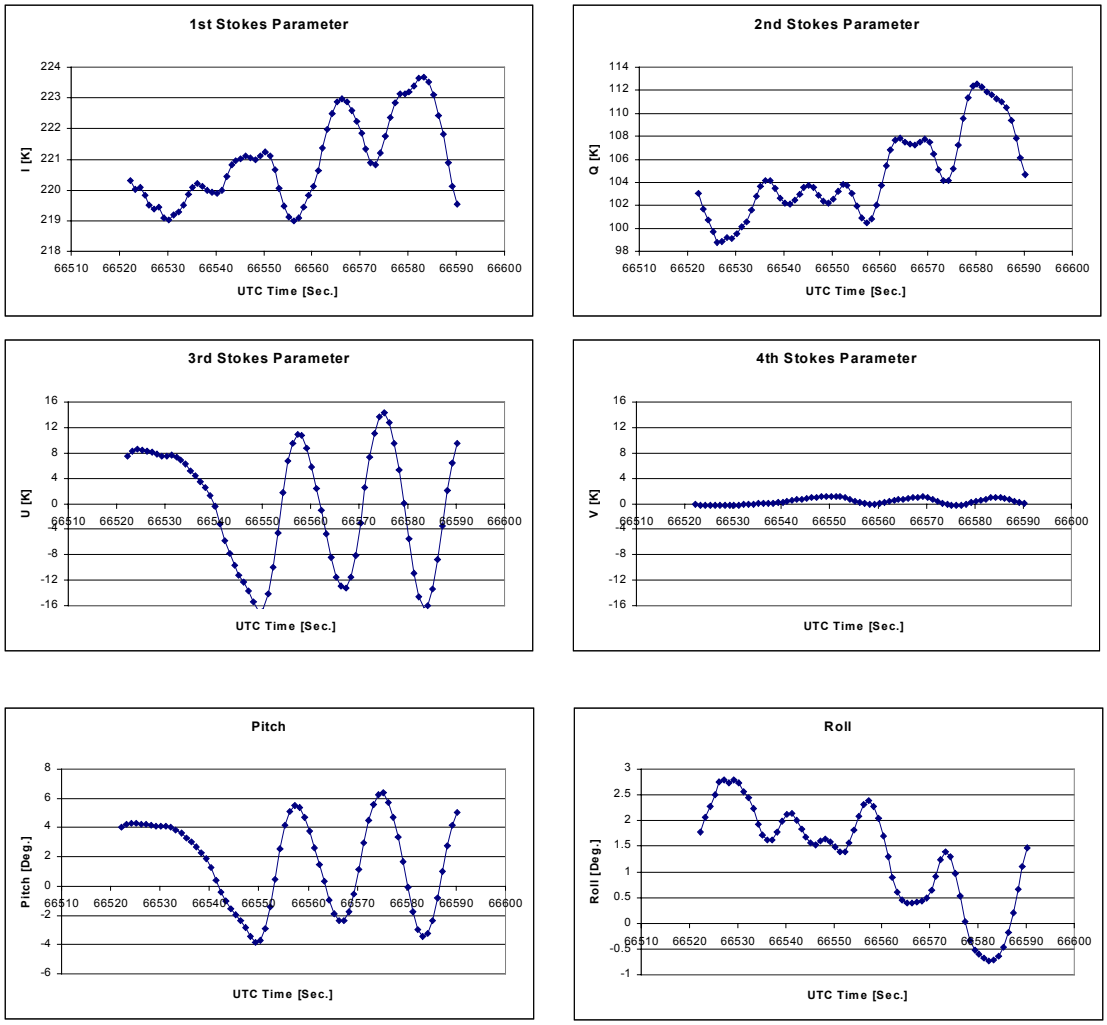

Figure 6.6. Raw data from ±5° nose wags, including the four Stokes parameters as well as pitch and roll data.

Figure 6.7b illustrates the 3rd Stokes parameter as a function of the antenna rotation angle, pitch, and it is seen that the relation is almost linear. An offset, probably due to the installation of the antenna and the inertial navigation unit in the aircraft, is noticed, but it may be easily determined from the figure, and included in the model. As for the incidence angle the curves may be averaged and low pass filtered, providing a model function for later antenna rotation corrections.

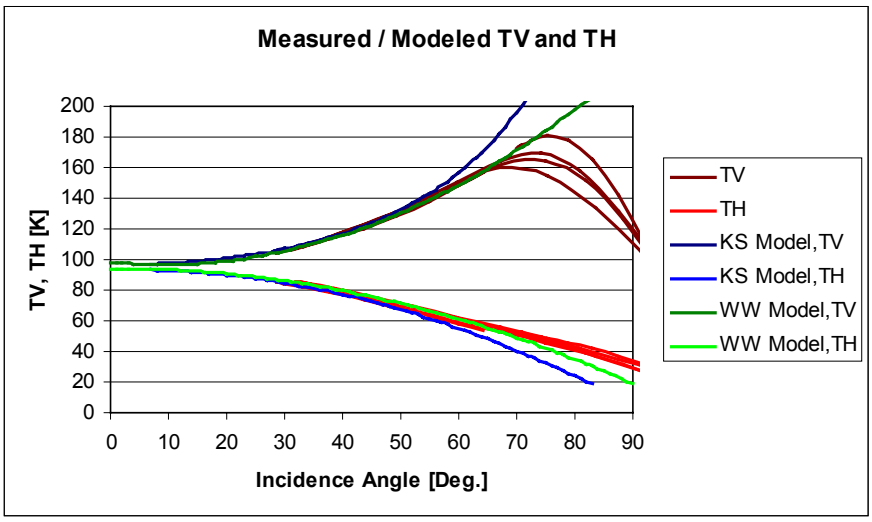

Figure 6.7a. Measured horizontal and vertical brightness temperatures (red curves) as functions of the incidence angle. Each polarization results in four measured curves, representing the increasing and decreasing roll for each of the two wags. The blue curves show the Klein-Swift model for the sea surface state, and the green curves show the average of the measured results after low pass filtering, intended for later incidence angle corrections.

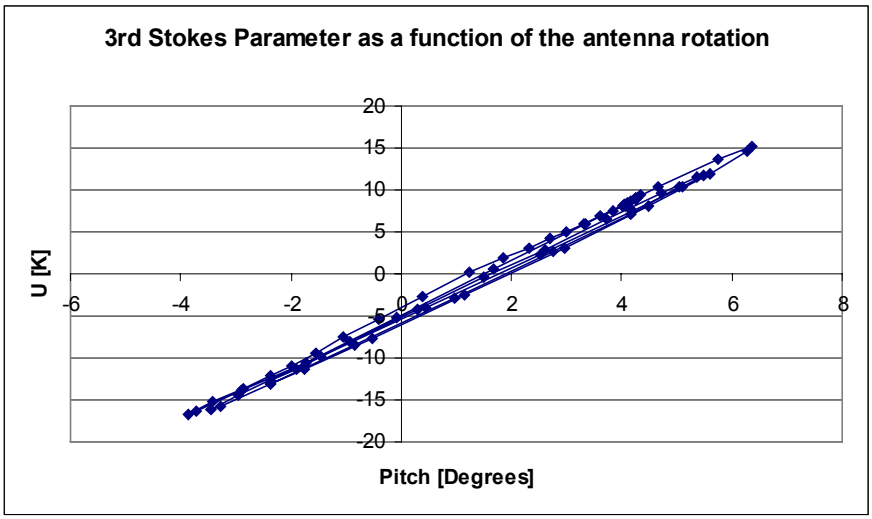

Figure 6.7b. Measured 3rd Stokes parameter as a function of the antenna rotation, pitch. The offset may origin from a mechanical offset between the antenna mounting and the inertial navigation unit.

The different correction types are carried out on the wing wags and the nose wags tracks, and the results are illustrated in the figures 6.8 to 6.17. As the wing wags are corrected only for incidence angles below 70°, a break in the curves, showing the 1st and 2nd Stokes parameters is seen for all corrections.

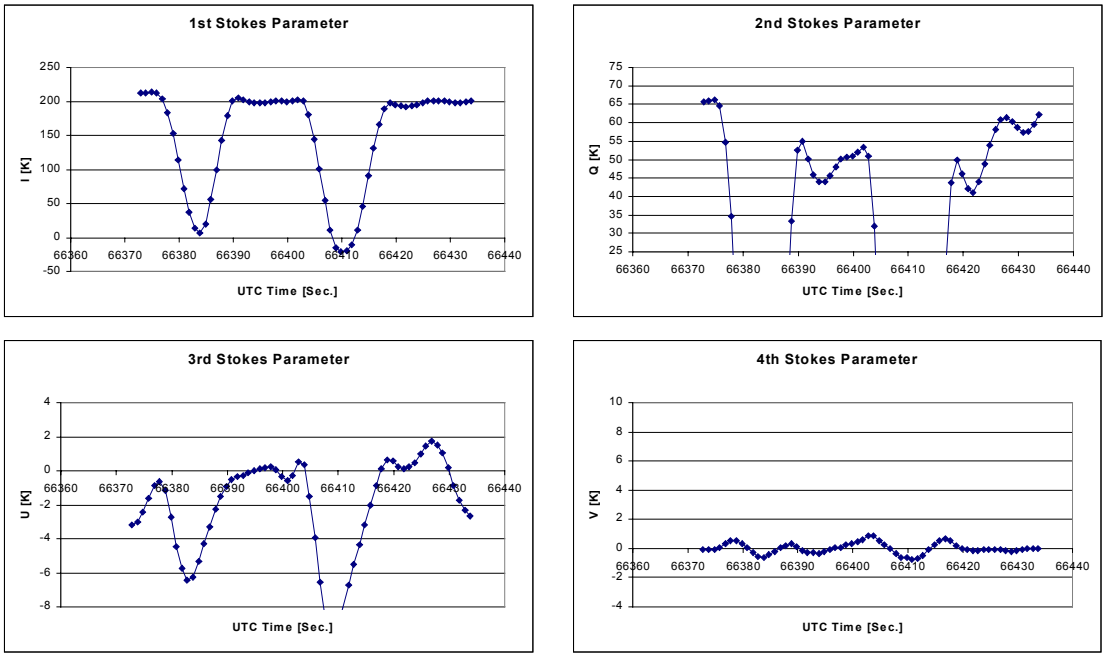

Figure 6.8. The four Stokes parameters from the ±45° wing wags, corrected using the linear regression method. Each parameter's linear dependence on the incidence angle and the antenna rotation is calculated, and corrections are applied according to equation 2.26.

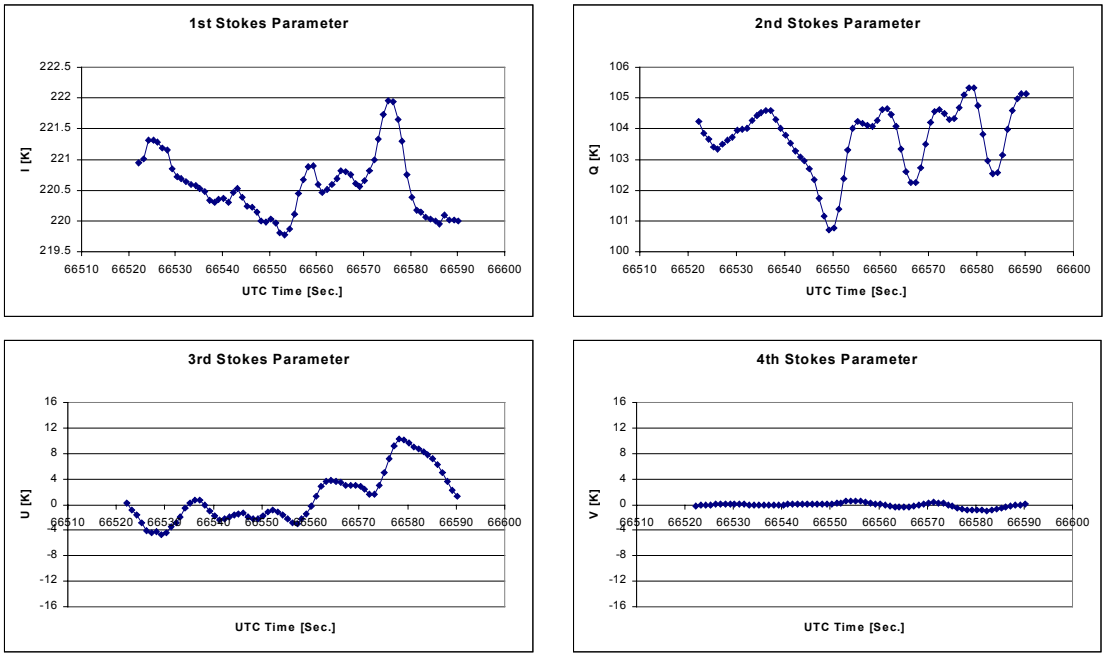

Figure 6.9. The four Stokes parameters from the ±5° nose wags, corrected using the linear regression method. Each parameter's linear dependence on the incidence angle and the antenna rotation is calculated, and corrections are applied according to equation 2.26.

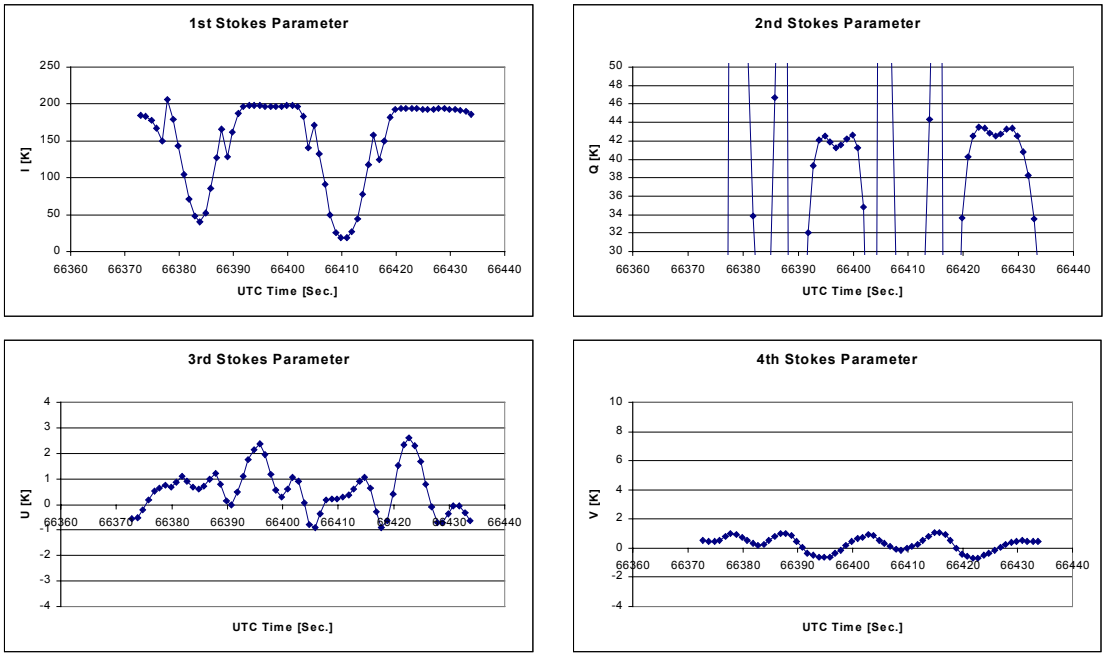

Figure 6.10. The four Stokes parameters from the ±45° wing wags, corrected using the Klein-Swift model and the antenna rotation matrix, equation 2.15. The theoretical error in each parameter is calculated, and the error is subtracted, using equation 2.24.

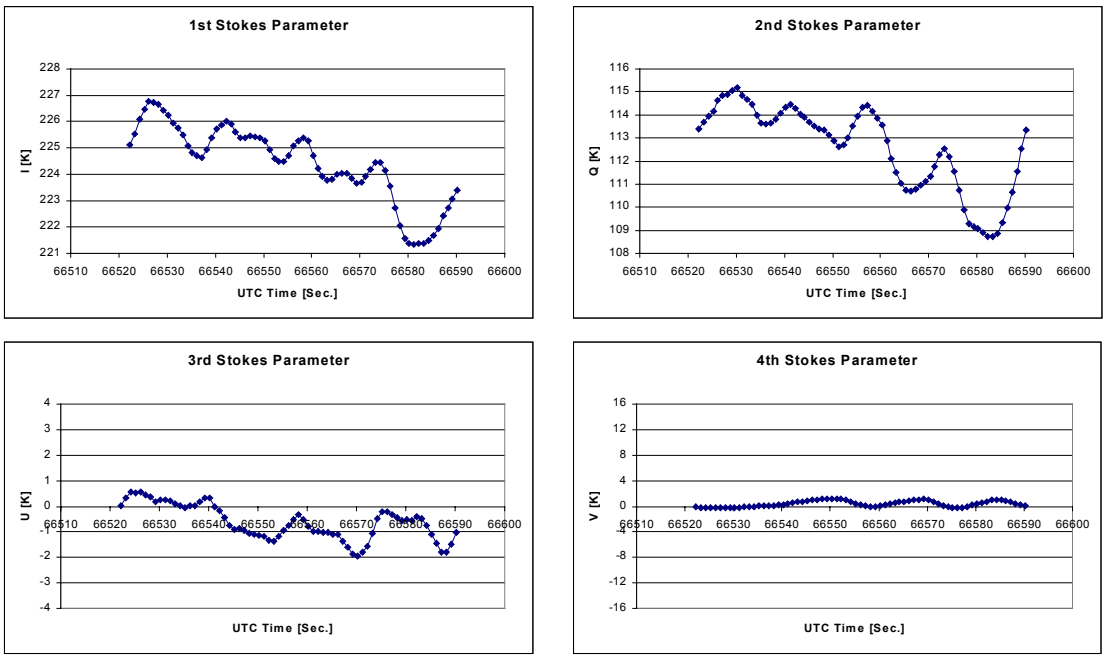

Figure 6.11. The four Stokes parameters from the ±5° nose wags, corrected using the Klein-Swift model and the antenna rotation matrix, equation 2.15. The theoretical error in each parameter is calculated, and the error is subtracted, using equation 2.24.

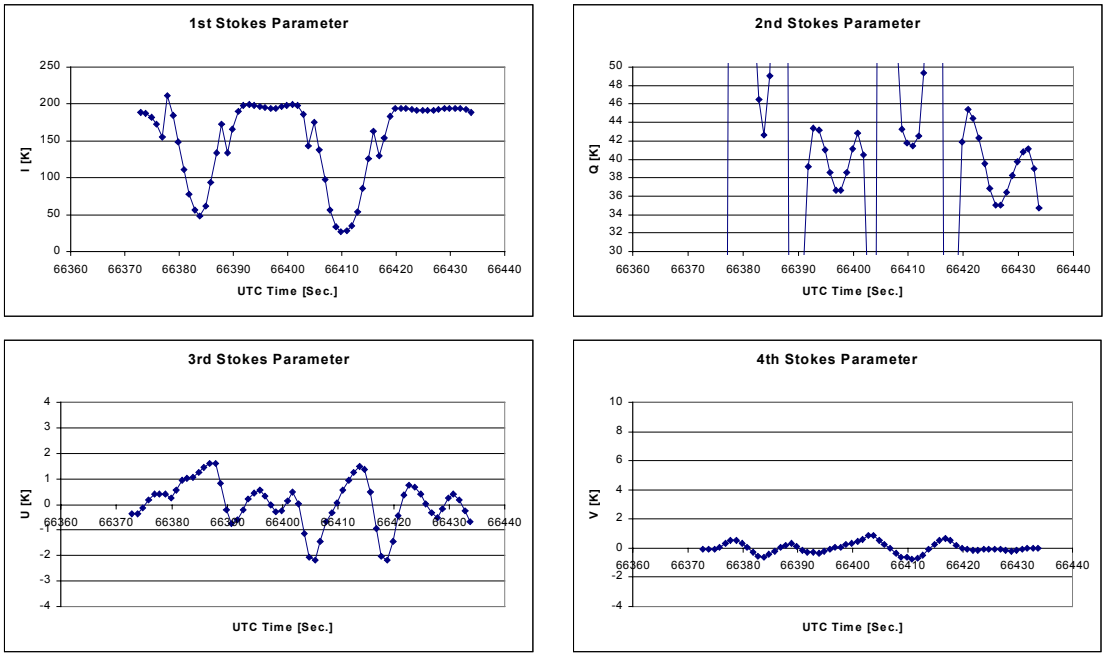

Figure 6.12. The four Stokes parameters from the ±45° degrees wing wags, corrected using the Klein-Swift model and the antenna rotation matrix, equation 2.15. Subsequently the parameters are corrected using the linear regression method.

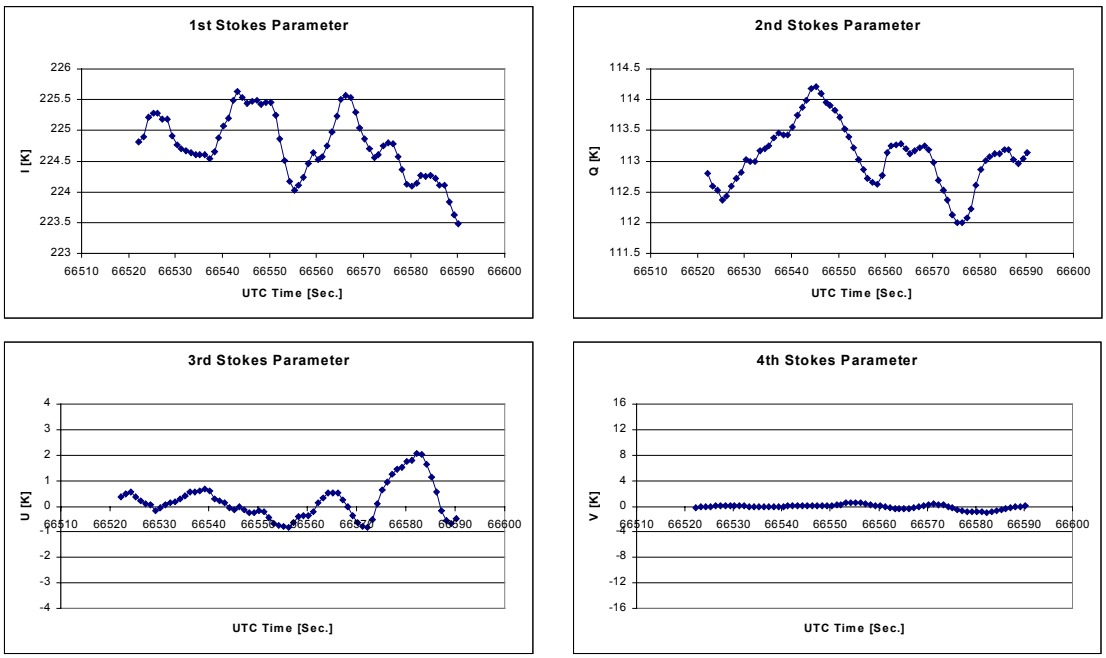

Figure 6.13. The four Stokes parameters from the ±5° nose wags, corrected using the Klein-Swift model and the antenna rotation matrix, equation 2.15. Subsequently the parameters are corrected using the linear regression method.

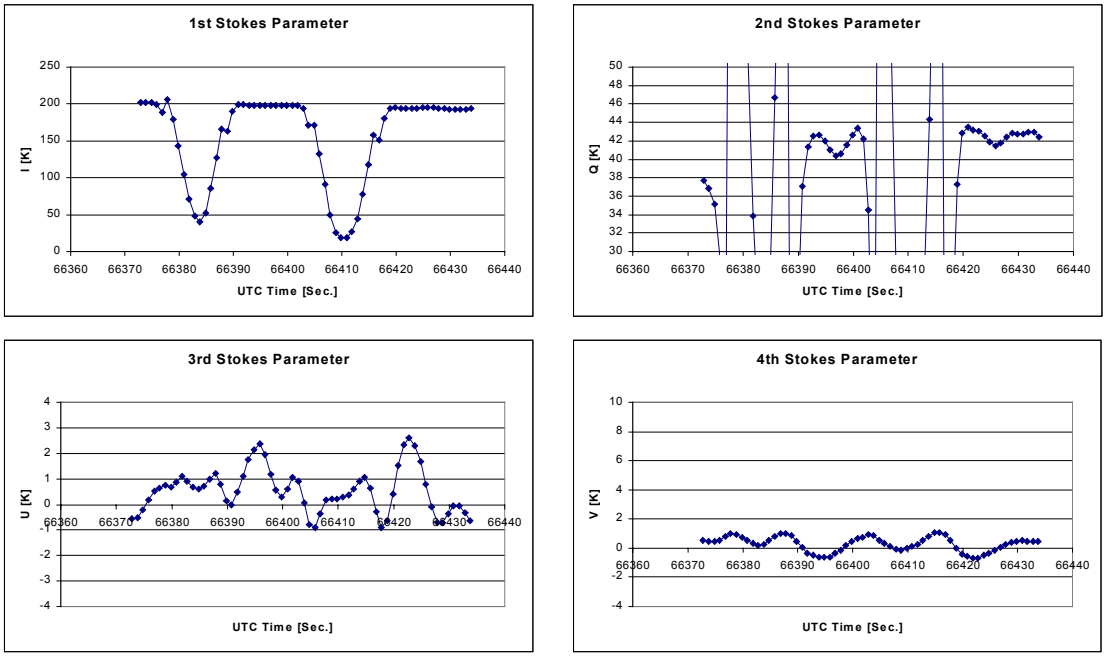

Figure 6.14. The four Stokes parameters from the ±45° wing wags, corrected using the model based on the low-pass filtered mean from the wing wags and the nose wags.

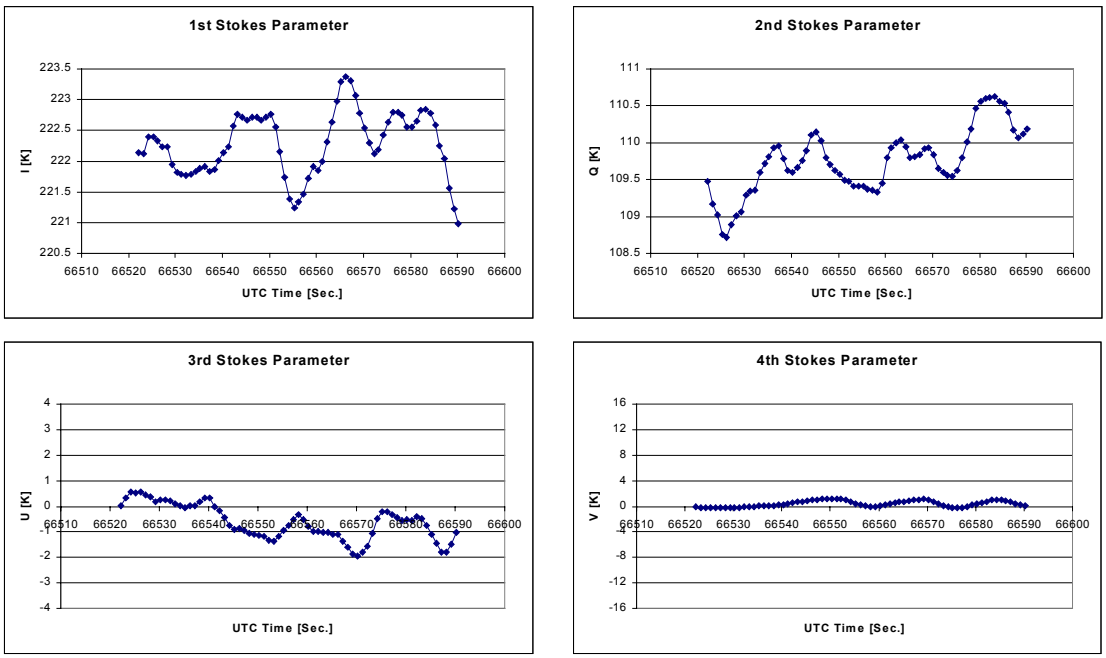

Figure 6.15. The four Stokes parameters from the ±5° nose wags, corrected using the model based on the low-pass filtered mean from the wing wags and the nose wags.

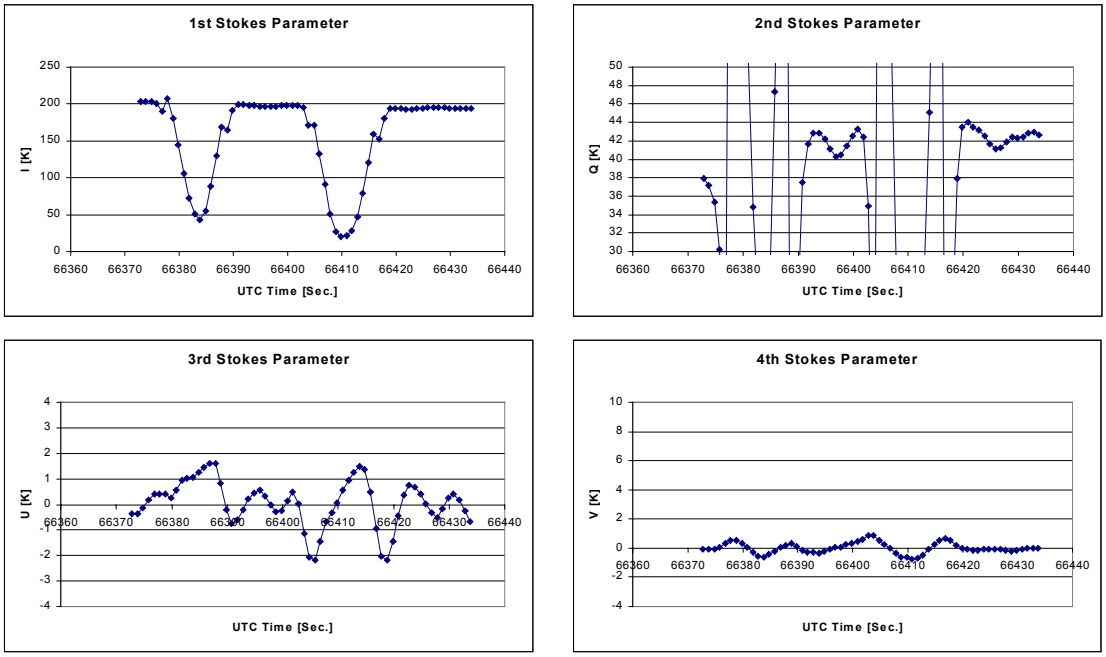

Figure 6.16. The four Stokes parameters from the ±45° wing wags, corrected using the model based on the low-pass filtered mean from the wing wags and the nose wags. Subsequently the parameters are corrected using the linear regression method.

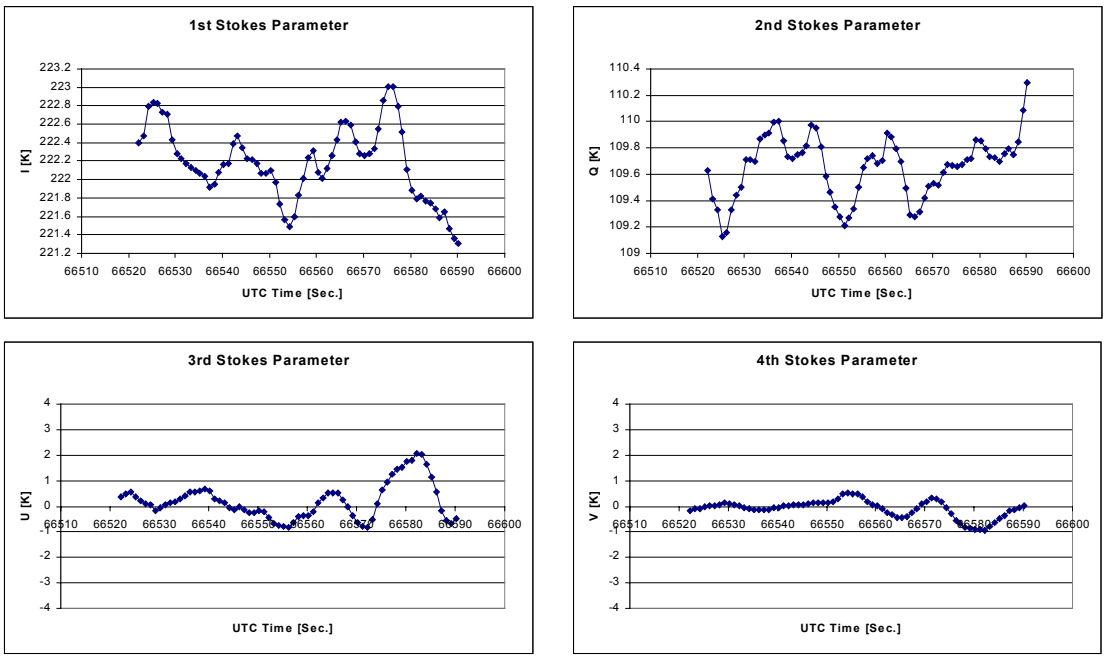

Figure 6.17. The four Stokes parameters from the ±5° nose wags, corrected using the model based on the low-pass filtered mean from the wing wags and the nose wags. Subsequently the parameters are corrected using the linear regression method.

The model-based corrections are seen to provide quite similar results, but it is noticed, that the Klein-Swift model has problems for low roll angles, where the returned brightness temperature is too low, corresponding to figure 6.7a. The result is thus an M-shaped pattern for positive roll angles. The fitted model causes the same basic shape, but the M-shape is wider, and the deviations for lower roll angles are smaller.

The additional linear regression has very small influence on the fitted model, indicating that almost no residual roll dependence, which can be fitted with a linear approximation, is left. For the Klein-Swift model, the regression corrects the edges, but meanwhile it leaves the middle of the pattern deeper. The same happens for the pure regression corection, and the basic problem is, that a linear fit to an M-shaped curve will trade deviations on the edges with deviation in the central part, but it will be unable to remove the ripple.

The result is a total M-shape in all five cases, but the ripple is different, and some methods will thus provide a better correction for the total track. As the overall purpose of the corrections is to get a flat pattern for the full pitch range and for the 0° to +45° roll range, the Stokes parameters dependence on roll, $dT/d\varphi$, and pitch, $dT/d\theta$, may be used to evaluate the methods. The pure regression and the Klein-Swift with regression both provide a peak-to-peak variation of 8 K in the 2nd Stokes parameter, resulting in a slope equal to 0.23 K/°. With typical roll variations within a track in the order of 1°, up to 0.23 K error is to expect, and for the scientific tracks, this is not acceptable. The Klein-Swift model alone, the fitted model, and the fitted model with regression provide smaller deviations, 2 K peak-to-peak, resulting in a maximum slope of only 0.08 K/°.

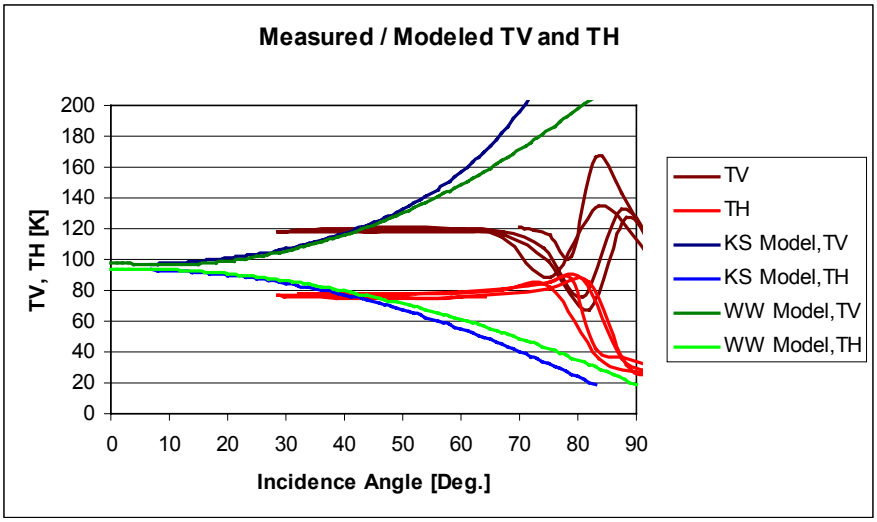

Figure 6.18. Corrected horizontal and vertical brightness temperatures (red curves) as functions of the incidence angle. The blue and green curves show the Klein-Swift model and the fitted model for the data, respectively.

The additional regression may be able to provide better results for smaller local ranges, as the reason for its problems in the example above is the M-shape, causing problems for the linear model. This is illustrated for the nose wags, where the fitted model along with linear regression provides the lowest variation over the full range. It is thus to expect, that corrections of the scientific tracks can be done to a precision not worse than the above

0.08 K/°. Figure 6.18 shows the wing wags data after correction, where a nominal roll angle of 25° has been selected.

For the nose wags, and the 3rd Stokes parameter correction, the basic impression is the same. The variations are too large to provide good results for the pure regression, while the other methods provide slopes of about 0.15 K/°. If only the first half on the track is regarded, the slope is down to 0.1 K/°. A possible explanation for this behavior may be the rapid pitch changes in the second part, causing each point, integrated over 1 sec. to be an average over a range of mixing angles, introducing an systematic uncertainty to the measurement. The theory is supported by figure 6.7b, where some deviation from the average track is observed. As realistic pitch variations are of the order of 1° over long time, the problem will not influence the scientific tracks, and it is believed that the slope can be kept below 0.1 K/°.

To demonstrate the correction technique on a normal flight track, the track, shown in figure 6.19 is selected. The track is a typical track with normal sized variations in pitch and roll, and the oscillations in the roll in the first part of the track makes it a good test case. The track is acquired on the October 25th 2001 flight with a nominal incidence angle of 45°.

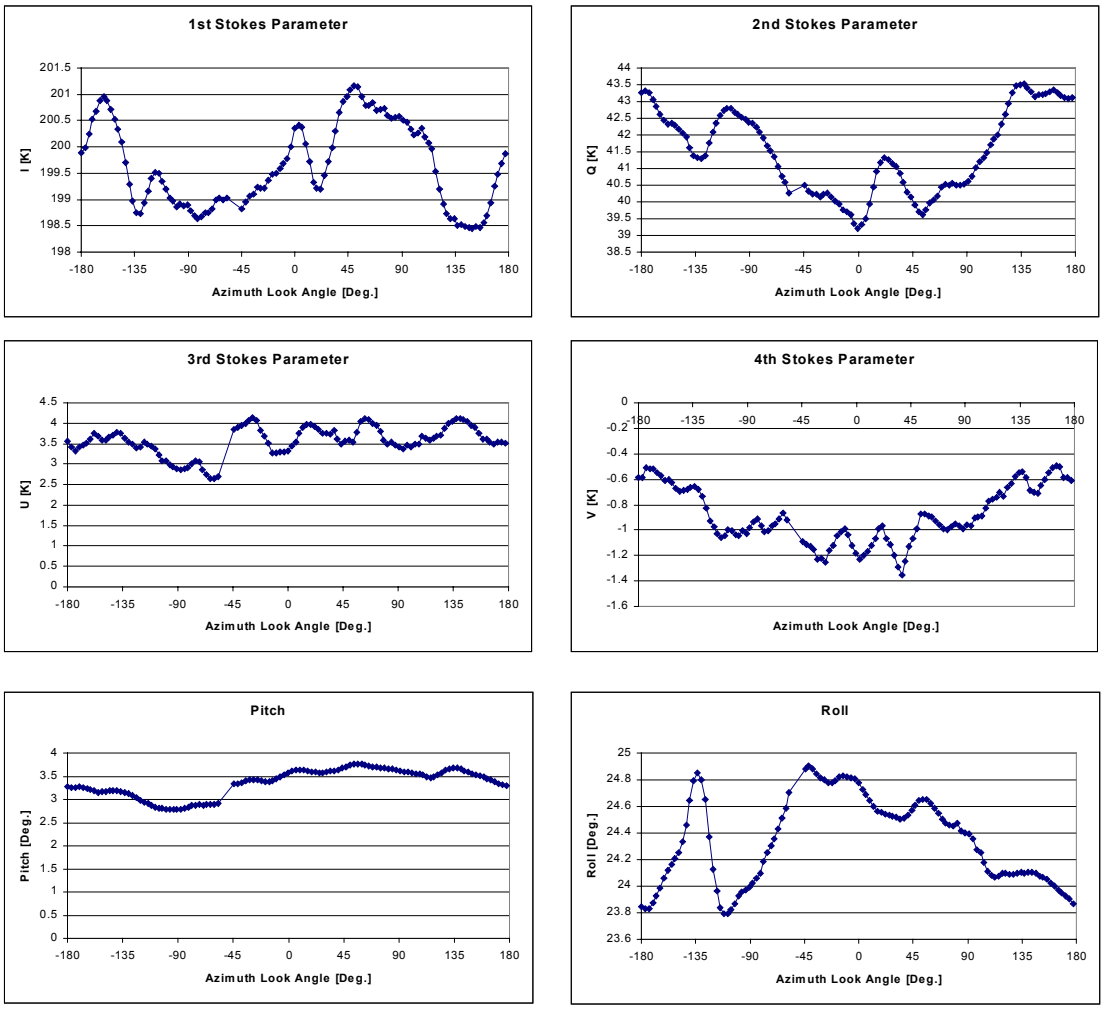

Figure 6.19. The raw four Stokes parameters from a circle flight track from the October 25th 2001 flight. The track is acquired with a nominal incidence angle of 45 °.

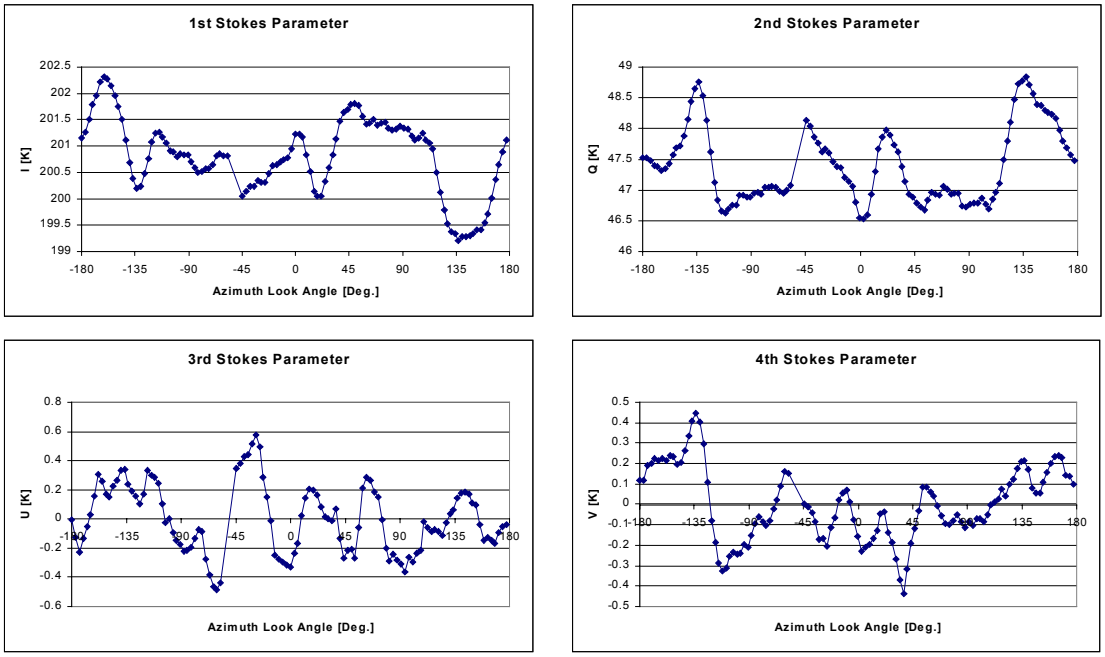

Figure 6.20. The four Stokes parameters from the circle flight track with 45° incidence angle from the October 25th 2001 flight. The track is corrected using the Klein-Swift model, and residual errors are removed with a linear regression.

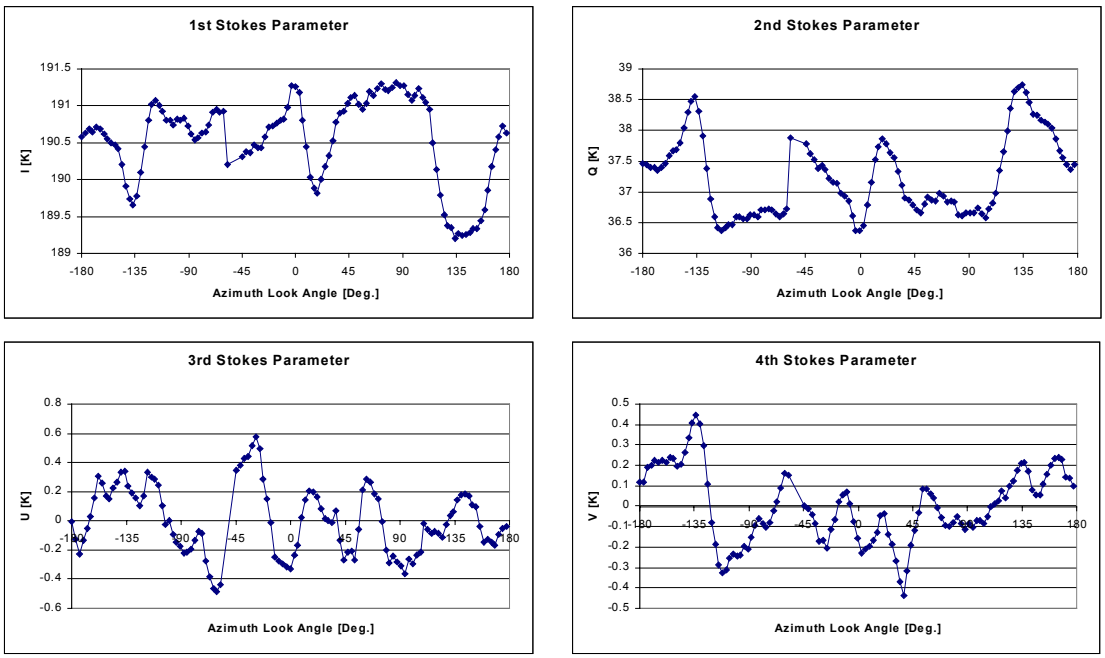

Figure 6.21. The four Stokes parameters from the circle flight track with 45° incidence angle from the October 25th 2001 flight. The track is corrected using the fitted model based on the wing wags, and residual errors are removed with a linear regression.

The different correction methods are applied to the track, and generally the impression is like for the wing wags and the nose wags, that the methods lead to quite similar curves. The results for the Klein-Swift model correction with regression and for the fitted model with

regression are shown in figure 6.20 and 6.21, respectively. It is seen that the two sets of curves are very similar, and an evaluation of the standard deviation of the difference between them shows values less than 10 mK for the 1st Stokes parameter and 35 mK for the 2nd. The small offset between the two sets is a result of the different model functions behind the corrections, but as the absolute level is not important to the azimuth signature evaluation, it has no influence on the further data processing.

The examples of correction with the different methods and the combinations of them show some differences regarding the large-scale corrections, and it is concluded that a model in combination with a linear regression to remove the residual error is a good solution. Two models, the theoretical Klein-Swift model as well as a fitted model based on the wing wags, have been tested. The fitted model is the response of the full installed system including antenna side-lobes etc., and as expected, it provides the best results for the large-scale variations. For smaller scale variations, the models turn out to give very similar results, and it may be concluded, that the choice of correction method is of minor influence to the final results. For the present flights, having typical variations of pitch and roll within 1°, it is believed that corrections can be done to a 100 mK level, which is satisfactory for the scientific campaign.

6.5. Results from the March 15th 2001 flight

The flight on March 15th 2001 was the first scientific measurements, and although the weather forecast predicted relatively low wind, approximately 5 m/sec. the flight was carried out, as a low wind case belongs to the total data set. Meteorological data was ordered from the oilrigs in the North sea, near the target area, but due to a data recorder fail, a standard data set from The Danish Meteorological Institute, DMI, is used as replacement. The data is measured at Hvide Sande at the Danish West Coast, and the data points for wind speed and wind direction are shown in figure 6.22 along with two vertical lines, indicating the time of flight over the target area.

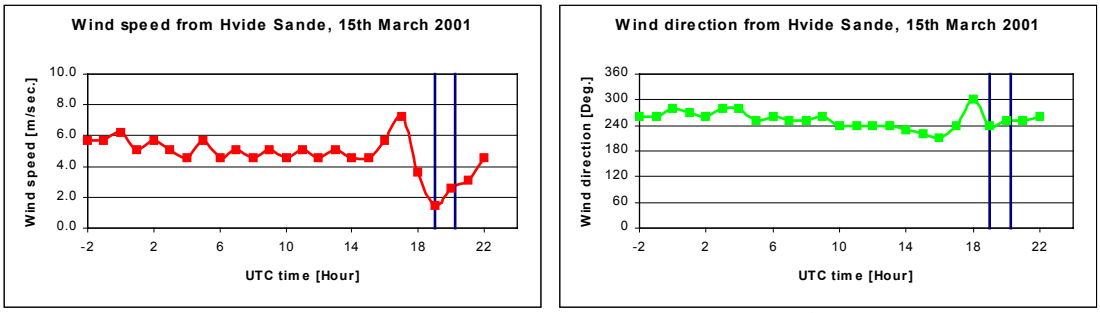

Figure 6.22. Wind speed and wind direction for March 15th 2001, measured at Hvide Sande at the Danish West Coast. The blue lines indicate the flight time.

As seen in the figure, the wind decreased rapidly right before the measurements and the direction changed between 230° and 300°. A risk thus exists, that the wind driven sea surface field was in an intermediate state, and that no homogenous pattern was established.

As indicated in table 6.1, four different incidence angles were covered during the flight, and to compare the stability of eventual signatures, it was decided to measure each circle three times. The data was pre-analyzed during the flight, and the standard deviation between data samples was evaluated for each circle. Some variation was noticed, but as no attitude correction was applied at this point, nothing unusual was seen, and indications for RF-interference were not found at this time.

After the flight, data was processed as described in the sections 6.2 and 6.3, and motion compensation was done according to section 6.4. It should be noticed, that the full absolute calibration precision is not available for this flight due to a control computer problem, leaving out the combined observation of the calibration load with the noise diode. Several Kelvin of absolute uncertainty is thus the result, but as the stability evaluation, illustrated in table 6.2, shows drifts in the order of 0.1 K maximum, the data is useful for determination of azimuth signatures anyway. The full data set is presented in the figures 6.23 to 6.34, where the data is aligned to the azimuth look direction.

For all data a quite large peak-to-peak signal is noticed, typically more than 1 K. The large extremes, however, are in some signatures caused by narrow peaks (point target like signatures), raising from the basic signal during 30° to 45°. It is seen that the peaks do not generally appear in the same position for different circles, and no system can be identified visually. The basic signal, i.e. the slower variations, are in some circles almost without variation, and in figures 6.32 and 6.34 for the 52° incidence angle, no clear 1^{st} or 2^{nd} harmonic variation is present. In figure 6.33, likewise from the 52° incidence angle measurements and obtained between the circles in 6.32 and 6.34, 1^{st} and 2^{nd} harmonics seem to be present in all Stokes parameters.

The two above observations may indicate that some random signal is present, and in this case, averaging could help to reduce the influence. As the three circles in the above example are obtained subsequently in identical conditions, averaging of the curves is possible. As they are not sampled at identical angles, however, the averaging can not be done data point by data point. The circles are thus resampled using an interpolation filter, and the figures 6.35 to 6.38 show the results for each of the four incidence angles. For 20° incidence, the 2^{nd} circle is left out, as figure 6.24 indicate the presence on single point RF-interference, while the other averaged curves are based on all three basic circles.

The result from the averaged curves show smaller peak-to-peak variations, almost all below 1 K, and the obvious presence of point target like signatures is reduced, although they are still present in all curves. To reduce the influence from the small peaks additionally, a harmonic analysis of the averaged Stokes parameters can be carried out, focusing on identification of 1^{st} and 2^{nd} harmonics, which are the components in the wind driven sea surface structures at higher frequencies [17]. This analysis is shown in table 6.3, where the magnitude and phase, i.e. the azimuth direction, for the first four harmonics are calculated for each Stokes parameter and for each incidence angle.

The table shows typical values between 50 mK and 250 mK for the magnitudes for all Stokes parameters, but no systematic behavior is observed. For the 1^{st} Stokes parameter, the 2^{nd} order component is two times larger than the 1^{st} order component for 35°, while the opposite

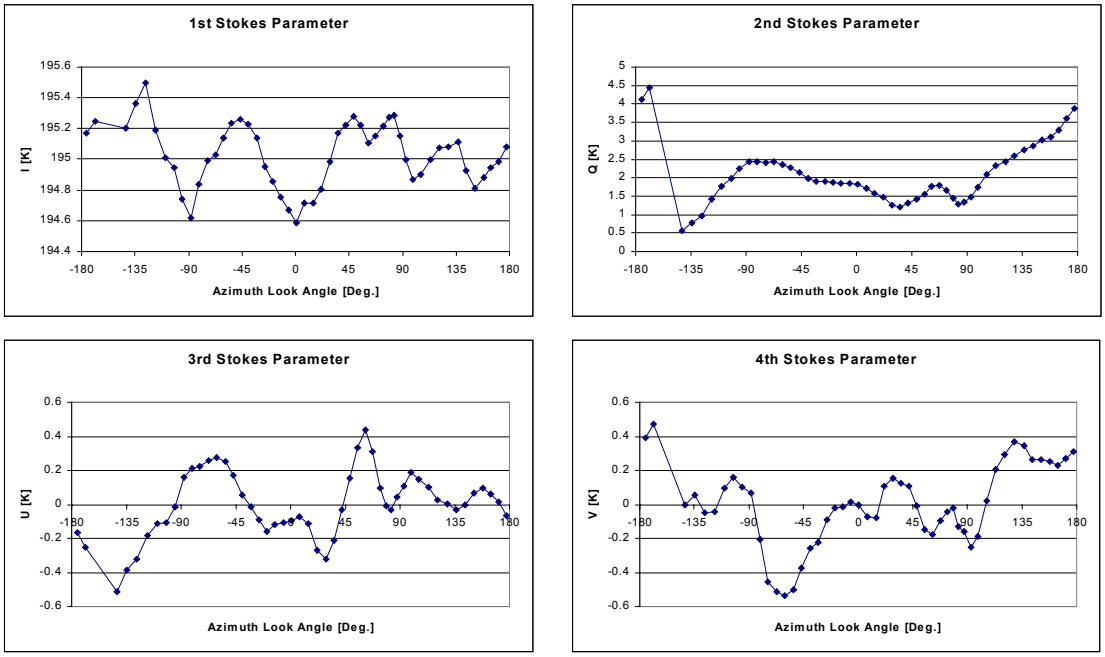

Figure 6.23. The four Stokes parameters from the 1st circle flight track with 20° incidence angle from the March 15th 2001 flight.

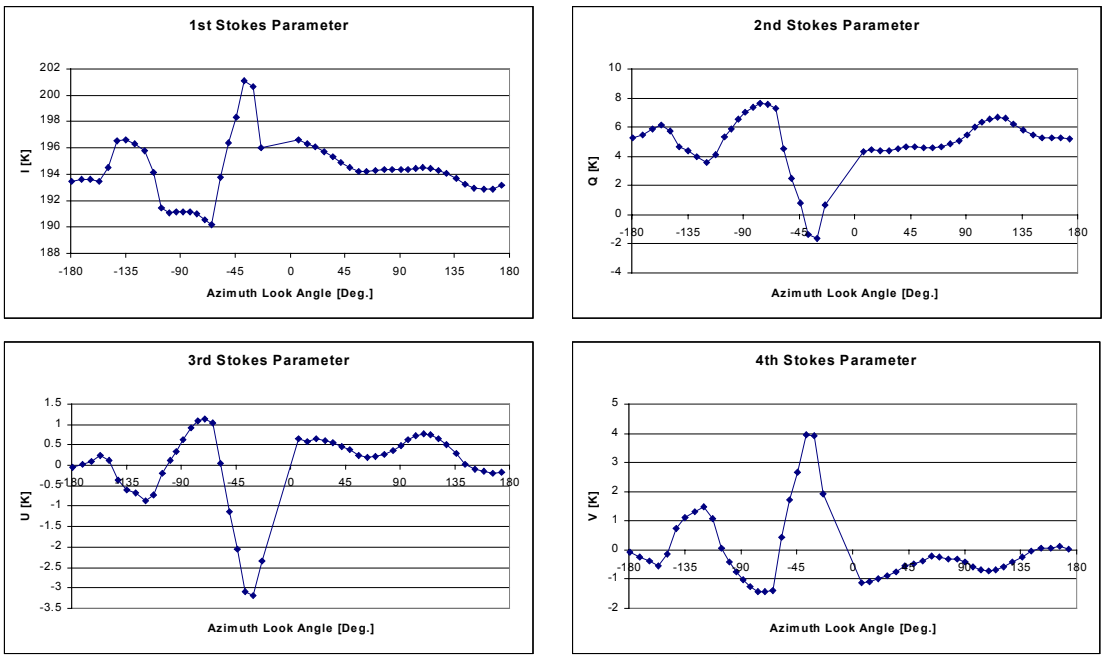

Figure 6.24. The four Stokes parameters from the 2nd circle flight track with 20° incidence angle from the March 15th 2001 flight.

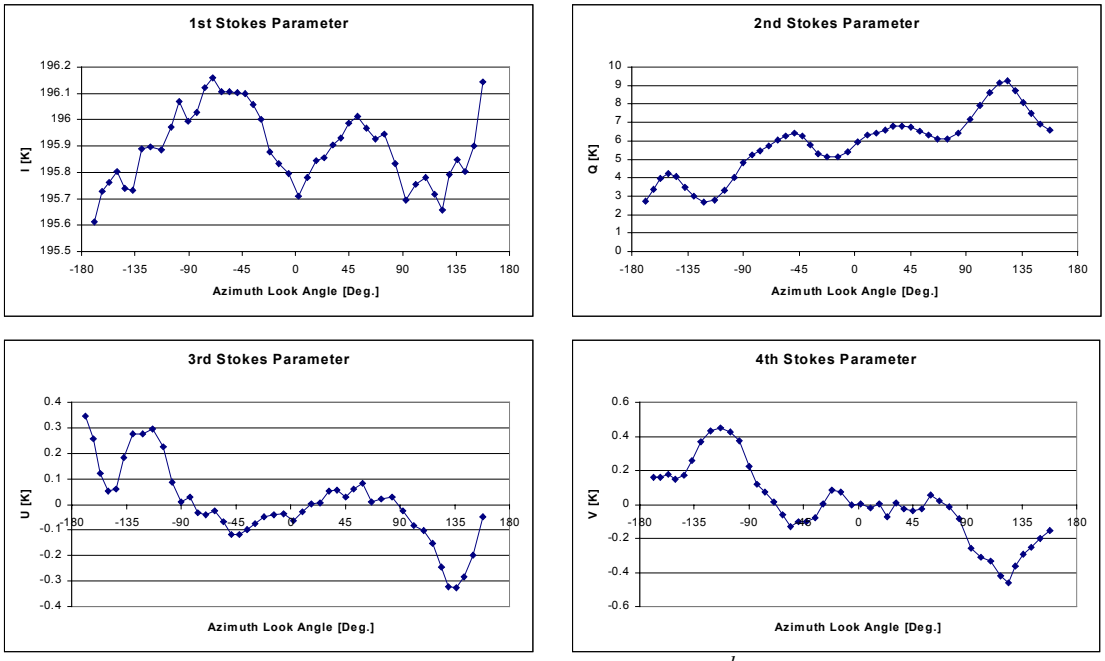

Figure 6.25. The four Stokes parameters from the 3rd circle flight track with 20° incidence angle from the March 15th 2001 flight.

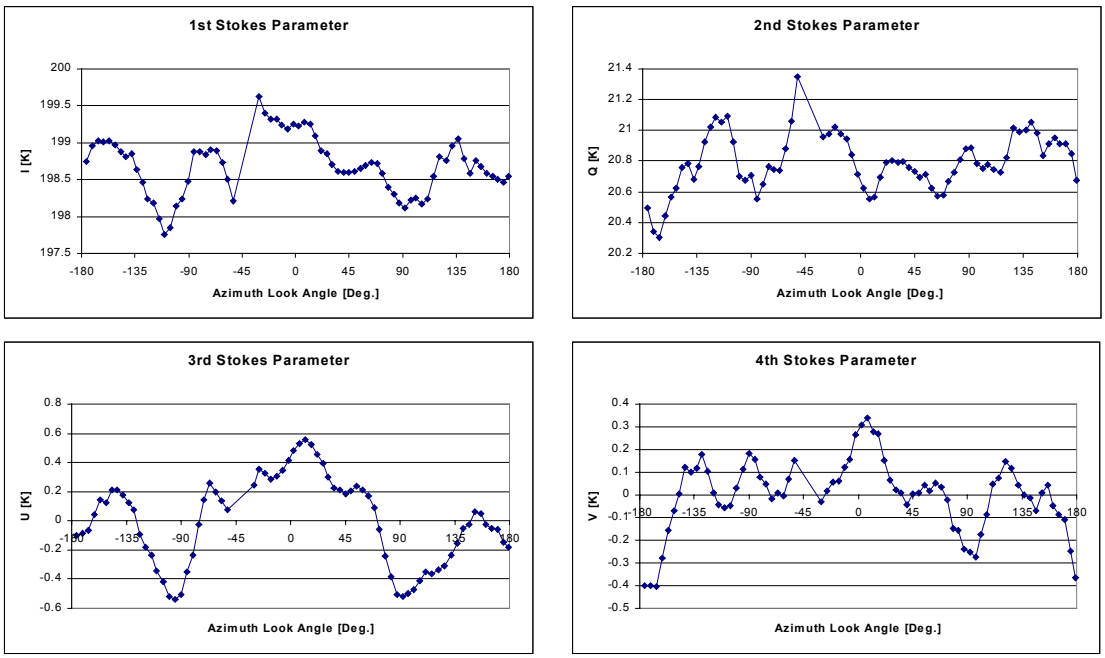

Figure 6.26. The four Stokes parameters from the 1st circle flight track with 35° incidence angle from the March 15th 2001 flight.

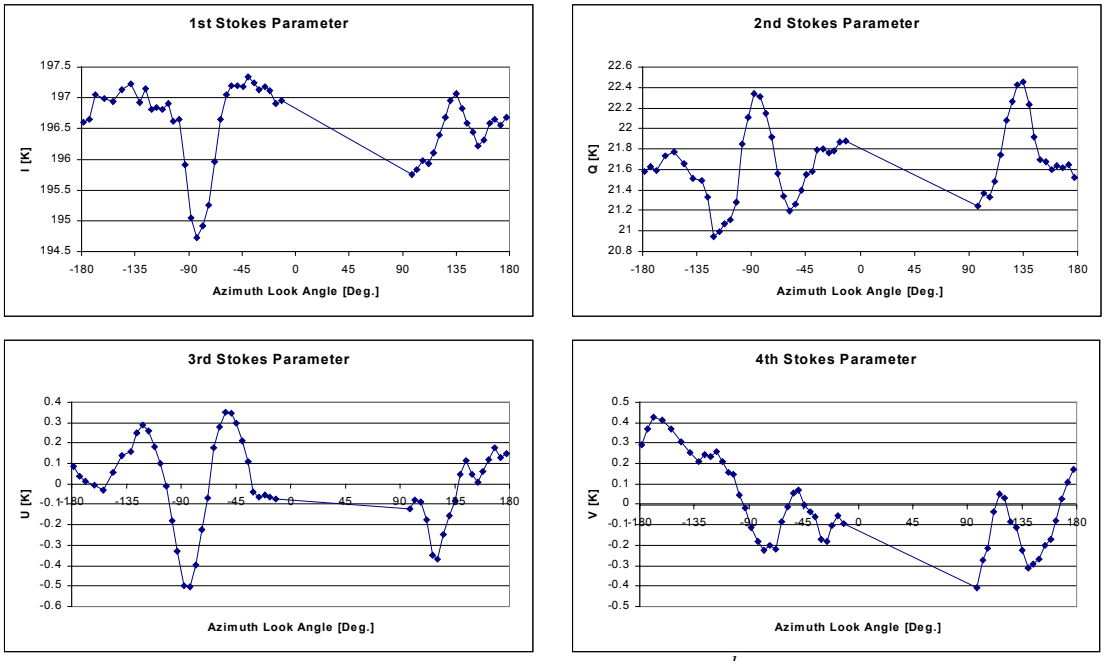

Figure 6.27. The four Stokes parameters from the 2nd circle flight track with 35° incidence angle from the March 15th 2001 flight.

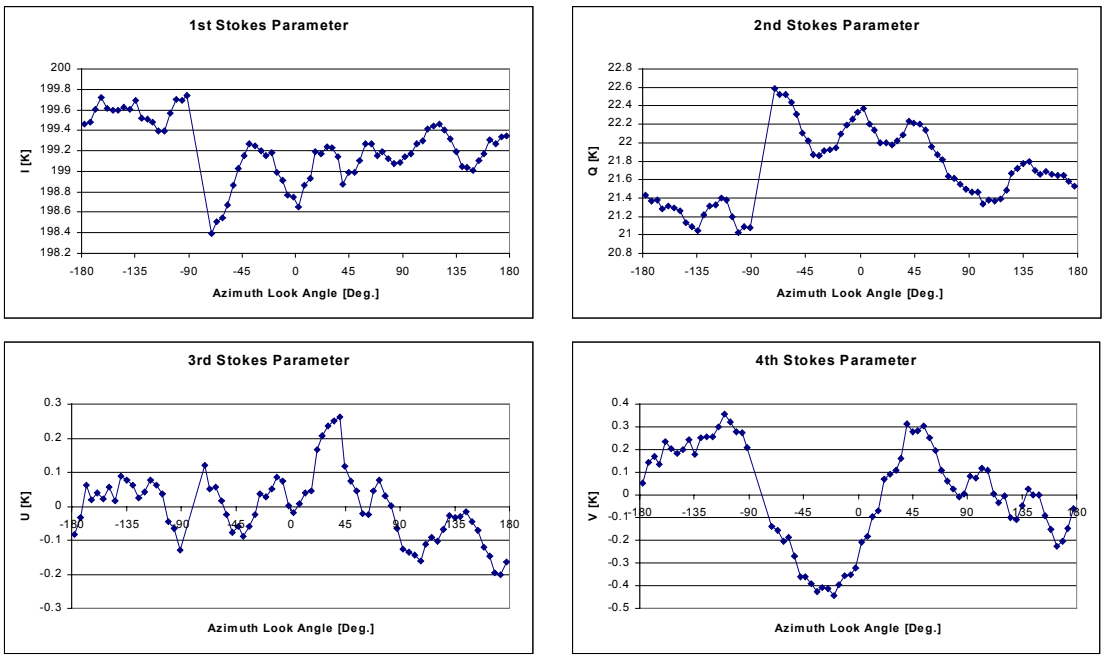

Figure 6.28. The four Stokes parameters from the 3rd circle flight track with 35° incidence angle from the March 15th 2001 flight.

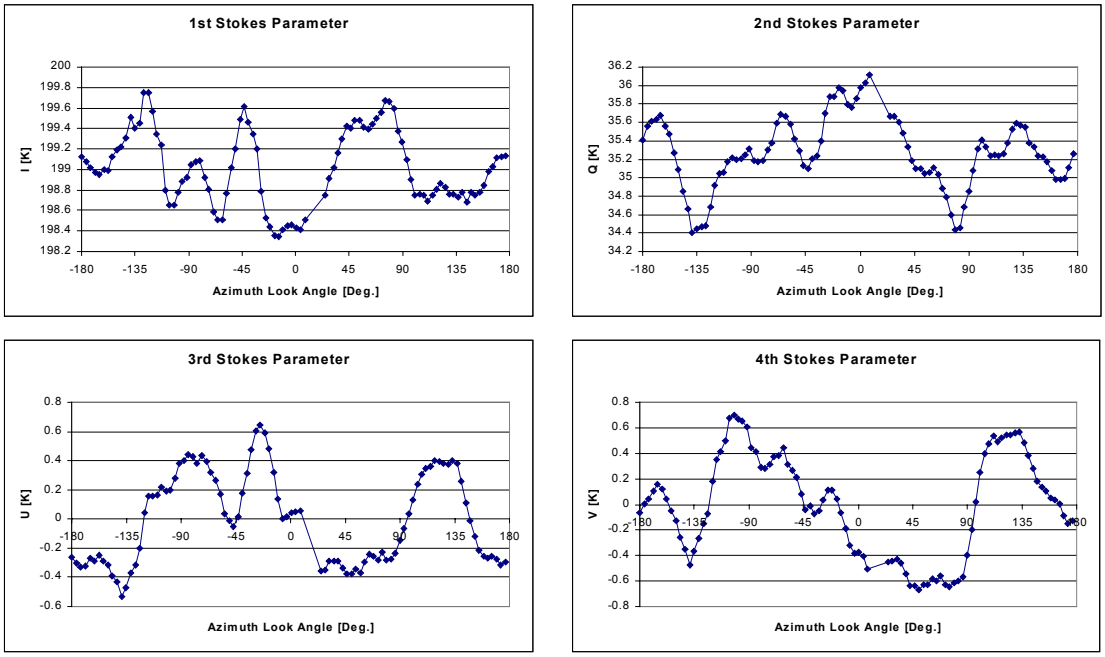

Figure 6.29. The four Stokes parameters from the 1st circle flight track with 42° incidence angle from the March 15th 2001 flight.

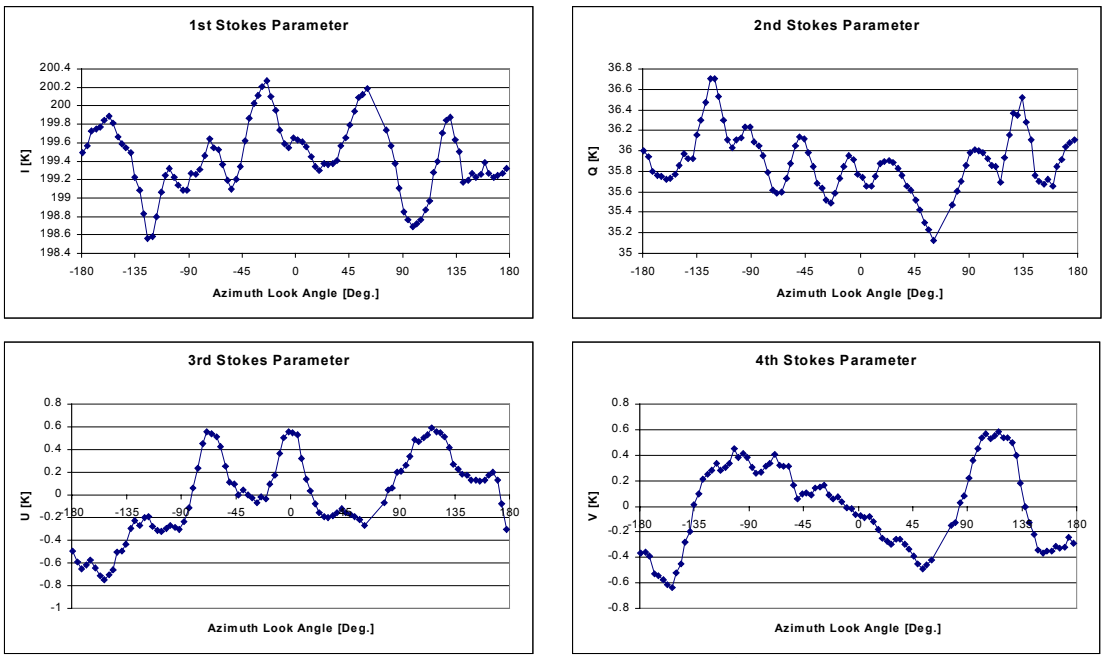

Figure 6.30. The four Stokes parameters from the 2nd circle flight track with 42° incidence angle from the March 15th 2001 flight.

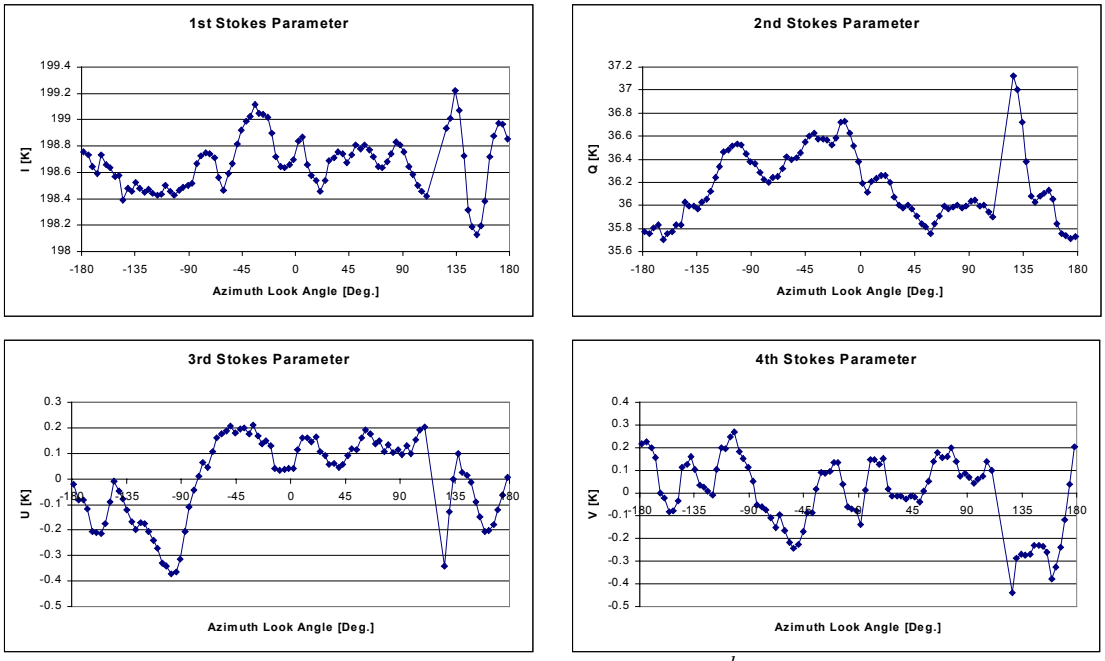

Figure 6.31. The four Stokes parameters from the 3rd circle flight track with 42° incidence angle from the March 15th 2001 flight.

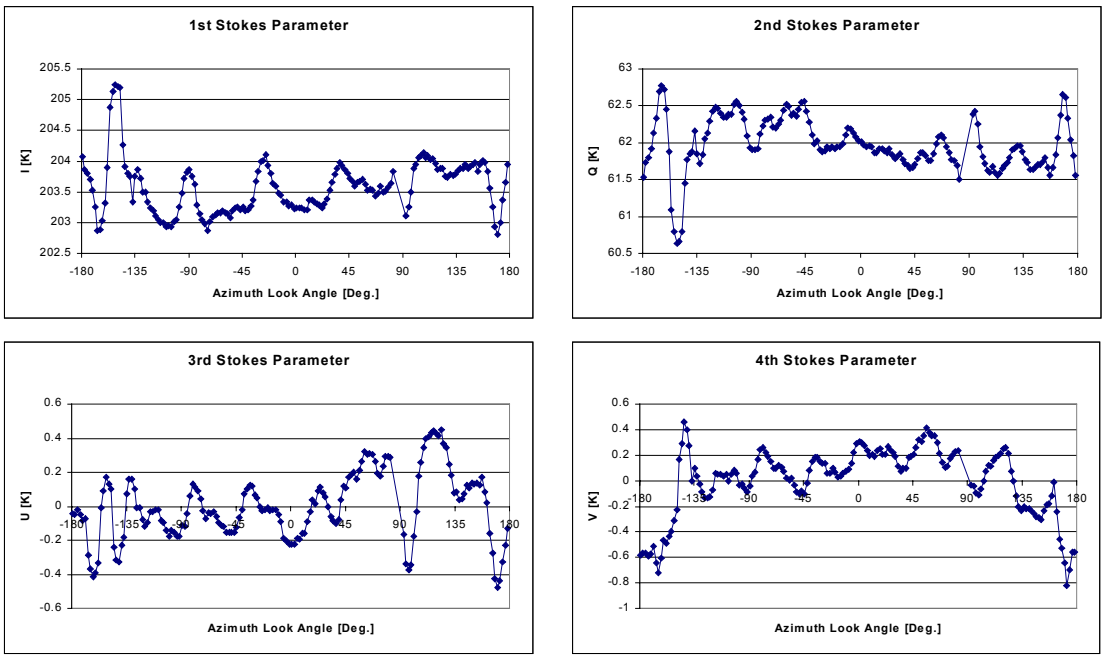

Figure 6.32. The four Stokes parameters from the 1st circle flight track with 52° incidence angle from the March 15th 2001 flight.

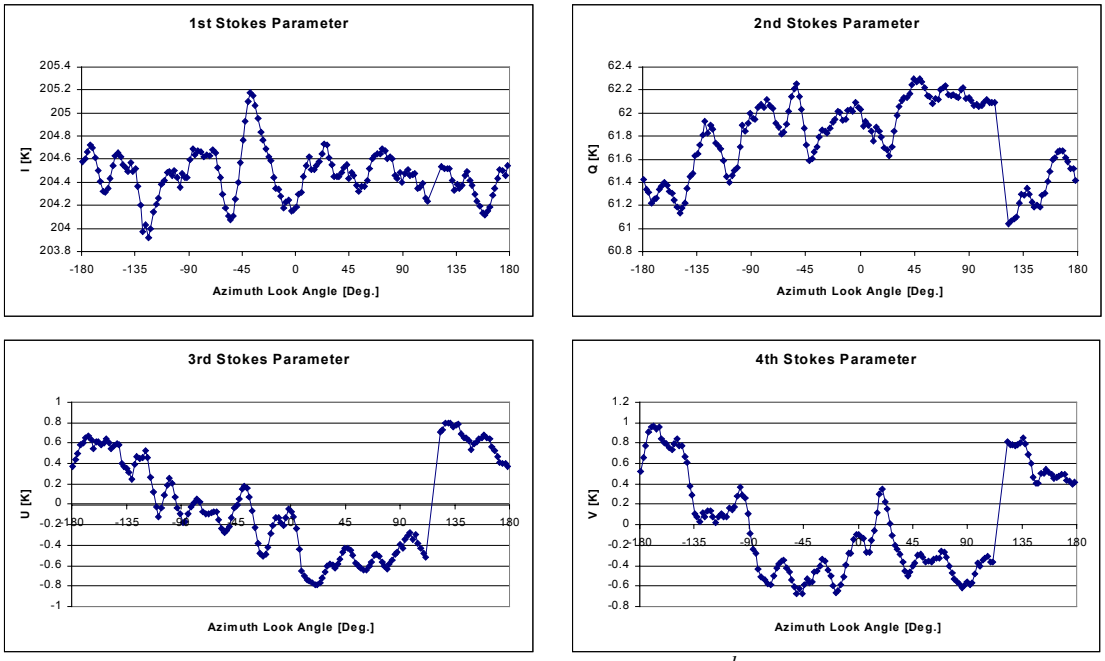

Figure 6.33. The four Stokes parameters from the 2nd circle flight track with 52° incidence angle from the March 15th 2001 flight.

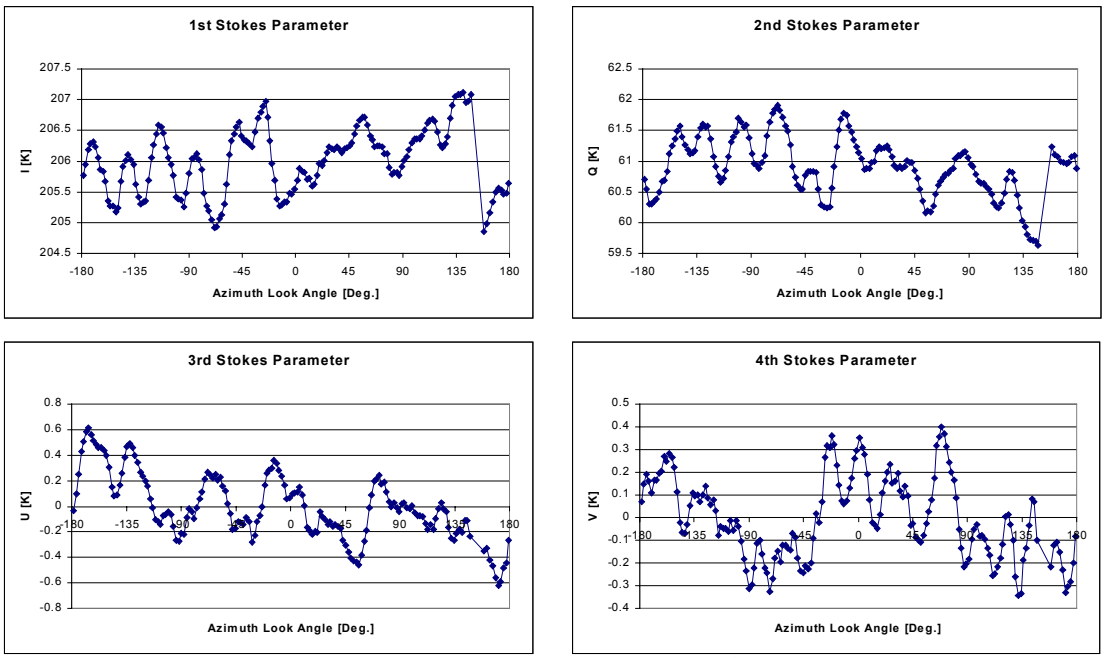

Figure 6.34. The four Stokes parameters from the 3rd circle flight track with 52° incidence angle from the March 15th 2001 flight.

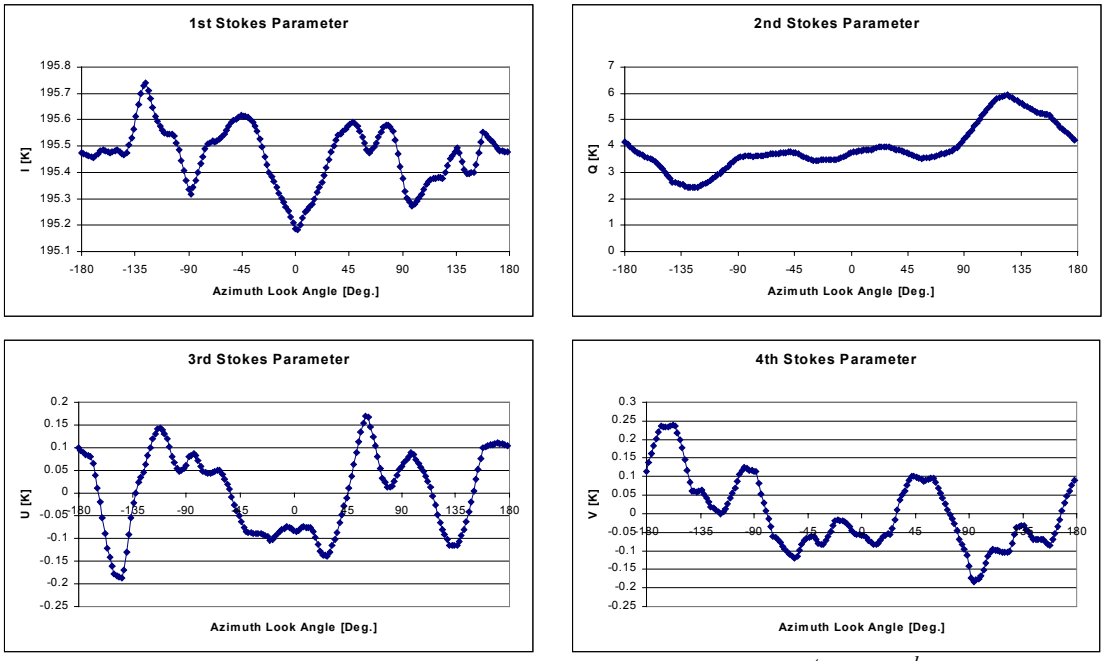

Figure 6.35. The averaged four Stokes parameters from the 1st and 3rd circle flight tracks with 20° incidence angle from the March 15th 2001 flight. The 2nd track is left out due to heavy interference.

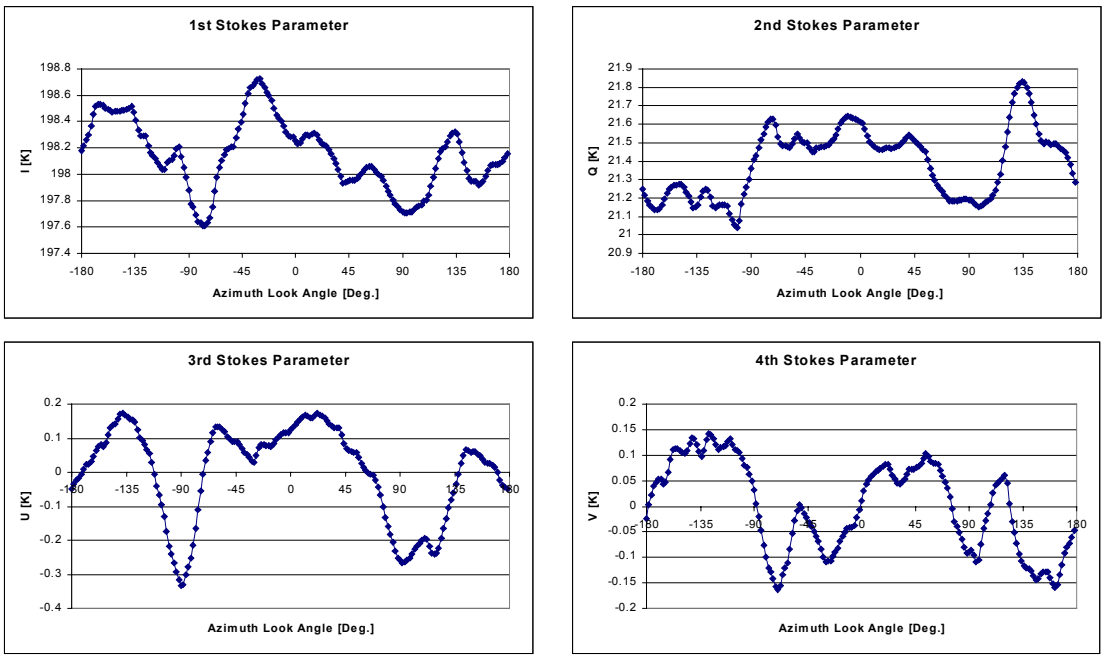

Figure 6.36. The averaged four Stokes parameters from the three circle flight tracks with 35° incidence angle from the March 15th 2001 flight.

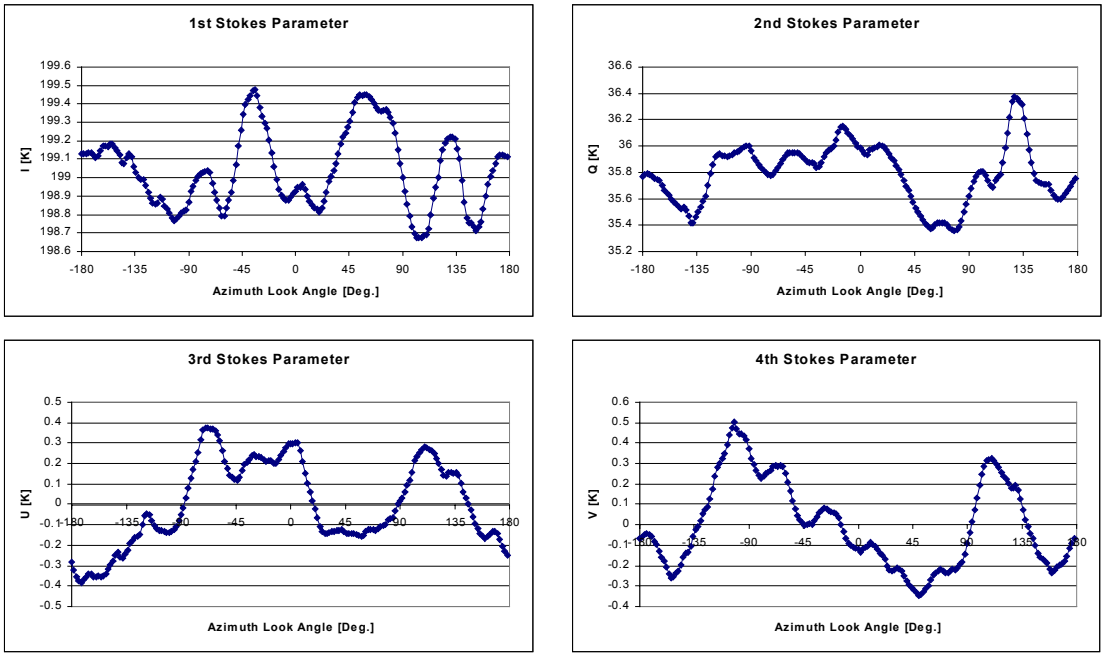

Figure 6.37. The averaged four Stokes parameters from the three circle flight tracks with 42° incidence angle from the March 15th 2001 flight.

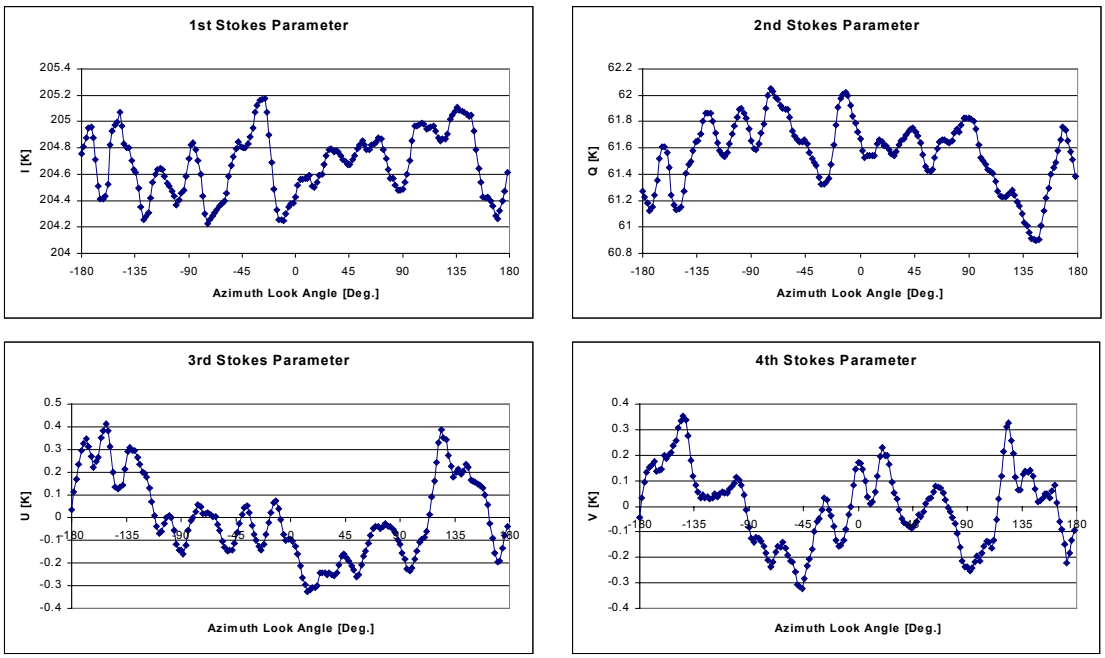

Figure 6.38. The averaged four Stokes parameters from the three circle flight tracks with 52° incidence angle from the March 15th 2001 flight.

result is observed for 52° incidence. The phases for the 1st Stokes parameter are likewise unsystematic, and variations cover all 360° of look direction.

Inc.	Harm.	I, Mag.	I, Phase	Q, Mag.	Q, Ph.	U, Mag.	U, Ph.	V, Mag.	V, Ph.
20°	1	0.06	124.45	0.86	-109.92	0.03	-179.94	0.06	140.80
	2	0.05	-135.06	0.76	87.33	0.06	-169.35	0.09	-71.04
	3	0.07	170.95	0.31	-74.43	0.05	-154.26	0.04	-175.62
	4	0.10	152.15	0.23	-90.18	0.06	43.48	0.00	14.68
35°	1	0.13	79.42	0.10	-14.87	0.06	38.63	0.02	94.12
	2	0.24	-1.82	0.17	58.54	0.14	-21.36	0.10	-92.95
	3	0.16	67.71	0.11	-84.16	0.01	161.61	0.03	18.44
	4	0.12	168.73	0.08	-167.49	0.09	178.05	0.03	-144.52
42°	1	0.07	-42.42	0.11	50.54	0.16	2.33	0.15	100.06
	2	0.06	-61.56	0.17	73.85	0.21	105.94	0.20	143.27
	3	0.18	145.42	0.18	-28.51	0.08	1.72	0.11	-18.08
	4	0.12	144.10	0.05	-71.36	0.04	-80.86	0.06	-36.00
52°	1	0.12	-104.88	0.21	35.09	0.19	162.35	0.07	-171.36
	2	0.06	100.81	0.13	-144.17	0.03	46.46	0.11	-49.15
	3	0.06	75.41	0.04	158.44	0.07	53.58	0.08	-16.13
	4	0.14	-171.05	0.12	8.43	0.07	-175.24	0.04	-156.93
35°, 45° and 52°	1	0.02	80.17	0.11	-13.05	0.01	-9.17	0.05	-179.28
	2	0.09	-6.88	0.09	77.45	0.07	66.74	0.03	-145.14
	3	0.10	96.76	0.07	-41.03	0.03	32.80	0.08	-16.79
	4	0.13	170.04	0.03	-23.16	0.04	-169.28	0.02	-100.94

Table 6.3. 1st, 2nd, 3rd, and 4th harmonic components in the averaged four Stokes parameters from the circle flights from March 15th 2001.

For the 2nd, the 3rd, and the 4th Stokes parameters, the same changing pattern is observed, and again the phases cover a large range of look directions. Some modulation might be expected with the changing incidence angle, but no systematic variation can be identified. The magnitudes for these three parameters are between 20 mK and 200 mK, typically, and also here, no systematic modulation is identified.

Noise and eventually some very small drifts may influence the results below 100 mK, and as the meteorological situation was a very low wind case with changing wind direction, the results may reflect these conditions. A 1st to 4th harmonic analysis of an average from all circles from 35° to 52° incidence angles, ignoring the changing angle, provides the last row in the table, reducing the magnitude of the signature further.

Using [17] and applying the wind direction $\psi = 240°$, the expected phases will be $\theta = +120°$ and $\theta = -120°$ for the 1st and 2nd harmonics of the 2nd Stokes parameter, $\theta = -150°$ and $\theta = -30°$ for the harmonics of the 3rd Stokes parameter, and $\theta = +150°$ for the 2nd harmonic of the 4th. No indication points to a result of this kind, however, and no alternative signature may be identified.

6.6. Results from the March 23rd 2001 flight

The 2nd scientific flight took place over the Kattegat target area due to icing conditions over the North Sea target site. The meteorological data is again a standard data set from The Danish Meteorological Institute, DMI, recorded at the island Anholt, and it is shown in figure 6.39. The data shows a slightly higher wind, and no changes right before the flight.

Five incidence angles were covered during this flight. All incidence angles, except 62° which needs about 15 minutes for a full circle, were measured three times, and the corrected data can be seen in the figures 6.40 to 6.53. The absolute calibration problem due to the missing observation of the calibration load and the noise diode was present also on this fight, and the absolute level may thus deviate several Kelvin from the expected level. As for the March 15th flight, however, the problem does not influence on the radiometer stability, and the azimuth signatures will be useable for analysis with respect to the wind direction. It is noticed, that the 3rd circle with 20° incidence angle, figure 6.42, is completely corrupted by RF-interference, and it is thus not included in further analysis.

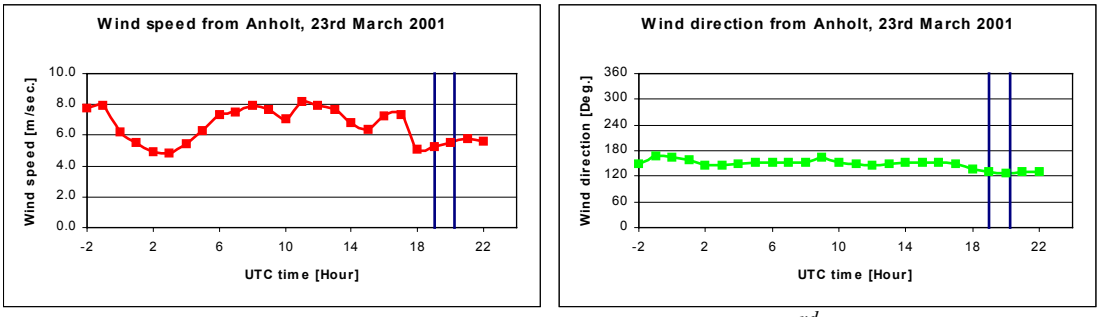

Figure 6.39. Wind speed and wind direction for March 23rd 2001, measured at the island Anholt in Kattegat. The blue lines indicate the flight time.

The basic large peak to peak variation, observed on the previous flight, is repeated in the March 23rd data, but the angular size of the peaks seems to be more varying. The two signatures with 62° incidence angle, figure 6.52 and 6.53, were recorded with only 5° roll, and the acquisition time was long compared to the circles with lower incidence angles. The sample density is thus larger, and it is noticed, that some peaks are shorter than the antenna beam width, excluding point targets at first view. Due to the low roll angle, however, the circle radius is about 6.5 km, and as the distance to the footprint is only 2.1 km from the flight track for the 1000 m flight altitude, point targets are flown by in a fraction of the circle, only equal to 4.9°. Point targets will thus appear as objects down to the size of 4.9°, still explaining the small peaks for the two circles.

Variations of the sea surface may be another origin for the peaks observed, and as for the March 15th flight, averaging of circles with equal incidence angle is applied to reduce the noise. The averaged circles are shown in figures 5.54 to 5.58, and generally it is noticed, that the small peaks reduce again, but the overall variations are seen to be larger than for the March 15th flight.

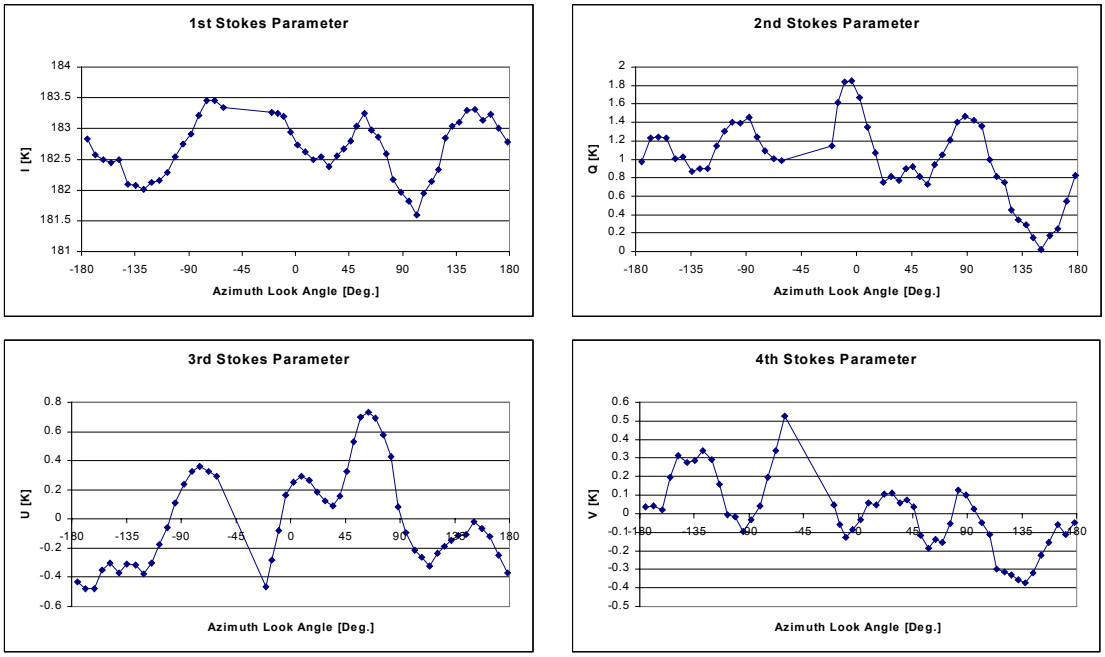

Figure 6.40. The four Stokes parameters from the 1st circle flight track with 20° incidence angle from the March 23rd 2001 flight.

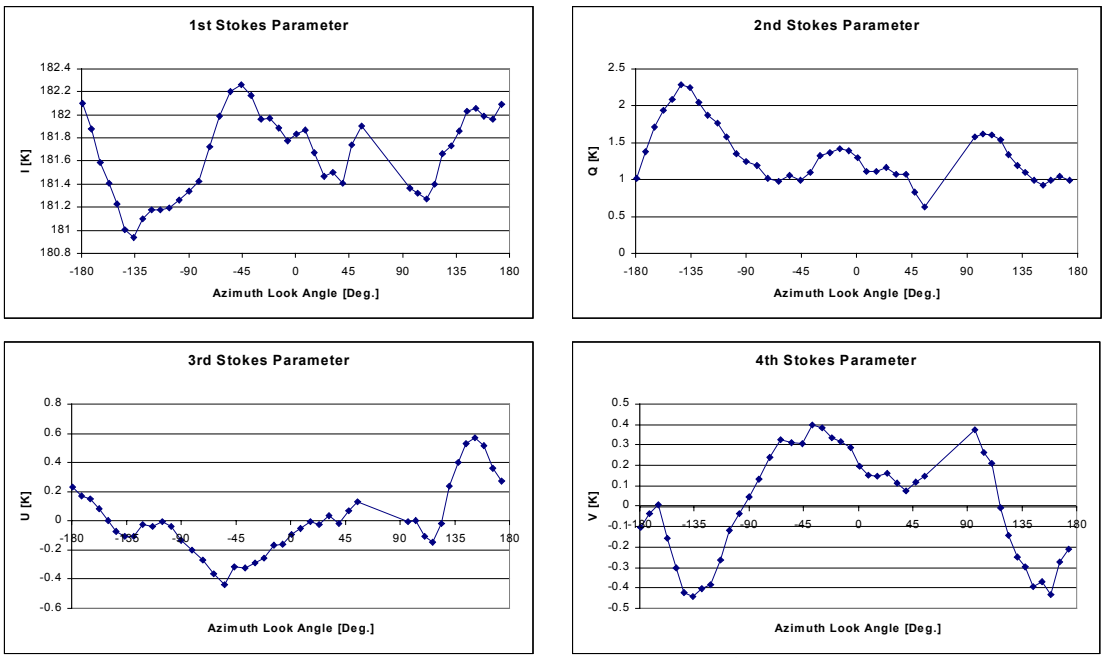

Figure 6.41. The four Stokes parameters from the 2nd circle flight track with 20° incidence angle from the March 23rd 2001 flight.

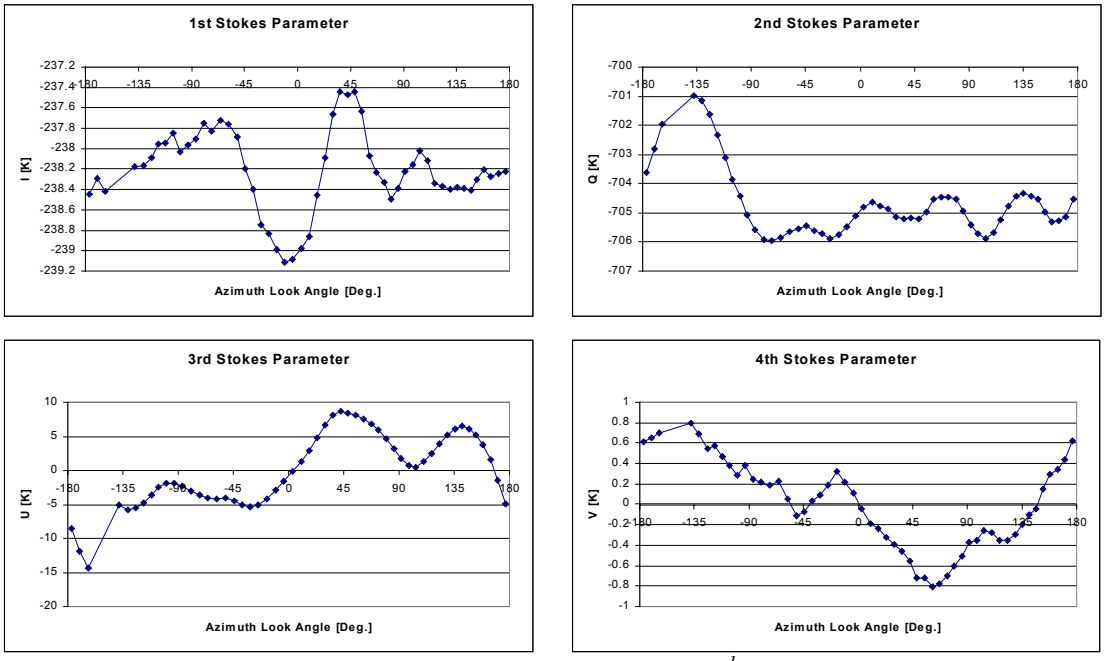

Figure 6.42. The four Stokes parameters from the 3rd circle flight track with 20° incidence angle from the March 23rd 2001 flight.

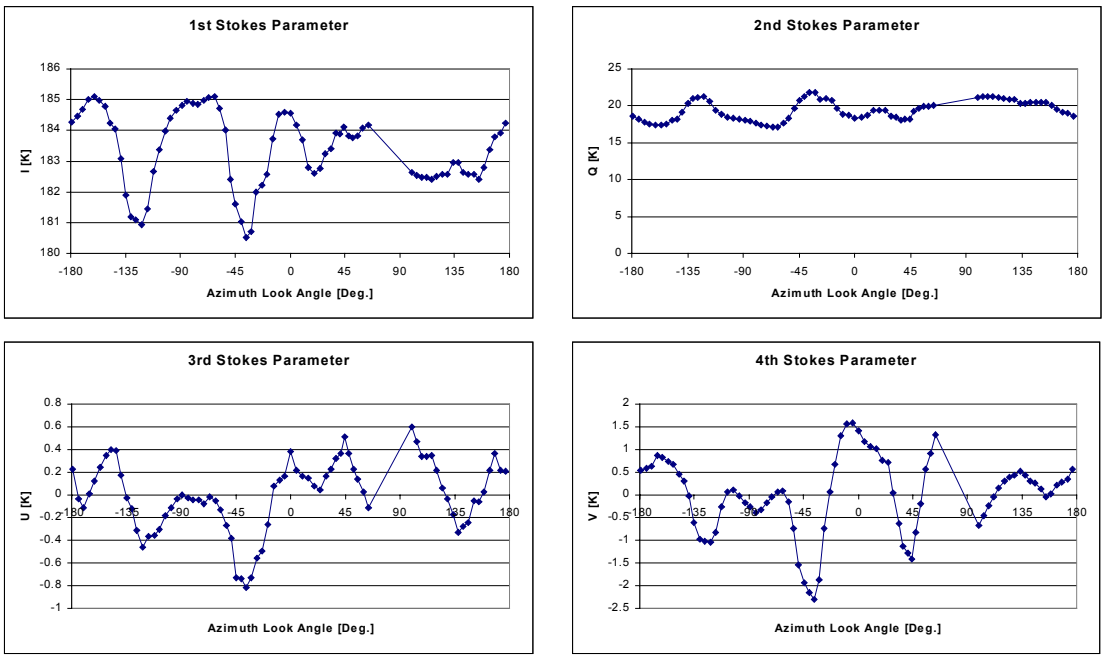

Figure 6.43. The four Stokes parameters from the 1st circle flight track with 35° incidence angle from the March 23rd 2001 flight.

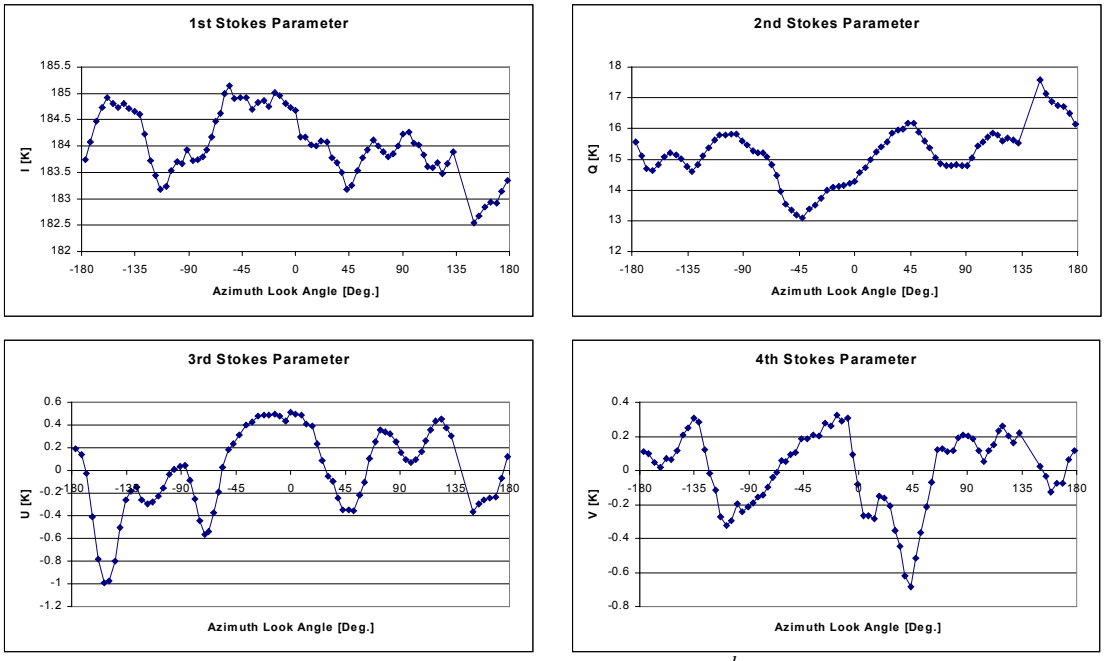

Figure 6.44. The four Stokes parameters from the 2nd circle flight track with 35° incidence angle from the March 23rd 2001 flight.

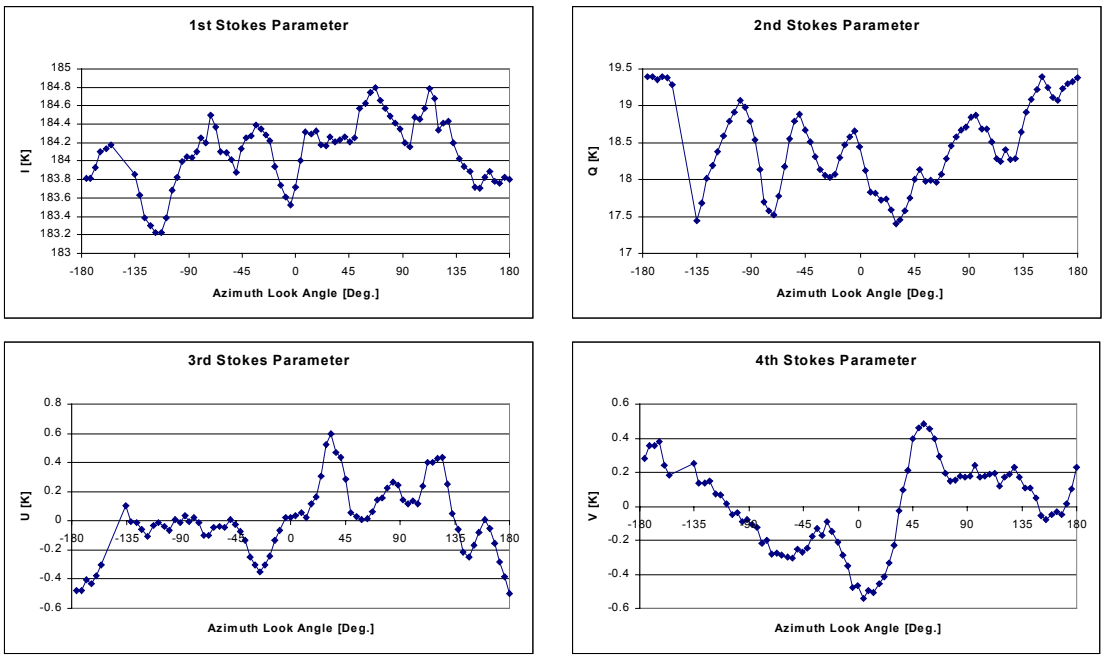

Figure 6.45. The four Stokes parameters from the 3rd circle flight track with 35° incidence angle from the March 23rd 2001 flight.

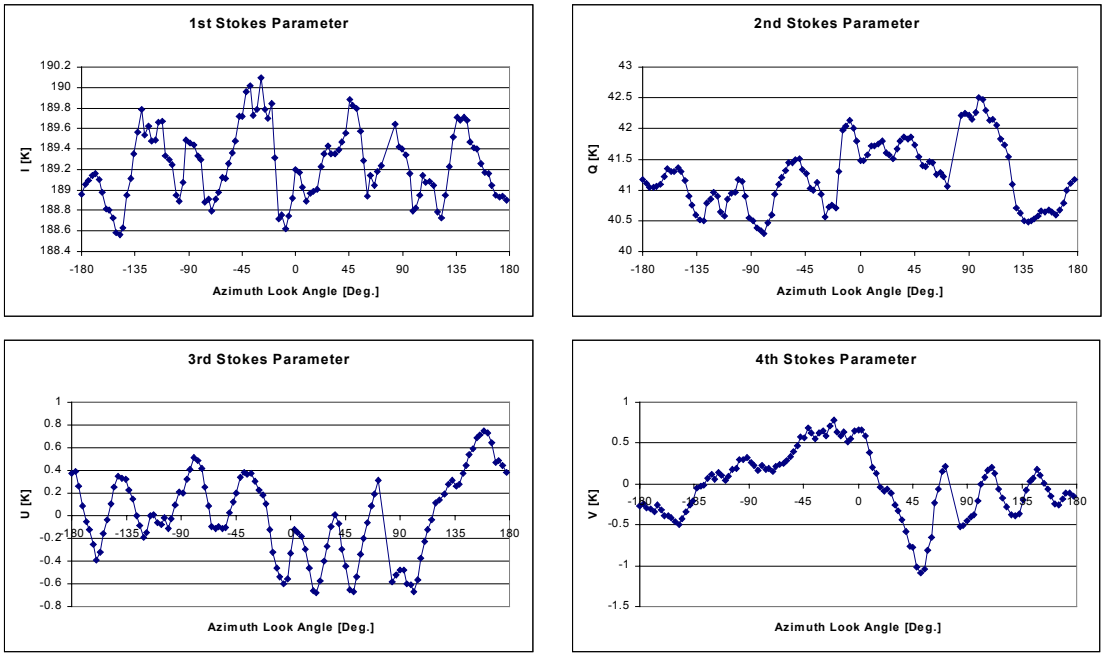

Figure 6.46. The four Stokes parameters from the 1st circle flight track with 47° incidence angle from the March 23rd 2001 flight.

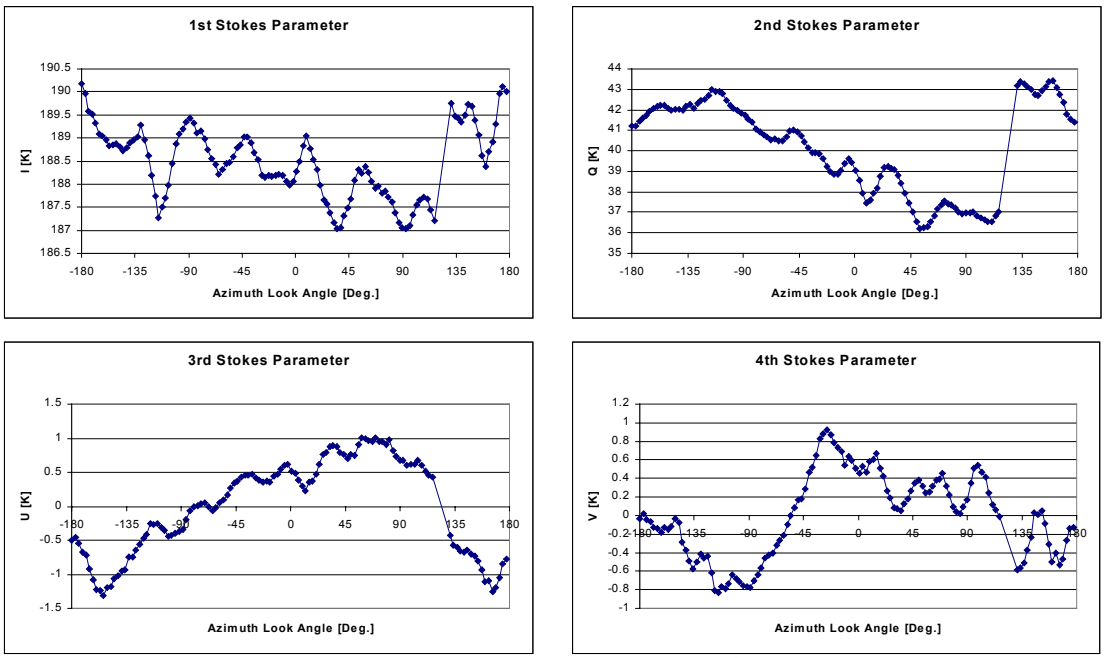

Figure 6.47. The four Stokes parameters from the 2nd circle flight track with 47° incidence angle from the March 23rd 2001 flight.

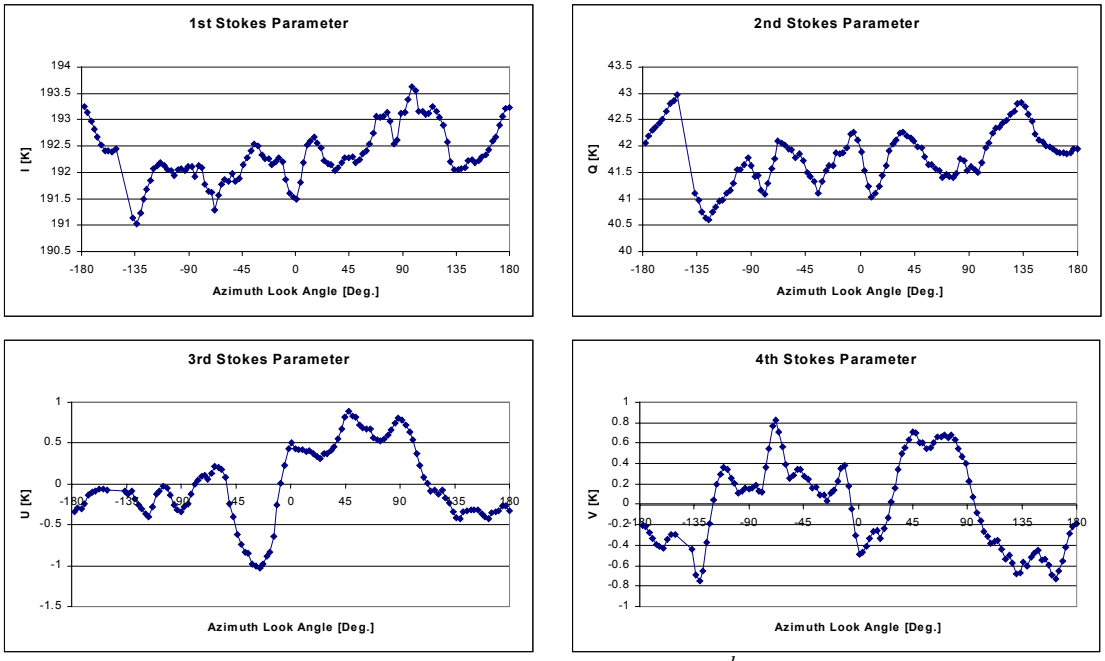

Figure 6.48. The four Stokes parameters from the 3rd circle flight track with 47° incidence angle from the March 23rd 2001 flight.

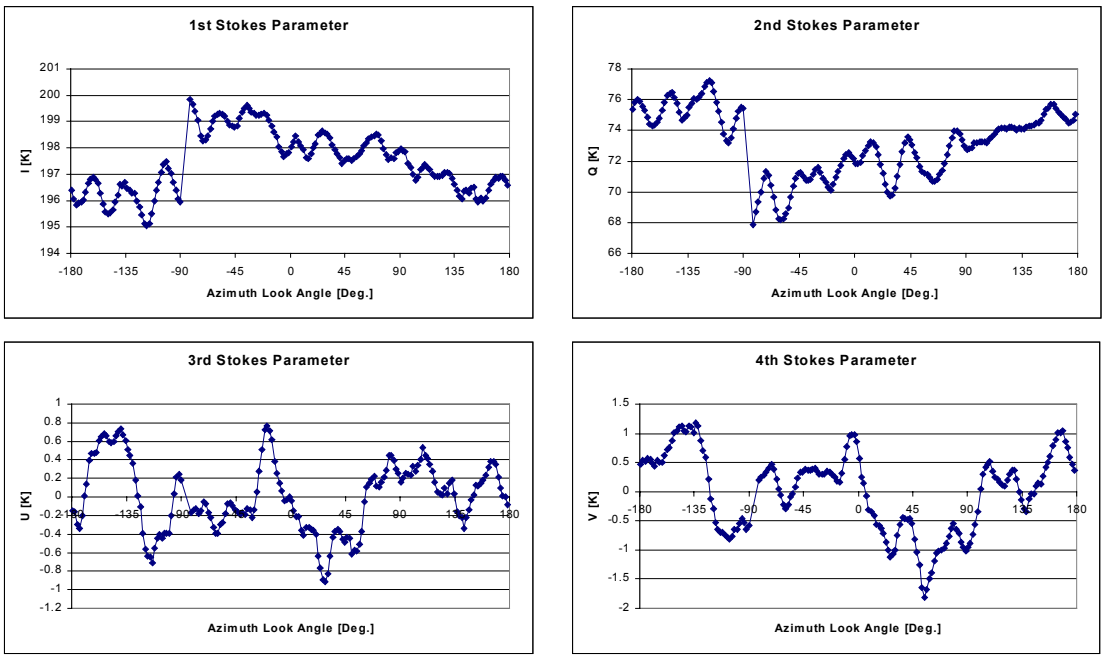

Figure 6.49. The four Stokes parameters from the 1st circle flight track with 57° incidence angle from the March 23rd 2001 flight.

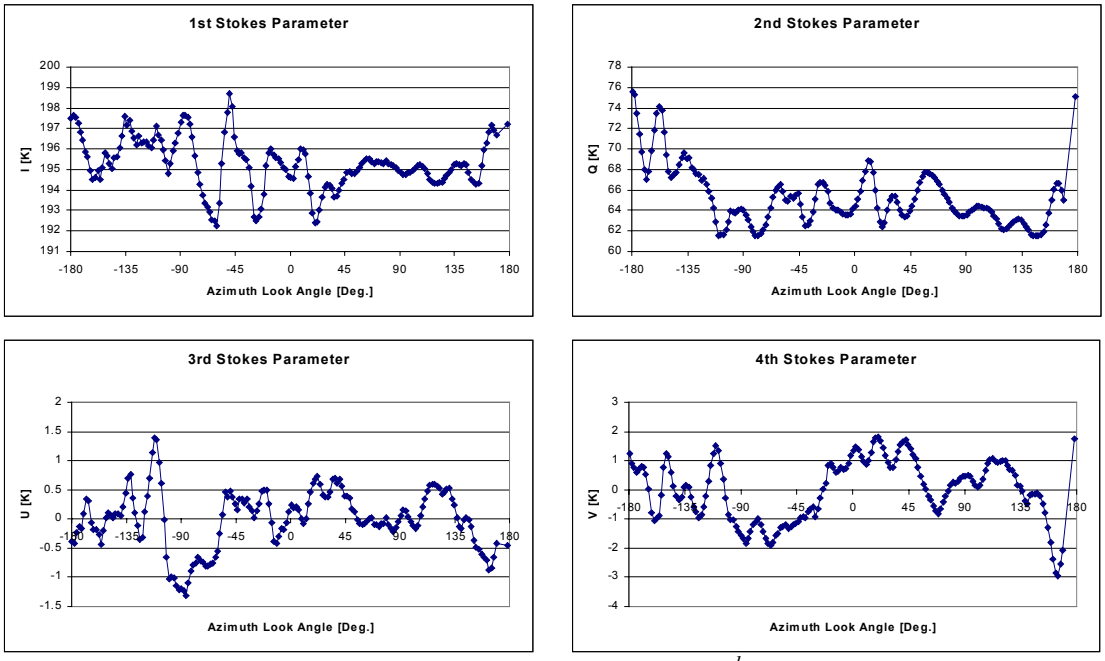

Figure 6.50. The four Stokes parameters from the 2nd circle flight track with 57° incidence angle from the March 23rd 2001 flight.

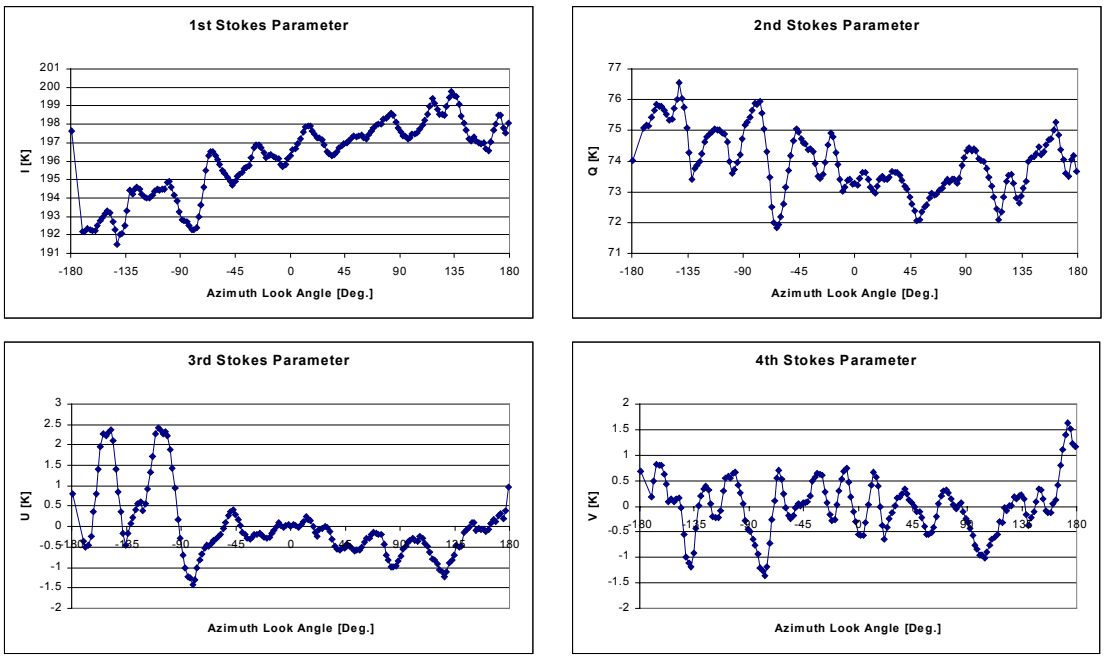

Figure 6.51. The four Stokes parameters from the 3rd circle flight track with 57° incidence angle from the March 23rd 2001 flight.

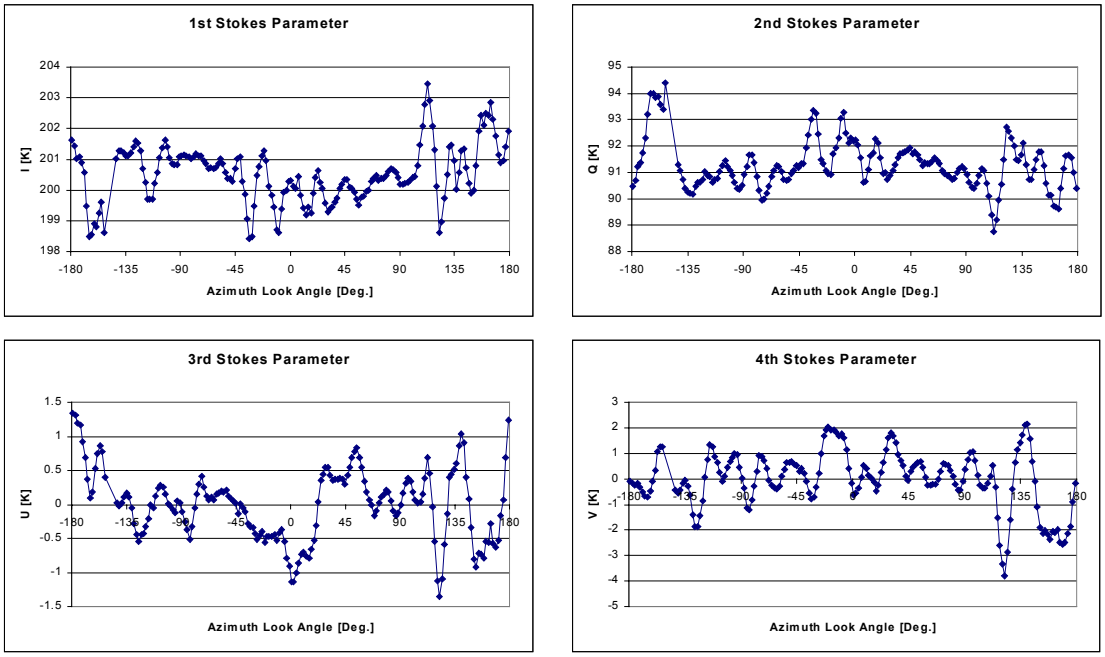

Figure 6.52. The four Stokes parameters from the 1st circle flight track with 62° incidence angle from the March 23rd 2001 flight.

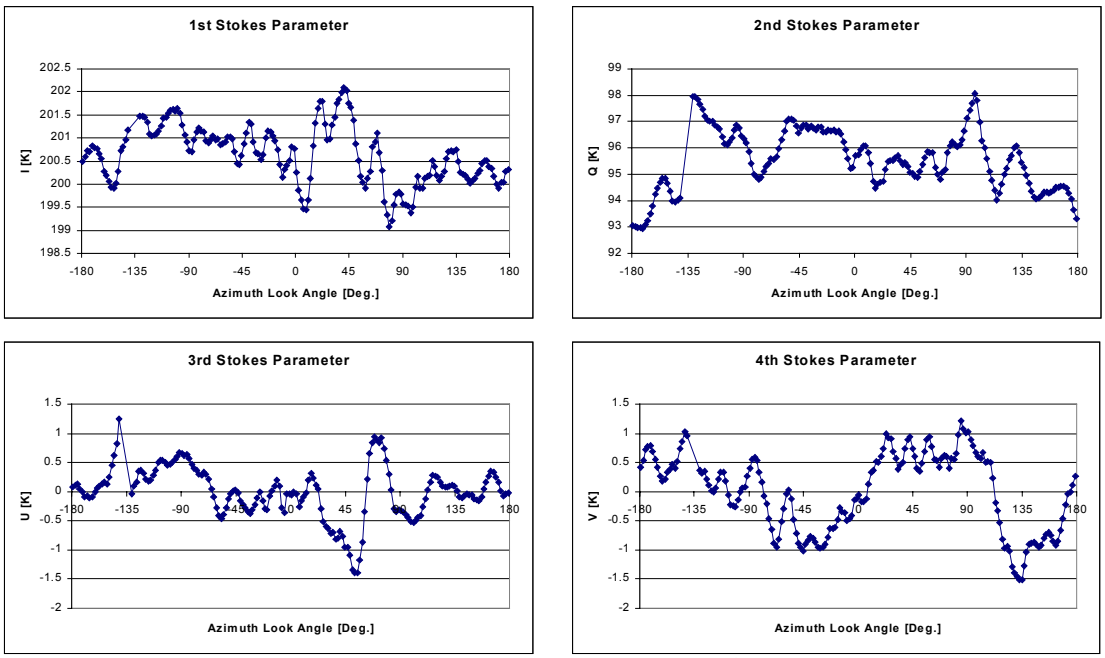

Figure 6.53. The four Stokes parameters from the 2nd circle flight track with 62° incidence angle from the March 23rd 2001 flight.

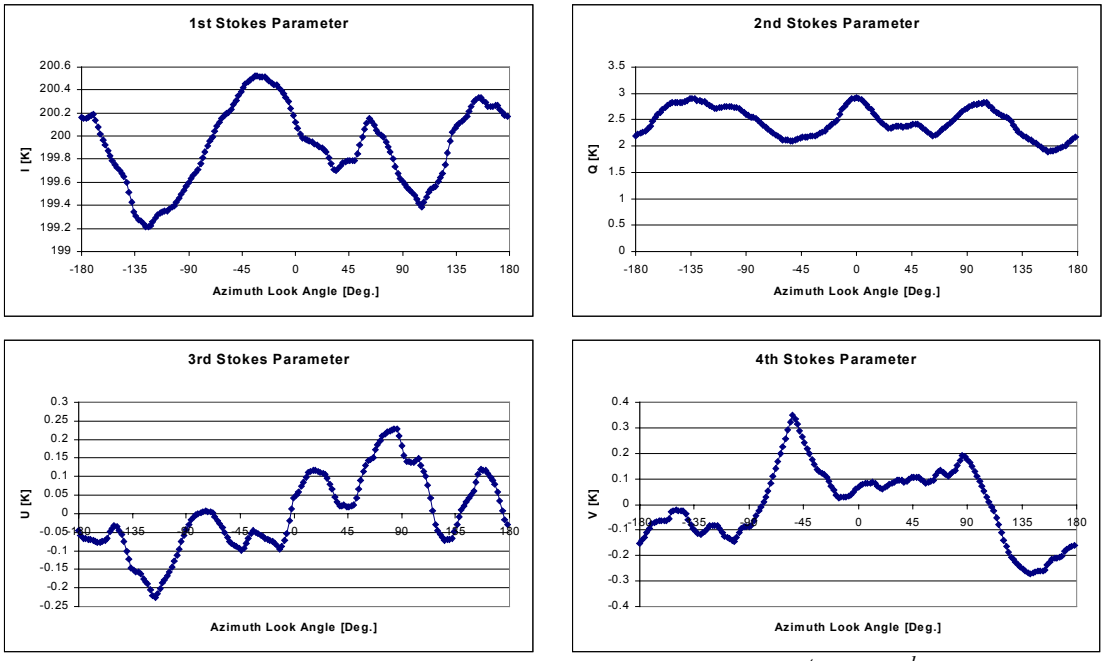

Figure 6.54. The averaged four Stokes parameters from the 1st and 2nd circle flight tracks with 20° incidence angle from the March 23rd 2001 flight. The 3rd track is left out due to heavy interference.

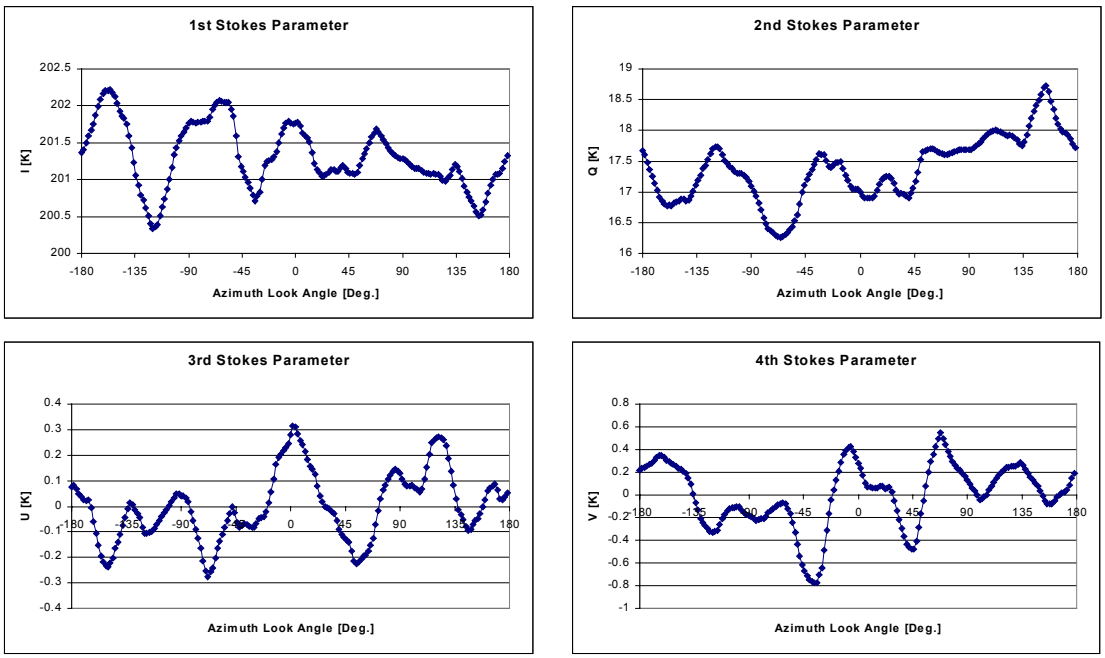

Figure 6.55. The averaged four Stokes parameters from the three circle flight tracks with 35° incidence angle from the March 23rd 2001 flight.

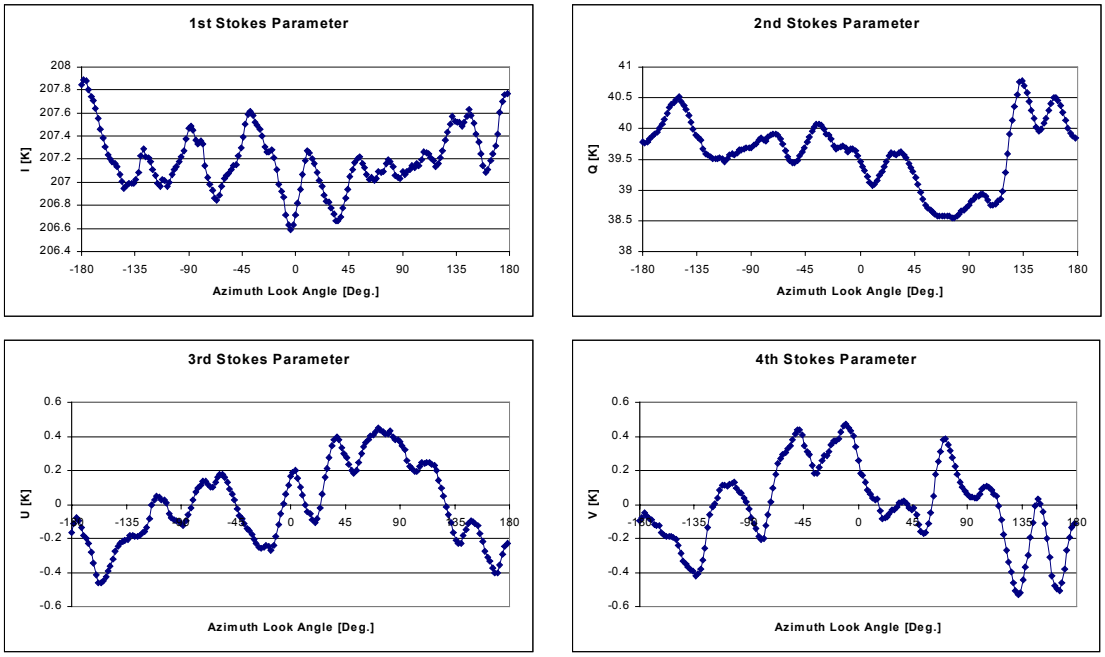

Figure 6.56. The averaged four Stokes parameters from the three circle flight tracks with 47° incidence angle from the March 23rd 2001 flight.

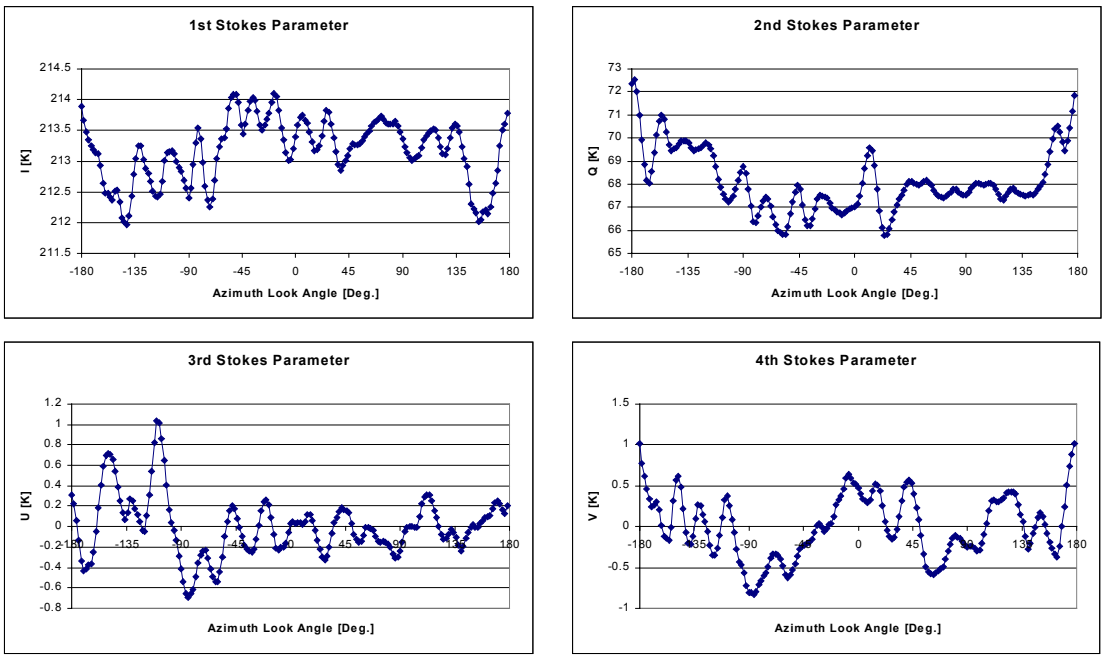

Figure 6.57. The averaged four Stokes parameters from the three circle flight tracks with 57° incidence angle from the March 23rd 2001 flight.

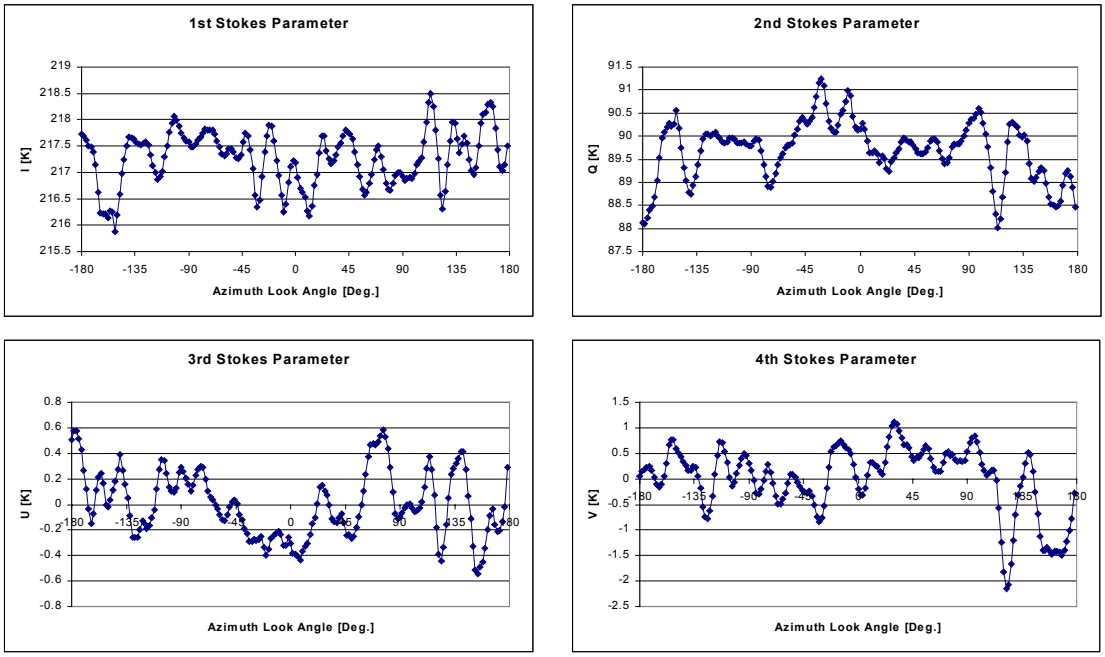

Figure 6.58. The averaged four Stokes parameters from the two circle flight tracks with 62° incidence angle from the March 23rd 2001 flight.

Inc.	Harm.	I, Mag.	I, Phase	Q, Mag.	Q, Ph.	U, Mag.	U, Ph.	V, Mag.	V, Ph.
20°	1	0.14	-8.87	0.06	75.35	0.12	-75.08	0.16	2.09
	2	0.39	42.73	0.21	-114.62	0.01	174.05	0.04	-167.50
	3	0.22	170.11	0.29	25.69	0.04	-171.33	0.11	128.61
	4	0.11	93.82	0.13	-41.34	0.05	-12.65	0.04	-98.92
35°	1	0.17	60.51	0.52	-124.70	0.07	-79.38	0.21	-123.60
	2	0.05	-76.16	0.17	86.65	0.06	52.14	0.09	-42.69
	3	0.25	147.12	0.16	-18.63	0.10	-3.10	0.06	49.57
	4	0.36	-56.74	0.40	94.17	0.09	-11.71	0.15	-16.66
47°	1	0.18	176.90	0.48	134.57	0.23	-46.92	0.24	9.59
	2	0.15	66.59	0.43	31.02	0.19	-168.93	0.08	120.69
	3	0.08	169.69	0.15	-81.13	0.04	-164.69	0.11	103.15
	4	0.04	62.05	0.19	-168.07	0.03	-58.91	0.09	38.18
57°	1	0.42	-21.18	1.28	175.49	0.12	168.92	0.13	-118.25
	2	0.16	85.67	0.88	-48.55	0.13	-66.24	0.34	-8.56
	3	0.19	106.28	0.24	121.99	0.14	22.45	0.18	12.60
	4	0.03	39.00	0.28	29.71	0.10	131.82	0.06	-64.16
62°	1	0.13	140.04	0.46	15.87	0.11	-177.83	0.34	-2.79
	2	0.22	131.35	0.11	159.03	0.15	-157.05	0.47	-104.70
	3	0.28	-99.45	0.38	56.31	0.10	174.04	0.16	87.03
	4	0.10	136.59	0.17	126.92	0.07	-46.65	0.15	-51.33
35° to 62°	1	0.04	60.67	0.19	-121.20	0.04	-125.31	0.01	-42.50
	2	0.11	100.88	0.22	-37.36	0.04	-147.05	0.12	-60.62
	3	0.09	176.05	0.06	108.03	0.05	52.60	0.11	48.33
	4	0.07	-43.20	0.17	120.71	0.02	26.15	0.12	-21.37

Table 6.4. 1st, 2nd, 3rd, and 4th harmonic components in the averaged four Stokes parameters from the circle flights from March 23rd 2001.

An analysis of the 1st to 4th harmonic components is carried out and presented in table 6.4. The results confirm the larger signals, and some magnitudes for the 2nd Stokes parameter are larger than 500 mK. The behavior in magnitude is not systematic, however, and no natural function of the incidence angle is observed. The phases are distributed over the azimuth angles again, and the random nature from the low wind case on March 15th is repeated.

Expected phases from [17] and from the wind direction, $\psi = 120°$, would be $\theta = -120°$ and $\theta = +120°$ for the first two harmonics of the 2nd Stokes parameter, $\theta = -30°$ and $\theta = -150°$ for the 3rd and $\theta = 30°$ for the 4th. No confirmation of these values is found, and again the total average from all circles with incidence angles from 35° to 62° is calculated, resulting in the last row of table 6.4. The result shows a decrease in the magnitudes, and it is thus an indication, that the signals still have random nature, rather than systematic wind direction dependence. The resulting phases still do not comply with the expected values, except for the 1st harmonic of the 2nd Stokes parameter, with the value $\theta = -121.20°$ and the 2nd harmonic of the 3rd Stokes parameter with $\theta = -147.05°$. The magnitude are 190 mK and 40 mK, but with only one example, it is not statistically provable, if the result origins from a wind driven sea surface pattern or if it is a statistical coincidence.

6.7. Results from the October 25th 2001 flight

The flight on October 25th 2001 took place over the primary target area over the North Sea, and all meteorological data acquisition system were operative. The data, received from the oilrigs, Gorm and Tyra located on either sides of the target area, is shown in figure 6.59, which also include measurements of the sea surface temperature. The blue lines on the figure indicate the flight time, and it is noticed, that the wind speed was approximately 11.0 m/sec. during the flight and that the wind direction was stable at $\theta = 190°$.

The flight altitude was increased on this flight from 1000 m to 2000 m to investigate, if the magnitude of the narrow peaks on the Stokes parameter signatures could be reduced, when the field of view, i.e. the spatial integration area, was increased. Four incidence angles were covered, and the results are shown in the figures 6.60 to 6.71. The general impression of the curves is similar to the previous two flights, and a large variation is noticed. Figure 6.63 and 6.65 show small variations for the 2nd, the 3rd and the 4th Stokes parameters, while the 1st Stokes parameter variation is of several Kelvin. The characteristic peak pattern is the same as for the two previous flights, and it is still noticed, that the width of the peaks in many cases is smaller for large incidence angles, i.e. for large circle diameters. The flight altitude is now higher, however, and even for the largest circles, flying by a point target will cause a peak of 15° width.

Calculation of averages follows the single tracks, and results are shown in the figures 6.72 to 6.75. Peaks are reduced again, and for some incidence angles, signatures similar to harmonics appear. The analysis of the 1st to 4th harmonics for each incidence angle is shown in table 6.5, and again the last row shows the harmonic analysis for the averaged track for all incidence angles from 29° to 55°.

With the wind direction, $\psi = 190°$, the expected azimuth angles from [17] would be $\theta = 170°$ and $\theta = -20°$ for the 2nd Stokes parameter, $\theta = -100°$ and $\theta = 70°$ for the 3rd, and $\theta = -110°$ for the 4th. The table shows some variation, and the random impression is similar to the two previous flights, although the wind speed is 11.0 m/sec., the highest in all the flights. The averaged track shows some similarity with the expected azimuth angles, especially for the 1st harmonics of the 2nd and 3rd Stokes parameters. For these contributions, however, the magnitudes are rather small, 40 mK and 30 mK, respectively, and too little data exist for a statistical confirmation.

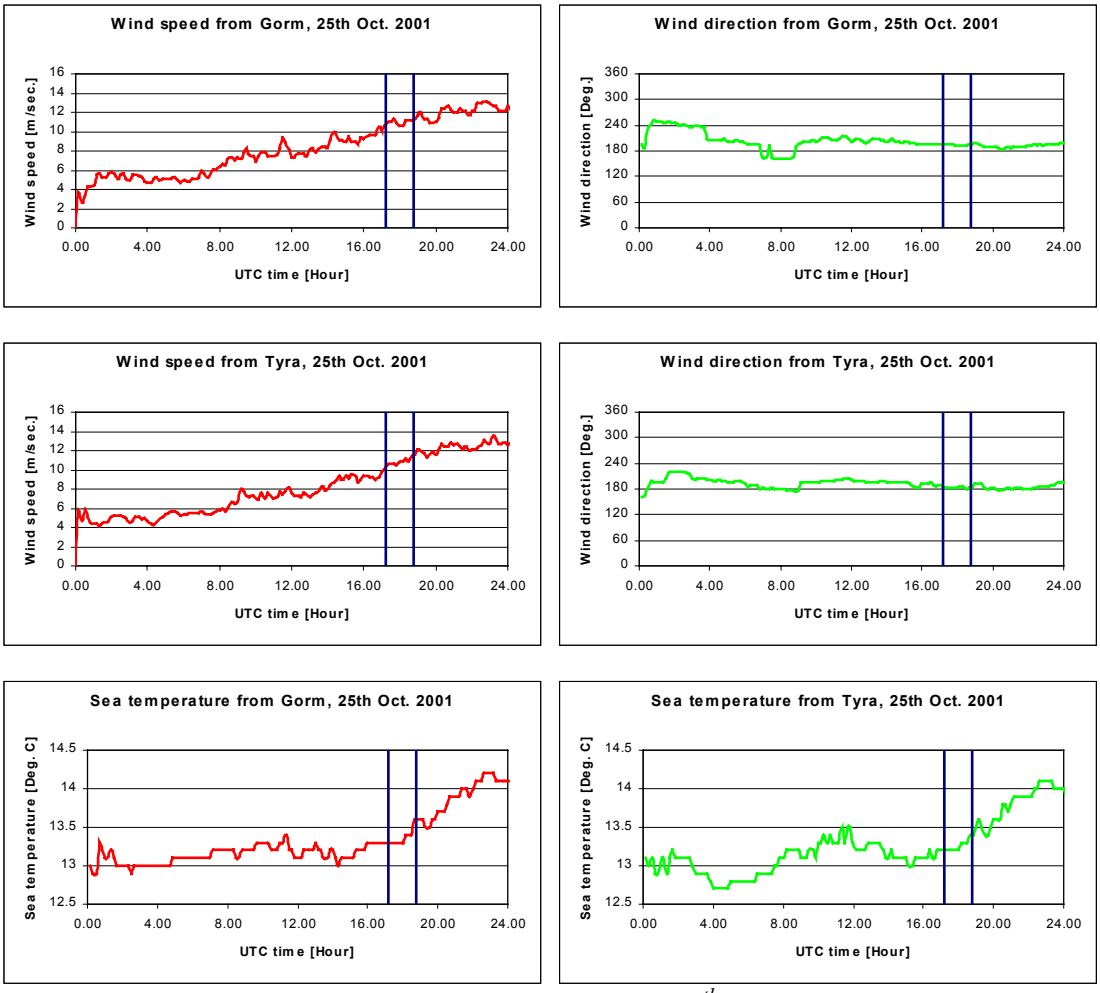

Figure 6.59. Meteorological data for October 25th 2001. Wind speed and wind direction as well as the sea surface temperature is measured at the two oilrigs Gorm and Tyra in the North Sea. The flight took place between the two locations. The blue lines indicate the flight time.

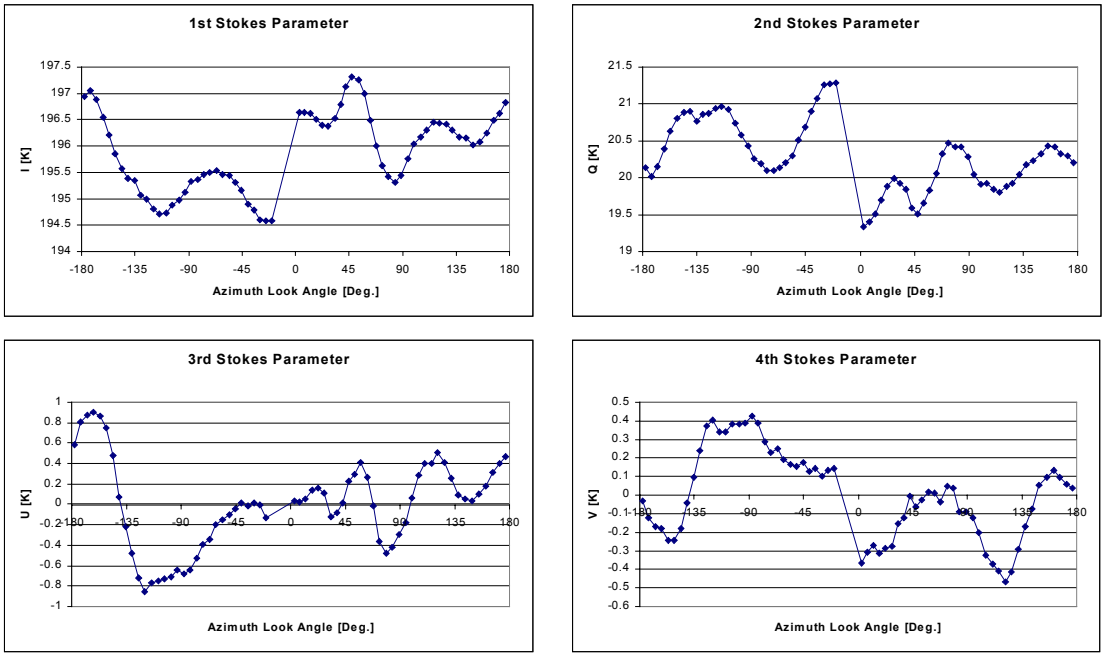

Figure 6.60. The four Stokes parameters from the 1st circle flight track with 29° incidence angle from the October 25th 2001 flight.

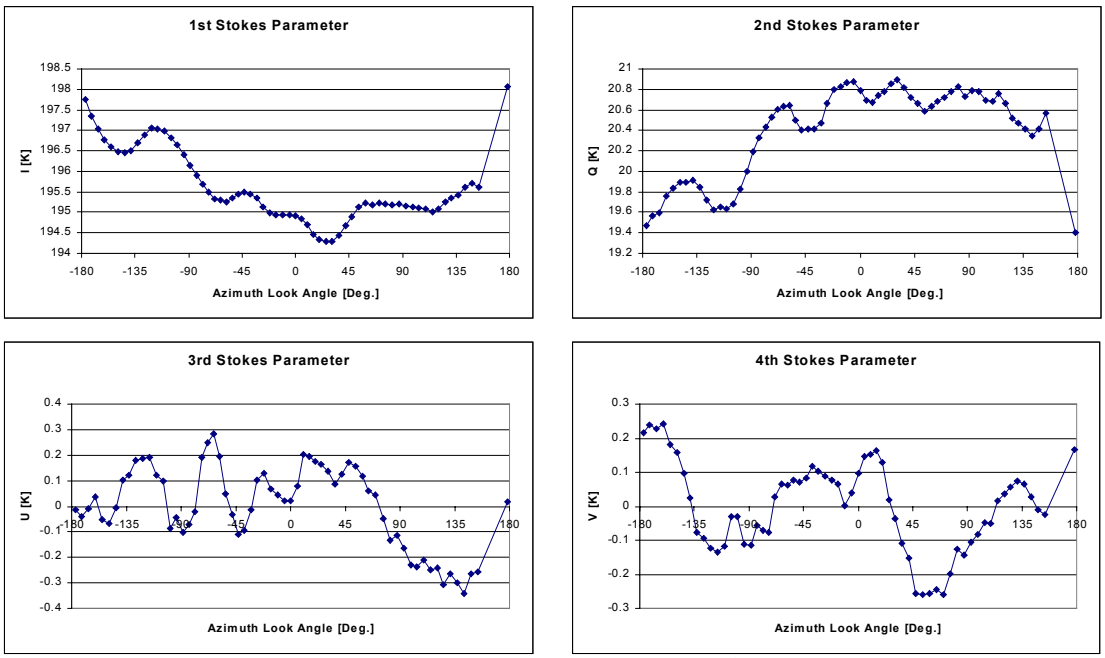

Figure 6.61. The four Stokes parameters from the 2nd circle flight track with 29° incidence angle from the October 25th 2001 flight.

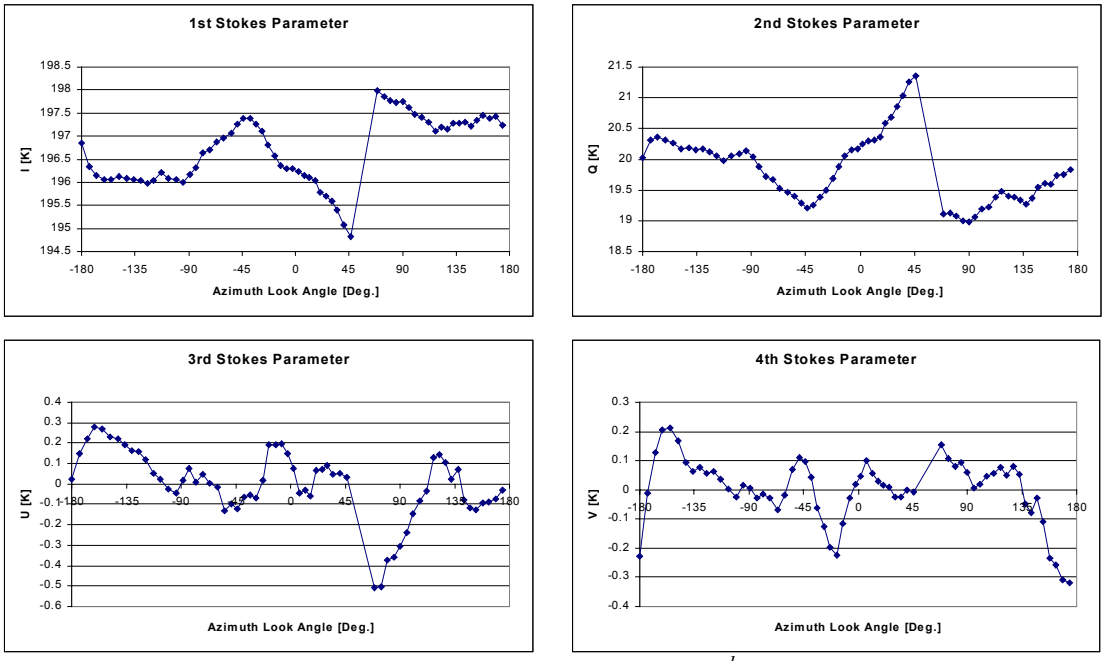

Figure 6.62. The four Stokes parameters from the 3rd circle flight track with 29° incidence angle from the October 25th 2001 flight.

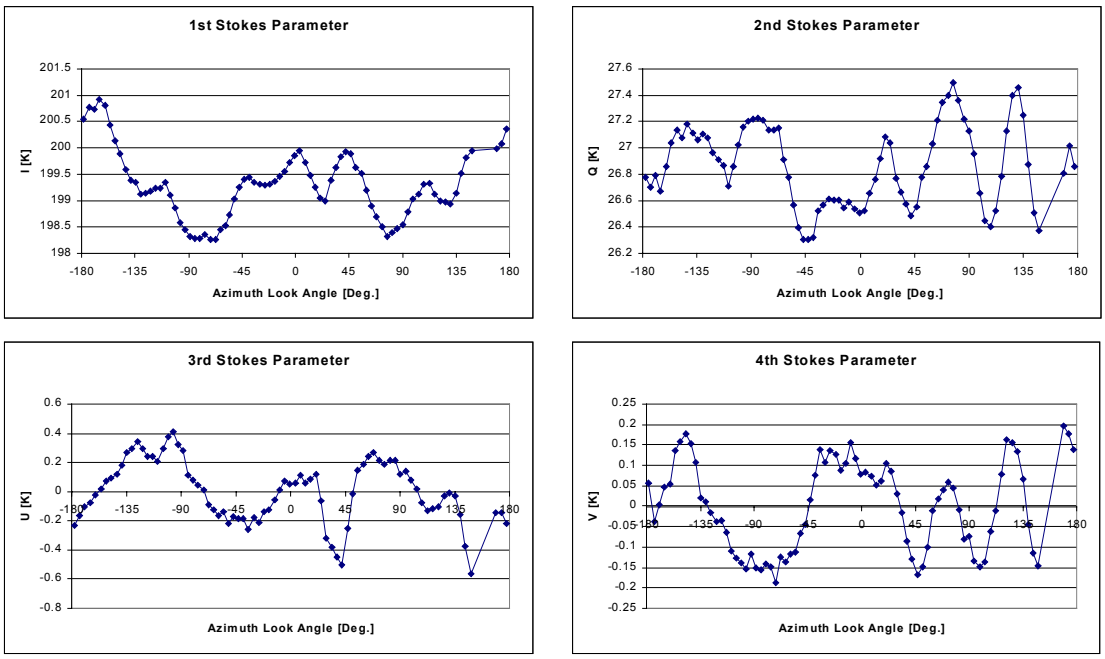

Figure 6.63. The four Stokes parameters from the 1st circle flight track with 35° incidence angle from the October 25th 2001 flight.

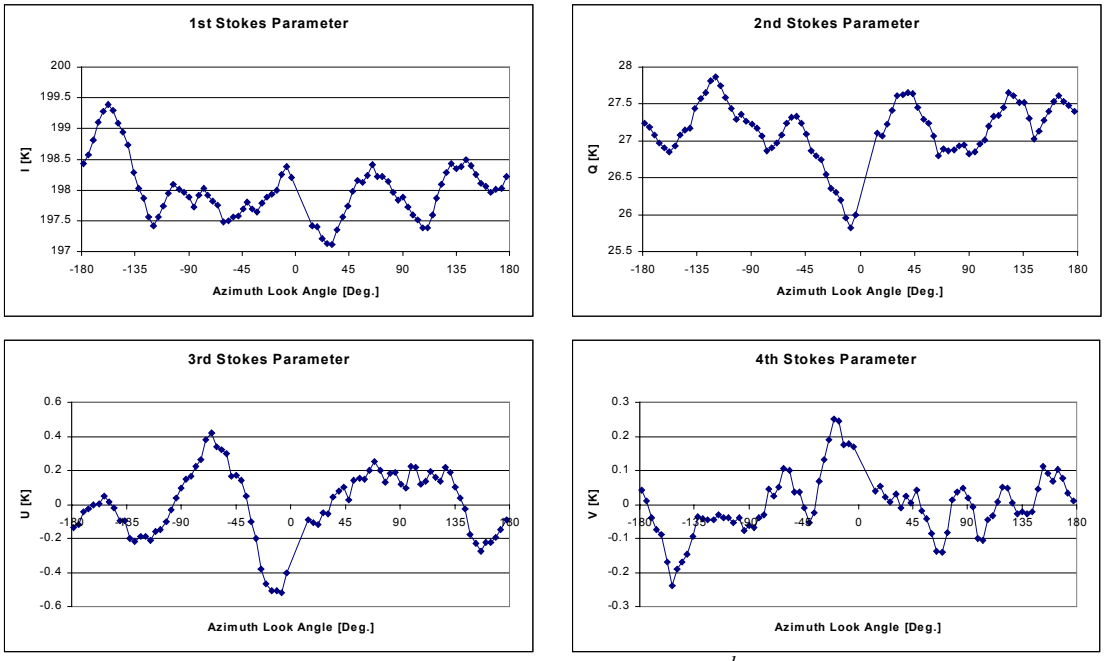

Figure 6.64. The four Stokes parameters from the 2nd circle flight track with 35° incidence angle from the October 25th 2001 flight.

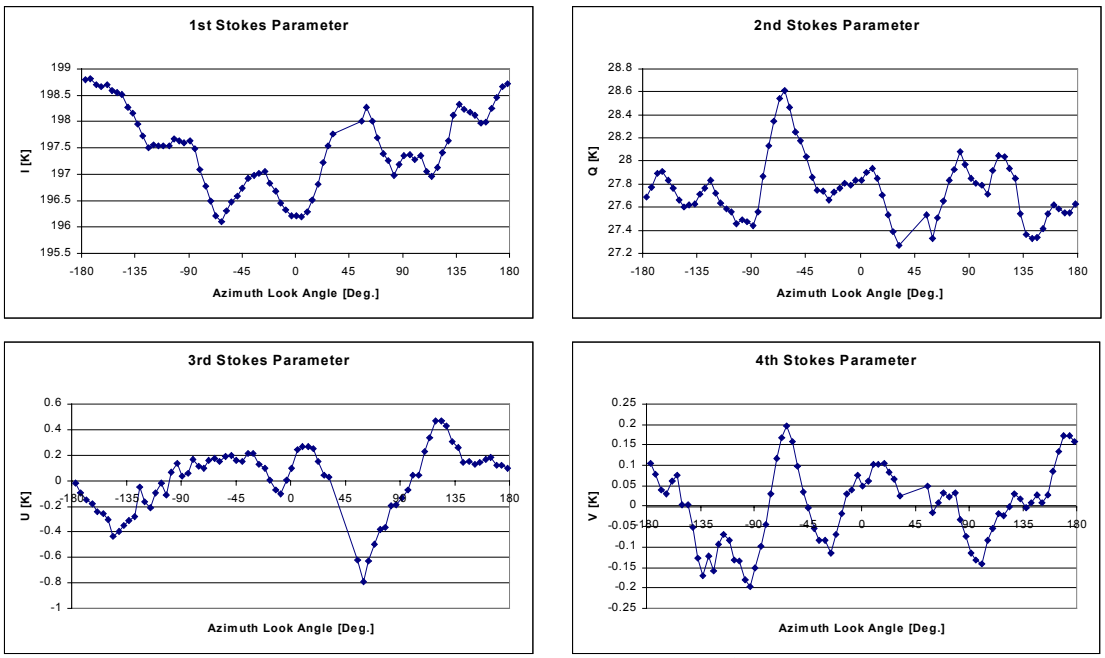

Figure 6.65. The four Stokes parameters from the 3rd circle flight track with 35° incidence angle from the October 25th 2001 flight.

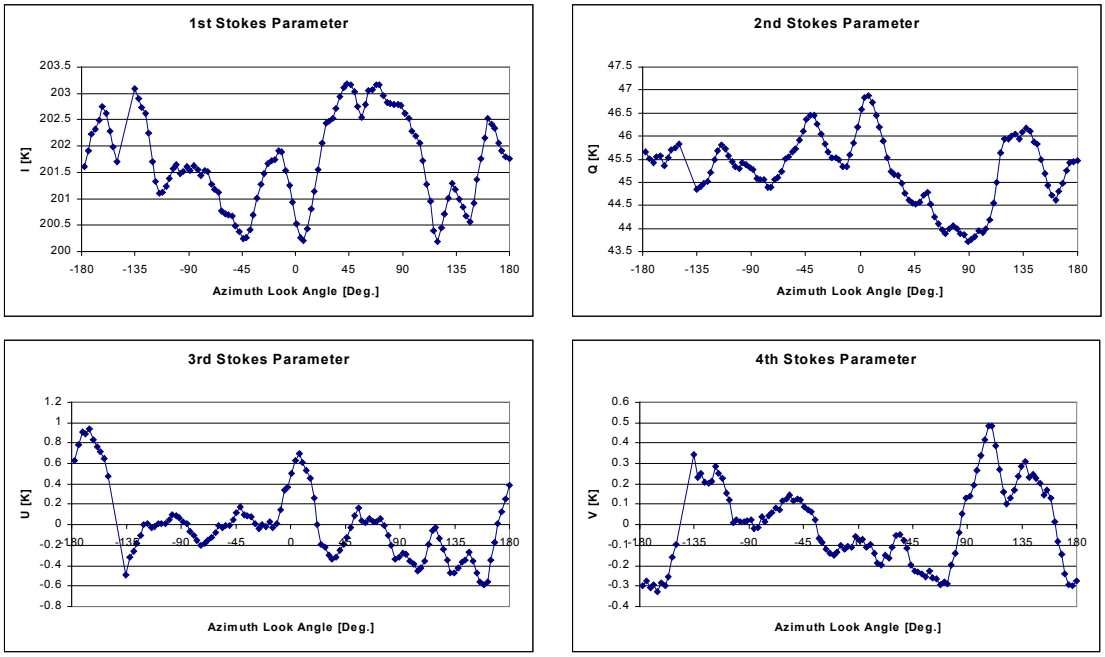

Figure 6.66. The four Stokes parameters from the 1st circle flight track with 45° incidence angle from the October 25th 2001 flight.

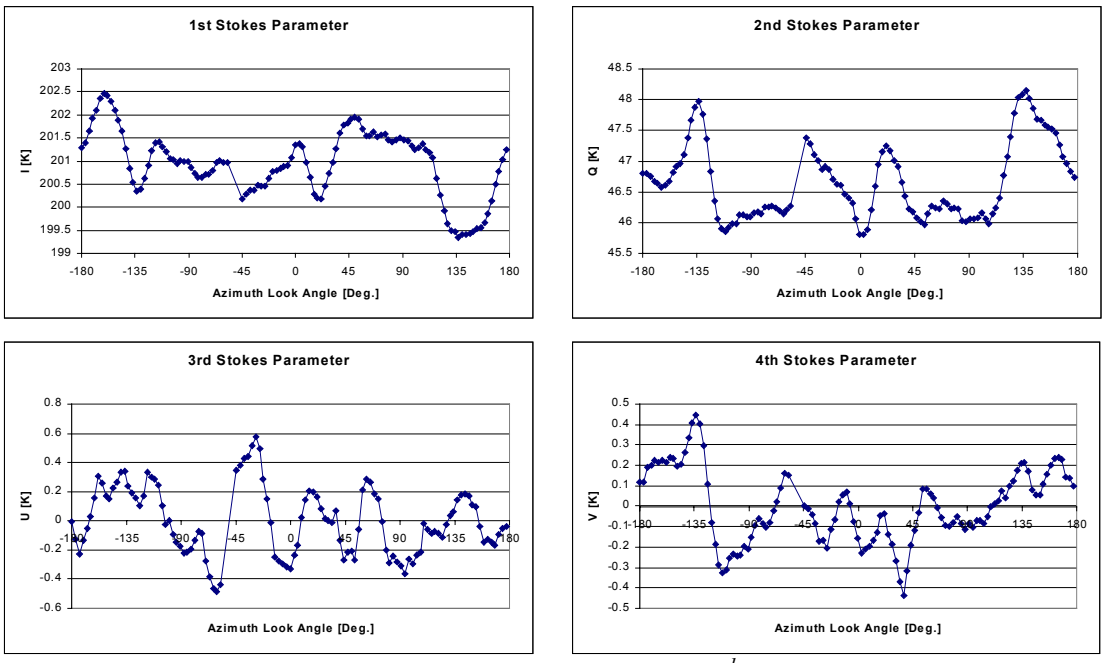

Figure 6.67. The four Stokes parameters from the 2nd circle flight track with 45° incidence angle from the October 25th 2001 flight.

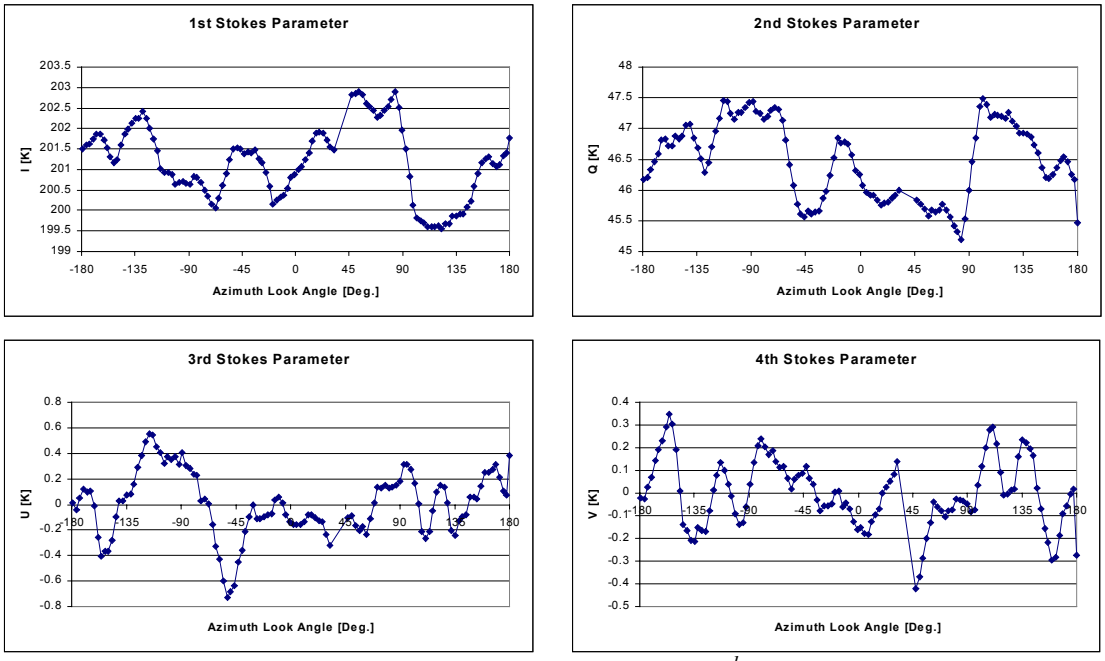

Figure 6.68. The four Stokes parameters from the 3rd circle flight track with 45° incidence angle from the October 25th 2001 flight.

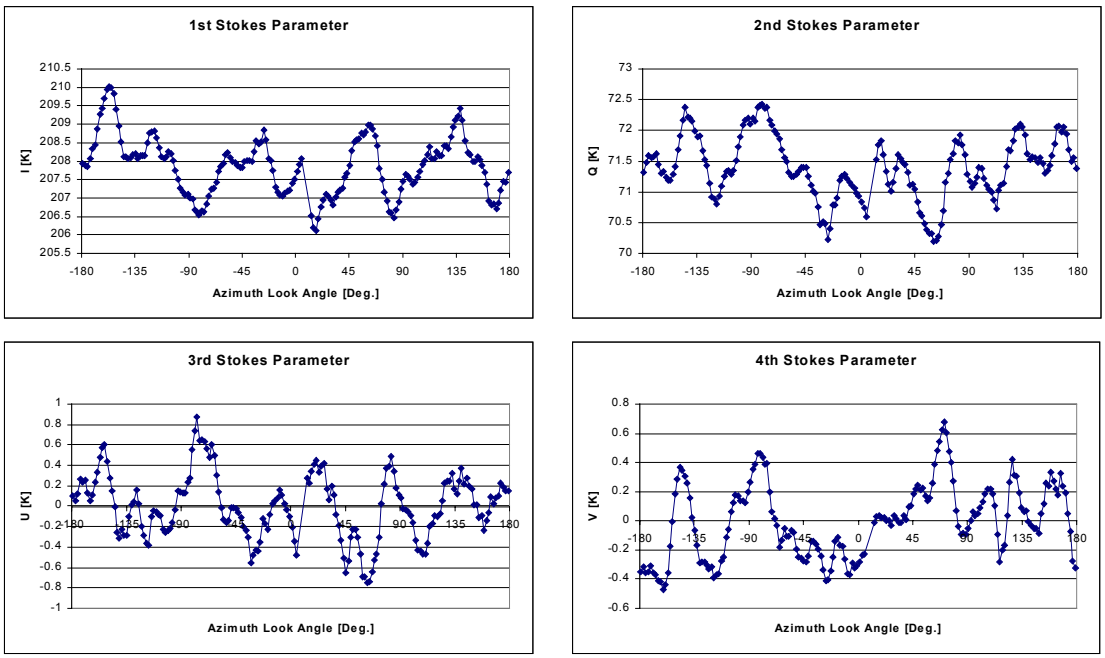

Figure 6.69. The four Stokes parameters from the 1st circle flight track with 55° incidence angle from the October 25th 2001 flight.

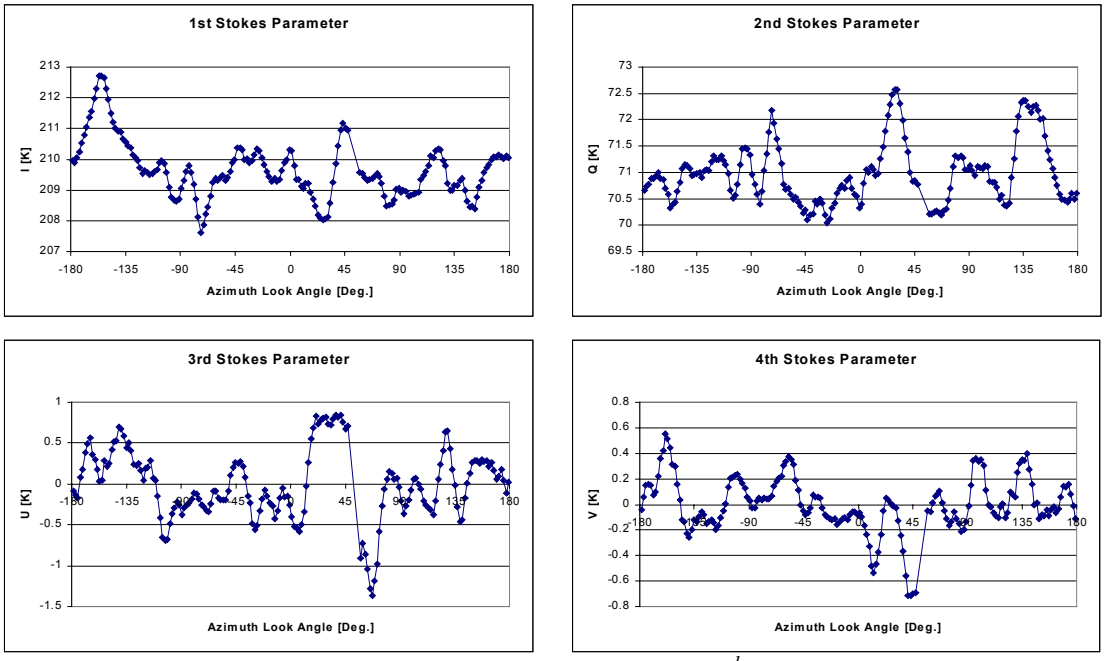

Figure 6.70. The four Stokes parameters from the 2nd circle flight track with 55° incidence angle from the October 25th 2001 flight.

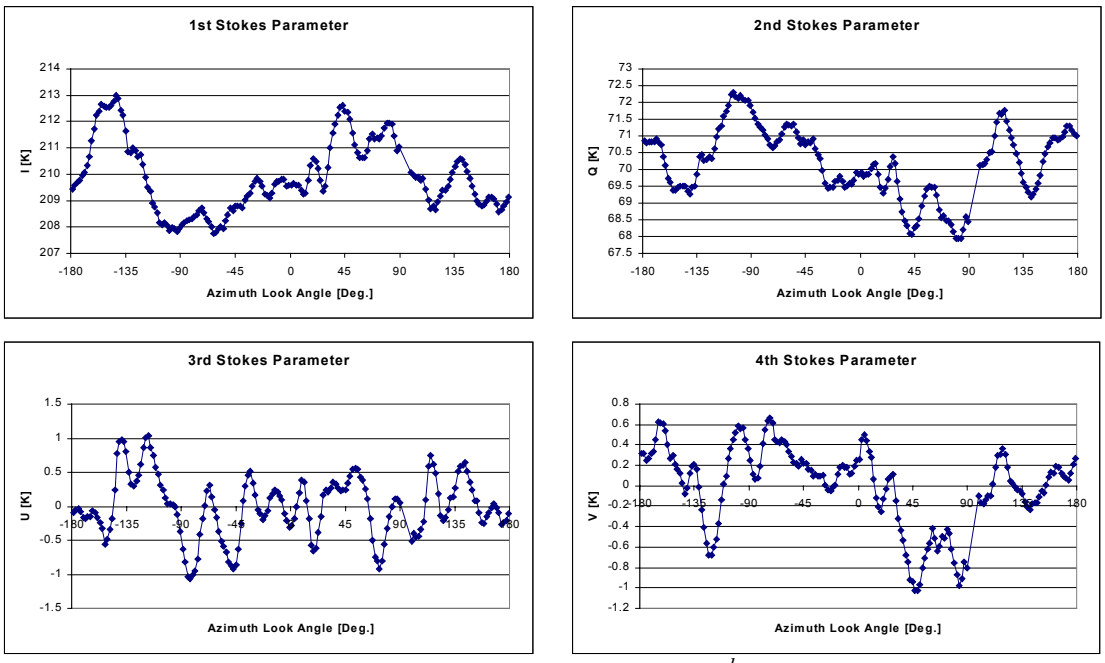

Figure 6.71. The four Stokes parameters from the 3rd circle flight track with 55° incidence angle from the October 25th 2001 flight.

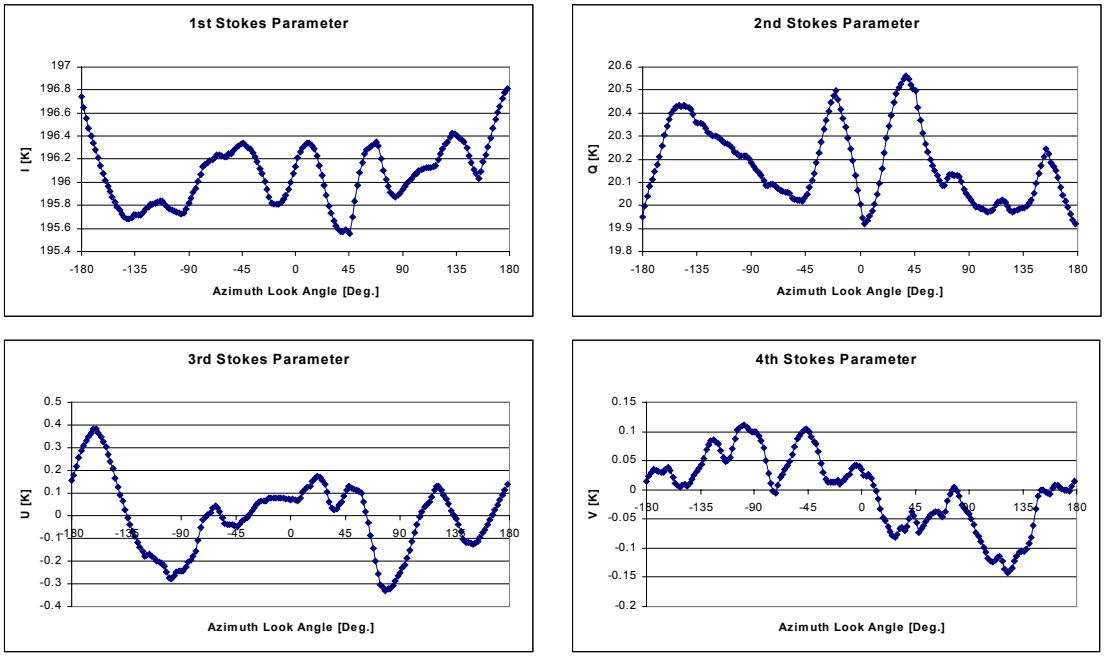

Figure 6.72. The averaged four Stokes parameters from the three circle flight tracks with 29° incidence angle from the October 25th 2001 flight.

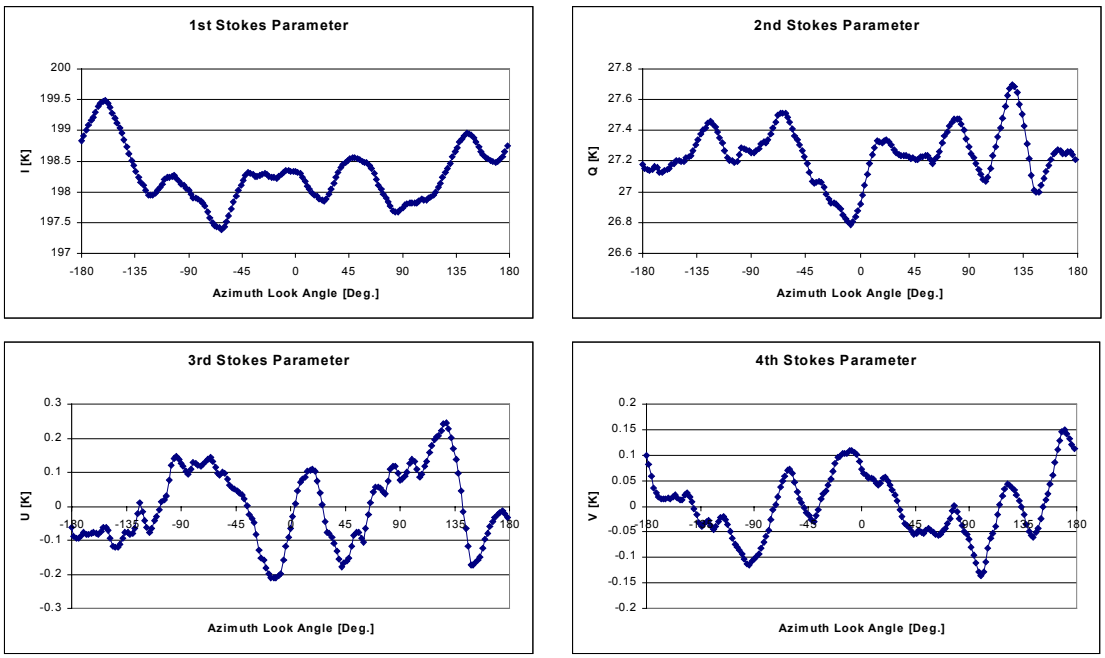

Figure 6.73. The averaged four Stokes parameters from the three circle flight tracks with 35° incidence angle from the October 25th 2001 flight.

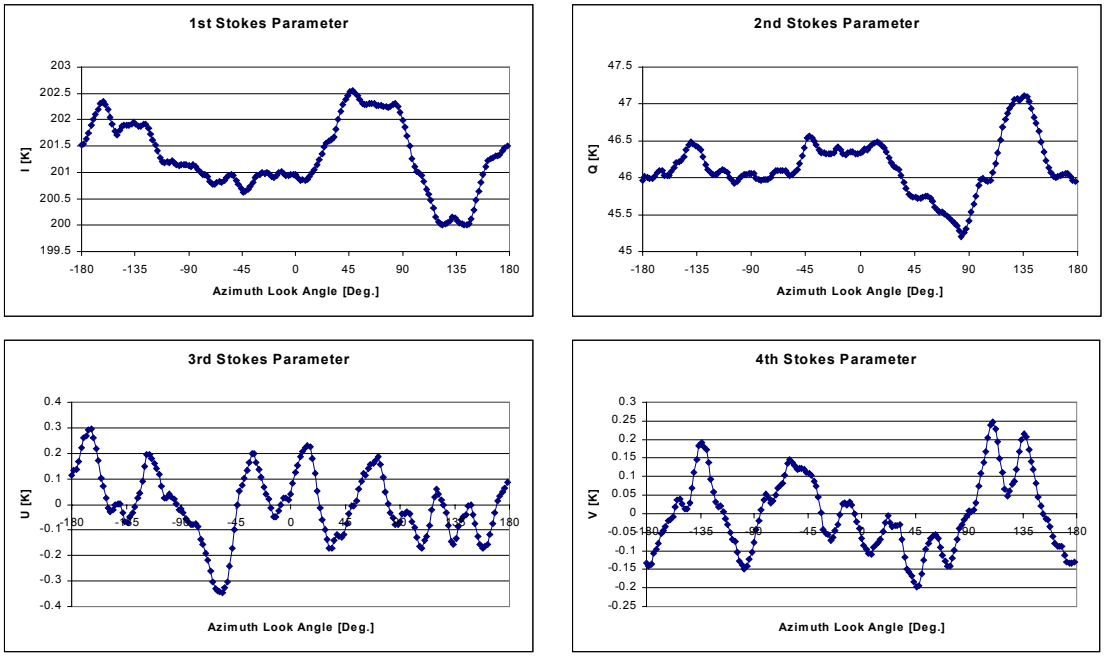

Figure 6.74. The averaged four Stokes parameters from the three circle flight tracks with 45° incidence angle from the October 25th 2001 flight.

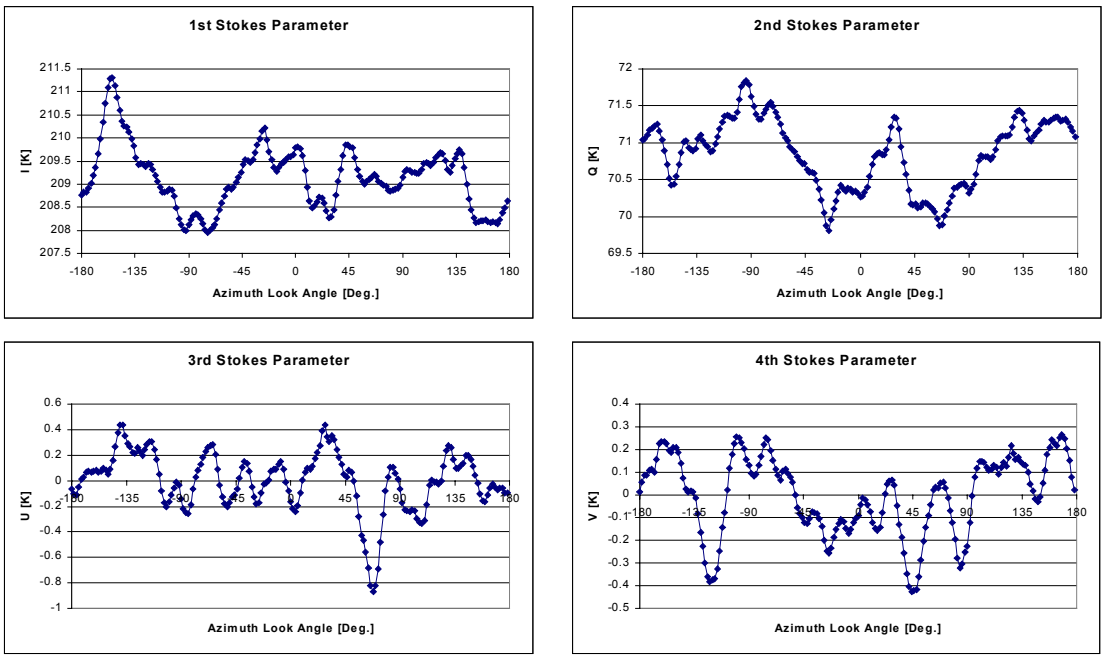

Figure 6.75. The averaged four Stokes parameters from the three circle flight tracks with 55° incidence angle from the October 25th 2001 flight.

Inc.	Harm.	I, Mag.	I, Phase	Q, Mag.	Q, Ph.	U, Mag.	U, Ph.	V, Mag.	V, Ph.
29°	1	0.12	-125.37	0.08	65.64	0.02	-155.76	0.08	86.26
	2	0.22	63.79	0.14	-69.30	0.16	-10.36	0.01	-71.19
	3	0.14	-167.84	0.03	50.82	0.04	119.55	0.02	151.33
	4	0.06	-28.56	0.08	148.65	0.12	-110.76	0.03	57.51
35°	1	0.34	-173.63	0.06	-163.36	0.01	-98.32	0.01	50.00
	2	0.41	-17.99	0.13	-175.15	0.11	149.28	0.07	16.99
	3	0.08	153.26	0.06	-112.80	0.02	-47.49	0.01	140.47
	4	0.11	145.18	0.10	-130.13	0.07	-72.34	0.01	-6.55
45°	1	0.10	-80.69	0.10	129.59	0.01	178.33	0.03	156.80
	2	0.79	-93.47	0.32	50.17	0.09	-52.00	0.07	117.11
	3	0.47	146.21	0.29	-18.28	0.05	58.75	0.06	35.98
	4	0.11	51.12	0.23	-156.67	0.07	43.31	0.08	-140.44
55°	1	0.08	-134.59	0.43	144.84	0.10	111.14	0.12	168.69
	2	0.30	-39.94	0.15	126.51	0.09	-22.34	0.08	93.94
	3	0.67	68.17	0.38	-79.46	0.11	-29.79	0.05	-126.79
	4	0.37	-159.27	0.18	-66.56	0.14	-143.15	0.10	-55.68
35°, 45° and 55°	1	0.15	-101.40	0.04	164.09	0.03	-92.64	0.12	114.38
	2	0.53	-68.90	0.18	92.19	0.03	-47.79	0.07	83.66
	3	0.35	120.79	0.19	-51.17	0.04	-14.54	0.01	36.43
	4	0.20	165.94	0.13	-119.99	0.04	-118.60	0.04	-90.25

Table 6.5. 1st, 2nd, 3rd, and 4th harmonic components in the averaged four Stokes parameters from the circle flights from October 25th 2001.

To provide a larger statistical material, however, and to investigate the influence from the higher flight altitude, i.e. larger spatial integration, an additional data series was acquired during the October 25th 2001 flight. A constant 45° incidence angle was chosen, and circles were flown in the altitude of 1000 m, 2000 m, and 3000 m, acquiring a total of nine additional tracks. These results are shown in the figures 6.76 to 6.84, and the means from each flight altitude are presented in figure 6.85 to figure 6.87.

Table 6.6 shows the square root of the total power (except DC) in the Stokes parameters for the nine tracks, taken in three different altitudes. The power is averaged for each altitude, and as a noise reduction is achieved by track averaging, the power for the averaged track for each altitude is also shown. Comparing the results, it is seen, that no systematic reduction of the noise power is gained when the altitude is changed, and for three of the four Stokes parameters, a small increase is even noticed, when changing from 1000 m to 3000 m. The changes are very small, less than 10 % typically, and as they are not systematic, it is most likely, that they are statistical coincidences. It must thus be concluded for the present configuration, that a change in the flight altitude has very little effect on the noise represented in the data, and that the flight altitude is a minor parameter in the definition of eventual future experiments.

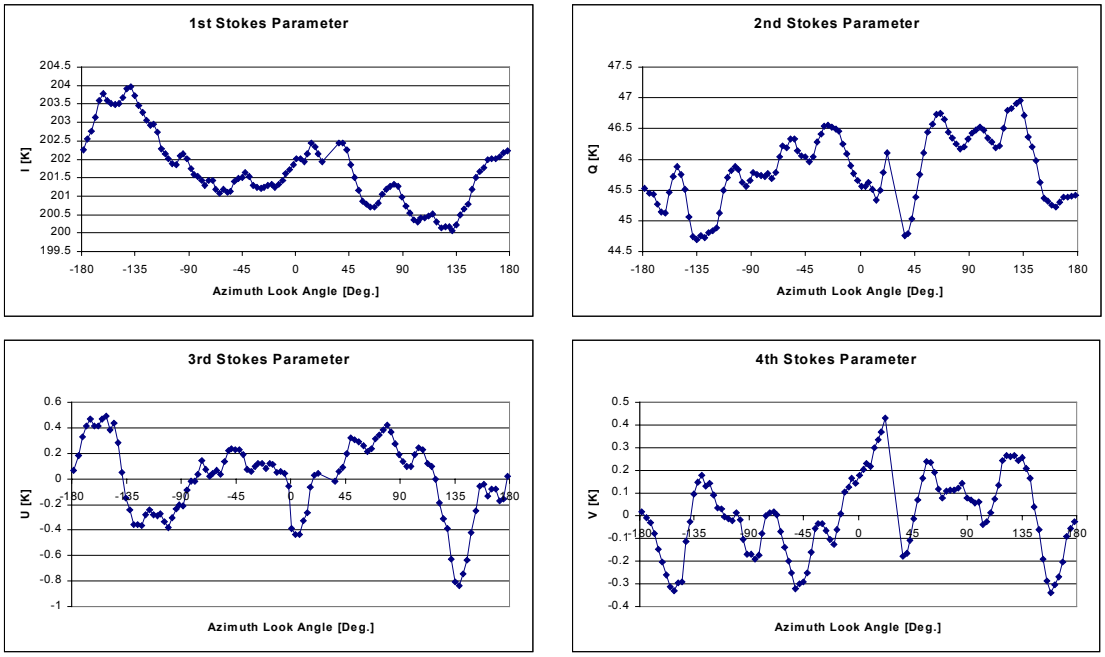

Figure 6.76. The four Stokes parameters from the 1st circle flight track with 45° incidence angle and 1000 m flight altitude from the October 25th 2001 flight.

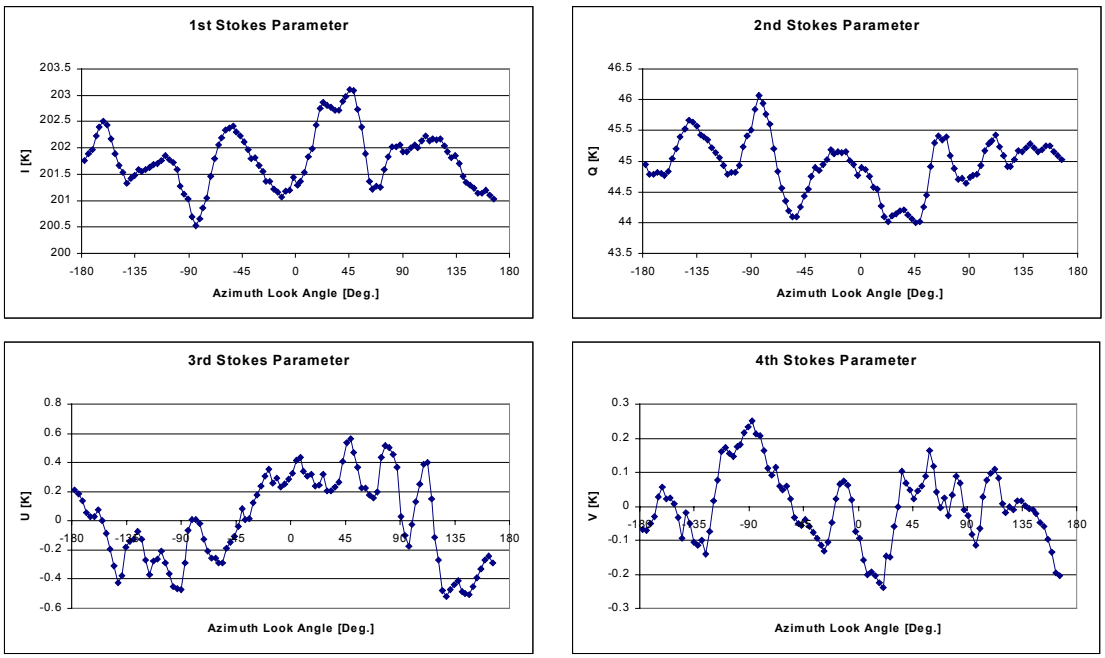

Figure 6.77. The four Stokes parameters from the 2nd circle flight track with 45° incidence angle and 1000 m flight altitude from the October 25th 2001 flight.

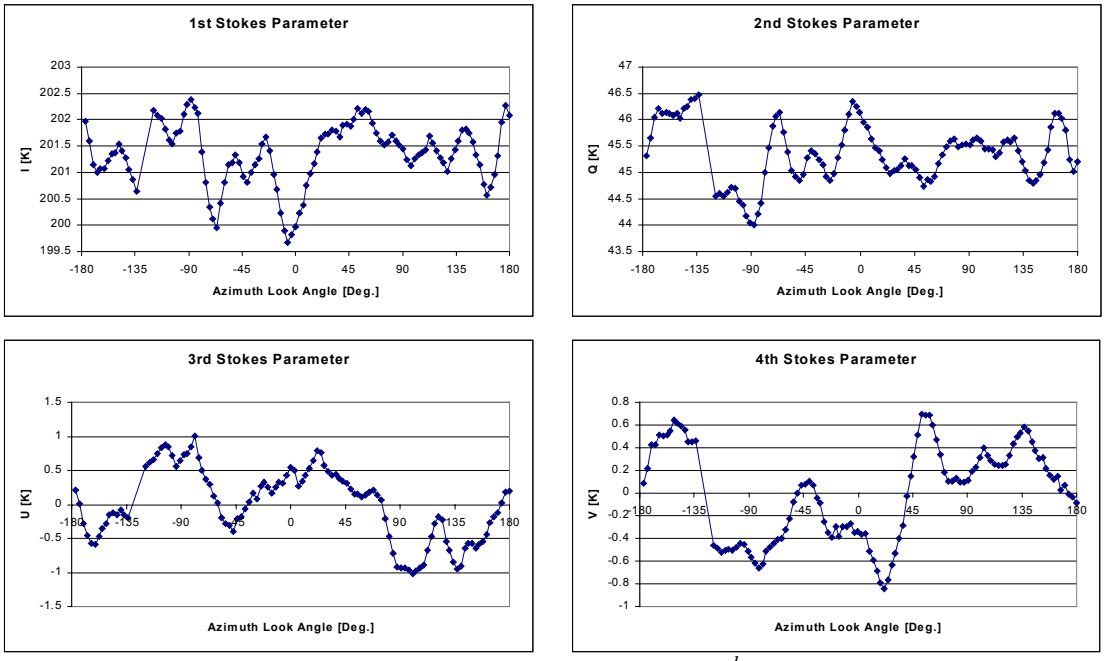

Figure 6.78. The four Stokes parameters from the 3rd circle flight track with 45° incidence angle and 1000 m flight altitude from the October 25th 2001 flight.

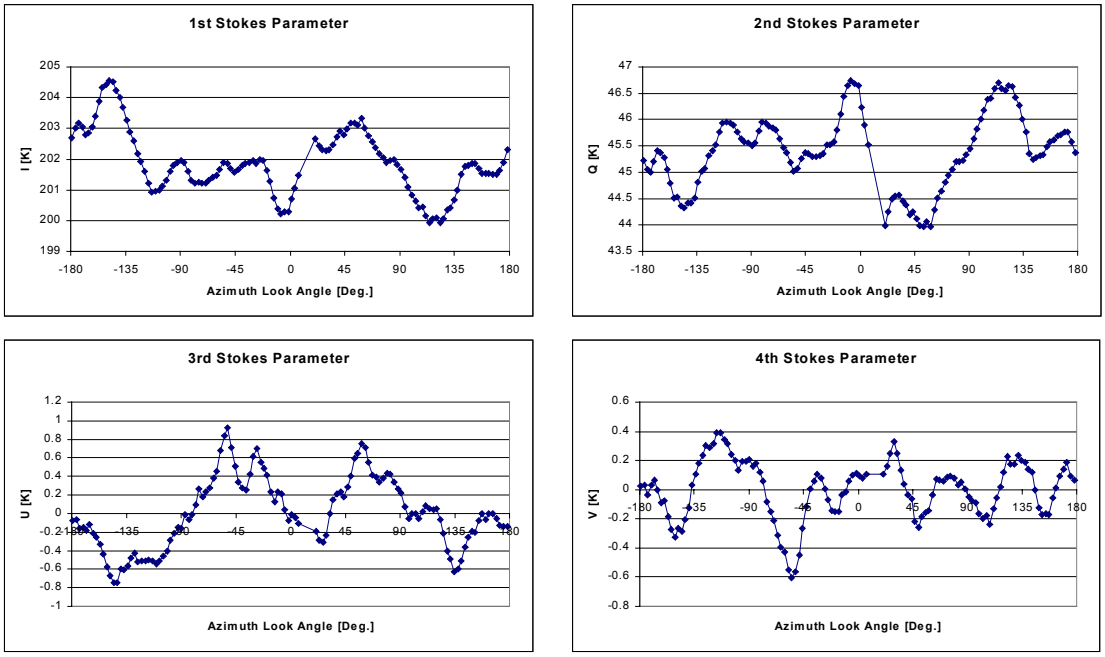

Figure 6.79. The four Stokes parameters from the 1st circle flight track with 45° incidence angle and 2000 m flight altitude from the October 25th 2001 flight.

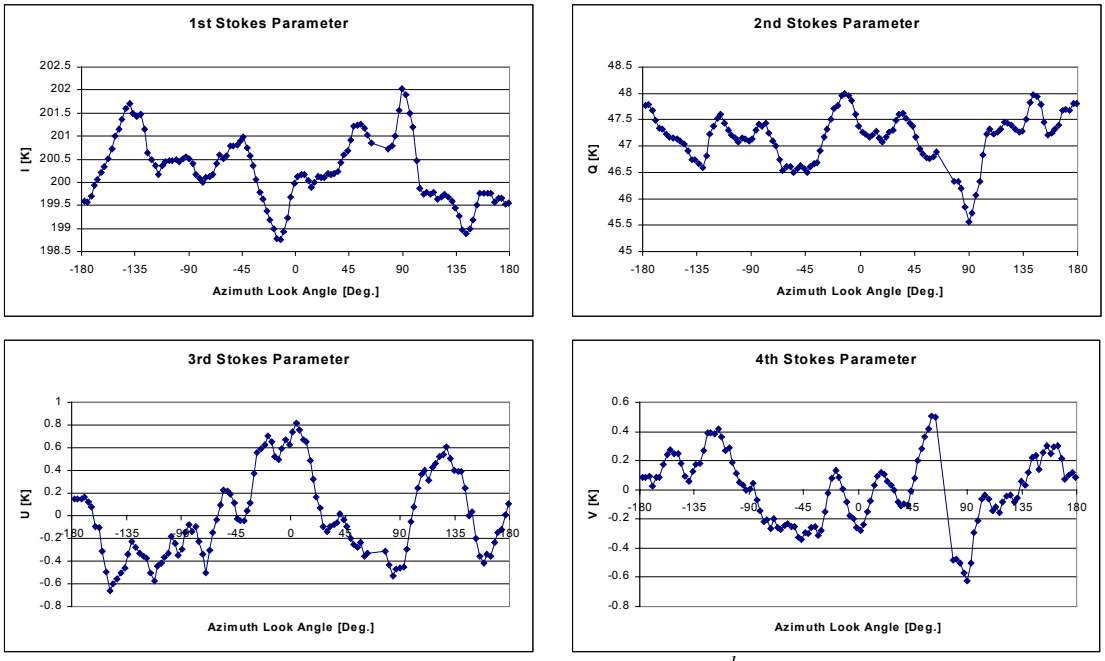

Figure 6.80. The four Stokes parameters from the 2nd circle flight track with 45° incidence angle and 2000 m flight altitude from the October 25th 2001 flight.

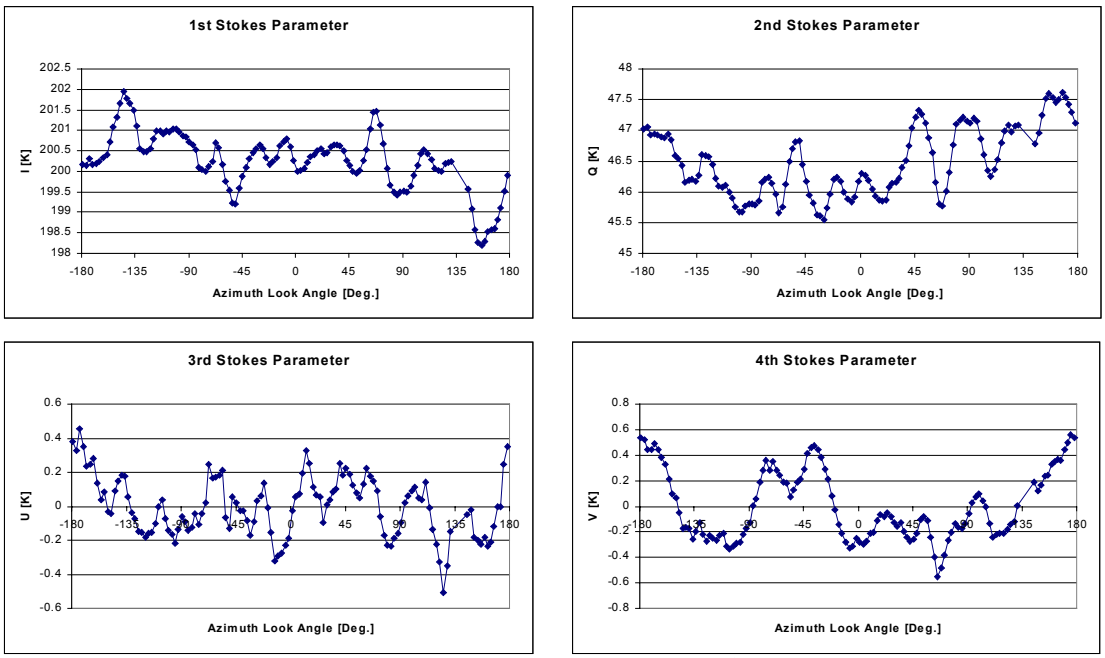

Figure 6.81. The four Stokes parameters from the 3rd circle flight track with 45° incidence angle and 2000 m flight altitude from the October 25th 2001 flight.

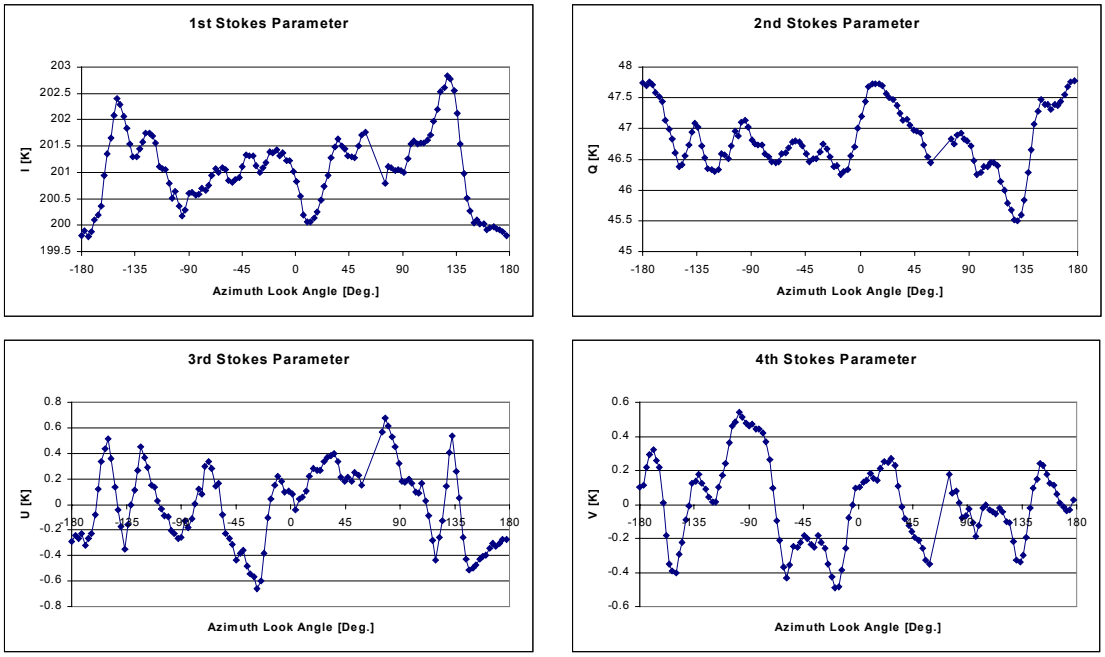

Figure 6.82. The four Stokes parameters from the 1st circle flight track with 45° incidence angle and 3000 m flight altitude from the October 25th 2001 flight.

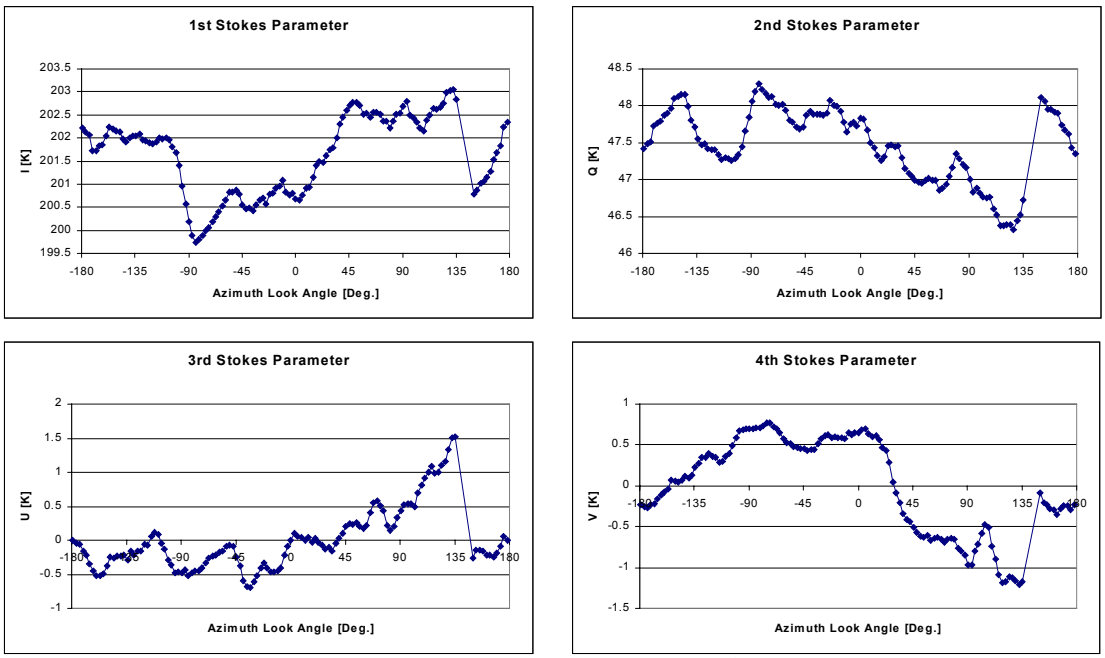

Figure 6.83. The four Stokes parameters from the 2nd circle flight track with 45° incidence angle and 3000 m flight altitude from the October 25th 2001 flight.

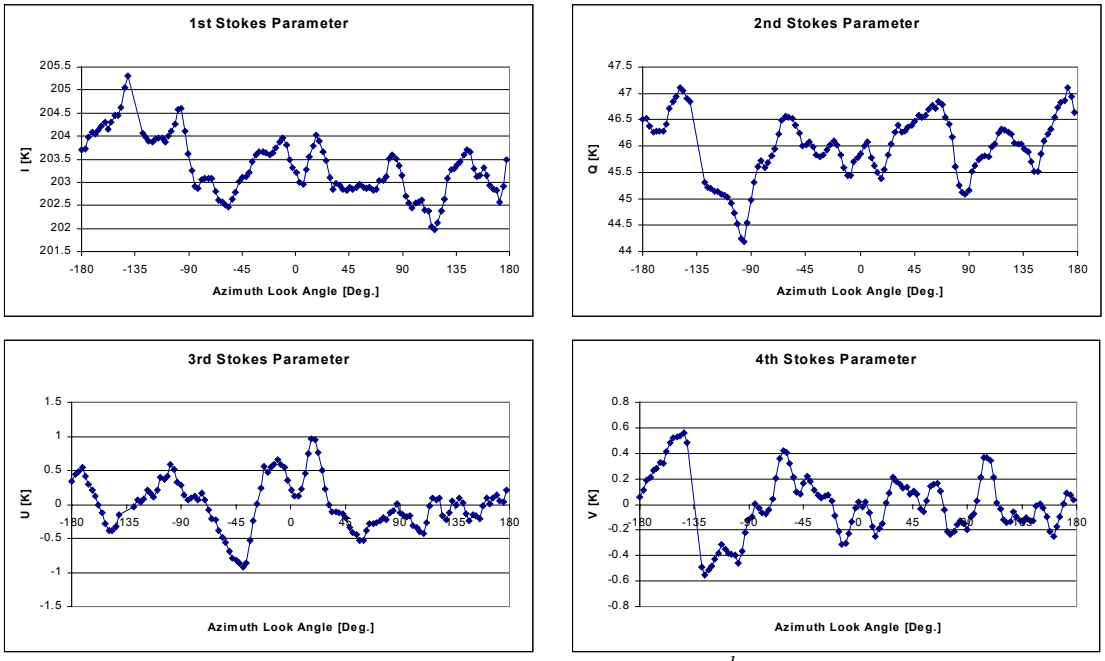

Figure 6.84. The four Stokes parameters from the 3rd circle flight track with 45° incidence angle and 3000 m flight altitude from the October 25th 2001 flight.

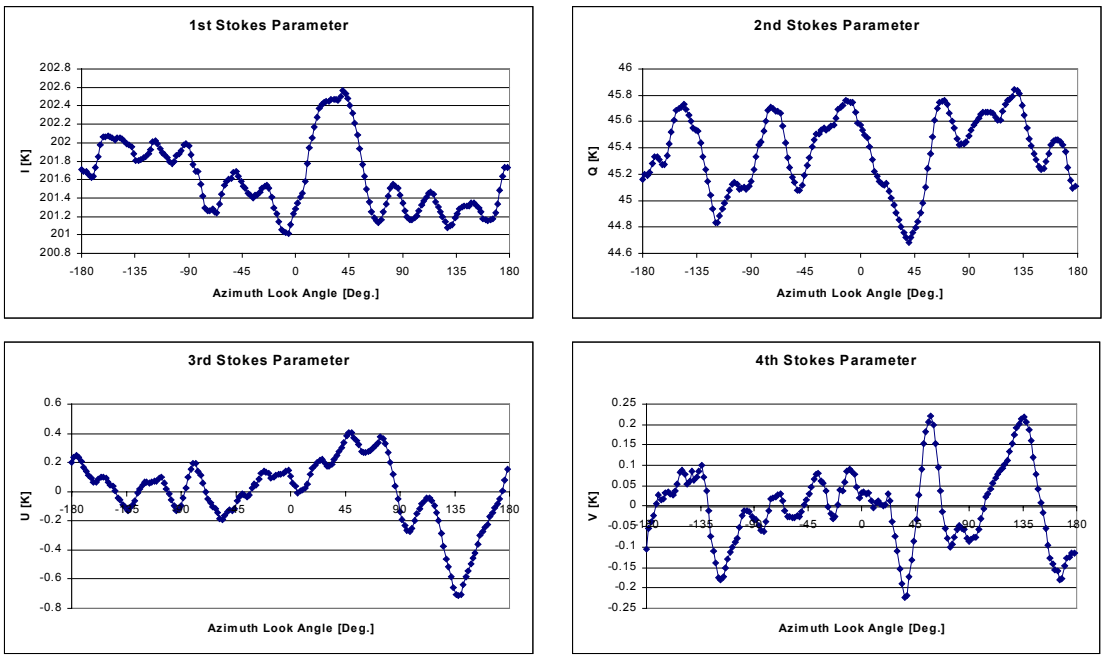

Figure 6.85. The averaged four Stokes parameters from the three circle flight tracks with 45° incidence angle and 1000 m flight altitude from the October 25th 2001 flight.

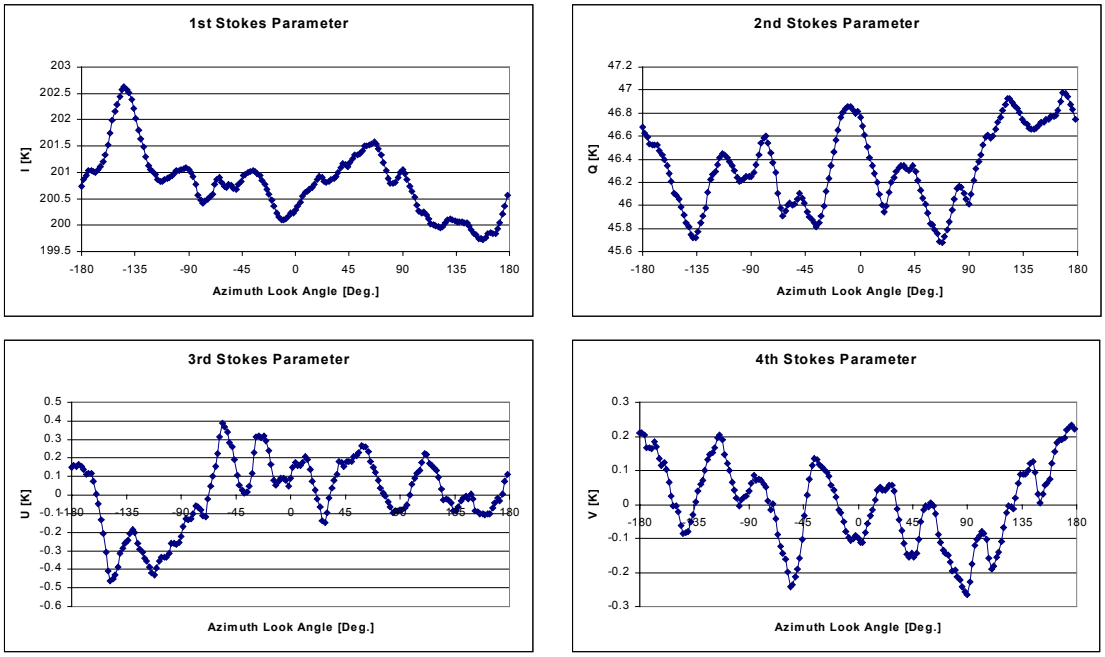

Figure 6.86. The averaged four Stokes parameters from the three circle flight tracks with 45° incidence angle and 2000 m flight altitude from the October 25th 2001 flight.

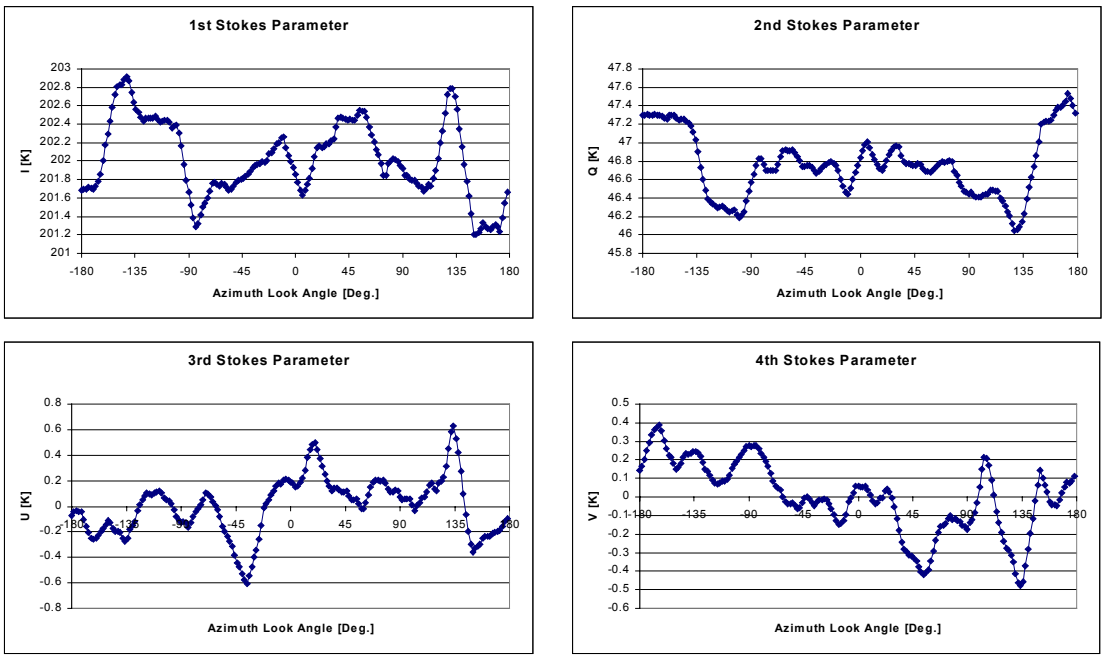

Figure 6.87. The averaged four Stokes parameters from the three circle flight tracks with 45° incidence angle and 3000 m flight altitude from the October 25th 2001 flight.

Circles	I, std.dev.	Q, std.dev.	U, std.dev.	V, std.dev.
1000m altitude 3 single circles	0.958	0.562	0.288	0.177
	0.552	0.455	0.298	0.107
	0.587	0.557	0.522	0.417
1000 m alt., average	0.699	0.525	0.369	0.234
1000 m alt., integrated	0.390	0.282	0.230	0.095
2000m altitude 3 single circles	1.045	0.700	0.384	0.199
	0.707	0.475	0.375	0.236
	0.719	0.552	0.175	0.271
2000 m alt., average	0.824	0.576	0.311	0.235
2000 m alt., integrated	0.617	0.345	0.194	0.121
3000m altitude 3 single circles	0.705	0.521	0.303	0.244
	0.858	0.492	0.462	0.589
	0.630	0.609	0.369	0.241
3000 m alt., average	0.731	0.541	0.378	0.358
3000 m alt., integrated	0.414	0.346	0.224	0.194
All integrated	0.404	0.167	0.123	0.068

Table 6.6. Square root of the total power (except DC) for the full signal in the four Stokes parameters from the nine circle flights with 45° incidence angle from October 25th 2001. The power is presented for single tracks, an average of three values, and the power of the integrated track.

With the very small influence from the changing flight altitude, the nine tracks may be regarded as acquired under equal conditions, and they can be used for a statistical analysis, illustrating the effect of integration. A total of 12 tracks are acquired with a 45° incidence angle, and table 6.7 shows the square root of the power, i.e. the rms. value, in each of the four stokes parameters, when the tracks are processed individually, and when they are averaged. After averaging the tracks three and three, the square root of the power in each of the resulting tracks is evaluated, and again the average power is calculated. Finally all tracks are fully integrated, and the power from the resulting track gives the last line in the table.

The table shows reductions of rms. noise for all Stokes parameters as a result of the averaging. If the data averaged was pure Gaussian distributed random data, the effect of averaging would be a reduction by the square root of N, when N tracks are averaged. In this case the decrease of the rms. noise should be a factor of 1.73 after the first averaging and an additional factor of 2 after the second averaging. For the 2nd Stokes parameter, the reductions are 1.66 and 2.01, respectively, and for the 3rd Stokes parameter, the values are 1.70 and 1.81. The 4th Stokes parameter is improved by a factor of 1.96 from the first averaging and additional 2.67 from the second. Most of these values are near to the expected improvements, with the maximum deviations of 33 % for the 4th Stokes parameter, being reduced too much.

For the 1st Stokes parameter, however, the improvements are poorer, and only a factor of 1.46 is gained by the first averaging, while the second gives 1.31. The conclusion from these results is, that the 2nd, 3rd, and 4th Stokes parameters primarily have a Gaussian nature, and the main part of their AC power is random noise. In the 2nd Stokes parameter, the improvement from second averaging was a factor of 2.01, reached by an rms. noise reduction from 338 mK to 168 mK. If a harmonic with a magnitude of 100 mK is added as a wind

driven signal to the parameter, it would contribute with 70 mK to the total power, and this contribution would not be reduced by the averaging. The reduction would then be (338 mK+70 mK)/(168 mK + 70 mK) = 1.71, which is 15% less than the measured value.

Circles		I, std.dev.	Q, std.dev.	U, std.dev.	V, std.dev.
1000m altitude 3 single circles		0.958	0.562	0.288	0.177
		0.552	0.455	0.298	0.107
		0.587	0.557	0.522	0.417
2000m altitude 6 single circles		0.848	0.734	0.343	0.200
		0.719	0.616	0.232	0.179
		0.875	0.621	0.255	0.150
		1.045	0.700	0.384	0.199
		0.707	0.475	0.375	0.236
		0.719	0.552	0.175	0.271
3000m altitude 3 single circles		0.705	0.521	0.303	0.244
		0.858	0.492	0.462	0.589
		0.630	0.609	0.369	0.241
Average, single		0.767	0.574	0.334	0.251
3 circles integrated	1000 m	0.390	0.282	0.230	0.095
	2000 m	0.674	0.378	0.135	0.102
		0.617	0.345	0.194	0.121
	3000 m	0.414	0.346	0.224	0.194
Average, 3 integrated		0.524	0.338	0.196	0.128
All 12 integrated		0.399	0.168	0.108	0.048

Table 6.7. Total rms. noise for the full signal in the four Stokes parameters from the 12 circle flights with 45° incidence angle from October 25th 2001. The circles are processed as single tracks, averaged as 4 times three circles and averaged totally.

Regarding the 3rd Stokes parameter's averaging from 4 to 1, the total reduction is 1.81, while the square root of 4, equal to 2, would be expected. This would be equal to a non-Gaussian component with a magnitude of 28 mK. For the 1st Stokes parameter the reduced improvements are equal to the presence of a non-Gaussian component with a 353 mK magnitude, while the 2nd and 4th Stokes parameters seem to have non-Gaussian components significant below the level of the noise, and hence significantly below the 150 mK signal present.

A harmonic analysis of the 1st to 4th order components of the data tracks is carried out in table 6.8, following the same integration as in the above example. The pattern from the previous flights is seen again, showing phases pointing to directions covering the full 360° range. The effect of integration is thus again a reduction of the magnitudes, illustrated in the last row. The expected azimuth angles would be $\theta = 170°$ and $\theta = -20°$ for the first two harmonics of the 2nd Stokes parameter, $\theta = -100°$ and $\theta = 70°$ for the 3rd, and $\theta = -110°$ for the 4th. Like in the previous tables, no correlation is observed, and magnitudes are found to be less than 100 mK, except for the 2nd harmonic of the 2nd Stokes parameter.

Altitude	Har.	I, Mag.	I, Phase	Q, Mag.	Q, Ph.	U, Mag.	U, Ph.	V, Mag.	V, Ph.
1000 m	1	0.12	64.15	0.08	-119.57	0.14	6.32	0.02	-80.04
	2	0.39	-80.74	0.17	98.84	0.21	-86.05	0.03	81.91
	3	0.13	-103.02	0.19	69.42	0.12	153.52	0.03	42.95
	4	0.20	-130.80	0.06	-28.19	0.08	6.99	0.05	-153.96
2000 m 1st group	1	0.10	-80.69	0.10	129.59	0.01	178.33	0.03	156.80
	2	0.79	-93.47	0.32	50.17	0.09	-52.00	0.07	117.11
	3	0.47	146.21	0.29	-18.28	0.05	58.75	0.06	35.98
	4	0.11	51.12	0.23	-156.67	0.07	43.31	0.08	-140.44
2000 m 2nd group	1	0.25	88.94	0.18	-146.43	0.17	-38.24	0.10	141.66
	2	0.63	-100.39	0.27	54.38	0.12	55.83	0.07	-2.34
	3	0.37	113.99	0.22	-50.49	0.10	155.79	0.05	-91.27
	4	0.24	-156.76	0.16	1.07	0.03	-99.69	0.04	77.36
2000 m All 6 circ.	1	0.18	-110.31	0.17	141.16	0.06	21.29	0.07	156.17
	2	0.64	-95.14	0.27	62.23	0.07	1.86	0.03	75.34
	3	0.41	132.79	0.21	-12.90	0.03	134.34	0.02	19.45
	4	0.04	179.73	0.09	-177.30	0.05	-6.15	0.04	171.62
3000 m	1	0.02	22.23	0.13	161.71	0.16	-62.12	0.20	118.67
	2	0.33	-99.38	0.32	-12.02	0.07	-123.63	0.05	-59.91
	3	0.23	28.35	0.28	173.55	0.16	-40.30	0.04	76.26
	4	0.30	178.71	0.07	-53.32	0.08	-53.49	0.13	-29.04
All 45° inc. circles	1	0.15	-126.77	0.04	136.75	0.05	-19.59	0.02	138.66
	2	0.49	-99.28	0.17	55.89	0.07	-50.69	0.02	99.54
	3	0.09	119.25	0.05	-10.04	0.02	99.29	0.01	68.76
	4	0.10	-134.28	0.04	-162.68	0.07	-17.36	0.03	-172.01

Table 6.8. 1st, 2nd, 3rd, and 4th harmonic components in the averaged four Stokes parameters from the circle flights from October 25th 2001. The incidence angle is kept constant at 45°, and the flight altitude is varied.

6.8. Discussion

The LOSAC campaign was originally planed to include a 5th flight, giving the opportunity to investigate the effects, observed on October 25th further. As this flight was postponed due to missing availability of the aircraft, conclusions have to be made, based on the existing data and the analysis carried out above.

All data show large peak-to-peak variations, typically in the order of several Kelvin. From a single circle, the identification of polarimetric signatures in the order of 100 mK is hence difficult or impossible. In all circles, narrow peaks are visible, and in some cases the peaks are narrower for larger circles. Point targets at the sea surface are shown to be a possible origin, as the antenna footprint will fly by the target, giving an almost constant fly by time. As the roll angle will determine the angular velocity, a constant fly by time will thus provide objects of varying angular size in the final signature as observed.

Point targets as the described kind can origin from different sources. As a basic for the selected flight pattern, it is assumed, that the ocean surface is homogeneous, and that the antenna footprint can move over the surface without influencing the measured data. If a ship

or another manmade object is present, however, a point target will appear, and data of the received kind will result. As point targets are present in all signatures, however, and as several are observed during a single signature, a large number of targets should be present on the sea surface. As no objects were visually identified in the clear weather conditions October 25th, however, it is unlikely, that all noise peaks origin from manmade objects.

Noise will also be observed, however, if the sea surface is not completely homogeneous. This may result from local changes in the wind field, causing the wind speed and thus the surface signal to fluctuate. The effect was investigated on the October 25th, where a straight track of 40 sec. was flown, resulting in the signature, shown in figure 6.88. As it is seen in the track, some variation in the Stokes parameters is noticed, but at first sight the magnitude of changes is observed to be a factor of 2 to 3 below the variations seen in the circle signatures. Variations have a length of approximately 10 sec., however, and this length is almost similar to the duration of the small peaks in the circular signatures. The length also might be similar to the time constant of the larger waves on the sea surface.

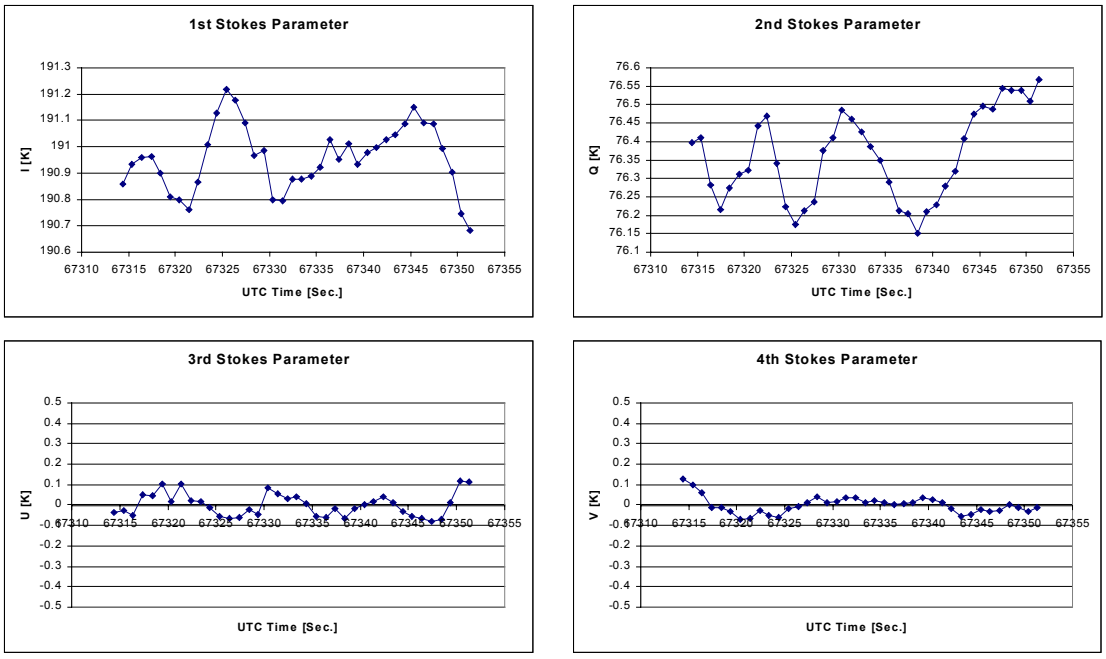

Figure 6.88. The four Stokes parameters from the straight flight track with 50° incidence angle, -38° azimuth look direction, and 2000 m flight altitude from the October 25th 2001 flight.

This might lead to the theory, that the signals in the circular signatures are results of combinations of different effects. A time constant variation of about 0.5 K magnitude, generated by the gravity wave pattern and a point target effect, generating variations, constant in angular space. As shown in table 6.7 and 6.8, a significant reduction of the present signal power can be reached, when signatures are averaged, and for the 2nd, the 3rd, and the 4th Stoke parameters it was shown, that the noise reduction follows the nature of a random Gaussian distributed signal. This supports the wave pattern theory, as the movement of waves would cause a random signal to the antenna, when the footprint turns and moves over the surface.

For the 1st Stokes parameter, I, the reduction of the noise did not fully support a random nature of the signal. The difference from this parameter to the three others may origin from the fact, that I is defined as a sum of two polarizations, while all the others are defined as a difference. Unpolarized point target effects, raising the total incident power, would hence be seen at full magnitude in I, while the signal would cancel partly in the 2nd Stokes parameter and fully in the 3rd and 4th.

Large point targets at far distances (typical RF-sources) reaching an antenna side lobe could be likely sources, as they would be expected to cover a constant angular range, independent from the circle radius and the circle size. Typically manmade sources are polarized, however, and the effect would thus appear in at least one of the other stokes parameters. Natural targets will typically be unpolarized, and one possible source of errors, the sun, was already included in the experiment planing. The sun occupies a mean angle of 0.5337° by 0.5337°, equal to a size of 6.81e-5 sr. With a 15° by 15° antenna beam, the sun with an L-band brightness temperature of the order of $T = 10^5$ K will provide a downwelling radiation equal to about 100 K. The reflection from the sea surface will thus result in a signal larger than 50 K.

As the flights take place after sunset, however, the sun is not a possible source of noise, but other objects on the sky could eventually cause similar effects. The moon occupies an angular space equal to the sun, but as the moon is a cold object, below 300 K, the downwelling radiation will be below 300 mK. The reflected power will thus be in the order of 150 mK, causing a visible effect in the polarimetric signature, but smaller than the observed signal in the 1st Stokes parameter.

Warm objects on the sky at larger distances will typically occupy a very small angular space, but at high concentration, they may contribute to the total background. With specific help from Dr. David M. LeVine, Goddard Space Flight Center, NASA, the background radiation for the total sky was evaluated for one of the 45° incidence angle flights on Octoer 25th 2001, the 2nd circle in the first data set, illustrated in figure 6.67. The curve is presented in figure 6.89

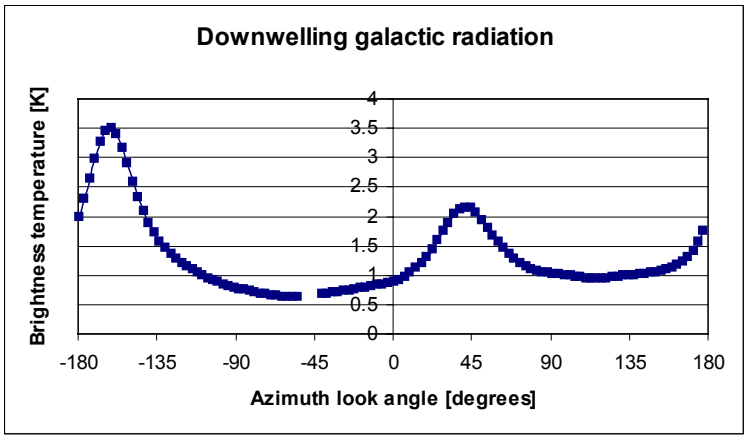

Figure 6.89. Downwelling radiation from the galactic background as a function of the azimuth look angle. The curve corresponds to the galactic constellation at 5:25pm UTC on October 25th 2001, observed from the target area with a 45° incidence angle.

As the radiation is unpolarized, it is assumed equally distributed between the horizontal and the vertical polarization. Corrected for the reflection coefficient at the sea surface, evaluated using the Klein-Swift model, the incident signal to the radiometer resulting from the galactic background can be calculated, and it can be subtracted from the measured horizontal and vertical signals. This is done in figure 6.90, illustrating the signal before (blue curves) and after (purple curves) the correction.

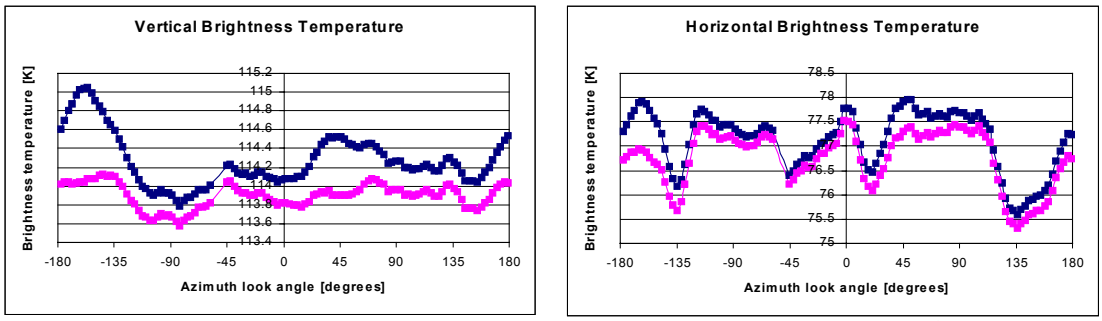

Figure 6.90. Vertical and horizontal brightness temperatures from the 2nd circle track with 45° incidence angle from October 25th 2001. The blue curve shows the measured brightness temperatures, and the purple curve is the result after correction for the downwelling galactic background radiation.

It is observed, that the vertical polarized signal has a very high correlation with the calculated galactic background radiation, and hence a good effect of the correction. The horizontal polarization is noisier and less correlated, but still an effect of the correction is noticed. For comparison it was tried to evaluate the galactic background radiation at an incidence angle of ±0.5° equal to the effect of roll variations over the track. It was seen, however, that the resulting changes were less than 10 mK for the downwelling signal, and thus of the order of 5 mK for the signal incident to the antenna.

The results from the evaluation of the galactic background influence show, that a signal with a magnitude about 0.5 K will result in the vertical and the horizontal channels for the 45° incidence angle. To verify the effect for other incidence angles, Dr. David M. LeVine calculated an additional signature for the galactic background, covering a 35° incidence angle. The signature was used to correct the 2nd circle with 35° incidence angle, acquired October 25th 2001, and the results may be seen in figure 6.91.

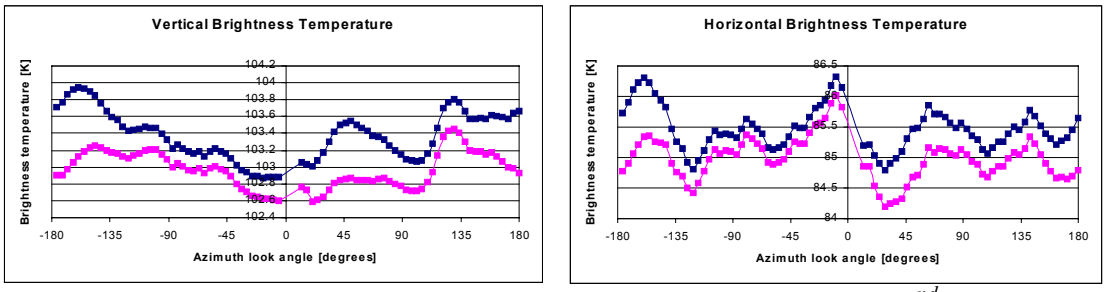

Figure 6.91. Vertical and horizontal brightness temperatures from the 2nd circle track with 35° incidence angle from October 25th 2001. The blue curve shows the measured brightness temperatures, and the purple curve is the result after correction for the downwelling galactic background radiation.

The 35° example confirms the effect, and again it is noticed that the horizontal polarization shows more noise than the vertical. It must be concluded, however, that the correction for the galactic background signal is essential for the interpretation of polarimetric signatures. Signatures, which might be seen as results of the sea surface state, can originate from the background radiation, and as the magnitude is above 500 mK, serious errors can influence measured results, if the source is ignored.

The correction from the 45° incidence angle example is applied to the integrated track, resulting from the averaging of all circles with 45° incidence angle, acquired on October 25th 2001. The track before and after the correction is presented in the figures 6.92 and 6.93, and the effect is clearly seen in the 1st Stokes parameter. The 2nd harmonic effect is significantly reduced, and the total peak-to-peak variation is within 800 mK, if the narrow peak at –165° look angle is ignored. The peak results from the correction, and it may be caused by the constellation change during data acquisition. More than an hour passed from the acquisition of the first circle to the last, and as the constellation is calculated based on the first circle, the Earth rotation may have caused up to 15° angular shift, adding an error of this size to the effect of the correction. It must thus be concluded, that a more thorough analysis of the galactic background has to be carried out in a future scientific project, and that individual corrections should be available for each circle.

The effect of the galactic correction is evaluated in the harmonic analysis in table 6.9, comparing the harmonic components before and after the correction.

All 45° inc. Galaxy Corrected	Har.	I, Mag.	I, Phase	Q, Mag.	Q, Ph.	U, Mag.	U, Ph.	V, Mag.	V, Ph.
	1	0.13	21.44	0.06	173.13	0.05	-19.59	0.02	138.66
	2	0.32	-156.15	0.16	36.74	0.07	-50.69	0.02	99.54
All 45° inc. circles	1	0.15	-126.77	0.04	136.75	0.05	-19.59	0.02	138.66
	2	0.49	-99.28	0.17	55.89	0.07	-50.69	0.02	99.54

Table 6.9. 1st and 2nd harmonic components in the averaged four Stokes parameters from circle flights from October 25th 2001, with constant incidence angle at 45°. Results are shown with and without correction for the downwelling radiation from the galaxy.

It is seen, that the magnitude of the 2nd harmonic of the 1st Stokes parameter is reduced from 490 mK to 320 mK, and a further reduction would be expected if individual galactic background tracks were available for each track. This also applies partly to the 2nd Stokes parameter, which in this correction does not show large changes. It is noticed, however, that the phases change slightly, indicating an effect. The expected wind driven azimuth angles for the 1st and 2nd harmonics would be $\theta = 170°$ and $\theta = -20°$, and resulting errors of 3.1° and 56.7° are found.

As the standard deviations of the 2nd, 3rd, and 4th Stokes parameters show random behavior when averaged, however, it is still likely that a significant fraction of the signal is random, removable with further averaging. As further measurements are not available, It can only be concluded, that an eventual wind driven signature has 1st order harmonic magnitudes below 60 mK, 50 mK, and 20 mK for Q, U and V, respectively, while the 2nd harmonic magnitudes are below 160 mK, 70 mK, and 20 mK.

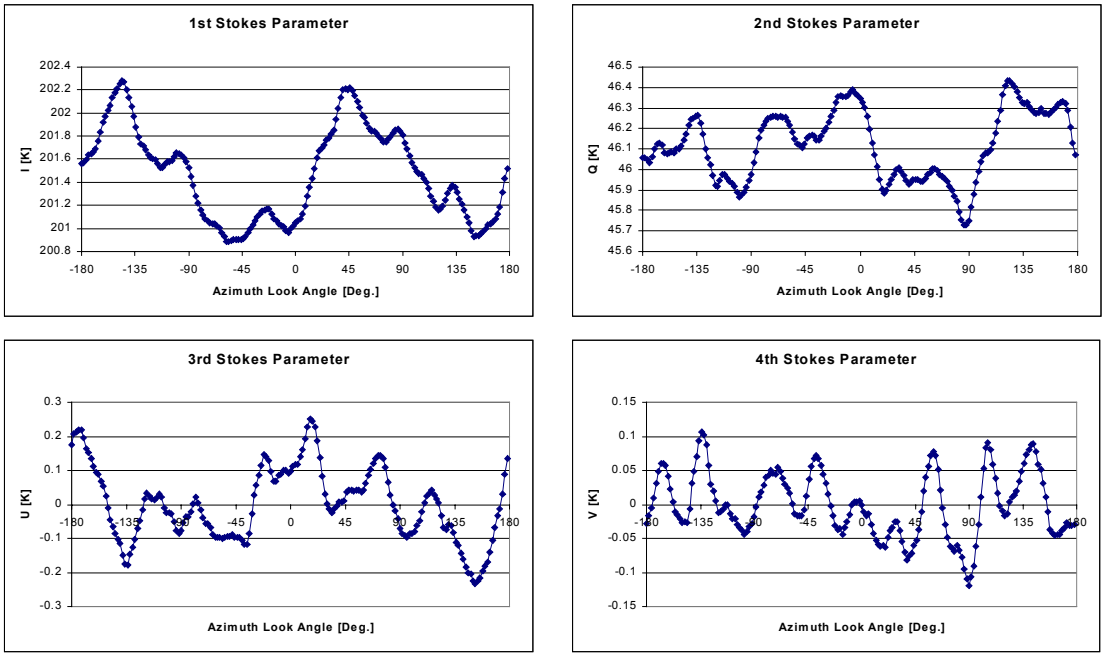

Figure 6.92. The averaged four Stokes parameters from all circle flight tracks with 45° incidence angle from the October 25th 2001 flight.

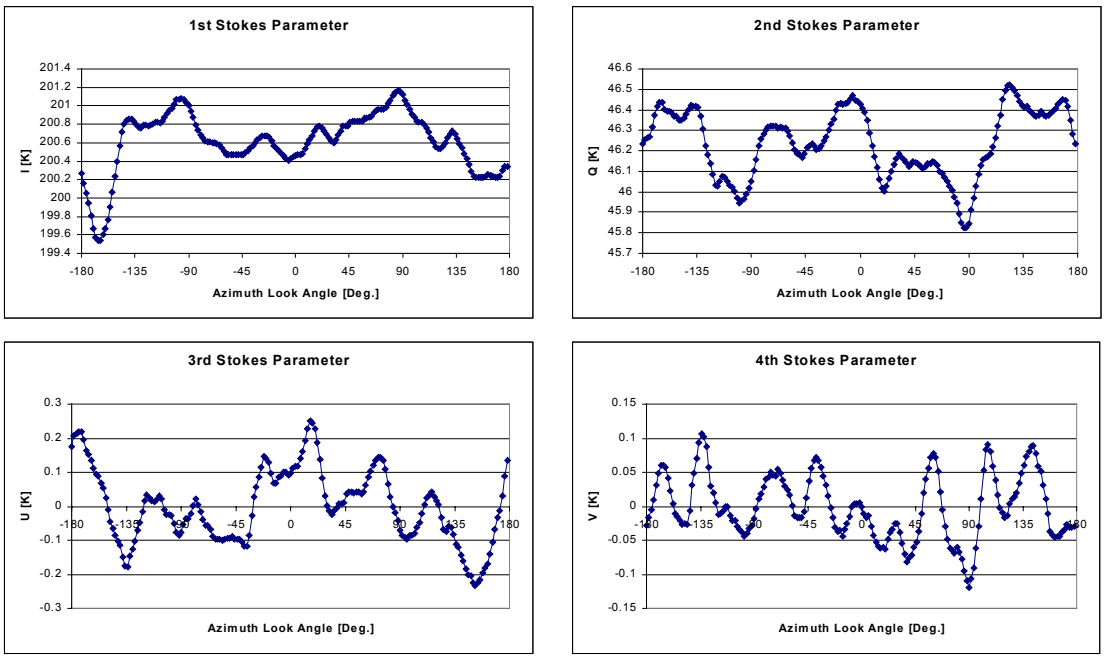

Figure 6.93. The averaged four Stokes parameters from all circle flight tracks with 45° incidence angle from the October 25th 2001 flight. Correction for the downwelling galactic radiation applied.

7. General discussions

This chapter discusses briefly some of the main observations from the work with the new EMIRAD L-band radiometer and its applications. A discussion of the digital radiometer with subharmonic sampling describes some of the advantages and drawbacks in the present implementation, and suggestions for future upgrades are made. For the Avignon experiment the setup is discussed, and eventual improvements for a new campaign are presented. Finally the LOSAC campaign is evaluated, and the chosen circle flight concept is discussed.

7.1. Implementation of polarimetric radiometers

The overall design driver for the implementation of the EMIRAD L-band radiometer was the stability with respect to short-term drifts, addressing for a drift below 100 mK for a 15 minutes period. Different classical polarimetric radiometer types were considered prior to the instrument assembly. All these instruments have a range of well proven advantages and drawbacks, and a parallel polarization combining radiometer as well as a classical correlation radiometer with down-conversion would be suitable implementations.

The technically new digital radiometer with subharmonic sampling was an interesting alternative, however, and with background in a thorough analysis of the possible instrument behavior, this radiometer was selected, although some possible drawbacks were identified. Main concern was pointed to the sampling delay adjustment and to the presence of high-speed digital electronics near the sensitive radiometer front end. Also the limited choice of digital front-end components and the constraints for the RF-filtering were identified as possible problems.

Generally the identified problems turned out to be present as expected, but the RF-filtering and the availability of analog to digital converters turned out to be minor problems, as modern technologies support manufacturing of components with the desired specifications. Especially concerning the converters, where present standard components feature over 2 GHz analog bandwidth and up to 2 GHz sampling rate, e.g. provided by Atmel or Maxim. The relatively high power consumption is still a problem, however, and digital radiometer front-ends with fewer quantization levels is an interesting alternative. [36] describes the implementation of digital correlators with down to one bit, loosing a maximum of $\pi/2$ in the sensitivity, and similar methods are described in [40] and [41] regarding the detection channels. Implementations with fewer bits will generally cause a more significant instrument unlinearity, but as the transfer function can be calculated as demonstrated in chapter 3 corrections can be found and applied – eventually as a part of the digital front-end hardware.

The sampling delay adjustment turned out to be critical, as the 1400 MHz input signal results in a sensitivity of only 2 psec./°. The converters vary typically 20 psec. over the normal operating temperature range, however, and adjustment on mission start as supported by the hardware in the present implementation thus turned out to leave a residual error of typically ±10°. The error will cause a cross coupling between the 3rd and the 4th Stokes parameters, but it can be corrected in the offline processing, when the noise diode signal is present. After this

correction, evaluations of the cross coupling from the beginning to the end of a track end up with typical errors less than 500 mK for the full 280 K noise diode input. The isolation is equal to 27.5 dB, which is satisfactory, but the next generation digital front-end should include an on-line correction as described in [37] and [38].

The stability evaluation of the digital radiometer shows a good performance, staying within the desired specifications. Typical short-term (15 minutes) drifts stay below 100 mK, and this parameter will strongly depend on the instrument implementation. A parallel polarization combining radiometer as well as a classical correlation radiometer might have reached the same level, but due to the necessary thermal isolation of the receiver, the result would have been a larger and heavier instrument. Modern MMIC components will help to decrease the size of an analog receiver, reducing the difference, but modern digital technologies, including application specific integrated circuits, ASICs, will also support smaller and less power consuming implementations of the digital front-end.

The opportunity for implementation of a selective digital filter to suppress RF-interference has not been used in the present radiometer due to the target areas, located far from most manmade noise sources. The potential is a unique feature for the digital radiometer, however, and with the experience from other campaigns [42], this advantage may gain importance in future radiometer constructions.

7.2. The EMIRAD field campaign, Avignon

The Avignon 2001 experiment aimed at traditional measurements of vertical and horizontal polarized signals as well as at full polarimetric measurements of azimuth signatures. The measurements were carried out with the desired precision of ±1 K, which is satisfactory for the soil moisture monitoring, planned by INRA, and also satisfactory for the determination of eventual azimuth signatures.

A major limitation in the experiment is the temporal sampling rate, limited by the work hours of the INRA security staff (Monday to Friday) and by the weather conditions. The mechanical installation was not certified to operate at wind speeds above 25 km/h, and the whole system was not installed in a waterproof encapsulation, being a limitation in wet and rainy weather conditions. In the spring in Avignon, however, rain is extremely rare, and the water protection was a minor problem. The wind is often above the 25 km/h level due to the Mistral wind phenomena, however, and as the wind typically lasts for several days, large sampling lacks occurred.

The wind limitation is a general problem at the Avignon site, and future installations at the present crane facility will have the same limitation. Likewise the security limitations, demanding the presence of technical staff, is unavoidable. An experiment with denser sampling must thus aim at a more stable mechanical installation, and a set up without the potential risks of the crane operation must be selected. Such set ups will loose some of the manoeuvring flexibility of the crane, and advantages and drawbacks should be analysed with respect to the desired campaign.

A future campaign for soil moisture monitoring might aim at uninterrupted data collection, which is not possible in the present system. The digital back end is designed to store all data in a local file, being kept open during all data acquisition, and it demands the physical presence of an operator to control the instrument. A new system should provide floating data output, and an option for remote control would ease the campaign logistics. Both options might be achieved by replacement of the simple instrument operator interface with a small single board computer with Internet access.

7.3. The EMIRAD field campaign, Ocean

The investigation of sea surface polarimetric signatures was based on a number of circle flights, carried out on three different days. Some problems turned out to be present, and especially the random noise content of the polarimetric signatures was a limitation. A future flight may be possible, if the C-130 aircraft will be available, and some considerations should be made, in order to improve the data material.

From the existing experiments it is seen, that typical rms-noise around 100 mK results from integration of 12 circles. As expected wind signatures are in the same order, at least a factor of 1.5 to 2 should be gained, resulting in the demand for 24 to 48 circles with equal incidence angle, target site, and wind conditions. This might be possible, but depending on the desired incidence angle, data acquisition might take from one hour to a full day. With the long data acquisition, a risk for changes in the sea stare rises, resulting in a degradation of the data set.

An alternative approach might be to reduce the sampling of azimuth look directions, focussing on the integration instead. This might be achieved with the flight pattern, shown in figure 7.1, where each track would take approximately two minutes plus the aircraft turning between the tracks.

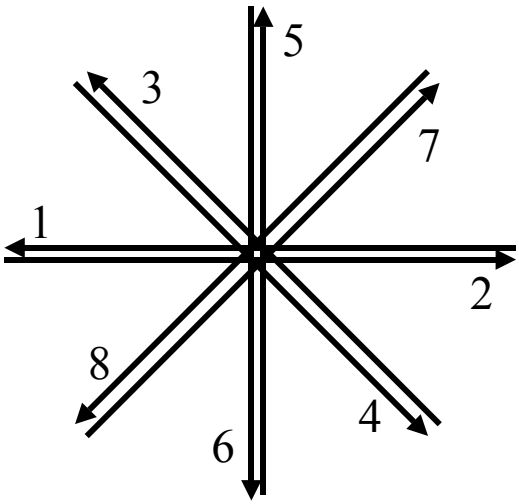

Figure 7.1. Alternative flight track, sampling only eight azimuth look directions, but improving the integration of each point.

With a present azimuth resolution of 2°, the observation time for each data point varies with the roll angle, being in the interval from 160 msec. to 5 sec. Even with the integration of 12

circles, the total observation time is limited to 60 sec. for the highest incidence angle, and for the analyzed 45° incidence angle case, the total observation time per data point was down to 10 sec. The pattern in figure 7.1 would thus give a 12 times improvement of the observation time, potentially reducing the rms-noise to less than 30 mK for a 2 minutes track length. This track length will be about 10 times longer than the observed temporal noise signals, observed on the circle flights, and statistically the calculated rms-noise reduction should result.

A problem of medium-term drifts rise, however, and the importance of receiver stability increases. Establishment of thermal stability before the first data take may be achieved by opening the aircraft door about 30 minutes before the first data take, creating a situation equal to the laboratory stability test, described in chapter 4. Furthermore a calibration sequence equal to the Avignon calibration should be used, giving a number of calibration point along each track. This is not possible in the circle flights, as intermediate calibration will cause loss of data in a range of azimuth look directions. In the straight tracks, however, the information, lost during the calibration, can be regained by an extension of the track. An additional advantage of the straight flight tracks will be the more stable aircraft attitude, decreasing the dependence on the motion compensation, described in section 2.5 and 6.4.

For the future interpretation of L-band data from the sea surface, the influence from the galactic background should be further analyzed. It has been proven, that a single track may contain errors larger than 500 mK, due to the reflected signal from the surface, but the influence is seen to be more obvious in the vertical polarization than in the horizontal polarization. Further analysis of the influence from the galactic background and the nature of the reflections must be done, and the necessary corrections for each of the two channels must be understood. Finally, the corrections must be included in the data processing along with a model of the constellation change during the data acquisition time.

8. Conclusion

This thesis addresses aspects of implementation of polarimetric radiometers and their applications. An L-band radiometer based on novel digital technology is designed and assembled, and field campaigns are carried out in order to cover two major applications of L-band polarimetric radiometry.

Alternative radiometer implementations are discussed, and with background in the development of digital components with still higher performance, a study of a new polarimetric radiometer concept is carried out: the direct digital subharmonic sampling radiometer. Using a minimum of traditional analog front-end components, the radiometric signal is directly sampled by a high-speed analog to digital converter without preceding down conversion. The converter does not digitize the full frequency spectrum from DC to the desired frequency band, however. It samples the radiometer spectrum with a selected lower frequency, which will cause a copy of the pass band to appear at base band, thus sampling and down converting the signal in one process. The mechanism is predicted by simple sampling theory, but it involves some constraints regarding the sampling frequency selection and the sampling synchronization between parallel channels. The full end-to-end performance of the digital radiometer, measuring all four Stokes parameters, is analyzed, and an analysis of potential advantages and drawbacks of the combined sampling and down conversion is done.

The digital radiometer contains two simple amplifier chains with a selective filter, thus leaving all further signal processing to the digital circuitry, and for the first two Stokes parameters digital detection is evaluated. The two last Stokes parameters may likewise be determined digitally, as the complex correlation between the sampled signals will directly lead to the desired output. Alternatively, the signals' sum and difference may be evaluated, followed by a digital detection, equal to the method used in traditional polarization combining radiometers. The digital radiometer hence contains elements from both traditional radiometer types.

Further perspective of digital radiometers is their use in larger synthetic aperture radiometers. This radiometer type is based on correlation measurement between the signals from a large antenna array, and the potential of the digital radiometer is to reduce the analog front-end electronics to a minimum, thus reducing the risk for thermal drifts. Another unique advantage of the digital radiometer is the option of sampling a larger frequency range at L-band than the traditional protected 27 MHz band. Adaptive digital filters, based on on-line frequency analysis of the sampled signals, would be able to remove eventual areas with RF-interference selectively, and a total larger band for observation would be available, opening a potential for better radiometer sensitivity. Alternatively the digital filtering could be used as a protection against unidentified interference in a part of the protected frequency band, e.g. by a digital subdivision of the full band in a range of narrower bands, analyzed and integrated individually.

With background in the instrument analysis it is decided to implement the new EMIRAD L-band instrument as a digital radiometer, and the potential of new technological opportunities is demonstrated. The assembled instrument is evaluated with respect to sensitivity, short-term stability and long-term stability. Concerning the sensitivity, the instrument performs similar to a traditional instrument. With respect to the stability, the digital radiometer, like any radiometer, is depending on thermal stability of the front-end components. The digital radiometer has the advantage, however, that the analog circuitry is reduced, thus easing the stabilization. The analog to digital converter turned out to be a critical component, and with present technology, the converter is rather power consuming, causing a potential risk for thermal instability. The assembled radiometer is evaluated to stay within 0.1 K over 1 hour of operation, when it is operated in a normal laboratory or aircraft environment. The stability is acceptable for the planned applications of the instrument, and further improvement might be reached by a more advanced temperature isolation and control as well as by a change of the analog to digital converter. A reduction of the number of sampled bits could increase the component choice, and the full potential of the digital radiometer would be gained. The present instrument, however, is a successful demonstration of the new concept.

The field experiment in Avignon was a combined instrument evaluation and scientific experiment. For INRA, traditional incidence angle scans were acquired, and for the polarimetric signature analysis, azimuth scans of 180° were performed over a cornfield. The experiment showed large harmonic components in the resulting azimuth signatures for the Stokes parameters, both for bare soil with plowing and sowing structures as well as for the grown corn. The signatures are identified as identical to the wind driven signatures expected from the ocean surface at higher frequencies, and a 1st harmonic as well as a 2nd harmonic is identified in the 2nd and 3rd Stokes parameters. The magnitude of the signatures are proven to be 10 K to 15 K for the newly sowed soil and for the grown crop, and for an airborne sensor, aimed at soil moisture determination, the risk for a systematic error rises.

The LOSAC campaign aimed at determination of polarimetric azimuth signatures on the ocean surface, and the project was part of the ESA preparations for the SMOS mission. For the sea surface salinity determination, knowledge of the influence from eventual other effects must be known to a 100 mK level, and the EMIRAD L-band radiometer was flown in circle patterns over two target areas over the North Sea and Kattegat in order to identify eventual signatures. An analysis of the influence from the aircraft platform motion was carried out for the present antenna configuration, and different methods for motion compensations were tested: a pure regression analysis with linear corrections based on the statistical parameter dependence, a model based correction, based on theoretical models for the parameter dependence, and a model based correction based on the data from large scale variations (±45° roll and ±5° pitch). The methods and combinations of them were evaluated with respect to the total remaining error after the correction and a combination of the large-scale variation model and linear regression was chosen for the further data analysis.

Two flight were carried out at low (3.6 m/sec.) and medium (5.1 m/sec.) wind speed, and no systematic signature could be identified. Typical peak-to-peak noise of several Kelvin were found in the individual signatures, and the azimuth direction for eventual harmonics showed a random nature, while magnitudes of the harmonic components were found to be below 200 mK. Averaging of all circle signatures decreased the magnitude to below 100 mK, but

still no polarimetric signal could be identified. A high wind case was flown (11.0 m/sec.) and additional tracks were added in order to investigate the effect of a larger flight altitude, i.e. a larger antenna footprint. The analysis of these tracks shows absolutely no reduction of the total signal noise, but as the extra tracks could be regarded as identical, a statistical analysis of the effect of averaging was carried out. This analysis shows an almost fully Gassian behavior of the 2^{nd}, 3^{rd}, and 4^{th} Stokes parameters, indicating maximum presence of harmonic components of the order of 30 mK, which is below the radiometer sensitivity. The very limited size of the statistical material gives a 100 % uncertainty, however, and further flights, in a new flight pattern allowing for heavier averaging, have to be carried out to understand the effect nearer.

For the first Stokes parameter a clear 2^{nd} harmonic component of 490 mK was identified. It was proven, however, that the signature could origin from the downwelling radiation from the galaxy and not from the wind driven sea surface pattern. A precise study of this effect has to be carried out for further correction, but initial analyses show a high correlation between the downwelling signal and the observed signature, thus identifying a necessary correction for the SMOS data in order to reach the desired accuracy.

Acronyms

ADC	Analog to digital converter
ASCII	American standard code for information interchange
ASIC	Application specific integrated circuit
BFP	Block floating point data format
C-130	RDAF transport aircraft
DAC	Digital to analog converter
DCRS	Danish Center for Remote Sensing
DFT	Digital Fourier transform
DigInt	Digital processing and integration software package
DMI	Danish Meteorological Institute
DTU	Technical University of Denmark
EGI	Embedded GPS/INU
EMI	Ørsted-DTU, Electromagnetic Systems
EMIRAD	EMI polarimetric radiometer system
ENOB	Effective number of bits
ESA	European Space Agency
FET	Field-effect transistor
FFT	Fast Fourier transform
FIR	Finite impulse response filter
FOV	Field of view
FPGA	Field programmable gate-array
GPS	Global Positioning System
H-pol	Horizontal polarization
hdg.	Aircraft heading
IF	Intermediate frequency
IIR	Infinite impulse response filter
INRA	Institut National de la Recherche Agronomique, France
INU	Inertial navigation unit
JPL	Jet Propulsion Laboratory, USA
Lat.	Latitude
LNA	Low noise amplifier
Long.	Longitude
LOSAC	L-band ocean salinity airborne campaign
LUT	Look-up table

MIRAS	Microwave imaging radiometer with aperture synthesis, ESA
MMIC	Microwave monolithic integrated circuit
NASA	National Aeronautics and Space Administration, USA
OMT	Orthomode transducer
PCB	Printed circuit board
pitch	Aircraft pitch angle
PrPre	Polarimetric preprocessing software package
RDAF	Royal Danish Air Force
RF	Radio frequency
RFI	RF-interference
rms	root-mean-square
roll	Aircraft roll angle
SARad	Synthetic aperture radiometer
SIN	Signal to integrated noise ratio
SMOS	Soil Moisture and Ocean Salinity, ESA mission
SNR	Signal to noise ratio
SSS	Sea surface salinity
SST	Sea surface temperature
trk.	Aircraft track
TUD	Technical University of Denmark
UPC	Universitat Politècnica de Catalunya, Spain
UTC	Universal time coordinate
V-pol	Vertical polarization
VF	Video frequency
WISE	Wind and salinity experiment, ESA and UPC

Bibliography

[1] S. Yueh, R. Kwok, F. Li, S. Nghiem, and W. Wilson, "Polarimetric passive remote sensing of ocean wind vectors", Radio Science, vol. 29, no. 4, pp. 799-814, 1994.

[2] S. Yueh, W. Wilson, F. Li, S. Nghiem, and W. Ricketts, "Polarimetric measurements of sea surface brightness temperatures using an aircraft K-band radiometer", IEEE Transactions on Geoscience and Remote Sensing, vol. 33, no. 1, pp. 85-92, 1995.

[3] S. Yueh, W. Wilson, F. Li, S. Nghiem, and W. Ricketts, "Polarimetric brightness temperatures of sea surface measured with aircraft K- and Ka-Band radiometers", IEEE Transactions on Geoscience and Remote Sensing, vol. 35, no. 5, pp. 1177-1187, 1997.

[4] Niels Skou and Brian Laursen, "Measurement of ocean wind vector by an airborne, imaging polarimetric radiometer", Radio Science, Vol. 33, no. 3, pp. 669-675, 1998.

[5] B. Laursen, S. S. Søbjærg and N. Skou, "Ocean winds measured by an imaging, polarimetric radiometer", pp. 29-37 in "Microwave radiometry and remote sensing of the Earth's surface and atmosphere", VSP, 2000.

[6] Brian Laursen and Niels Skou, "Wind direction over the ocean determined by an airborne, imaging, polarimetric radiometer system", IEEE Transactions on Geoscience and Remote Sensing, vol. 39, no. 7, pp. 1547-1555, 2001.

[7] SMOS95, "Conclusions and recommendations from SMOS", Proceedings of the Consultative Meeting on Soil Moisture and Ocean Salinity: Measurement Requirements and Radiometer Techniques, (ESA wpp-87 ESTEC), 1995.

[8] F. Bayle, J-P. Wigneron, Y. H. Kerr, P. Waldteufel, E. Anterrieu, J-C. Orlhac, A. Chanzy, O. Marloie, M. Bernardini, S.S. Søbjærg, J-C. Calvet, J-M. Goutoule and N. Skou, "Two-dimensional synthetic aperture images over a land surface scene, IEEE Transactions on Geoscience and Remote Sensing, vol. 40, no. 3, pp. 710-714, March 2002.

[9] Y. H. Kerr, "SMOS, Proposal in answer to the Call for Earth Explorer Opportunity Missions", Cesbio, November 1998, available online: http://www.cesbio.ups-tlse.fr/proposal.html.

[10] P. Sivestrin, M. Berger, Y- H. Kerr, J. Font, "ESA's second Earth explorer opportunity mission: The soil moisture and ocean salinity mission – SMOS", IEEE Geoscience and Remote Sensing Newsletter, No. 118, pp. 11-14, March 2001.

[11] Y. H. Kerr, P. Waldteufel, J-P. Wigneron, and J. Font, "The soil moisture and ocean salinity mission: The science objectives of an L-band 2-D interferometer", proceedings of IGARSS'2000, pp. 2969-2971, July 2001.

[12] Y. H. kerr, P. Waldteufel, J-P. Wigneron, J. Font, and M. Berger, "The objectives and rationale of the soil moisture and ocean salinity (SMOS) mission", proceedings of IGARSS'01, pp. 1004-1006, July 2001.

[13] Available online: http://www.cesbio.ups-tlse.fr/images/ramses2.jpg.

[14] D. M. LeVine, "Synthetic aperture radiometer systems", IEEE Transactions on Microwave Theory and Techniques, vol. 47, no. 12, pp. 2228-2236, 1999.

[15] B. Laursen and N. Skou, "Synthetic aperture radiometry evaluated by a 2-channel demonstration model", IEEE Transactions on Geoscience and Remote Sensing, vol. 36, no. 3, pp 822-832, May 1998.

[16] L. A. Klein and C. T. Swift, "An improved model for the dielectric constant of sea water at microwave frequencies", IEEE Transactions on Antennas and propagation, vol. AP-25, no. 1, January 1977, pp. 104-111.

[17] S. Yueh, "Modeling of wind direction signals in polarimetric sea surface brightness temperatures", IEEE Transactions on Geoscience and Remote Sensing", vol. 35, no. 6, pp. 1400-1418, 1997.

[18] J-P. Wigneron, T. Schmugge, A. Chanzy, J-C. Calvet, and Y. Kerr, "Use of passive microwave remote sensing to monitor soil moisture", Agronomie, vol. 18, pp. 27-43, 1998.

[19] J-P. Wigneron, A. Chanzy, J-C. Calvet, and N. Bruguier, "A simple algorithm to retrieve soil moisture and vegetation biomass using passive microwave measurements over crop fields", Remote Sensing of Environment, vol. 51, pp. 331-341, 1995.

[20] J. M. Lopez-Sanchez, A. Camps, M. Vall-llossera, N. Duffo, A. Martinez, "Polarimetric emissivity of vegetation-covered soils: Simulation results", proceedings of IGARSS'01, pp. 2439-2441, July 2001.

[21] F. Ulaby, R. Moore, and A. Fung, "Microwave remote sensing. Active and passive", vol. 1, "Fundamentals and radiometry", Addison-Wesley Publishing Company, 1981.

[22] J. D. Kraus, "Radio Astronomy", 2nd edition, Cygnus-Quasar Books, 1986.

[23] N. Skou, "Microwave radiometer systems: design and analysis", Artech House, Inc., 1989.

[24] A. Camps, J. Font, J. Etcheto, A. Weill, V. Caselles, I. Corbella, M. Vall-llossera, F. Torres, N. Duffo, R. Villarine, L. Enrique, J. Miraanda, A. Julia, C. Gabarró, J. Boutin, R. Niclós, P. Wursteisen, M. Berger, M. Martín-Neira, "L-band sea surface emissivity radiometric observations under high winds: preliminary results of the wind and salinity experiment WISE-2001.

[25] Y. H. Kerr, P. Waldteufel, J. Font, and N. Skou, "SMOS campaign requirements", Cesbio, October 2000, online: http://www.cesbio.ups-tlse.fr/pdf/campaign.pdf.

[26] C. S. Ruf, "Constraints on the polarization purity of a Stokes microwave radiometer", Radio Science, vol. 33, no. 6, pp. 1617-1639, 1998.

[27] C. Ruf, "polarimetric radiometry – coherent vs. incoherent detection", proceedings of IGARSS'98, pp 2181-2183, 1998.

[28] A. J. Gasiewski, "Calibration and applications of polarization-correlating radiometers", IEEE Transactions on Microwave Theory and Techniques, vol. 41, no. 5, pp. 767-773, may 1993.

[29] "Prime item development specification for the embedded GPS/INS (EGI) H-764", DS34200300 Rev. F, Part I, Honeywell Inc. Military avionics division, 1995.

[30] L. Brøndum and J. D. Monrad, "Statistik I + II", Den private ingeniørfond, 1996.

[31] N. Skou, B. Laursen, and S. S. Søbjærg, "Polarimetric radiometer configurations: potential accuracy and sensitivity", IEEE Transactions on Geoscience and Remote Sensing, vol. 37, no. 5, pp. 2165-2171, 1999.

[32] H. Baker, "Analog & digital signal processing", Wiley, 1990.

[33] J. H. Jørgensen, "Digital demodulator for wide bandwidth SAR", proceedings of IGARSS'2000, pp. 2269-2271, July 2000.

[34] J. Dall and E. L. Christensen, "Multiplier-free filters for wideband SAR", proceedings of IGARSS'01, pp. 1568-1570.

[35] P. Beckmann, "Elements of applied probability theory", Harcourt, Brace & World, Inc. 1967.

[36] A. Thompson, J. Moran, and G. Swenson, "Interferometry and synthesis in radio astronomy", Krieger Publishing Company, 2nd edition, 1991.

[37] J. Dall and S. S. Søbjærg, "Synchronization of tandem A/D converter for SAR", proceedings of EuSAR 2002, pp 323-326.

[38] S. S. Søbjærg and E. L. Christensen, "2 GHz Self-aligning Tandem A/D Converter for SAR", proceedings of IGARSS'01, pp. 2028-2030, July 2001.

[39] A. V. Oppenheim and R. W. Schafer, "Digital signal processing", Prentice-Hall, 1975.

[40] M. A. Fischman and A. W. England, "An L-band direct-sampling digital radiometer: Design and performance evaluation", proceedings of IGARSS'99, pp. 237-239, June 1999.

[41] M. A. Fischman and A. W. England, "Sensitivity of a 1.4 GHz direct-sampling digital radiometer", IEEE Transactions on Geoscience and Remote Sensing, vol. 37, pp. 2172-2180, September 1999.

[42] A. Camps, I. Corbella, M. Vall-Ilossera, R. Villarino, L. Enrique, J. Font, A. Kulia, C. Gabarró, J. Etchetto, J. Boutin, A. Weill, F. Torres, N. Duffo, R. Niclós, V. Caselles, P. Wursteisen, M. Martín-Neira, "Sea surface emissivity observations at L-band: First preliminary results of the wind and salinity experiment WISE-2000", proceedings of IGARSS'01, pp. 1371-1373, July 2001.

2 GHz Self-aligning Tandem A/D Converter for SAR

STEN SCHMIDL SØBJÆRG and

ERIK LINTZ CHRISTENSEN

Ørsted-DTU, Electromagnetic Systems, Building 348

Technical University of Denmark

DK 2800 Lyngby, Denmark

This conference paper is published in the Proceedings of IGARSS'01, vol. V, pp. 2028-2030, July 2001.

2 GHz Self-aligning Tandem A/D Converter for SAR

Sten Schmidl Søbjærg and Erik Lintz Christensen
Ørsted•DTU, Technical University of Denmark,
DK-2800 Kgs. Lyngby, Denmark (e-mail: sss@oersted.dtu.dk).

Abstract-- A new generation of the Danish synthetic aperture radar system (EMISAR) is under development targeting a bandwidth of 800 MHz and a corresponding range resolution of around 25 cm. Two alternative approaches to achieve the wide bandwidth are considered. The one is to use analog I/Q demodulation before digitizing, and the other is to digitize the signal before digital I/Q demodulation [1]. In both cases the digitizing may be performed by a digital front end (DFE) with two parallel analog-to-digital-converters (ADCs) sampling at 1 GHz in phase or in anti-phase respectively, provided the analog bandwidth of the ADC is sufficient. In the first case each ADC has to digitize a 0-400 MHz signal, and in the second case both ADCs have to digitize a 100-900 MHz signal. In both cases the sampling time alignment is a critical parameter. The paper addresses some aspects of ADC alignment in the implementation of a DFE for the EMISAR system.

I. Introduction

Two ADCs in tandem can be used to double the sampling rate provided the analog bandwidth of the ADCs is sufficiently high and the sampling timing is properly aligned. A digital correlator can be used for automatic control of the sampling time. The correlator multiplies the input signals from the two ADCs and integrates the product, and the result is used as feedback to programmable digital delay devices in the clock circuit of each ADC. The delay devices allow a direct digital adjustment of ± 2 ns, and a fine-tuning to sub-picoseconds, using an analog input.

II. Correlation Measurement

For a radar using a coded pulse with a large time-bandwidth product, the reflected radar signal may be regarded as a stochastic signal with a Gaussian voltage distribution. For the two channel case, the input voltage may be regarded as two stochastic, Gaussian distributed variables, X and Y, characterized by the mutual correlation, ρ. The joint probability density function will have the form

$$p(x,y)=\frac{1}{2\pi\sigma^2\sqrt{1-\rho^2}}\exp\left(\frac{-\left(x^2+y^2-2\rho xy\right)}{2\sigma^2\left(1-\rho^2\right)}\right) \qquad (1)$$

where σ is the rms. signal level in each channel.

The correlator will sample, multiply, and integrate the two input voltages during a specified time, and the output will be given by

$$\rho=\frac{\langle X(t)*Y(t)\rangle}{\sqrt{\langle X^2(t)\rangle\langle Y^2(t)\rangle}} \qquad (2)$$

where "<>" represents the mean over the period T. For Gaussian distributed signals, the mean-square values will approach the rms. signal levels, σ_x and σ_y, for the two channels for long integration times.

The length of the integration period, T, is determined by the required precision in the measurement. Generally, for a Gaussian distributed signal, the standard deviation on the correlation measurement is given by

$$\Delta\rho=\frac{\sqrt{1+\rho^2}}{\sqrt{f_S T}} \qquad (3)$$

where f_s is the sampling frequency of the correlator. The standard deviation will be degraded, however, if subsequent samples are correlated, e.g. due to over-sampling.

Assuming a rectangular frequency characteristic, the autocorrelation function will be a sinc function

$$R(t)=\frac{\sin(2\pi Bt)}{2\pi Bt} \qquad (4)$$

where B is the signal bandwidth. The maximum will occur at zero delay difference, and zeros will be found at $t=n/(2B)$, where n is an integer. The situation for $n=1$ is the Nyquist sampling, but it is seen from the autocorrelation function, that the independence condition is fulfilled for all subsets of the signal, when sampled at Nyquist.

III. The Self-aligning parallel I/Q Receiver

The traditional wide-band DFE implementation includes two parallel channels for sampling an I/Q demodulated signal. In this application, a total bandwidth of 800 MHz is desired, and it may be implemented, using two ADCs, sampling simultaneously at 1 GHz.

For a single frequency input, the correlator output is a measure of the sampling misalignment between the two ADCs added to the phase difference from the demodulator. Assume sinusoidal signals, having the amplitudes, $A_1=A_2=\mathrm{sqrt}(2)$, and the phase difference, φ, applied to the input channels. The correlator output will be

$$\rho = \frac{1}{T}\int_0^T \sqrt{2}\cos(2\pi ft)\sqrt{2}\cos(2\pi ft + \varphi)dt \quad (5)$$

which may be rewritten as

$$\rho = \frac{1}{T}\int_0^T \cos(4\pi ft + \varphi)dt + \frac{1}{T}\int_0^T \cos(\varphi)dt \quad (6)$$

The first term will give a zero mean, and a standard deviation depending on the integration time. The latter term directly gives the cosine of the phase difference.

For a perfect I/Q demodulation in front of the correlator, a single frequency input signal results in correlator input signals, separated 90 degrees. The output may be considered as $\varphi_t = \pi/2 + \varphi_e$, where φ_t is the total measured phase difference, and φ_e is the phase error caused by the ADC timing error. Removing $\pi/2$ causes a change from cosine to sine in the correlator output, directly giving the relation

$$\rho = \sin(\varphi_e) \quad (7)$$

The delay error may be calculated from

$$t_D = \frac{\varphi_e}{2\pi f} \quad (8)$$

when the input frequency is known. For an input signal consisting of a band of frequencies, *B*, the measured quantity will be an average over the band, and the output correlation will be determined by

$$\rho = \frac{1}{B}\int_{f_1}^{f_2} \sin(2\pi f t_D)df \quad (9)$$

Unfortunately a consequence of this result is, that a symmetric band of frequencies around f_0=0 will always give a zero correlation for any delay error. It is hence not possible to use the normal radar input signal as basis for the correlation calculation, and a dedicated test signal is needed during delay alignment.

A limitation on the test signal frequency is noted. The sinusoidal behavior of the correlation function causes delay error ambiguity at high frequencies, or at relatively long delays. Long delays, exceeding the unambiguous range may appear at system initialization due to the manufacturing tolerances and temperature differences, and it must be solved online by injection of a low frequency calibration signal during system initialization. Subsequent drift can be corrected automatically by a simple regulation system during the measurement sequence, as time slots without data recording will be free to apply the test signal and correct the alignment.

An obvious problem in the analog I/Q demodulation is the DC offset. Since the correlator is a simple multiplier with integration, it will not only be sensitive to the signal I/Q correlation, but it will also be strongly influenced by any DC in the I and/or Q signals, and this error must be eliminated before the correlation calculation.

A DC in I, V_I, and in Q, V_Q, will change the output to

$$\rho_{DC} = \rho + V_I V_Q \quad (10)$$

where ρ is the true correlation. The traditional way of solving offset problems in a digital correlator is by phase shifting the test signal. It includes application of a modulation function to the input signals before the ADC and, using orthogonal modulations for the two channels, the DC can be eliminated. The simplest modulation functions may be a constant, $m_1(t)$=1, to the I channel and a 50% duty cycle, $m_2(t)$=±1, to the Q channel. For $m_2(t)$=+1, the output from the correlator will be equal to the situation without modulation, while the $m_2(t)$=-1 period will give

$$\rho_{DC} = -\rho + V_I V_Q \quad (11)$$

With the 50% duty cycle, the true correlation may be found directly by subtraction.

An alternative solution to the DC offset problem might be adjusting the offset directly on the ADC. As it is sensitive to temperature drifts, however, it needs frequent correction, and for a coherent radar application, the DC in the I and Q channels contain information, which makes it problematic to use the normal data for DC offset determination. An obvious solution is again to take advantage of the test signal, used for delay adjustment, and as this signal can be generated DC free, a simple integration of the signal voltage will provide sufficient information on the DC level, and the ADC DC adjust voltage can be set.

IV. The Digital Demodulator

An alternative solution to the DFE implementation uses digital I/Q demodulation after down-conversion to e.g. 500 MHz±400 MHz and sampling and digitizing the full-bandwidth signal at 2 GHz. This approach requires a 2 GS/s ADC or a tandem pair of ADCs with at least 2 GHz analog bandwidth, clocked at 1GHz with 180 degrees phase difference.

The input signals to each of the two ADCs will be exactly equal, but using digital demodulation with carrier reference signals sin(ω_S/4*t) and cos(ω_S/4*t), where ω_S is 2π times the sampling frequency, the usual I and Q channels are generated. [1 and 2].

The correlation technique can be used for delay adjustment. In this case each of the ADCs with a sampling frequency of 1 GHz will under-sample the signal. The full bandwidth input signal will appear aliased in the sampled spectra, which will, however, still represent the original bandwidth. This results in an autocorrelation function, which will still give its maximum, ρ_A=1, for t=0, and which will decrease monotonously until t=1/2B. Taking advantage of the symmetry of the autocorrelation function, an algorithm for adjusting the delays can be developed.

With the normalized sampled signals from each of the two ADCs, $v_{1,1}$, $v_{1,2}$, $v_{1,3}$… and $v_{2,1}$, $v_{2,2}$, $v_{2,3}$… respectively, two correlations can be calculated

$$\rho_1 = \sum_{n=1}^{N} v_{1,n} v_{2,n} \qquad \rho_2 = \sum_{n=1}^{N} v_{1,n} v_{2,n+1} \tag{12}$$

where N is the integration length. First assume that the two ADCs have been adjusted to simultaneous sampling. It means, that the correlation, ρ_1, will be equal to 1, as samples are identical, while the correlation, ρ_2, will be equal to the autocorrelation for $t=1/f_s$. Now increasing the sampling delay between the two ADCs, ρ_1 will decrease, while ρ_2 will increase. Adjusting until the difference between the two correlations is zero will lead to a perfect alignment of the two sampling times (i.e. sampling in anti-phase).

Similar to the situation when using analog I/Q demodulation, the manufacturing tolerances and temperature differences can cause ambiguities to occur, and at system power up, there must be a coarse adjustment of the two ADCs to approximately equal delays. Subsequent one delay may be increased by 1/(2GHz) = 500 ps to reduce the settling time of the regulation loop.

The initial coarse alignment can be performed by applying a slow cosine test signal at the input. This will result in a cosine autocorrelation with maximum at t=0, slowly decreasing according to the frequency of the signal. At this point the regulator should search the maximum correlator output, which can be done by a simple iterative regulation.

With the offset input frequency it is possible to use the radar signals to adjust the DC offset, and a simple integrator, which integrates the signal amplitudes continuously, will provide sufficient information on the DC level to set the regulation voltage directly on the ADC.

V. The complete digital front end

The complete DFE is constructed to support both types of demodulation. This is achieved by connecting the two ADCs to a large field programmable gate array (FPGA), which will store the sampled data and regulate the sample delays.
As the correlator includes an 8*8 multiplier, according to the number of bits from the ADC, and a large adder to perform the integration, it is a major challenge to utilize the full bandwidth, when sampling at 1 GHz per ADC. In the FPGA these functions must be paralleled by a factor of 8, increasing significantly the amount of resources needed. An obvious solution is to limit the sampling speed, since it has been shown, that an under-sampling will not influence the result of the correlation, while the standard deviation will be increased by a factor of sqrt(N), when under-sampled by a factor of N.

An alternative to the under-sampling is a reduction of the number of bits in the calculation of the correlation. It can be shown [3], that even a severe reduction, down to a single bit, will only increase the standard deviation by a factor of $\pi/2$ compared to a real number representation. And with 2 bits, the loss is down to a factor 1.14.

VI. conclusions

This paper describes the implementation of a digital front end for the EMISAR system, using two 1Gs/s A/D converters in tandem to achieve a bandwidth of 800 MHz. For traditional I/Q operation, it is shown, that a test signal is necessary to carry out the sampling delay alignment, since the full bandwidth I and Q signals will always de-correlate. DC offset canceling must be available, as the correlator result will be corrupted by the presence of DC. As the coherent radar signal contains a DC component, either a correction of the ADC input circuit using the test signal must be implemented, or phase switching must be applied.

The alternative digital front end implementation samples directly the 800 MHz bandwidth signal with 500 MHz center frequency, clocking the two ADCs 180 degrees out of phase. In this case the DC adjustment is simple, as the radar data, which contain no DC component, may be used directly. Likewise the sampling delay adjustment can be carried out using the radar data, and it is shown, how a simple measurement of the autocorrelation can be used to adjust the clock delays.

References

[1] J.H. Jørgensen, ”Digital Demodulator for Wide Bandwidth SAR”, Proceedings of the International Geoscience and Remote Sensing Symposium, IGARSS’2000, Vol. V, pp.2269-2271, July 2000.
[2] J. Dall and E. Lintz Christensen: “Multiplier-free Filters for Wideband SAR”; published at IGARSS 2001
[3] Thompson, Moran, Swenson: ”Interferometry and Synthesis in Radio Astronomy”; John Wiley & Sons, 1986

L-Band Polarimetric Correlation Radiometer with Subharmonic Sampling

JESPER ROTBØLL,

STEN SCHMIDL SØBJÆRG, and

NIELS SKOU

Ørsted-DTU, Electromagnetic Systems, Building 348

Technical University of Denmark

DK 2800 Lyngby, Denmark

This conference paper is published in the Proceedings of IGARSS'01, vol. IV, pp. 1571-1574, July 2001.

L-Band Polarimetric Correlation Radiometer with Subharmonic Sampling

Jesper Rotbøll, *Member, IEEE*, Sten Schmidl Søbjærg, *Student Member, IEEE*,
and Niels Skou, *Senior Member, IEEE*
Ørsted•DTU, Technical University of Denmark,
DK-2800 Lyngby, Denmark (e-mail: ns@oersted.dtu.dk).

Abstract—A novel L-band radiometer trading analog complexity for digital ditto has been designed and built. It is a fully polarimetric radiometer of the correlation type and it is based on sub-harmonic sampling principle in which the L-band signal is directly sampled by a fast A to D converter at a frequency well below L-band. Stability has been a design driver, and the instrument is intended for airborne measurements of polarimetric sea signatures.

I. Introduction

A L-band (1.4 GHz) radiometer system, based on novel interferometric techniques, and known under the acronym SMOS (soil moisture ocean salinity), has been selected as one of ESA's Earth Explorer Opportunity Missions. Measuring the L-band brightness temperature over the oceans enables a determination of sea salinity.

The brightness temperature sensitivity to salinity is typically (open ocean with high salinity) $\Delta T_B / \Delta S$ = 1K / psu (vertical polarization, 50° incidence angle). Hence, to find salinity to the 0.1 psu level requires radiometric measurements to better than 0.1 K and knowledge concerning the influence of other effects to the same level. Sea surface temperature is one of these effects, and it must be measured and corrected for. This is doable, however, as it is a well modeled and understood effect, and the ocean temperature is well monitored. But, the knowledge about the influence of wind on the brightness temperature has been identified as insufficient. Measurements and model work have concentrated on higher frequencies, and very little knowledge about any polarimetric signature - i.e. the brightness temperature dependence on azimuth viewing angle relative to the wind direction - exist. The present paper describes actions taken with the aim of helping to fill this void by designing and developing a suitable L-band polarimetric radiometer and antenna system, and carry out airborne campaigns in order to experimentally determine the radiometric response of the ocean to wind speed and direction relative to the observing direction.

II. Polarimetry and Stokes Parameters

The (brightness) Stokes vector is:

$$\overline{T_B} = \begin{pmatrix} I \\ Q \\ U \\ V \end{pmatrix} = \begin{pmatrix} T_V + T_H \\ T_V - T_H \\ T_{45^\circ} - T_{-45^\circ} \\ T_l + T_r \end{pmatrix} = \frac{\lambda^2}{k \cdot z} \begin{pmatrix} \langle E_V^2 \rangle + \langle E_H^2 \rangle \\ \langle E_V^2 \rangle - \langle E_H^2 \rangle \\ 2\,\mathrm{Re}\langle E_V E_H^* \rangle \\ 2\,\mathrm{Im}\langle E_V E_H^* \rangle \end{pmatrix}$$

where z is the impedance of the medium in which the wave propagates, λ is the wavelength and k is Boltzmanns constant. T_V is the vertical and T_H the horizontal brightness temperature. T_{45° and T_{-45° represent orthogonal linearly polarized measurements skewed 45° with respect to normal and T_l and T_r refer to left-hand and right-hand circular polarized quantities. I represents the total power, and Q the difference of the vertical and horizontal power components. The first and second Stokes parameters are measured using vertically and horizontally polarized radiometer channels, followed by addition or subtraction of the measured brightness temperatures.

The third Stokes parameter can be found as the real part of the cross correlation of the vertical and horizontal electrical fields. The fourth Stokes parameter can be measured as the imaginary part of the cross correlation of the vertical and horizontal electrical fields.

III. The Polarimetric Radiometer

The L-band polarimetric radiometer measures all four parameters of the Stokes vector simultaneously, using the correlation principle. Further information on different radiometer configurations for measuring polarimetric signatures can be found in [1]. The fundamental difference between a traditional polarimetric correlation radiometer (Figure 1) and a subharmonic sampling polarimetric correlation radiometer (Figure 2) is the use of fast A/D converters, not only for detection and correlation (in order to derive the Stokes vector), but also for frequency shift from RF to baseband (subharmonic sampling).

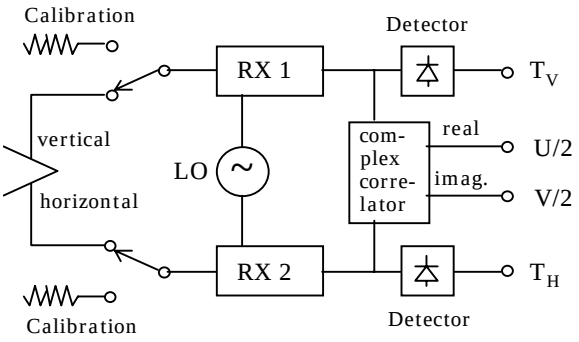

Figure 1: Basic correlation radiometer.

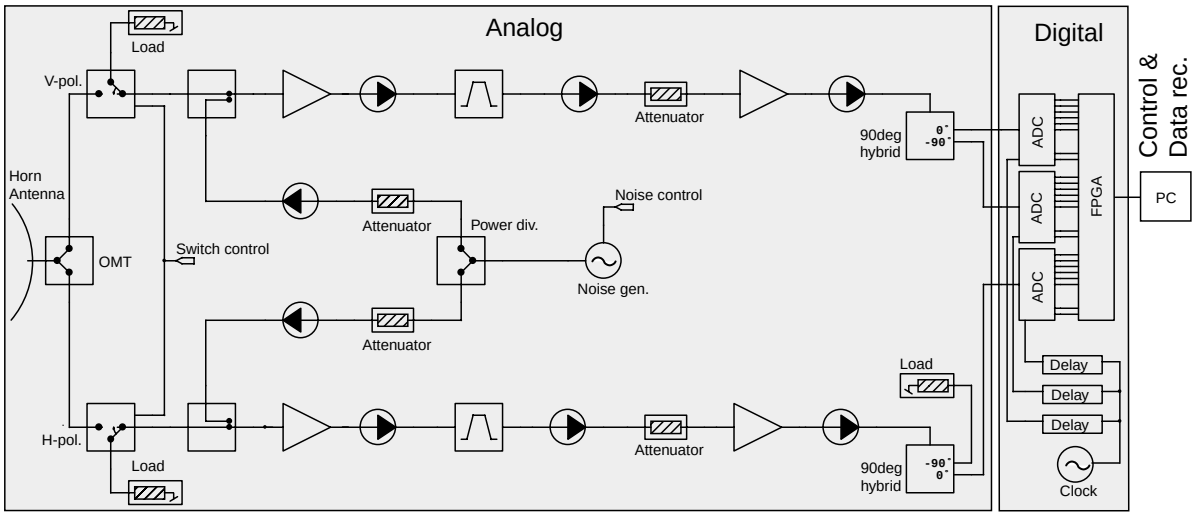

Figure 2: Subharmonic sampling correlation radiometer.

A. The Analog Part

The antenna must be large measured in wavelengths in order to ensure a reasonably narrow angular beamwidth, hence a small range of incidence angles over which the measurements are integrated. Due to the long L-band wavelength this results in a physically large antenna. For the present purpose circle flights with the antenna looking out to the side of the aircraft is the optimum solution. This way different circles with different bank angles will directly reveal the azimuthal signatures as functions of incidence angles, provided the antenna is mounted properly. The side-looking geometry limits the aperture to 90 cm taking advantage of the aft parachute doors of a C-130 airplane. 90 cm aperture corresponds to a 15° beamwidth, which is considered acceptable. A large horn with a 90 x 90 cm square aperture and a length of 200 cm has been constructed. This antenna option has been selected due to simplicity and good performance – especially concerning loss, which is of prime importance in the present case. An ortho-mode transducer enables retrieval of H and V polarizations.

Figure 2 shows the analog radiometer section, consisting of two total-power radiometer channels, and two calibration circuits for gain and correlator calibration. Each channel has a total noise figure NF = 1.4 dB, corresponding to a noise temperature T_N = 119 K (system temperature stabilized at 313 K), and a filter bandwidth BW = 27 MHz (1400 MHz – 1427 MHz). Thus the sensitivity is ΔT = 0.1 K for 1 sec. integration period, when viewing a 300 K target.

As the A/D conversion is not only a media conversion but also introduces a frequency shift as mentioned above, special requirements to the analog RF-filter arise, due to the risk of aliasing from other frequency bands. Figure 3 shows the spectral behavior of a subharmonic sampling, using a sampling frequency f_s = 63.5 MHz, a filter bandwidth BW = 27 MHz and an overall system bandwidth $BW_{sys} \approx$ 300 MHz, limited by the OMT. The chosen f_s will be discussed in the next section. We here notice that four harmonics of f_s fall within the system bandwidth BW_{sys}, causing heavily aliasing at IF level in a case with poor RF-filter stopband attenuation, because every harmonic of f_s converts noise around it to baseband (IF). The filter stopband attenuation is set to 60 dB at the frequencies 1390 MHz and 1437 MHz, due to the risk that interference signals outside the limited filter bandwidth add up at baseband (IF), but more importantly because 60 dB stopband attenuation is standard in a traditional superheterodyne correlation radiometer, using two filters (RF and IF).

Another aspect to consider when designing a subharmonic sampling radiometer is the analog RF gain. In a traditional superheterodyne radiometer the gain can be divided between the RF- and the IF-circuit. This is not the case in a subharmonic sampling radiometer where the overall gain is at RF-level, with a potential risk of generating feed-back problems, e.g. from the analog output, through the air and into the antenna. With an overall gain of approximately 100 dB even a small leak can be fatal. Standard SMA-connectors are used to connect the RF-components in the radiometer channels, right from the antenna output to the A/D converter printed circuit board (PCB). The leak in a standard SMA-connector is specified to be below –100 dB, and the antenna back lobe level is approximately –25 dB (the antenna is pointing away from the radiometer). This provides at least 135 dB isolation, which is sufficient to avoid feed-back. Experience has, however, shown that insufficient shielding of the digital A/D converter PCB can cause problems, as even a short line on the PCB will act as a radiating antenna at L-band.

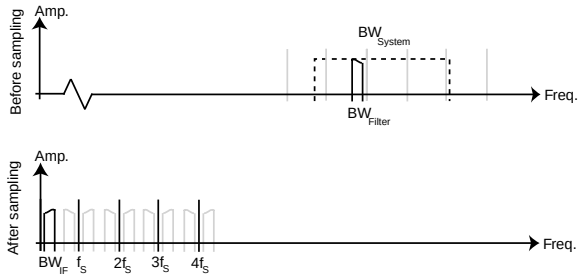

Figure 3: Spectral behavior of a subharmonic sampling.

Important is not only the isolation between the output and input of the analog channels, but also the isolation between the two channels. The result of poor isolation between the channels is correlation, i.e. offsets on the output of the correlator (third and fourth Stokes parameters), as the leak signal and the original signal will correlate. Two circuits, the correlated noise injection calibration circuit and the antenna (actually the OMT), provides a direct path between the two radiometer channels, and are therefore especially critical. In the correlated noise injection calibration circuit an isolation of approximately 72 dB is obtained. The OMT has an isolation of approximately 40 dB, which could easily be improved by adding an isolator in each channel, however resulting in higher loss and degraded sensitivity.

As in any other correlation radiometer phase coherence between the two receivers is required, in order to measure the complex correlation between the input signals. In the analog part of the system the components are matched in a way that the overall phase difference between the two channels is less than 5°. A phase difference will cause a shift of U signal into the V channel and V into U. Fine tuning can be done in the digital part of the radiometer (described in the next section III-*B*).

The analog part of the radiometer includes two calibration circuits, a noise diode arrangement for correlator calibration, and coax switches with heated loads for total power channel calibration. The calibration procedure is described in section III-*C*. The last component in the analog part of the radiometer is a quadrature hybrid, used for generating in-phase and 90° out-of-phase signals for the correlator.

A. The Digital Part

Using modern analog-to-digital converters (ADC), it is possible to sample the L-band signal directly, without down-conversion to base-band. The Maxim MAX104 ADC is an example of the available technology, and it provides an analog 3 dB bandwidth better than 2 GHz and sampling speeds better than 1 GHz, providing at least 6.5 effective bits over all the frequency range.

From the general sampling theory, it is well known, that the periodic sampling of an analog signal returns a spectrum, which is described by the convolution of the original signal's spectrum and a train of infinitesimally short pulses, spaced by the sampling frequency, f_s. This means, that the resulting base-band spectrum will be formed as an infinite sum of the original base-band spectrum, added to the specters around n times the sampling frequency, where n is an integer. Traditionally this leads to a low pass filter applied in front of the sampling circuit to limit the signal bandwidth, but using an ADC with high analog bandwidth, a narrow band RF/IF signal may be digitized directly, according to Figure 3. This process is known as subharmonic sampling, and the figure shows, that the sampled spectrum contains the same information as the original signal. The choice of sampling frequency, f_s, however, is essential for the preservation of information. The general sampling theorem, stating that $f_s \geq 2 \cdot BW$, must be fulfilled, but additionally it must be observed, that $n \cdot f_s$, where n is an integer, does not falls within the pass-band of the original signal. This will result in overlap from the two side-bands, causing loss of information. For the present radiometer, covering the bandwidth from 1400 MHz to 1427 MHz, a sampling frequency of 63.5 MHz has been chosen, placing the sampled spectrum from 3 MHz to 30 MHz.

The subharmonic sampled signal may be regarded as equivalent to a down converted, sampled signal, providing the same properties of linearity and standard deviation. The linearity depends on the level of saturation, i.e. the min/max values for the ADC output. For the MAX104, the input range is ±250 mV, approximately equal to 1 dBm @ 50 Ω. Choosing the input signal level to −10 dBm, the effect of unlinearity will be negligible.

For the standard deviation, it can be shown [2], that the standard deviation of a radiometer signal, sampled with an infinite number of bits, will be equal to the standard deviation of the unsampled signal, if the whole bandwidth is preserved during the sampling. The effect of quantization may be regarded as the addition of a small noise signal with the power $e_0^2/12$, where $e_0 = 500 \text{ mv}/2^8$ for the 8 bit MAX104/108. At 50 Ω this is equal to −52 dBm, which is negligible.

The complete digital radiometer basically consists of three parallel correlators, where the first and second Stokes parameters are formed by selfcorrelation of the horizontal and vertical brightness temperatures. The third correlator calculates the complex correlation between the two polarizations, giving the third and fourth Stokes parameters.

An important issue in the implementation of correlators is that a DC component in the input signal will severely influence the output. The A/D converters themselves provide a DC offset adjustment pin, and using input signals without DC, the mean voltage value can be calculated from the radiometer data, and a simple regulation loop may be applied, feeding the adjustment pin from a small digital-to-analog converter. Alternatively the DC component can be removed in the digital circuit, using a DC block filter, when the sampled signal does not cover all the bandwidth down to DC. As we here use frequencies from 3 MHz to 30 MHz, the digital DC removal has been implemented in the present system.

A final aspect to consider in the implementation of the subharmonic sampling is the exact alignment of sampling times for the three ADC's, relating to the frequency of the input RF signal. The delays are adjusted using dedicated delay circuits, digitally programmable in a ±2 ns range and with a possibility of sub-psec. precision using an analog input. The delay setting is calculated using the correlators and the noise diode of the radiometer. When applying in-phase correlated noise to the two radiometer channels, the real output from the digital correlator will calculate the level of correlation, while the imaginary part should return a zero result, when the ADC's are perfectly aligned. Likewise, the correlation between the 0 degrees and the 90 degrees shifted inputs from the same channel should be zero. Implementing a special test mode to calculate the two zero correlations, a simple regulation of the sampling delays can be done before final assembly of the system.

B. Overall system considerations

Aspects such as stability and absolute accuracy are important when you design a microwave radiometer. In the present L-band radiometer system this is obtained by in-flight calibration and temperature stabilized design.

The system is temperature stabilized using a regulator and heaters to heat a box to 313 K within a few tenths of a degree. The analog part of the radiometer is then located inside the box, without having direct thermal contact to the temperature regulated box, i.e. a box in a box principle. The digital PCB is temperature stabilized in a simple way, using the heat generated by the A/D converters, for heating the shielded box in which the PCB is located. Data from several internal (analog and digital box) and external (OMT and RF-cables) temperature sensors is stored on the PC, making temperature compensation of the data possible.

Using the coax switches with the heated loads before and after each track ensures good absolute accuracy of the detection (total power) channels. The coax switches and the heated loads can also be used for injection of uncorrelated noise in the two receiver channels, making offset calibration of the correlator possible. Furthermore a noise generator can inject correlated noise into the two receiver channels, and the degree of correlation at the receiver output can be precisely calculated using the measurements from the detection channels. Hence absolute calibration of the radiometer is possible, even during flight.

IV. THE EXPERIMENTS

Two flights have been carried out over Danish waters during 2001. During both flights, conditions were favorable for microwave radiometer measurements, with no heavy clouds or rain. The data recorded has not yet been processed, i.e. calibrated and corrected for airplane attitude (e.g. roll and pitch), yet it is clear, that there was no interference. Preliminary results show a small polarimetric (U and V) response, if any.

V. FUTURE PLANS

The L-band polarimetric correlation radiometer is designed with field programmable gate arrays (FPGA) in the digital front-end, giving full flexibility for reconfiguration.

- An increase in the RF bandwidth would result in a better sensitivity, but also a higher probability of interference signals. In the digital domain, a second filter can provide additional modification to the frequency band selected by the RF-filter, allowing selective suppression of possible interference signals.
- A special time-domain filtering may be applied to avoid pulsed interference signals. Making the integration periods shorter, and evaluating the power level of each integration period, will enable rejection, if the signal level changes significantly beyond the level of radiometric noise. The short integration period can then be followed by a longer integration to e.g. 8 msec. (to reduce the data amount), keeping the number of rejected short integration periods in mind.
- A phase shift like the one provided by the two analog quadrature hybrids, can also be made digitally, or alternatively a full digital I/Q demodulaton can be implemented. A digital solution would reduce the number of components, analog as well as digital, i.e. reduce size, weight, power consumption and cost.

VI. CONCLUSIONS

A new polarimetric correlation radiometer has been designed, build and operated. As the radiometer employs subharmonic sampling, special considerations regarding the analog and digital circuit has been discussed. The system features several advantages as compared with a traditional superheterodyne: weight, size and flexibility for reconfiguration. The system is being used for measuring the brightness temperature over the ocean in experiments carried out in 2001, in order to determine the influence of the wind at the L-band brightness temperature. Preliminary results seems very encouraging and will soon be the subject of proper publications.

REFERENCES

[1] Niels Skou, Brian Laursen and Sten Søbjærg: "Polarimetric Radiometer configurations: Potential Accuracy and Sensitivity", IEEE Trans. Geo. Remote Sensing, vol 37, pp. 2165-2171, sep.99

[2] Thompson, Moran, Swenson: "Interferometry and Synthesis in Radio Astronomy"; John Wiley & Sons, 1986

A novel L-band polarimetric radiometer featuring subharmonic sampling

JESPER ROTBØLL,

STEN SCHMIDL SØBJÆRG, and

NIELS SKOU

Ørsted-DTU, Electromagnetic Systems, Building 348

Technical University of Denmark

DK 2800 Lyngby, Denmark

This journal paper is accepted for publishing in a special issue of Radio Science, following the Specialist Meeting on Microwave Remote Sensing, 5-9 November 2001, Millennium Hotel, Boulder, Colorado.

RADIO SCIENCE, VOL. 38, NO. 0, XXXX, doi:10.1029/2002RS002666, 2003

A novel L-band polarimetric radiometer featuring subharmonic sampling

Jesper Rotbøll, Sten Schmidl Søbjærg, and Niels Skou

Ørsted/DTU, Electromagnetic Systems, Technical University of Denmark, Lyngby, Denmark

Received 11 March 2002; revised 17 June 2002; accepted 18 July 2002; published XX Month 2003.

[1] A novel L-band radiometer trading analog components for digital circuits has been designed, built and operated. It is a fully polarimetric radiometer of the correlation type, and it is based on the subharmonic sampling principle in which the L-band signal is directly sampled by a fast A to D converter at a frequency well below L-band. Overall stability has been a design driver, as the instrument is intended for airborne measurements of polarimetric sea signatures. *INDEX TERMS:* 4294 Oceanography: General: Instruments and techniques; 6994 Radio Science: Instruments and techniques; 6969 Radio Science: Remote sensing; 6974 Radio Science: Signal processing; *KEYWORDS:* radiometer, L-band, subharmonic sampling, digital downconversion, stability, ocean remote sensing

Citation: Rotbøll, J., S. S. Søbjærg, and N. Skou, A novel L-band polarimetric radiometer featuring subharmonic sampling, *Radio Sci., 38*(0), XXXX, doi:10.1029/2002RS002666, 2003.

1. Background (SMOS Project and Campaign Needs)

[2] An L-band (1.4 GHz) radiometer system, based on novel interferometric techniques, and known under the acronym SMOS (soil moisture ocean salinity), has been selected as one of ESA's Earth Explorer Opportunity Missions. Measuring the L-band brightness temperature over the oceans enables a determination of sea salinity.

[3] The brightness temperature sensitivity to salinity at open ocean and with high salinity (optimum conditions) is $\Delta T_B/\Delta S$ = 1K/psu (practical salinity unit), when measuring the vertical polarization and with a incidence angle of 50°. Hence, to find salinity to the 0.1 psu level requires radiometric measurements to better than 0.1 K and knowledge concerning the influence of other effects to the same level. Sea surface temperature is one of these effects, and it must be measured and corrected for. This is doable, however, as it is a well modeled and understood effect, and the ocean temperature is well monitored. But, the knowledge about the influence of wind on the brightness temperature has been identified as insufficient. Measurements and model work have concentrated on higher frequencies, and very little knowledge about any polarimetric signature - i.e. the brightness temperature dependence on azimuth viewing angle relative to the wind direction - exist. The present paper describes actions taken with the aim of helping to fill this void by designing and developing a suitable L-band polarimetric radiometer and antenna system, and carry out airborne campaigns in order to experimentally determine the radiometric response of the ocean to wind speed and direction relative to the observing direction.

0048-6604/03/2002RS002666$11.00

2. Instrument

2.1. Stokes Parameters

[4] The L-band polarimetric radiometer measures all four parameters of the Stokes (brightness) vector, which is described as:

$$\overline{T_B} = \begin{pmatrix} I \\ Q \\ U \\ V \end{pmatrix} = \begin{pmatrix} T_V + T_H \\ T_V - T_H \\ T_{45^\circ} - T_{-45^\circ} \\ T_l - T_r \end{pmatrix} = \frac{\lambda^2}{k \cdot z} \begin{pmatrix} \langle E_V^2 \rangle + \langle E_H^2 \rangle \\ \langle E_V^2 \rangle - \langle E_H^2 \rangle \\ 2\ \mathrm{Re}\langle E_V E_H^* \rangle \\ 2\ \mathrm{Im}\langle E_V E_H^* \rangle \end{pmatrix}$$

where z is the impedance of the medium in which the wave propagates, λ is the wavelength and k is Boltzmanns constant. As the radiometer features a fast digital correlator, all the Stokes parameters are measured simultaneously. The first (I) and second (Q) Stokes parameters are measured using vertically (T_V) and horizontally (T_H) polarized radiometer channels, followed by addition or subtraction of the measured brightness temperatures. The third and fourth Stokes parameters (U and V) can be found as the real and imaginary part of the cross-correlation of the vertical and

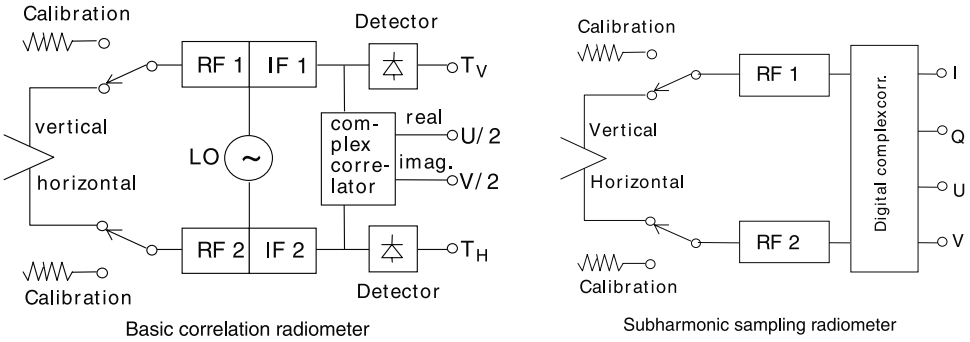

Figure 1. Comparison of a traditional and a subharmonic sampling polarimetric correlation radiometer.

horizontal electrical fields respectively. Alternatively the third Stokes parameter can be found by using T_{45° and T_{-45°, which represent orthogonal linearly polarized measurements skewed 45° with respect to normal. The fourth Stokes parameter can be found by using T_l and T_r, which refer to left-hand and right-hand circular polarized quantities. Further information on different radiometer configurations for measuring polarimetric signatures is given by *Skou et al.* [1999]. The present radiometer is designed as a correlation radiometer, i.e. using a complex correlator to measure the real and imaginary part of the cross-correlation of the vertical and horizontal electrical fields.

2.2. Subharmonic Sampling Principle

[5] The novel aspect in the L-band polarimetric radiometer design, consist in the use of fast analog-to-digital converters (ADC), not only for detection and correlation (in order to derive the Stokes vector), but also for frequency shift from RF to baseband (subharmonic sampling). Figure 1 shows a comparison of a traditional polarimetric correlation radiometer utilizing mixers and a local oscillator for the frequency shift, and a subharmonic sampling polarimetric correlation radiometer, where the signals are sampled and frequency-shifted in one process. The advantages of a subharmonic sampling radiometer as compared to a traditional radiometer are less analog components, i.e. less weight and size, and easy reconfiguration of the digital part of the radiometer. The subharmonic sampling principle in a radiometer context is, however, a relatively unknown principle, and the need for very large gain at RF-level could also be considered as a disadvantage, due to the risk of generating an undesirable feed-back loop.

[6] Figure 2 shows the spectral behavior of a subharmonic sampling, using a sampling frequency f_s = 63.5 MHz, a bandwidth BW_{filter} = 27 MHz (1400 MHz to 1427 MHz) and an overall system bandwidth $BW_{sys} \approx$ 300 MHz, limited by the remaining analog components. From the general sampling theory, it is well known, that the periodic sampling of an analog signal returns a spectrum, which is described by the convolution of the original signal's spectrum and a train of delta functions, spaced by the sampling frequency, f_s. This means, that the resulting base-band spectrum will be formed as an infinite sum of the original base-band spectrum, added to the spectra around n times the sampling frequency, where n is an integer.

[7] The choice of sampling frequency, f_s, however, is essential for the preservation of information. The general sampling theorem, stating that $f_s \geq 2 \cdot BW$, must be

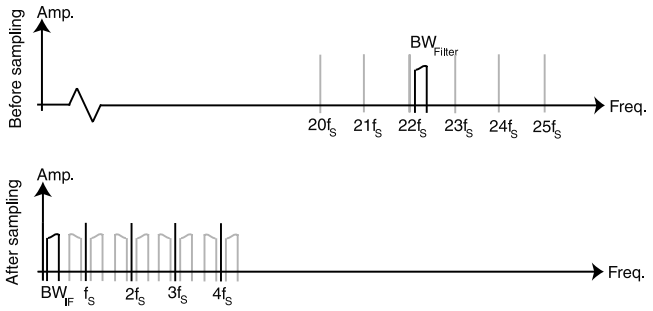

Figure 2. Spectral behavior of a subharmonic sampling.

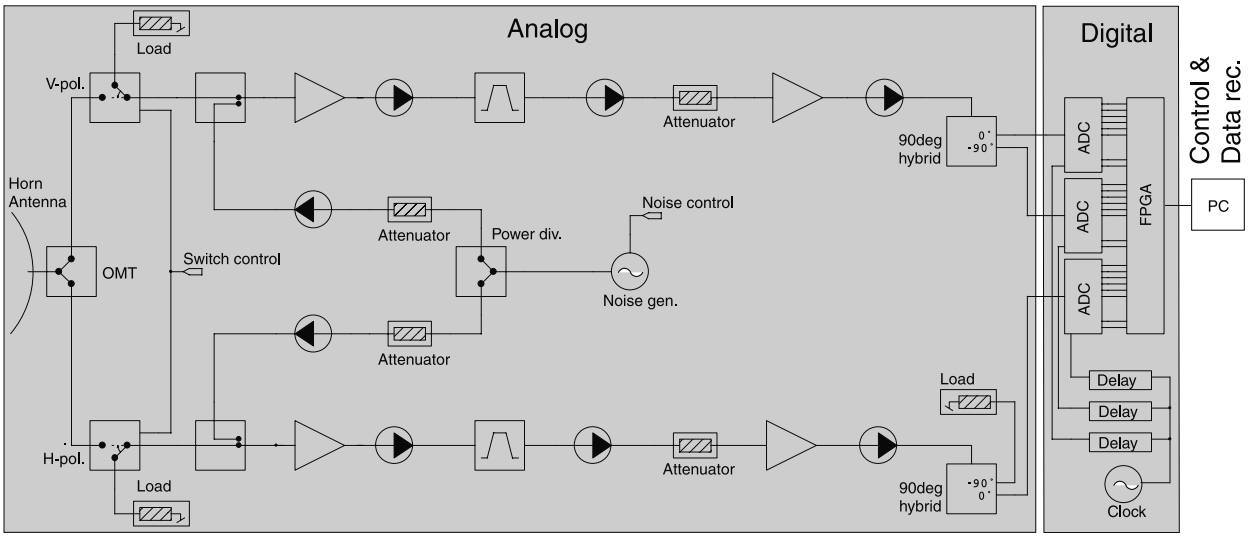

Figure 3. Subharmonic sampling polarimetric correlation radiometer.

fulfilled, but additionally it must be observed, that no harmonic of the sampling frequency falls within the passband of the original signal $n \cdot f_s \neq [f_0 \pm BW/2]$. This will result in overlap from the two sidebands, causing loss of information, due to the stochastic nature of the signals. Actually it is required that the harmonics of the sampling frequency falls some MHz next to the filter bandwidth, due to the non-ideal edges of the analog filters. For the present radiometer, covering the bandwidth from 1400 MHz to 1427 MHz, a sampling frequency of 63.5 MHz has been chosen, placing the sampled spectrum from 3 MHz to 30 MHz. The subharmonic sampled signal may be regarded as equivalent to a down-converted, sampled signal, providing the same properties of linearity and standard deviation.

2.3. Digital Parts

[8] The complete digital radiometer (Figure 3) basically consists of three parallel correlators, where the first and second Stokes parameters are formed by self-correlation of the horizontal and vertical brightness temperatures. The third correlator calculates the complex correlation between the two polarizations, giving the third and fourth Stokes parameters.

[9] The Maxim MAX104 ADC is an example of the available technology. It provides a 3 dB Track/Hold bandwidth better than 2.2 GHz, sampling speeds up to 1 GHz, and a typical sample jitter below 0.5 ps, providing at least 6.5 effective bits over the radiometer input frequency range. The linearity depends on the level of saturation, i.e. the min/max values for the ADC input. For the MAX104, the input range is ±250 mV, approximately equal to 1 dBm @ 50 Ω. Choosing the input signal level to −10 dBm, the effect of unlinearity will be negligible.

[10] For the standard deviation, it can be shown [*Thompson et al.*, 1986], that the standard deviation of a radiometer signal, sampled with an infinite number of bits, will be equal to the standard deviation of the unsampled signal, if the whole bandwidth is preserved during the sampling. The effect of quantization to N bits may be regarded as the addition of a small noise signal, described by a stochastic variable with an uniform distribution from $-e_0/2$ to $e_0/2$, where $e_0 = 500\ mv/2^N$, equal to the step between two quantization levels [*Oppenheim and Schafer*, 1975]. The power of the signal equals $e_0^2/12$, and for the 8 bit MAX104 with a 50 Ω input this is equal to −52 dBm, which is negligible, compared to approximately −10 dBm signal level.

[11] An important issue in the implementation of correlators is that a DC component in the input signal will severely influence the output. The A/D converters themselves provide a DC offset adjustment pin, and using input signals without DC, the mean voltage value can be calculated from the radiometer data, and a simple regulation loop may be applied, feeding the adjustment pin from a small digital-to-analog converter. Alternatively the DC component can be removed in the digital circuit, using a DC block filter, when the sampled signal does not cover all the bandwidth down to DC. As we here use frequencies from 3 MHz to 30 MHz, the digital DC removal has been implemented in the present system.

[12] A final aspect to consider in the implementation of the subharmonic sampling is the exact alignment of sampling times for the three ADC's, relating to the phase of the input RF signal. The delays are adjusted using dedicated delay circuits (Motorola MC100E196), digi-

Table 1. Radiometer Specifications (The Digital Part)

	Digital Part
Maxim MAX104	8-bit ADC
Analog bandwidth	BW > 2 GHz
Sampling frequency	f_S = 63.5 MHz
Sampled spectrum	From 3 MHz to 30 MHz
Clock adjust	Sub-psec. (before final assembly)
Quantization noise	<−50 dBm (for the 8-bit MAX104)
Input power	$P_{IN} \approx -10$ dBm (1 dBm is max.)
Integration	4 msec. to 1 sec. (typically)
Temperature reg.	319 K (±0.2 K)

tally programmable in a ±2 ns range and with a possibility of sub-psec. precision using an analog input. The delay setting is calculated using the correlators and a noise diode, positioned in the analog part of the radiometer. When applying in-phase correlated noise to the two radiometer channels, the real output from the digital correlator will return the correlation coefficient, while the imaginary part should return a zero result, when the ADC's are perfectly aligned. Likewise, the correlation between the 0 degrees and the 90 degrees shifted inputs from the same channel should be zero. Implementing a special test mode to calculate the two zero correlations, a simple regulation of the sampling delays can be done before final assembly of the system. The overall specifications of the digital part of the radiometer can be found in Table 1.

2.4. Analog Parts

[13] Even though the novel aspect in this radiometer is the digital part, a important part of the system is still analog (the front end as seen in Figure 3). Actually special requirements to the analog components arise, which are described in this section.

[14] The first analog component is the antenna, which must be large measured in wavelengths in order to ensure a reasonably narrow angular beam width, hence a small range of incidence angles over which the measurements are integrated. Due to the long L-band wavelength this results in a physically large antenna. A large horn with a 90 × 90 cm square aperture and a length of 200 cm has been designed and constructed. The horn antenna has been designed as a standard-gain horn, with a 15° beam width, which is considered acceptable, and has been selected due to simplicity and good performance - especially concerning loss, which is of prime importance in the present case (the horn parameters have not yet been measured). An ortho-mode transducer enables retrieval of H and V polarizations.

[15] Figure 3 shows the analog radiometer section, consisting of two total-power radiometer channels, and two calibration circuits for gain and correlator calibration. Each channel has a total noise figure NF = 1.4 dB, corresponding to a noise temperature TN = 119 K (system temperature stabilized at 313 K), and a filter bandwidth BW = 27 MHz (1400 MHz–1427 MHz). Thus the sensitivity is $\Delta T = 0.1$ K for 1 sec. integration period, when viewing a 300 K target.

[16] As the A/D conversion is not only a media conversion but also introduces a frequency shift as mentioned above, special requirements for the analog RF-filter arise, due to the risk of aliasing from other frequency bands. We here notice (Figure 2) that some harmonics of fs fall within the system bandwidth Bwsys (not shown), causing heavy aliasing at IF level in a case with poor RF-filter stopband attenuation, because every harmonic of fs converts noise around it to baseband (IF). The filter stopband attenuation is set to 25 dB at the frequencies 1394 MHz and 1433 MHz (60 dB at f = 1390 MHz and f = 1437 MHz), due to the risk that interference signals outside the limited filter bandwidth add up at baseband (IF), but more importantly because 60 dB stopband attenuation is typical in a traditional superheterodyne correlation radiometer, using two filters (RF and IF). As in any other correlation radiometer phase coherence between the two receivers is required, in order to measure the complex correlation between the input signals. A small phase difference will cause a shift of U signal into the V channel and V into U, while larger differences will result in de-correlation. In the analog part of the system the components are matched in a way that the overall phase difference between the two channels is less than 5°. Fine tuning can be done in the digital part of the radiometer, as a tuning of the ADC sampling times (for a narrowband signal) has approximately the same effect as a phase adjustment in the analog part of the radiometer.

[17] By selecting the components for the noise-injection circuit, it is possible to construct two almost identical noise-injection channels (from power splitter input to output of the two directional couplers). Network analyser measurements show less than 0.5 deg. phase difference and less than 0.05 dB amplitude difference between the two channels. This phase difference corresponds to less than 0.01 K shift in U/V, assuming approximately 1K signal in U and V (1K * Sin(0.5 deg) < 0.01K).

[18] Another aspect to consider when designing a subharmonic sampling radiometer is the analog RF gain. In a traditional superheterodyne radiometer the gain can be divided between the RF- and the IF-circuit. This is not the case in a subharmonic sampling radiometer where the overall gain is at RF-level, with a potential risk of generating feed-back problems, e.g. from the analog output, through the air and into the antenna. With an overall gain of approximately 90 dB even a small leak can be fatal. Standard SMA-connectors are used to connect the RF-components in the radiometer channels, right from the antenna output to the A/D converter

Table 2. Radiometer Specifications (The Analog Part)

	Analog Part
Frequency	f = 1.400–1.427 GHz
Filter stopband	G < −25 dB (at BW_{Filter} ± 6 MHz) G < −60 dB (at BW_{Filter} ± 10 MHz)
RF gain	G ≈ 90 dB
Noise Figure (total)	NF = 1.4 dB
Noise temp.	T_N = 119 K (System temp. 313 K)
Sensitivity	ΔT = 0.1 K (1 sec. int., 300 K target)
Phase match	Better than 5° (V- and H-channel)
Calibration	Internal load and noise diode
Temperature reg.	313 K (±0.1 K)
Temp. sensors	19 (in the complete system)

printed circuit board (PCB). The leak in a standard SMA-connector is specified to be below −100 dB, and as the antenna is pointing away from the radiometer, the isolation is further improved and sufficient to avoid feedback. Experience has, however, shown that insufficient shielding of the digital A/D converter PCB can cause problems, as even a short line on the PCB will act as a radiating antenna at L-band.

[19] What is important is not only the isolation between the output and input of the analog channels, but also the isolation between the two channels. Poor isolation between the channels will cause offsets on the output of the correlator (third and fourth Stokes parameters), as the leak signal and the original signal will correlate. Two circuits, the correlated noise injection calibration circuit and the antenna (actually the OMT), provides a direct path between the two radiometer channels, and are therefore especially critical. In the correlated noise injection calibration circuit an isolation of approximately 72 dB is obtained, which is suitable for this type of radiometer [*Skou et al.*, 1999]. The OMT has an isolation of approximately 40 dB, resulting in offsets on the correlator output. This contribution is, however, very stable and we can correct for this. The relatively poor isolation could easily be improved by adding an isolator in each radiometer channel, however, resulting in higher loss and degraded sensitivity, i.e. a degradation of one of the most important system parameters.

[20] The analog part of the radiometer includes two calibration circuits, a noise diode arrangement and coax switches with heated loads for correlator and total power channel calibration. The last component in the analog part of the radiometer is a quadrature hybrid, used for generating in-phase and 90° out-of-phase signals for the correlator. The overall specifications of the analog part of the radiometer can be found in Table 2.

2.5. Common System Parts

[21] Aspects such as stability and absolute accuracy are important when you design a microwave radiometer. In the present L-band radiometer system this is obtained by in-flight calibration and temperature stabilized design.

[22] The system is temperature stabilized using a regulator and heaters to heat a box to 313 K within a few tenths of a degree. The analog part of the radiometer is then located inside the box, without having direct thermal contact to the temperature regulated box, i.e. a box in a box principle. The digital PCB is temperature stabilized, by using the heat generated by the A/D converters, for heating the shielded box in which the PCB is located, and then regulate the cooling-fans in order to keep the temperature at 319K, also within a few Kelvin. Data from 14 internal (analog and digital box) and 4 external (OMT and RF-cables) temperature sensors is stored on the PC, making temperature compensation of the data possible.

[23] Using the coax switches with the heated loads before and after each data acquisition flight track ensures good absolute accuracy of the detection (total power) channels. The coax switches and the heated loads can also be used for injection of uncorrelated noise in the two receiver channels, making offset calibration of the correlator possible. Furthermore a noise generator can inject correlated noise into the two receiver channels, and the correlation coefficient, at the receiver output, can be precisely calculated using the measurements from the detection channels. Hence absolute calibration of the radiometer is possible, even during flight.

3. Experiments

[24] Several flights have been carried out over Danish waters during 2001. The data recorded have not yet been completely processed, i.e. calibrated and corrected for aircraft attitude (e.g. roll and pitch), yet it is clear, that there was no problems with external interference.

[25] For the present purpose circle flights with the antenna looking out to the side of the C-130 aircraft, using the aft parachute door is the optimum solution. The flights consists of a number of circles at different constant roll angles (i.e. different incidence angles), and for each circle, data will be searched for polarimetric signatures in azimuth. Preliminary reviews indicate that an eventual polarimetric signature in second, third, and fourth Stokes parameters is very small, if present. A more thorough data analysis will be subject of further investigations, and the results mentioned in this paper will concentrate on data takes from calibration targets in order to evaluate the radiometer performance.

[26] Each data take includes a pre- and a post-calibration sequence, where the radiometer receiver observes internal targets, i.e. a matched load in the temperature stabilized environment, and the load (or antenna) along with 140 K from the built-in noise diode. A typical data

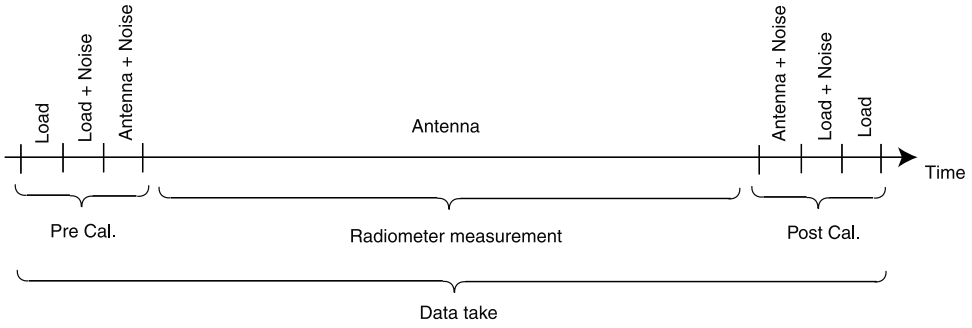

Figure 4. Measurement sequence of a data take (circle flight).

take is illustrated in Figure 4, and as data obtained from the internal targets, "Load" and "Load + Noise", are not influenced by aircraft attitude and external signals, it is normally used to calibrate the radiometer. It may also, however, be used for evaluation of the stability of the radiometer, if a constant calibration set (constant gain and noise figure values) is applied to the full data set, giving a measure of the drift during a data take.

[27] A circle flight is typically between 2 min. and 5 min., depending on the aircraft roll angle (due to different circle diameters), and each circle is repeated three times. The average drift, i.e. the numerical value of the change in brightness temperature from pre- to post-calibration measurements $\Delta = |T_{B\ post} - T_{B\ pre}|$, in the two radiometer channels for each data take length is shown in Table 3, a mean is calculated, and for comparison the radiometric sensitivity for the calibration period length (about 1,5 sec.) is shown.

[28] From the table it is seen, that there is some drift in the instrument output. The deviations, however, are of the order of the radiometric sensitivity, and with the relatively small number of tracks to average, a fraction of the changes may result from the stochastic nature of the signals. Calculating the mean drift from the two channels and the two targets, a drift of 0.16 K is found for the detection channels.

[29] For the correlation channels, results from pre- and post-calibration may be evaluated using the same procedure. It must be noticed, however, that the measurement with the noise diode is essential for the adjustment of sampling delays, which means that this measurement can not be used for the measurement of drift as well. For measurements with the matched load, the results are shown in Table 4. The radiometric ΔT has increased to 0,14 K, due to the factor $\sqrt{2}$ from Stokes vector definition. Again it is seen, that the mean deviation for the circles is of the order of the radiometric sensitivity, and a mean for the two correlation channels of 0.16 K is observed.

[30] Generally it may be concluded from the observations of the calibration targets, that the radiometer has some small deviations over a data take, but taking the radiometric sensitivity into account, it seems likely, that a drift of 0.10 K over a full circle flight is a realistic value. In the data processing of the ocean measurements the calibration targets are used to correct the acquired data, and a first order correction for the drift is applied. With this result a further analysis of the radiometric data with respect to eventual wind signatures of the sea surface is believed to be possible with sufficient accuracy. This analysis is ongoing, and will soon be the subject of proper publications.

4. Instrument Improvements

[31] The L-band polarimetric correlation radiometer is designed with a field programmable gate array (FPGA)

Table 3. Radiometer Drift in Detection Channels During Data Take of a Full Circle[a]

	Horizontal Channel		Vertical Channel	
Data Take Length, s	Δ, K (Ld)	Δ, K (Ld + N)	Δ, K (Ld)	Δ, K (Ld + N)
84	0.12	0.36	0.01	0.31
96	0.08	0.29	0.11	0.24
135	0.17	0.15	0.11	0.28
258	0.09	0.06	0.03	0.11
Mean of all circles	0.12	0.22	0.07	0.24
Radiometric ΔT	0.10	0.14	0.10	0.14

[a]Here Ld means load and N means noise diode.

Table 4. Radiometer Drift in Correlation Channels During Data Take of a Full Circle

	Third Stokes (U)	Fourth Stokes (V)
Data Take Length, s	Δ, K (Load)	Δ, K (Load)
84	0.1	0.05
96	0.15	0.06
135	0.21	0.15
258	0.25	0.31
Mean of all circles	0.18	0.14
Radiometric ΔT	0.14	0.14

in the digital front-end, giving full flexibility for reconfiguration.

1. In order to exploit the analog RF-filter stopband attenuation completely, a different sampling frequency is required, as the image spectrum is situated only 6 MHz away from the selected filter bandwidth. By increasing the distance to 10 MHz, a image rejection of more than 60 dB could be obtained (compared to 25 dB in the present configuration).

2. An increase in the RF bandwidth would result in a better sensitivity, but also a higher probability of interference signals. In the digital domain, a second filter can provide additional modification to the frequency band selected by the RF-filter, allowing selective suppression of possible interference signals. This would, however, also require a higher sampling frequency, as the general sampling theorem, stating that $f_s \geq 2 \cdot BW$, must be fulfilled.

3. A special time domain filtering may be applied to avoid pulsed interference signals. Dividing each integration period into shorter sub-periods, and evaluating the power level of each sub-period, will enable rejection, if the signal level changes significantly beyond the level of radiometric noise. The sub-period integration can then be followed by a longer integration to e.g. 8 msec. (to reduce the data amount), keeping the number of rejected sub-periods in mind.

4. A phase shift like the one provided by the two analog quadrature hybrids, can also be made digitally, or alternatively a full digital I/Q demodulaton can be implemented. A digital solution would reduce the number of components, analog as well as digital, i.e. reduce size, weight, power consumption and cost. Demand for higher sampling frequency and digital processing power will arise, but modern FPGA technologies provide sufficient resources to implement the necessary logic.

5. Conclusions

[32] A new polarimetric correlation radiometer has been designed, build and operated. As the radiometer employs subharmonic sampling, special considerations regarding the analog and digital circuit has been discussed. The system features several advantages as compared with a traditional superheterodyne receiver: weight, size and flexibility for reconfiguration. The system has been used for measuring the brightness temperature over the ocean in experiments carried out in 2001, in order to determine the influence of the wind at the L-band brightness temperature. With respect to stability, preliminary results show good overall radiometer stability, within the time it takes to do a circle flight (maximum 5 min).

References

Oppenheim, A. V., and R. W. Schafer, *Digital Signal Processing*, Prentice-Hall, Old Tappan, N. J., 1975.

Skou, N., B. Laursen, and S. Søbjærg, Polarimetric radiometer configurations: Potential accuracy and sensitivity, *IEEE Trans. Geosci. Remote Sens.*, *37*, 2165–2171, 1999.

Thompson, A. R., J. M. Moran, and G. W. Swenson, *Interferometry and Synthesis in Radio Astronomy*, John Wiley, New York, 1986.

J. Rotbøll, N. Skou, and S. S. Søbjærg, Ørsted/DTU, Electromagnetic Systems, Technical University of Denmark, DK-2800 Lyngby, Denmark. (ns@oersted.dtu.dk)

Synchronization of tandem A/D converter for SAR

JØRGEN DALL,

STEN SCHMIDL SØBJÆRG, and

ERIK LINTZ CHRISTENSEN

Ørsted-DTU, Electromagnetic Systems, Building 348

Technical University of Denmark

DK 2800 Lyngby, Denmark

This conference paper is published in the Proceedings of EuSAR 2002, pp. 323-326, 2002.

SYNCHRONIZATION OF TANDEM A/D CONVERTER FOR SAR

J. Dall, S.S. Søbjærg, and E.L. Christensen

Electromagnetic Systems, Ørsted•DTU, Technical University of Denmark
Ørsteds Plads 348, DK-2800 Kongens Lyngby, Denmark
Tel: +45 4525 3800, Fax: +45 4593 1634, E-mail: jd@oersted.dtu.dk

ABSTRACT

Synthetic Aperture Radar (SAR) receivers are typically based on quadrature demodulation. Until recently, wideband quadrature demodulation has been confined to the analog domain, but technology now allows implementation in the digital domain. Digital demodulation requires the sampling rate to be doubled, but some analog-to-digital converters (ADCs) have an analog bandwidth exceeding twice their maximum sampling rate. This enables two ADCs to be operated in tandem, acquiring the even samples and odd samples, respectively. In this case both the analog and the digital quadrature receivers require two ADCs each sampling at a rate no less than the single-sided bandwidth of the radar signal, and both implementations call for an accurate ADC synchronization. This paper shows that under certain circumstances this synchronization can be controlled with a signal derived from the SAR data.

1 INTRODUCTION

A new generation of the Danish airborne SAR is under development. Technology now allows the analog-to-digital conversion in wideband SAR systems to be moved from baseband to intermediate frequency. Therefore, it has been decided to develop two different receivers in parallel. Ultimately, the more successful candidate will be integrated in the SAR system.

One receiver converts the received RF signal down to an intermediate frequency where it is sampled and transferred to a digital quadrature demodulator. The other receiver converts the received RF signal down to an intermediate frequency where an analog quadrature demodulation converts the signal to baseband I/Q signals. Monolithic Microwave Integrated Circuit (MMIC) technology has been adopted for the down-converter and the analog quadrature demodulator to assure the required bandwidth with minimum distortion.

When sampling the in-phase and quadrature signals provided by an analog quadrature demodulator, the two analog-to-digital converters (ADC) must be clocked simultaneously. In wideband SAR systems the sampling interval is on the order of 1 ns and hence the relative timing errors must be much smaller than that.

Digital quadrature demodulation has several advantages [1], [2]. For instance, the digital demodulator does not have low frequency or DC offset problems as the DC ends up outside the bandwidth of the signal. Since the local oscillator signals are digitally generated they have perfect orthogonality, and proper choice of the local oscillator frequency makes the mixing extremely simple.

When two ADCs are operated in concert to sample a single real signal they must be clocked exactly 180° out of phase in order to ensure equidistant sampling. Any inaccuracy in the clock synchronization will deteriorate the signal a way similar to that of an imperfect quadrature demodulator.

In the analog and digital quadrature receivers self-aligning ADCs are preferable in order to prevent clock drift. The following sections demonstrate that clock synchronization can be ensured with a control signal based on the cross-correlation of the two ADC output signals. The basic technique has been proposed previously [3]. The control signal is used as feedback to programmable digital delay devices in the ADC clock circuits. Under certain circumstances no dedicated test signals are required, only the ordinary backscatter data.

Section 2 addresses the ADC synchronization in case of an analog demodulator with ideal quadrature properties. Section 3 addresses the ADC synchronization in relation to the digital quadrature demodulator and finally, Section 4 summarizes the results.

2 IDEAL I/Q DEMODULATOR

In this section the cross-correlation of the sampled demodulator outputs is derived (6) and its potential for ADC clock control is assessed.

It is assumed that the analog quadrature demodulator is perfect, i.e. its local oscillators are in exact quadrature, the I and Q transfer functions are identical, and the I and Q signals are perfectly lowpass filtered. This is illustrated in Figure 1a-e, where $R(f)$ is the spectrum of the real input signal, S_{cos} and S_{sin} are the spectra of the two local oscillator signals, $\cos(2\pi f_o t)$ and $-\sin(2\pi f_o t)$, respectively, and I_a and Q_a are the spectra of the two analog quadrature signals. Figure 1f-g shows the spectra of the quadrature signals sampled at a rate f_s

$$\begin{aligned} i(n) &= i_a(t) \quad , t = n/f_s \\ q(n) &= q_a(t-\tau), t = n/f_s, \quad \tau \approx 0 \end{aligned} \qquad (1)$$

The sampling frequency must exceed the signal bandwidth, but not necessarily be twice the local oscillator frequency, as in Figure 1. If the synchronization of the two ADCs is perfect, i.e. if $\tau = 0$, the lower band (the dashed one which is the complex conjugate of the solid one) cancels in the complex signal

$$c(n) = i(n) + jq(n) \qquad (2)$$

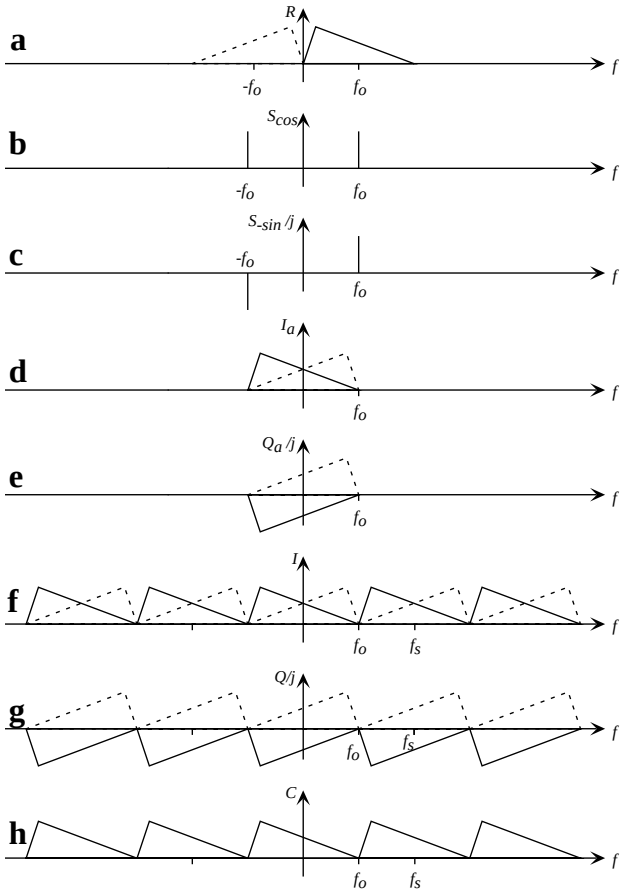

Figure 1: *Spectra related to analog I/Q demodulation.*

This is illustrated in Figure 1h. In terms of the spectrum, C, of this complex signal the spectra of the sampled quadrature signals are

$$\begin{aligned} I(f) &= \frac{1}{2}\Big(C^*(-f)+C(f)\Big) \\ Q(f) &= \frac{j}{2}\Big(C^*(-f)-C(f)\Big)\, e^{-j2\pi f\tau} \end{aligned} \qquad (3)$$

If $i(n)$ and $q(n)$ each have N real samples the correlation is

$$R_{iq}(\tau) = \sum_{n=0}^{N-1} i(n)q(n) \qquad (4)$$

Application of (A2) from Appendix A and subsequent insertion of (3) gives

$$\begin{aligned} R_{iq}(\tau) &= \frac{1}{2f_o}\int_{-f_o}^{f_o} I(f)Q^*(f)\,df = \\ &-\frac{j}{8f_o}\int_{-f_o}^{f_o}\Big(|C(-f)|^2-|C(f)|^2\Big)e^{j2\pi f\tau}\,df \\ &+\frac{j}{8f_o}\int_{-f_o}^{f_o}\Big(C^*(-f)C^*(f)-C(f)C(-f)\Big)e^{j2\pi f\tau}\,df \end{aligned} \qquad (5)$$

Appendix B shows that for a SAR signal the last integral has zero mean. The first integral is the inverse Fourier transform of the difference between two power spectra, i.e. the difference between two autocorrelation functions

$$\begin{aligned} R_{iq}(\tau) &\approx \frac{j}{4}\Big(R_c(\tau)-R_c(-\tau)\Big) \\ &= \frac{j}{2}\mathrm{im}\Big(R_c(\tau)\Big) \end{aligned} \qquad (6)$$

im(z) denotes the imaginary part of z. (6) takes advantage of the complex conjugate symmetry of R_c, the autocorrelation function of the complex signal c. R_{iq} is zero if the ADCs are perfectly synchronized, but the correlation technique fails if the SAR signal has a real, even R_c because this makes R_{iq} zero, independently of the timing error, τ. R_c is even and real if c has an even power spectrum i.e. if the real input for the quadrature demodulator has an upper power spectrum that is symmetric about the local oscillator frequency f_o, see Figure 1a.

Fortunately, R_{iq} is quite sensitive to deviations from spectral symmetry. The reason is that both the mean and the standard deviation of the estimated R_c difference in (6) tend towards zero as τ approaches zero, no matter if C is symmetric or not. Thus, the zero is not obscured by a large standard deviation. Indeed, the integral that was ignored in (6) has a finite, τ-independent standard deviation, but this is proportional to the square root of the number of samples while the mean of R_c is proportional to the first power of the number of samples.

It is emphasized that a symmetric R-spectrum is not prohibitive unless the point of symmetry is f_o. If for instance R a is rectangular spectrum with a bandwidth B that is offset from f_o by f_Δ, then (6) becomes

$$R_{iq}(\tau) \approx -\frac{1}{2}\frac{\sin(\pi B\tau)}{\pi B\tau}\sin(2\pi f_\Delta\tau) \qquad (7)$$

R_{iq} is zero when the ADC synchronization is perfect. Also, R_{iq} is an odd function of τ, which is good when the control loop has to keep the test parameter at zero.

Søbjærg and Christensen suggested using a dedicated test signal [3]. This is necessary if the odd component of C is too small for (6) to be applied reliably to the radar signal. For a deterministic test signal (5) should be preferred to (6), as the assumption leading to (6) is generally not valid, cf. Appendix B.

3 DIGITAL I/Q DEMODULATOR

In this section the cross-correlation of the signals constituted by even and odd samples is derived (16) and its potential for ADC clock control is assessed.

In the physical implementation the two ADCs are fed with the same analog signal, a, and they are clocked at the same rate, $f_s/2$, but 180° out of phase. Note that f_s is not the sampling frequency of a single ADC but that resulting when interleaving the samples from the even ADC and the odd ADC. To take full advantage of the digital quadrature demodulation the frequency of the digital local oscillators must be $f_o = f_s/4$.

The following analysis is simplified by assuming the even and odd signals to be generated with an alternative approach. The result, however, is exactly the same as that of the physical implementation. The ADCs are now assumed to be fed with signals having a relative shift, τ, which is ideally one sample

$$\begin{aligned} e_a(t) &= a(t) \\ o_a(t) &= a(t-\tau), \quad \tau \approx 1/f_s \end{aligned} \tag{8}$$

and the ADCs are assumed to be clocked simultaneously

$$\begin{aligned} e(n) &= \begin{cases} e_a(t), & n \text{ even}, t = n/f_s \\ 0, & n \text{ odd} \end{cases} \\ o(n) &= \begin{cases} o_a(t), & n \text{ even}, t = n/f_s \\ 0, & n \text{ odd} \end{cases} \end{aligned} \tag{9}$$

This means that the combined digital signal becomes

$$d(n) = e(n) + o(n+1) \tag{10}$$

Figure 2 illustrates the spectra. First the spectrum of the analog complex baseband signal, c. c is equivalent to the real signal with the spectrum in Figure 2b. The temporal shift of o_a adds the linear spectral phase in Figure 2d to the phase of the original spectrum in Figure 2c. In terms of the spectrum, C, of the complex signal the spectra of the analog signals e_a and o_a can be expressed as

$$\begin{aligned} E_a(f) &= C(f-f_o) + C^*(-f_o-f) \\ o_a(f) &= C(f-f_o)\, e^{-j2\pi ft} + C^*(-f_o-f)\, e^{-j2\pi ft} \end{aligned} \tag{11}$$

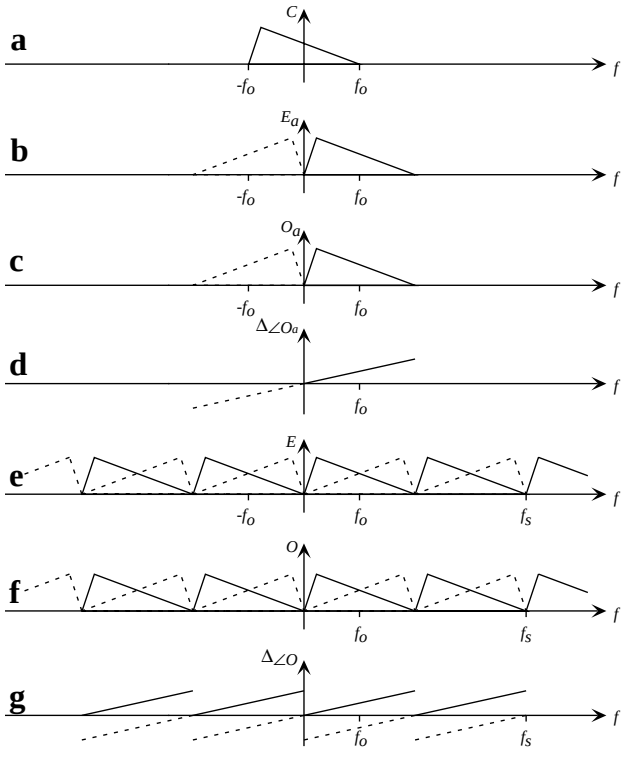

Figure 2: *Spectra related to digital I/Q demodulation.*

Since the spectra of the sampled signals repeat with a period of $f_s/2 = 2f_o$ they are subject to aliasing as shown in Figure 2e-g. The result for $0 \le f \le f_s/2$ can be found by substituting f-$2f_o$ for f in the last terms in (11)

$$\begin{aligned} E(f) &= C(f-f_o) + C^*(f_o-f) \\ O(f) &= C(f-f_o)\, e^{-j2\pi ft} + C^*(f_o-f)\, e^{-j2\pi(f-2f_o)\tau} \\ &= \left(C(f-f_o) + C^*(f_o-f)\, e^{j\pi f_s\tau} \right) e^{-j2\pi ft} \end{aligned} \tag{12}$$

The correlation of N real samples from each of the signals $e(n)$ and $o(n)$ is

$$R_{eo}(\tau) = \sum_{n=0}^{2N-2} e(n)o(n) \tag{13}$$

Using (A1) and the spectral periodicity, this correlation can be rewritten as

$$R_{eo}(\tau) = \frac{1}{2f_o} \int_0^{2f_o} E(f)O^*(f)\, df \tag{14}$$

Now a frequency substitution is introduced in order to simplify the integration after insertion of the spectra from (12)

$$\begin{aligned} R_{eo}(\tau) &= \int_{-f_o}^{f_o} E(f+f_o)O^*(f+f_o)\, df = \\ &\int_{-f_o}^{f_o} \left(|C(f)|^2 + |C(-f)|^2\, e^{-j\pi f_s\tau} \right) e^{j2\pi(f+f_o)\tau}\, df \\ &+ \int_{-f_o}^{f_o} \left(C(f)C(-f)\, e^{-j\pi f_s\tau} + C^*(-f)C^*(f) \right) e^{j2\pi(f+f_o)\tau}\, df \end{aligned} \tag{15}$$

Appendix C shows that for a SAR signal the last integral has zero mean. The first integral is the inverse Fourier transform of the sum of two power spectra, i.e. it is the sum of two autocorrelation functions

$$\begin{aligned} R_{eo}(\tau) &\approx \left(R_c(\tau) + R_c(-\tau)\, e^{-j\pi f_s\tau} \right) e^{j2\pi f_o\tau} \\ &= R_c(\tau)\, e^{j2\pi f_o\tau} + R_c(-\tau)\, e^{-j2\pi f_o\tau} \\ &= 2 \cdot re\left(R_c(\tau)\, e^{j\pi f_s\tau/2} \right) \end{aligned} \tag{16}$$

re(z) denotes the real part of z. (16) takes advantage of the complex conjugate symmetry of R_c, the autocorrelation function of the complex signal c. If R_c is an even, real function, i.e. if the power spectrum of c is even, (16) becomes

$$R_{eo}(\tau) \approx 2 \cdot R_c(\tau) \cdot \cos(\pi f_s\tau/2), \quad |C(f)| \text{ even} \tag{17}$$

In this case, perfect ADC synchronization ($\tau = 1/f_s$) results in total decorrelation. It is noted that the first zero of R_c is located at $\tau > 1/f_s$ and consequently, a positive or

negative correlation corresponds to a τ that is slightly too small or too large, respectively.

(16) shows that if the power spectrum of c has an odd component the phase of R_c displaces the R_{eo}-zero from $\tau = 1/f_s$. Computing the difference between two correlation coefficients eliminates this problem

$$\begin{aligned}\Delta_R &= \sum_{n=0}^{2N-2} e(n)o(n) - \sum_{n=0}^{2N-2} e(n)o(n+1) \\ &= R_{eo}(\tau) - R_{eo}(\tau - 2/f_s) \\ &= R_{eo}(\Delta_\tau + 1/f_s) - R_{eo}(\Delta_\tau - 1/f_s) \\ &\approx 2\,re\left(\left(R_c(1/f_s + \Delta_\tau) + R_c^*(1/f_s - \Delta_\tau)\right)e^{j\pi(f_s\Delta_\tau+1)/2}\right)\end{aligned} \qquad (18)$$

To emphasize the symmetry, $\Delta_\tau + 1/f_s$ has been substituted for τ. The R_c-sum in (18) is an even function of Δ_τ and hence Δ_R is an odd function of Δ_τ. This is favorable to a zero-searching control loop. For almost perfect sampling ($\Delta_\tau \approx 0$), (18) can be approximated as

$$\Delta_R \approx 4 \cdot re\left(R_c(1/f_s)\right) \cdot \sin(\pi f_s \Delta_\tau / 2) \qquad (19)$$

Søbjærg and Christensen [3] have also suggested computing the quantity Δ_R, but their purpose was not to eliminate the effect of spectral asymmetry.

4 CONCLUSIONS

This paper has analyzed the potential of estimating the synchronization error in two tandem ADC applications, viz. analog and digital quadrature demodulation. Based on the cross-correlation of the two ADC output signals the estimated error should be fed back to programmable digital delay devices in the ADC clock circuits.

If the spectrum of the complex SAR signal out of the analog demodulator is even it cannot be used for the correlation. A minor spectral asymmetry/shift with respect to the local oscillator frequency is likely to suffice, but if not, a dedicated test signal must be used. The correlation technique provides a control signal, which is an odd function of the clock error. This implies a zero for perfect ADC synchronization.

A symmetric SAR spectrum is not a problem in relation to sampling of a real signal with tandem ADCs. In this case the cross-correlation provides a control signal that has a zero and a sign change when the ADC clocking is perfect. This is not the case if the SAR signal has a spectral asymmetry. However, the difference between two cross-correlation coefficients constitutes a control signal, which excels by being an odd function with a zero at perfect synchronization.

5 APPENDIX A

The cross-correlation of two complex signals is the inverse Fourier transform of the cross-spectrum

$$\sum_{n=0}^{N-1} a(n+k)b^*(n) = \frac{1}{2f_o}\int_{-f_o}^{f_o} A(f)B^*(f)\,e^{j2\pi kf/f_s}\,df \qquad (A1)$$

For $k = 0$ (A1) becomes

$$\sum_{n=0}^{N-1} a(n)b^*(n) = \frac{1}{2f_o}\int_{-f_o}^{f_o} A(f)B^*(f)\,df \qquad (A2)$$

6 APPENDIX B

Interpreting the last integral in (5) as an inverse Fourier transform converts it to a convolution of two complex signals in the time domain

$$\begin{aligned}x(\tau) &= j\int_{-f_o}^{f_o}\left(C^*(-f)C^*(f) - C(f)C(-f)\right)e^{j2\pi f\tau}\,df \\ &= j\left(c^*(\tau)\otimes c^*(-\tau) \;-\; c(\tau)\otimes c(-\tau)\right) \\ &= 2\cdot im\left(c(\tau)\otimes c(-\tau)\right)/j\end{aligned} \qquad (B1)$$

x has a zero mean for c a linear chirp (correlation of up- and down chirp). Also, the mean is zero for c a SAR pulse reflected from a distributed scene (circular symmetric Gaussian signal). However, x does not always have a zero mean, e.g. $c(\tau) = (1+j)\cos(2\pi f\tau)$.

7 APPENDIX C

Interpreting the last integral in (15) as an inverse Fourier transform converts it to a convolution of two complex signals in the time domain

$$\begin{aligned}y(\tau) &= \int_{-f_o}^{f_o}\Big(C(f)C(-f)\,e^{-j\pi f_s\tau} + \\ &\qquad C^*(-f)C^*(f)\Big)e^{j2\pi(f+f_o)\tau}\,df \\ &= c(\tau)\otimes c(-\tau)e^{-j2\pi f_o\tau} + c^*(\tau)\otimes c^*(-\tau)e^{j2\pi f_o\tau} \\ &= 2\cdot re\left(c(\tau)\otimes c(-\tau)\,e^{-j2\pi f_o\tau}\right)\end{aligned} \qquad (C1)$$

The comments to (B1) apply to (C1), too.

8 REFERENCES

[1] J.H. Jørgensen, "Digital Demodulator for Wide Bandwidth SAR", Proceedings of the International Geoscience and Remote Sensing Symposium, IGARSS´2000, Vol. V, 2000, pp. 2269-2271.

[2] J. Dall and E. Lintz Christensen: "Multiplier-free Filters for Wideband SAR", Proceedings of the International Geoscience and Remote Sensing Symposium, IGARSS´2001, Vol. IV, 2001, pp. 1568-1570.

[3] S. Schmidl Søbjærg and E. Lintz Christensen, "2GHz Self-aligning tandem A/D Converter for SAR", Proceedings of the International Geoscience and Remote Sensing Symposium, IGARSS´2001, Vol. V, 2001, pp. 2028-2030.

Measurement of Wind Signatures on the Sea Surface using an L-band Polarimetric Radiometer

STEN SCHMIDL SØBJÆRG,

JESPER ROTBØLL, and

NIELS SKOU

Ørsted-DTU, Electromagnetic Systems, Building 348

Technical University of Denmark

DK 2800 Lyngby, Denmark

This conference paper is published in the Proceedings of IGARSS'02, vol. V, pp. 1364-1366, July 2002.

Measurement of Wind Signatures on the Sea Surface using an L-band Polarimetric Radiometer

Sten Schmidl Søbjærg, *Student Member*, *IEEE*, Jesper Rotbøll, *Member*, *IEEE*
and Niels Skou, *Senior Member*, *IEEE*
Ørsted•DTU, Technical University of Denmark,
DK-2800 Kgs. Lyngby, Denmark (e-mail: sss@oersted.dtu.dk)

Abstract – A series of circle flights have been carried out over the wind driven sea, using the EMIRAD L-band polarimetric radiometer, described in [1]. Data are calibrated and corrected for aircraft attitude, and 360 degrees azimuth profiles are generated. The results show some variation over a full circle, typically about 1 K, and no clear, repeated azimuth signature from circle to circle is identified. Averaging reduces the variations, and frequency analysis of the profiles show an almost flat spectrum, which excludes a simple extrapolation of wind signatures, known at higher frequencies.

I. Introduction

An L-band (1.4 GHz) radiometer system, based on novel interferometric techniques, and known under the acronym SMOS (soil moisture ocean salinity), has been selected as one of ESA's Earth Explorer Opportunity Missions. Measuring the L-band brightness temperature over the oceans enables a determination of sea salinity.

The brightness temperature sensitivity to salinity is at best (open ocean with high salinity) $\Delta TB / \Delta S = 1K / psu$ (vertical polarization, 50° incidence angle). To find salinity to the 0.1 psu level hence requires radiometric measurements to better than 0.1 K, and knowledge concerning the influence from other effects to the same level.

Sea surface temperature is one of these effects, but as it is well modeled and understood, and the ocean temperature is well monitored by other sensors, the correction is doable. But, the knowledge about the influence of wind on the brightness temperature has been identified as insufficient. Measurements and model work have concentrated on higher frequencies, and very little knowledge about any polarimetric signatures – i.e. the brightness temperature dependence on azimuth viewing angle - exists. The paper will discuss the results from an airborne campaign, aimed at filling this void, and data for different wind conditions are analyzed for presence of eventual harmonic components in the azimuth signatures.

II. The L-band radiometer

The EMIRAD Radiometer is a polarimetric radiometer, measuring the full Stokes vector simultaneously. For brightness temperatures the Stokes vector is defined as

$$\overline{T_B} = \begin{pmatrix} I \\ Q \\ U \\ V \end{pmatrix} = \begin{pmatrix} T_V + T_H \\ T_V - T_H \\ T_{45^\circ} - T_{-45^\circ} \\ T_l - T_r \end{pmatrix} = \frac{\lambda^2}{k \cdot z} \begin{pmatrix} \langle E_V^2 \rangle + \langle E_H^2 \rangle \\ \langle E_V^2 \rangle - \langle E_H^2 \rangle \\ 2\,\mathrm{Re}\langle E_V E_H^* \rangle \\ 2\,\mathrm{Im}\langle E_V E_H^* \rangle \end{pmatrix} \quad (1)$$

where z is the impedance of the medium in which the wave propagates, λ is the wavelength, and k is Boltzmanns constant. T_V is the vertical and T_H the horizontal brightness temperature. T_{45° and T_{-45° represent orthogonal linearly polarized measurements, skewed 45° with respect to normal, and T_l and T_r refer to left-hand and right-hand circular polarized fields.

The EMIRAD radiometer uses two detection channels to measure T_V and T_H, and I and Q are found from addition and subtraction. U and V are calculated from the real and imaginary parts of the complex cross correlation between T_V and T_H.

The radiometer is based on digital down conversion and detection techniques, and it covers the same frequency band as SMOS. It has been applied for a series of measurements over Danish waters in order to understand polarimetric L-band signatures from the ocean. Two flights were carried out in the spring of 2001 and one in October 2001.

A C-130 aircraft is used as platform, and the instrument is mounted side looking with a fixed depression angle of 23 degrees, enabling measurements at incidence angles from 22 degrees to 62 degrees by varying the aircraft banking. Each flight consists of a number of full 360 degrees circles around the same target area. The incidence angles is kept unchanged for three circles, then increased by steps of 10 degrees, thus sampling a set of full azimuth signatures.

III. Data calibration and stability

For the data calibration, the radiometer has a built-in reference load in each channel. The receiver inputs are connected to the loads or the antenna, using a standard coaxial switch. The radiometer also features a noise diode, injecting correlated noise into the two receivers along with the antenna/load signal. This gives a second calibration point

for the two detection channels, along with a test signal to the digital correlators.

Before and after each data acquisition, the radiometer carries out a sequence, observing the load, the load with the noise diode, and the antenna with the noise diode for about 500 msec each. A first order interpolation of the calibration data can be made for the time of data acquisition, and with the two internal calibration points from the load and from the load with noise, a calibration of gain and noise temperature of the instrument at the input ports can be estimated.

Finally the measured brightness temperatures are corrected for external losses, i.e. antenna, cables, and orthomode transducer. The external components are monitored by temperature sensors, and using these data for a simple calibration along with the estimated losses, the radiometer data may reach a level of absolute calibration about a few Kelvin, which is sufficient for this kind of experiment.

The relative accuracy depends on the stability of the instrument within the duration of a full circle, typically from 30 sec to 5 minutes. Experiments with the instrument exposed to changing environmental conditions indicate, that a typical drift is below 0.1 K, with even better potential, when the instrument is given time to stabilize its temperature. Calibration data from the flights have been investigated regarding drifts, and typically the value is below 0.05 K, which is satisfactory for the experiment.

IV. Attitude Correction

The calibrated data represent the incident field on the radiometer antenna in the aircraft coordinate system. When the aircraft moves, the coordinate system changes relative to the ground coordinate system, and the measured Stokes parameters will vary with aircraft pitch, roll, and yaw.

An aircraft pitch will rotate the antenna aperture around the antenna pointing vector, rotating the receiving H-V with respect to the desired plane. The measured stokes vector can be expressed as

$$\begin{pmatrix} I_m \\ Q_m \\ U_m \\ V_m \end{pmatrix} = \begin{pmatrix} 1 & 0 & 0 & 0 \\ 0 & \cos(2\theta) & \sin(2\theta) & 0 \\ 0 & -\sin(2\theta) & \cos(2\theta) & 0 \\ 0 & 0 & 0 & 1 \end{pmatrix} \cdot \begin{pmatrix} I \\ Q \\ U \\ V \end{pmatrix} \quad (2)$$

where θ is the rotation angle. It can be calculated, that even a small pitch of 1° will result in an error of about 1 K in the third Stokes parameter, when a typical value of Q=25 K is assumed. Corrections can be applied, however, if the aircraft pitch is known, multiplying the inverse matrix to the measured data.

For roll variations, the antenna pointing is changed, i.e. the incidence angle is not constant. For the 23 degrees of antenna depression, the actual incidence angle is given by

$$\alpha = 90^O - 23^O - \varphi \quad (3)$$

where φ is the roll angle. Due to the changing incidence angle, the measured first and second Stokes parameters will vary during a circle flight as described in the Klein-Swift model [2]. T_H and T_V may be corrected using the model, however, giving a circle profile at a nominal incidence angle. The corrected signal is found by

$$T_C = T_M - \left(M(\varphi) - M(\varphi_N)\right) \quad (4)$$

where T_C is the corrected brightness temperature, T_M the measured brightness temperature, and M represents the modeled brightness for the actual roll angle, φ, and the nominal roll angle, φ_N. For a typical incidence angle, the sensitivity of the second Stokes parameter to attitude variations is of the order of 1 K per degree roll.

To correct the pitch and roll errors, the aircraft attitude is measured continuously during the flights using an INU (Inertial Navigation Unit), mounted directly on the aircraft floor. The unit gives the wanted parameters with a precision of 0.1 degree, along with the ground speed, the aircraft position and the true heading.

V. Data Presentation

Data from the three flights are subject to the same processing, which consists of the mentioned calibration and the attitude corrections. Moreover the data are integrated to 5 sec., giving a theoretical sensitivity less than $\Delta T = 0.05$ K. Finally the data sets are aligned to the true heading, enabling comparison of subsequent circles for recognition of eventual signatures or for integration of tracks.

Flights have been carried out for medium wind speeds of 5 m/s, 8 m/s and 10 m/s, and a typical full Stokes parameter signature is seen in figure 1a-d, carried out nominally at 42 degrees incidence angle.

In some cases azimuth signals seem stable over two circles, but then change in a third. In the example from figure 1a-d, the curves show the first circle out of three, but the profile shape is repeated in the second circle. In the third circle, however, the profile appears as shown in figure 2a-d.

For the other incidence angles, the same type of signatures are seen, typically showing variations up to ±1 K, without clear repetition from circle to circle. Calculating the mean profile from three circles reduce the variations, but still no clear profile appears.

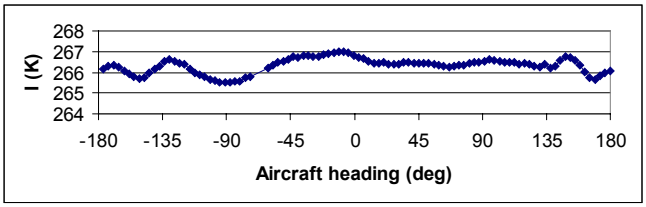

Fig.1a, 1st Stokes parameter, I, for 42 deg. incidence angle

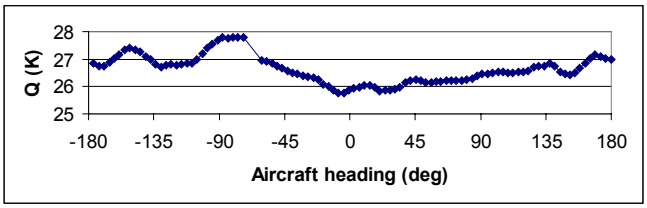

Fig.1b, 2nd Stokes parameter, Q, for 42 deg. incidence angle

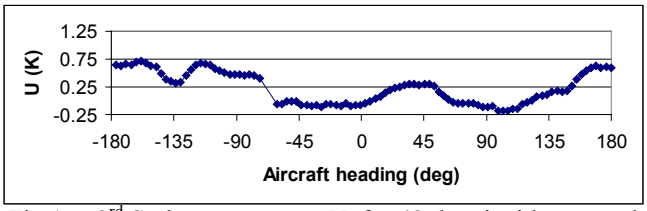

Fig.1c, 3rd Stokes parameter, U, for 42 deg. incidence angle

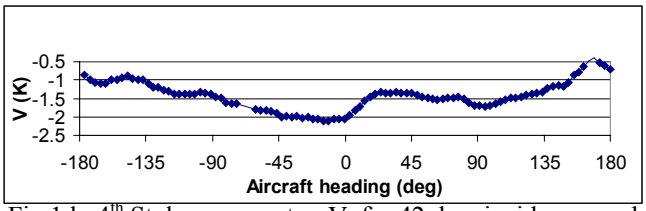

Fig.1d, 4th Stokes parameter, V, for 42 deg. incidence angle

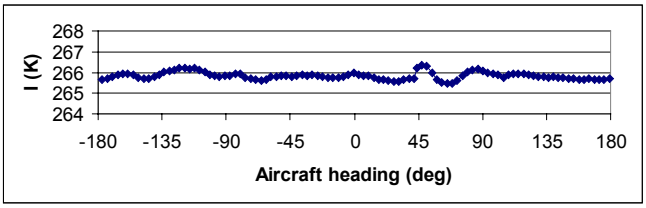

Fig.2a, 1st Stokes parameter, I, for 42 deg. incidence angle

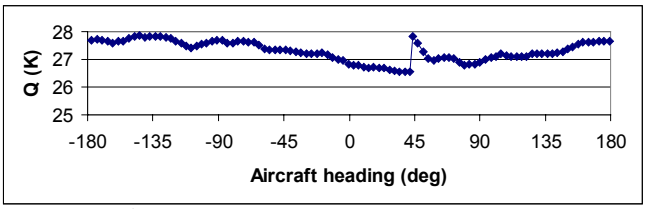

Fig.2b, 2nd Stokes parameter, Q, for 42 deg. incidence angle

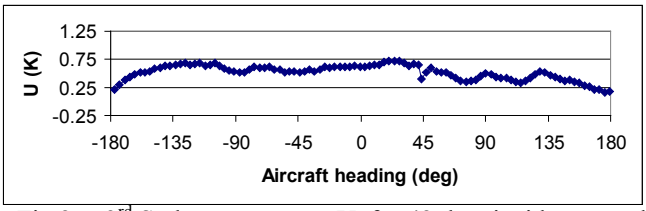

Fig.2c, 3rd Stokes parameter, U, for 42 deg. incidence angle

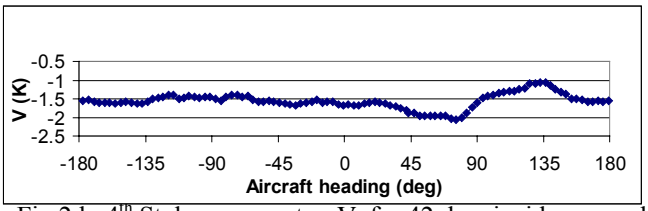

Fig.2d, 4th Stokes parameter, V, for 42 deg. incidence angle

Finally it has been tried to make a harmonic analysis in order to identify an eventual first or second harmonic, relative to the wind direction. Results, however, show an almost flat frequency spectrum without a clear peak, and the phase of the first and second harmonic is random from circle to circle.

VI. CONCLUSIONS

Generally it can be concluded, that no unique signature can be identified from the three flights with the present processing. Instrument stability is considered, and from the reference data, acquired right before and right after each data take, it may be concluded, that typical drifts are about 0.05 K.

Geophysical noise may explain some of the observed variations, as the antenna footprint only covers an area of 500 m by 500 m. Changing the flight altitude to improve spatial integration has been tried during the latest flight, but no clear reduction of the noise is observed. Larger wave structures as well as local changes in wind speed and wind direction may create some variations in the received signals, and future flights will focus on the problem of geophysical noise, taking a larger number of circles at each incidence angle. Averaging may finally help to identify eventual wind driven, polarimetric signatures at L-band.

REFERENCES

[1] J. Rotbøll, S.S. Søbjærg and N. Skou, "L-Band Polarimetric Correlation Radio Radiometer with Subharmonic Sampling", *Proceedings of the International Geoscience and Remote Sensing Symposium, IGARSS 2001*, Vol. IV, pp1571 - 1574.

[2] L.A. Klein and C.T. Swift, "An Improved Model for the dielectric constant of Sea Water at Microwave Frequencies", *IEEE Trans. on Antennas and Propagation*, Vol. AP-25, No. 1, January 1977, pp 104 - 111.